THE STRUCTURES OF CLEAN RHODIUM SURFACES STUDIED BY LOW-ENERGY ELECTRON DIFFRACTION

by

PHILIP RICHARD WATSON

B.A. (Nat. Sci.) Hons, Oxford University, 1974

A THESIS SUBMITTED IN PARTIAL FULFILLMENT OF
THE REQUIREMENTS FOR THE DEGREE OF
DOCTOR OF PHILOSOPHY

in

THE FACULTY OF GRADUATE STUDIES
(Department of Chemistry)

We accept this thesis as conforming
to the required standard

THE UNIVERSITY OF BRITISH COLUMBIA

October, 1978

In presenting this thesis in partial fulfilment of the requirements for an advanced degree at the University of British Columbia, I agree that the Library shall make it freely available for reference and study. I further agree that permission for extensive copying of this thesis for scholarly purposes may be granted by the Head of my Department or by his representatives. It is understood that copying or publication of this thesis for financial gain shall not be allowed without my written permission.

Department of CHEMISTRY

The University of British Columbia
2075 Wesbrook Place
Vancouver, Canada
V6T 1W5

Date Nov. 14, 1978

ABSTRACT

This thesis describes the determination of the structures of the (111), (100) and (110) surfaces of rhodium by low-energy electron diffraction (LEED). In this work the photographic method of Stair et al was refined so that LEED patterns stored on photographic film were analysed by a computer-controlled Vidicon T.V. camera system to give intensity v. energy, or I(E), curves for the various diffracted beams. This approach was tested for a Cu(111) surface; I(E) curves determined in this new way were compared with intensities measured previously with a Faraday cup collector.

Structural analyses were performed by comparing experimental intensities with those calculated with the multiple-scattering programs of Van Hove and Tong. Checks were made against some previously published calculations to ensure that the programs were running correctly. For calculations on surfaces of both rhodium and copper, an ion-core scattering potential from a band structure calculation was compared with one constructed by superposing the charge densities of a cubo-octahedral cluster of metal atoms.

The degree of agreement between experimental and calculated diffracted beam intensities was determined with a reliability-index proposed recently by Zanazzi and Jona. Here, the analysis of Zanazzi and Jona was extended to enable assessments to be made of the uncertainties in the structural parameters which give the best correspondence between experimental and calculated

I(E) curves. The effects of independent measurements of intensities, and of changes in the non-structural parameters for the calculations upon the reliability of the derived structural results were also examined in some detail.

All three rhodium surfaces were found to be unreconstructed at room temperature and above, each surface being a simple termination of the bulk crystalline stacking sequence. However, the topmost interlayer spacing did show some variation from the bulk value. The (110) surface showed a contraction of 2.7±2.0% relative to the bulk interlayer separation, while the (111) and (100) surfaces showed small (-1±3%) and 0±2.5% contractions respectively.

TABLE OF CONTENTS

LIST OF FIGURES

LIST OF TABLES

ACKNOWLEDGEMENTS

When I review the work that went into this thesis it quickly becomes apparent that I owe a large number of debts to the many people who contributed, in large measure or small, to its eventual completion.

First of all I must thank my co-supervisors Professors Keith Mitchell and Dave Frost for their guidance and support throughout the course of this work.

I would also like to express my sincere gratitude to those individuals from other institutions who generously supplied materials and computer programs. Dr. D. P. Woodruff (University of Warwick, U.K.), Professor G. A. Somorjai (University of California at Berkeley) and Dr. C. W. Tucker (General Electric Corporation) loaned crystal samples. Dr. E. Zanazzi and Professor F. Jona (Stonybrook) provided a copy of their reliability-index program while Dr. M. A. Van Hove (University of California at Berkeley) and Dr. S. Y. Tong (University of Wisconsin) kindly donated a set of multiple-scattering programs. Dr. Michel Van Hove was a constant source of advice and encouragement on the use and modification of these programs.

At UBC Dr. Louis Noodleman assisted in the construction of superposition potentials and Dr. A. Akhtar of the Metallurgy Department offered advice on crystal cutting and polishing. The experiments would have been impossible to perform without the skill and willing co-operation of the staff of the electrical and mechanical workshops of the Chemistry Department under the

able supervision of Joe Sallos and Brin Powell. Many persons took part in the construction and repair of equipment, particularly Don Catt, Brian Greene, Mike Hatton and Joe Shim of the Electronics Workshop and Bill Henderson, Charlie McCafferty, Emil Matter and Cedric Neale of the Mechanical Workshop.

I thank my fellow workers, both past and present, in the Surface Chemistry Group --- Sunantha Hengrasmee, Tom Moore and Dr. Rick Streater --- for their enjoyable company and co-operation. Especial mention must be made of my good friend Dr. Frank Shepherd, who was my close collaborator throughout the duration of this work, and without whose cheerful expertise, particularly in mini-computer programming, this project would have been a protracted and much less enjoyable experience.

Finally, I wish to thank Sheila Lidwill for her assistance in the preparation of this thesis.

FIG

CHAPTER 1

INTRODUCTION

1.1 Surface Techniques

Many aspects of present technology depend on processes that occur upon the surfaces of solids. The ultimate understanding of many fields of research, in particular heterogeneous catalysis, would seem to require detailed knowledge of surface processes at the atomic level. One approach has been to study well-defined single crystal surfaces (of e.g. a catalytic metal) rather than the complex and ill-defined surfaces with structural defects and uncertain chemical composition which are typical of practical situations. The primary goal of such fundamental studies is thus to provide accurate descriptions of surfaces in geometrical and energetic terms.

There are many techniques available for the surface scientist to investigate the composition, geometry and electronic structure of surfaces. These various surface techniques employ many types of surface probe, detect an equally large variety of particles or radiation and have spawned a bewildering array of acronyms. In Table 1.1 is presented a summary of the most important methods, their acronyms, probe and detected particles and the information that can be derived from each method about the surface. It can readily be seen that each technique in general yields different information and that a complete description would invclve correlating the results from several methods. This has resulted in the evolution of the so-called "multi-technique strategy" in which several different types of experiment are performed in situ on the same sample without changing the experimental conditions.

Technique	Acronym	Probe particle	Detected particle	Information
Low energy electron diffraction	LEED	electrons 10-300eV	primary electrons	surface structure
Auger electron spectroscopy	AES	electrons 1-10KeV	secondary electrons	elemental composition
U.V. photoemission spectroscopy	UPS	photons 10-40eV	electrons	valence energy levels
Angle-resolved UPS	ARUPS	photons 10-40eV	electrons	surface structures?
X-ray photoemission spectroscopy	XPS	photons 0.5-2KeV	electrons	core levels elemental comp.
Ion-scattering spectroscopy	ISS	ions 0.5-2KeV	primary ions	elemental comp. surface structures?
Ion channeling		ions 1-2MeV	primary ions	elemental comp. surface structures?
Secondary-ion mass spectrometry	SIMS	ions 1-30KeV	sputtered ions	elemental composition
Field-ion microscopy	FIM	field 10^8 V/cm	imaging gas ions	defects, surface mobility

Table 1.1 Comparison of some of the most important surface techniques. More details can be found in reference [22].

The most basic information that we can wish to know about a surface is

(i) what is the identity of the atoms making up the surface?

(ii) where are these atoms situated?

That is, we wish to know the elemental composition and geometrical structure of the surface. Of the techniques listed in Table 1.1 the most common and convenient method used to

answer the first question is Auger electron spectroscopy(AES). The reasons for this are its experimental simplicity compared to e.g. ion channeling, which requires a particle accelerator and the ease of interpretation compared to e.g. secondary ion mass spectrometry(SIMS). Auger electron spectroscopy is also more surface-sensitive than X-ray photoelectron spectroscopy (XPS) owing to the shallower penetration depth of the exciting electrons compared with the X-rays of XPS. Auger spectroscopy is easily fitted into the "multi-technique strategy" and has become a routine tool for surface composition analysis (see Ch. 2).

There is only one technique that has really proven itself to answer the second question convincingly --low-energy electron diffraction(LEED). Field ion microscopy(FIM) is restricted in its usefulness by the experimental requirements of very high electric fields and a sample, of high cohesive strength, in the form of a needle. The relatively new methods of angle-resolved ultraviolet photoelectron spectroscopy(ARUPS) and ion channeling are still in the first stages of development and, while showing great potential for the determination of surface structures, do not have as yet the base of successful results that LEED has provided during the last decade.

1.2 Historical Development Of LEED

The origins of LEED are closely bound up with the developments of atomic theory and quantum mechanics. In his thesis, de Broglie [1] postulated in 1924 the wave nature of mattter, where a flux of particles with velocity v and mass m is correlated with a wavelength $\lambda = h/mv$. Hence a beam of 150 eV electrons have a wavelength of about 1Å and might be expected to diffract from periodic crystal structures.

Shortly before the publication of de Broglie's thesis, experiments concerning electrons backscattered from polycrystalline nickel targets showed anisotropies in the angular distributions [2] but these were interpreted as experimental artefacts [3].

The essential insight was, however, achieved as the result of an accident. In 1925 Davisson and Germer began a series of experiments on a polycrystalline nickel sample that was annealed at high temperatures from time to time in order to obtain reproducible results. During one such heating cycle the glass apparatus was damaged and the hot nickel sample severely oxidised. In order to restore the initial conditions, the crystal was heated for some time in hydrogen; this procedure apparently caused the growth of larger single crystal grains which then gave rise to pronounced maxima in the angular distribution of backscattered slow electrons. While the first interpretation of these results was based on a directional "crystal transparency" to particles, more detailed investigations showed that this was a wave interference effect

and in 1927 Davisson and Germer [4] reported an analysis of the diffraction maxima on the basis of de Broglie's equation.

This historic experiment was performed in glass apparatus which, after initial evacuation to about 10^{-6} Torr, was sealed off and further pumped below the detection limit for that time of about 10^{-8} Torr by a charcoal sorption pump and evaporated getter metal. Even in this early work the importance of ultra-high vacuum (UHV), usually defined as $< 10^{-9}$ Torr, to minimise contamination of the sample surface was recognised.

However, the use of LEED to study surfaces was not developed at that time. Due to the difficulty of producing UHV conditions and the lack of a surface analysis technique, results could often reflect the condition of an oxide or other surface layer. The small penetration of the sample by low energy electrons (usually defined as having energies between 0 and 500 eV) made transmission experiments on even the thinnest films difficult whereas in reflection only a small fraction of the incident beam is backscattered, raising problems of sensitivity. The more easily generated and controlled high energy electron beams, with their greater penetrating power, and the simplifications brought about in the effective scattering power of atoms at high incident energies, which made the theory more tractable, all ensured that at this stage high energy electron diffraction was the more interesting field.

Interest in LEED revived in the early 1960's. Sensitivity was improved by advances in experimental design, and control of the composition of surfaces was made possible by ion-bombardment and annealing. Commercial vacuum systems that could routinely

attain UHV became available to reduce background gases to the point where deposition of a layer of foreign atoms took hours rather than minutes. In the late 1960's the techniques became available to detect Auger electrons emitted from surfaces, and Auger electron spectroscopy (see Chapter 2) provided a convenient monitor of surface composition.

Theoretical explanations of the diffraction phenomena also advanced in the late 1960's. Application of the Bragg treatment used in X-ray diffraction showed that a complete description of the directions of the diffraction maxima was possible but not of the intensities. The directions could be observed directly in a typical LEED display-type apparatus and allowed the size and shape of the surface unit cell, in directions parallel to the surface, to be determined. The determination of the basis however required an analysis of the intensities of the diffraction maxima, as in X-ray diffraction. That these intensities could not be simply described by the Born approximation adopted for X-ray diffraction had been realised very soon after the publication of the results of Davisson and Germer. The development of practical multiple-scattering programs did not come to pass until the early 1970's, mainly due to the necessity of large digital computers to compute the large numbers of interactions involved. Many different methods for the calculation of LEED intensities have been proposed and will be discussed in Ch. 3. The theory has advanced to the stage where the diffraction process is essentially completely understood; the difficulty lies in finding methods that will provide accurate intensities without massive computational

effort for systems of chemical interest.

Many hundreds of papers have appeared on LEED in the last decade. Most confine themselves to descriptions of the diffraction patterns, in comparatively few cases have intensities been measured and compared with accurate calculations. Very good agreement between experiment and theory has been achieved for diffraction from some clean metal surfaces; a particularly good example being the low index faces of nickel [11]. In several cases unknown structures, produced by simple gaseous adsorption onto metallic substrates, have been determined by intensity analyses. A selection of important papers and reviews are listed as references [6-10] (mainly experimental) and [11-15] (mainly theoretical).

1.3 Thesis Outline

This thesis describes a detailed study of the structures of the clean (111), (100) and (110) surfaces of rhodium using LEED. This catalytically important face-centred cubic metal, in contrast to most of the other platinum group metals, has received scant attention by surface scientists. Studies of any sort on single crystal surfaces of this metal are rare; apart from early qualitative work by Tucker [16-17], who did not have a surface composition monitor and hence whose results are open to doubt, and recent chemisorption studies on the Rh(100) and (111) [18,131], and (110) surfaces [133], the present work represents the first detailed investigation of clean rhodium surfaces using modern methods.

As surface science is a new field in this institution the experimental equipment had to be commissioned, or in some cases built, and computer programs had to be adapted for use here as well as several smaller data handling and manipulation programs written. The Cu(111) surface, which has been studied in some detail previously [19-20], was used as a test case for both the experimental techniques and to check the correctness of calculations. Only when it was certain that the data of other workers for this surface could be reproduced were studies on the rhodium surfaces commenced. Examples from this preliminary copper work are often used in the text in an illustratory manner.

Chapter 2 is devoted to a brief review of basic ideas that underlie LEED. Surface structures, the reciprocal lattice and a simple explanation of the formation of the diffraction pattern and its intensity are discussed in outline. The production of Auger electrons and the use of Auger electron spectroscopy as a surface analysis tool is also summarised.

Chapter 3 outlines the theoretical basis of the calculations that, when compared with experiment, yield the surface structure. The necessary programs are rapidly becoming more available and commonplace and hence standard results are quoted with little attempt to explain the computational complexities; in such cases the reader is referred to standard texts. Rather, attention is focussed on the structural and non-structural parameters that enter into the calculations, their meaning and importance, and the overall construction and flow of the programs. In particular, the ion-core scattering potential

that leads to backscattering of the incident low-energy electrons must be correctly specified to obtain reliable theoretical intensities. In this work two types of potentials were used, band-structure potentials and potentials constructed by the method of linear superposition of charge densities for a cluster of metal atoms.

In Chapter 4 can be found details of the experimental apparatus and procedures. The vacuum system and the production of a clean sample, as judged by AES, are described. An innovative new method of measuring the experimental intensities, employing a computer-controlled Vidicon T.V. camera system [21], based on the photographic method of Stair et al [88], is covered in some detail. This method has significant advantages over the conventional techniques of spot-photometry or use of a Faraday-cup collector, particularly in terms of speed and convenience. The former methods necessitated hours of data collection to produce even a small base of experimental data, during which time the surface could become seriously contaminated. This new Vidicon method reduces data collection times to a few minutes and provides a hard-copy photographic record that can be analysed at leisure to yield a very large data base which unambiguously relates to the same original surface.

Chapter 5 describes progress to date in LEED surface crystallography, including a bibliography of metal clean surface structure determinations. The preferred surface structure is found by comparing calculated reflected intensities for a wide variety of possible structural models with experimental data.

Traditionally, comparisons of experimental and theoretical data have been carried out visually or by very crude numerical matching of major features. Hence a recurring problem in LEED crystallography has been that of establishing limits on the accuracy and reliability of the surface structures thus determined. Despite a long-standing concern over this problem, only very recently has a detailed, objective method been proposed [23] that attempts to numerically compare all the essential features of the experimental data with various theoretical model predictions. This reliability-index, or R-factor, method is described together with some additions and refinements developed during the application of this index to the determination of the structures of the Rh(111),(100) and (110) surfaces.

The actual determination of the surface structures of these three low-index faces of rhodium is presented in Chapters 6-8. Fine details of the cleaning procedures, which can vary from sample to sample depending upon their origins and pre-treatment, are discussed. The structure derivations performed by the reliability-index method are closely examined to assess uncertainties in the results from experimental (or calculational) artefacts and fortuitous circumstances. Duplicate sets of data from different experiments are used to assess the reliability of the experimental data and the results from independent data sets, collected at various angles of incidence, compared to test the consistency of the method.

All three surfaces retain the structure expected for a simple truncation of the bulk crystal. While this is normal for

the close-packed (111) surfaces of face-centred cubic metals, some (110) and (100) faces are known to perform surface structural reconstructions or re-arrangements of a generally complex and as yet unknown nature [24]. The (100) faces of e.g. platinum [25] and iridium [26] are normally observed in this condition. Rigorous examination of the Rh(100) and (110) surfaces at room temperature and above revealed no such tendency. All three surfaces were found to have the surface layer at a distance from the second layer close to, or a little contracted from, the bulk interlayer distance.

Finally, a comprehensive set of experimental data for the three rhodium surfaces is collected in the appendices. Examples are used in the main body of the text for illustratory purposes.

This thesis is preliminary in the sense that a large part of the work that went into it was concerned with developing these new, for this laboratory, experimental and theoretical techniques. Moreover, these new results, while in themselves they form a reasonably complete study, are also preliminary to the understanding of the adsorption properties and heterogeneous catalytic activity of rhodium [26]. Just as we cannot hope to understand catalysis at the atomic level if we cannot locate adsorbed atoms, so we cannot understand chemisorption if we do not have a precise description of the clean surface. I hope this work provides the latter information and will lay a solid foundation for later studies of rhodium, its chemisorption properties and ultimately its catalytic activity.

CHAPTER 2

LOW-ENERGY ELECTRON DIFFRACTION (LEED) AND AUGER ELECTRON SPECTROSCOPY (AES)

2.1 Basic Considerations

2.1(a) secondary electron distribution

Electrons with energies between about 10 and 1000 eV are ideally suited to investigate the topmost layers of solids because the probabilities for inelastic scattering are high. A parameter frequently used in this context is the electron mean free path length, L. This is the mean distance travelled by an electron before it is scattered inelastically and can be expressed by

$$I(E) = I_0(E) \exp [-l/L(E)]$$

where the incident intensity $I_0(E)$ for energy E is attenuated to I(E) on passage through distance l.

The characteristic dependence of this property on the electron energy is shown in Fig. 2.1. Although it is somewhat difficult to obtain exact quantitative data, the general features of this diagram have been well established. A minimum in the mean free path of only a few Å occurs at energies between 40 and 100 eV. While the curve increases steeply at low energies, at higher energies the increase in the mean free path is slow and at 1000 eV is still only a few atomic layers.

In the LEED experiment a beam of electrons with a definite primary energy E_p impinges on the crystal surface and those electrons that are elastically backscattered are collected. Fig. 2.2 shows a schematic energy distribution, N(E), of the back-scattered electrons as a function of energy. This

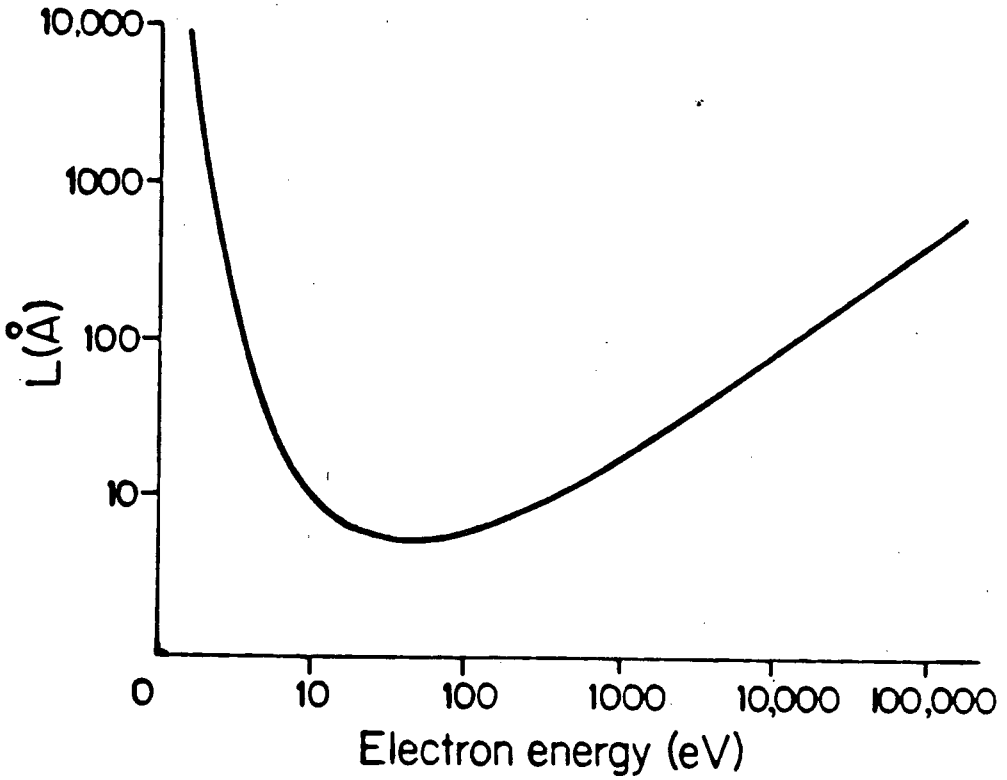

Figure 2.1 Schematic diagram of the mean free path L(Å) of electrons in metallic solids as a function of their energy (eV).

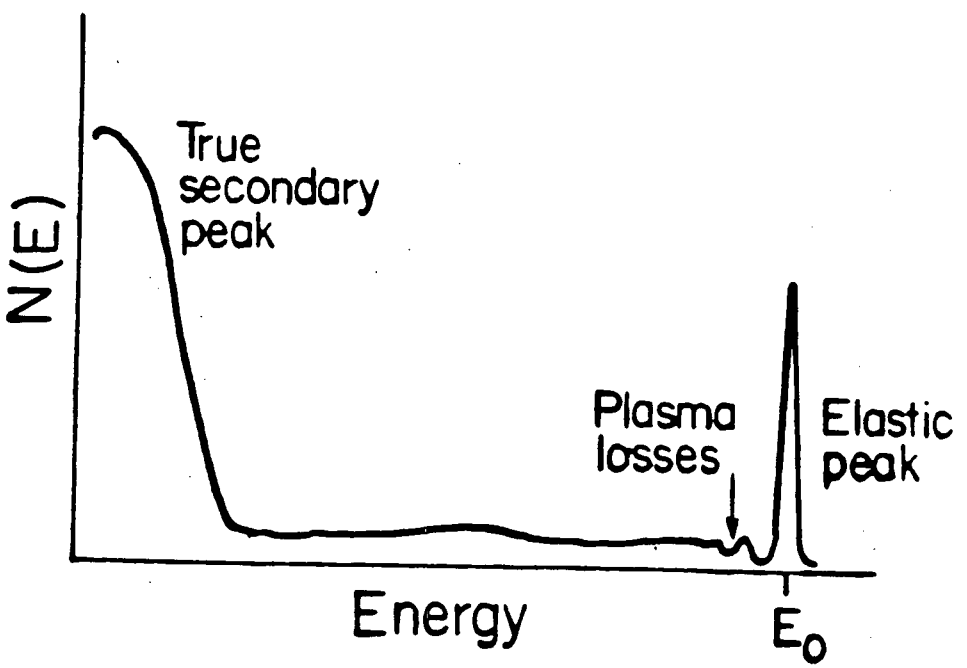

Figure 2.2 Schematic energy distribution N(E) of backscattered elcw electrons as a function of their energy for a primary beam energy E_0.

"secondary electron distribution" can be divided into three main regions:

i) the large peak at low energies contains "secondary electrons" created as a result of inelastic collisions between incident electrons and electrons bound in the solid. In each collision process a relatively small amount of energy is transferred so that a single primary electron can create a cascade of secondaries that contribute to the large broad peak at low energies;

ii) the medium energy range is characterised by a smooth background upon which are superimposed small features due mainly to the emission of Auger electrons (see Section 2.4) and energy losses to core electrons, single and collective valence electron excitations [28] ;

iii) a small fraction (typically a few %) is back-scattered elastically at energy E_0 to form the "elastic peak". This peak actually also contains "quasi-elastically scattered" electrons that have undergone phonon scattering, that is an interaction with the vibrating crystal lattice. These interactions produce energy changes of the order of 10 meV. The energy resolution of typical LEED instruments is insufficient to observe such losses or gains and hence, as far as LEED is concerned, the whole of the high-energy peak is often loosely termed the "elastic peak".

In the LEED experiment the elastically scattered electrons

are filtered out of the general secondary electron distribution and, usually, displayed on a fluorescent screen. We shall see in later sections of this chapter how these elastically scattered electrons behave spatially and their energy dependence.

2.1(b) surface structure classifications

The region of an ordered surface probed by LEED has two-dimensional symmetry parallel to the surface but no periodicity normal to it. As with triperiodic crystal structures, perfect diperiodic surface stuctures may be classified into certain lattice types; for many pure substances the symmetry of the surface is given simply by that of the perfect bulk crystal in a plane parallel to the surface under consideration.

Surfaces are usually named after the planes of the bulk crystal to which they are parallel e.g. (100), (110) etc. Their structures can be described in terms of a unit mesh with unit vectors $\underline{s}_1$ and $\underline{s}_2$ lying in the surface plane. All the points which are connected by translation vectors

$$\underline{T} = h'\underline{s}_1 + k'\underline{s}_2 \qquad h',k' = \text{integers} \qquad (2.1)$$

form a Bravais net. In two-dimensional crystallography the terms "lattice" and "cell" of triperiodic crystallography are replaced by the terms "net" and "mesh" respectively. The 14 Bravais lattices of triperiodic crystallography are reduced to 5 nets for diperiodic surface structures. These five types of

net, as represented by models of some surfaces of face-centered cubic (FCC) and body-centred cubic (BCC) metals, are shown in Fig. 2.3.

Details of various conventions in surface crystallography can be found in an article by Wood [29] and in the International Tables for X-ray Crystallography [30]. For our purposes it suffices to observe that in the bulk, crystal structures can be built up from identical layers of atoms parallel to the surface. An atom in one layer is related to an identical atom in the next by a vector $\underline{c}$; each layer is regarded as separated by an interlayer distance d. The orientation of the incident beam of electrons relative to the surface is described by two angles, θ and ϕ ; the polar angle θ is between the beam and the inward-pointing surface normal and ϕ, the azimuthal angle, is the angle between the plane containing the surface normal and incident beam, and the x-axis. Fig. 2.4 clears up any ambiguities.

2.1(c) the reciprocal net

Another type of Bravais net can be constructed for each of those shown in Fig. 2.3 ; these are called "reciprocal nets". The reciprocal net corresponding to a real net defined by vectors $\underline{s}_1$ and $\underline{s}_2$ is

$$\underline{g} = h\underline{s}_1^* + k\underline{s}_2^* \qquad (2.2)$$

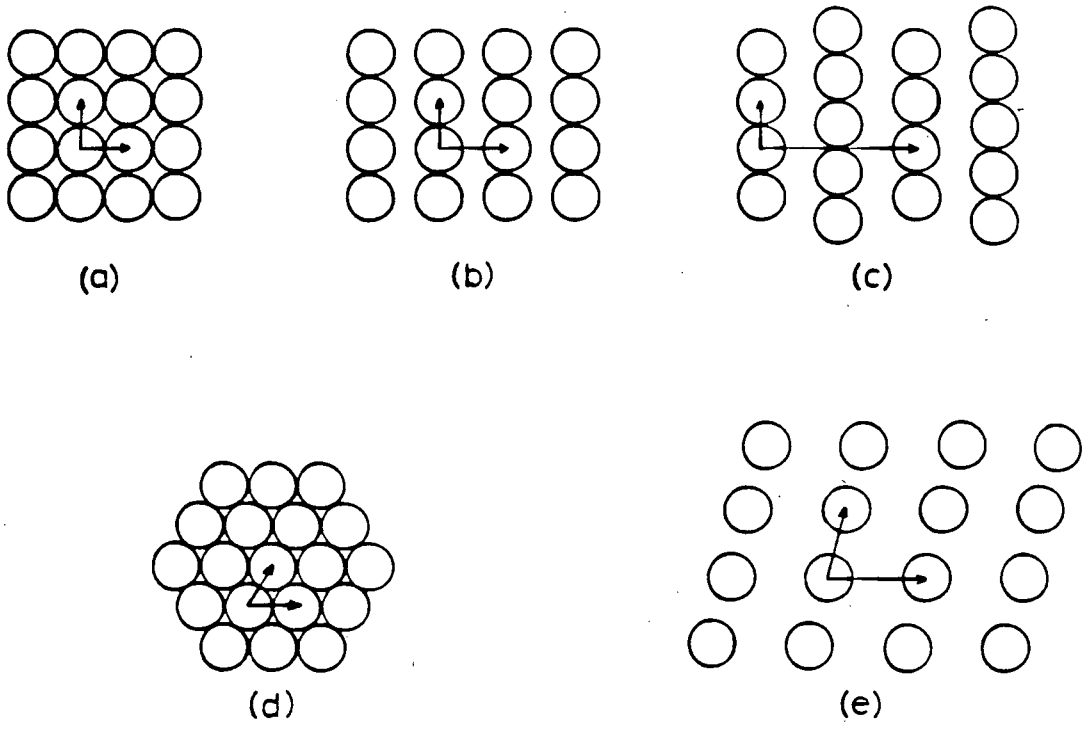

Figure 2.3 Examples of the 5 diperiodic nets as represented by models of surfaces of face-centred cubic (FCC) and body-centred cubic (BCC) metals; sides a_1, (short axis) and a_2, internal angle α:

(a) square $a_1 = a_2$, $\alpha = 90°$, e.g. FCC(100), BCC(100);
(b) primitive rectangular $a_1 \neq a_2$, $\alpha = 90°$, e.g. FCC(110), BCC(211);
(c) centred rectangular $a_1 \neq a_2$, $\alpha = 90°$, e.g. FCC(311), BCC(110);
(d) hexagonal $a_1 = a_2$, $\alpha = 60°$, e.g. FCC(111);
(e) oblique $a_1 \neq a_2$, $\alpha \neq 90°$, e.g. FCC(321);

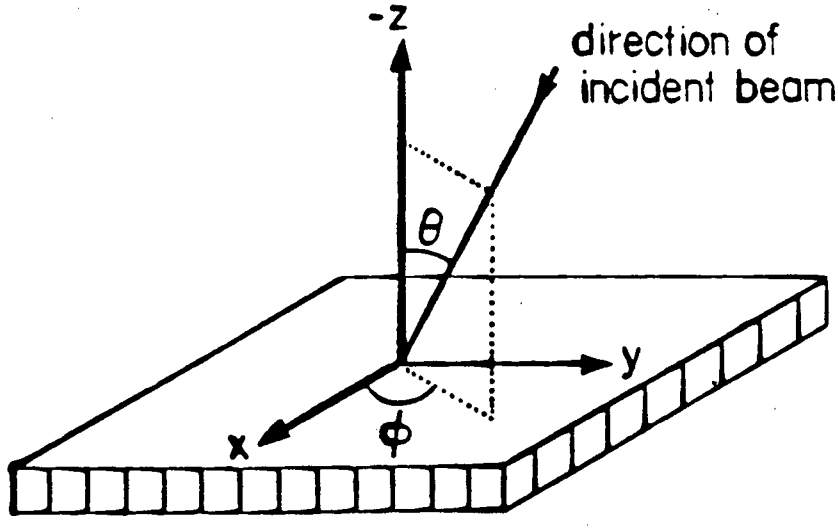

Figure 2.4 Angle conventions for incidence of an electron beam on a surface

$$\text{with} \quad \underline{s}_1^* = 2\pi(\underline{s}_2 \times \underline{z})/(\underline{s}_1 \cdot \underline{s}_2 \times \underline{z}) \tag{2.3}$$

$$\text{and} \quad \underline{s}_2^* = 2\pi(\underline{s}_1 \times \underline{z})/(\underline{s}_2 \cdot \underline{s}_1 \times \underline{z})$$

where $\underline{z}$ is a unit vector perpendicular to $\underline{s}_1$ and $\underline{s}_2$, as shown in Fig. 2.5. The reciprocal nets corresponding to the real nets shown in Fig. 2.4 are given in Fig. 2.6.

At this stage the reciprocal net appears as an abstract construction but we shall see in the following section that it has a very direct interpretation in LEED experiments.

2.2 Formation Of The Diffraction Pattern

We shall consider a mono-energetic, collimated electron beam incident on a perfectly clean well-ordered surface. This is, of course, a theoretical abstraction as even the most carefully prepared surface has a degree of roughness that can be seen on electron micrographs. However, because of limits on the collimation achievable in low energy electron guns, the incident beam is coherent only over restricted areas (of the order of 100 Å^2), and therefore LEED is sensitive to atomic order only over distances of this magnitude. A typical LEED pattern from a Cu(111) surface is shown in Fig. 2.7(a).

Our interest will centre on the elastically scattered electrons that produce most of the structure in the diffraction pattern. Their behaviour can be described by a Schrödinger equation of the form (in atomic units)

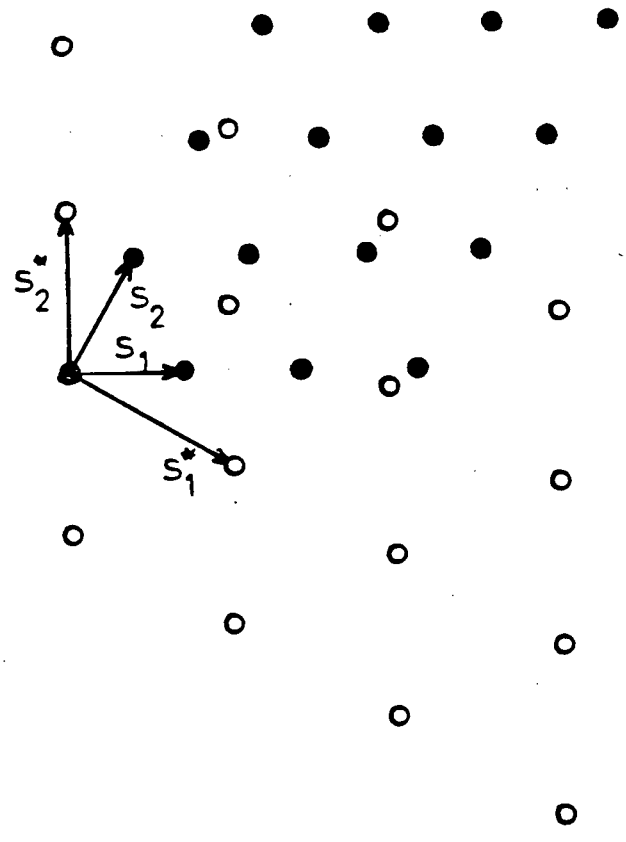

Figure 2.5 A two-dimensional real net, described by s_1, s_2, (dark circles) and its associated reciprocal net s_1^*, s_2^* (open circles).

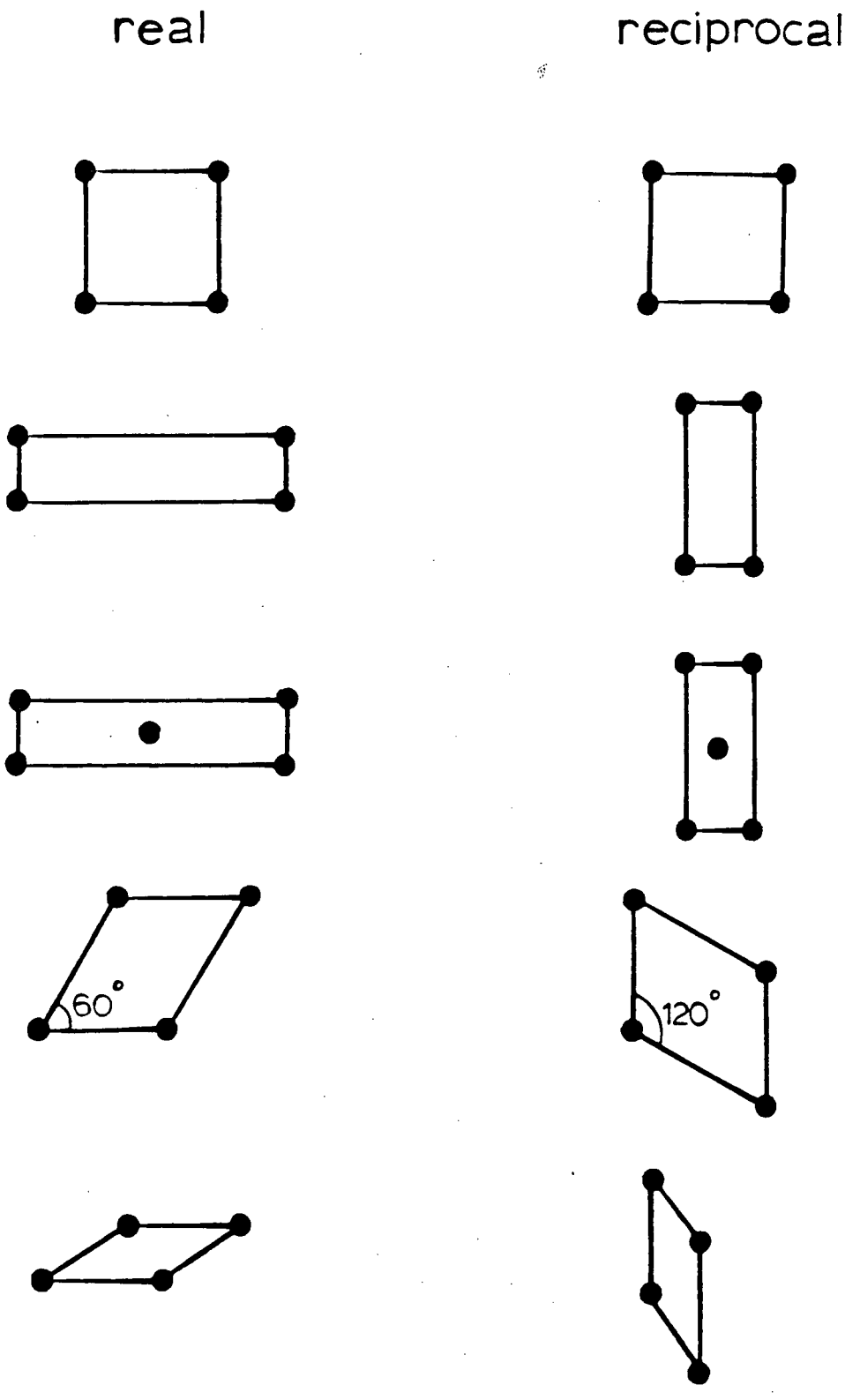

Figure 2.6 Unit meshs of the corresponding real and reciprocal two-dimensional nets as in Figure 2.3.

$$-1/2\,\nabla^2\psi(\underline{r}) + V(\underline{r})\psi(\underline{r}) = E\psi(\underline{r}) \qquad (2.4)$$

Far from the crystal the effect of the crystal potential, $V(\underline{r})$, can be neglected and the effect of the interaction will be shown by the change in the wave-vector of the plane-wave eigenstates

$$\psi_{\underline{k}}(\underline{r}) = \exp(i\underline{k}.\underline{r}) \qquad (2.5)$$

before and after diffraction.

For elastic scattering by the diperiodic arrangement of atoms in the surface region, the wave-vectors $\underline{k}'$ of the diffracted electrons are determined by conservation of energy and momentum parallel to the surface [12]

$$E(\underline{k}') = E(\underline{k}) \qquad (2.6)$$

before (unprimed) and after (primed) diffraction

$$\underline{k}'_{||} = \underline{k}_{||} + \underline{g}(hk) \qquad (2.7)$$

with the reciprocal net vector $\underline{g}(hk)$ discussed in Section 2.1(c) as

$$\underline{g}(hk) = h\underline{s}_1^* + k\underline{s}_2^* \qquad (2.8)$$

Physically then, the diffracted wavefield has, independent of the exact scattering mechanisms involved, the form of a series of discrete beams each with a different parallel

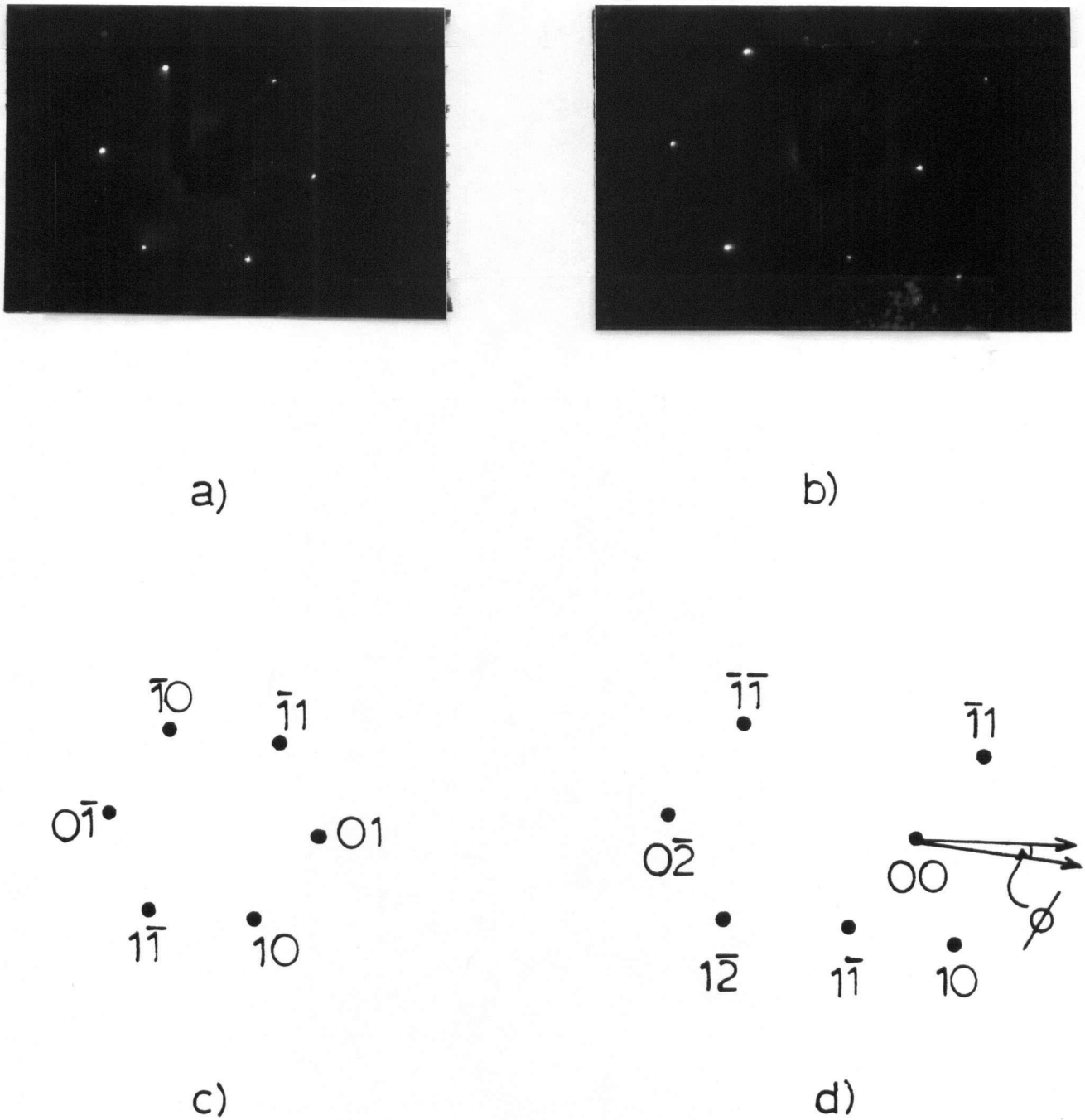

Figure 2.7 (a) Photograph of the LEED pattern from a Cu(111) surface at (a) normal incidence and 90 eV beam energy (b) $\theta = 12^{o}$, $\phi = 6^{o}$ at 44eV beam energy, (c) and (d) labelling of the diffraction spots.

component of momentum $(\underline{k}_{||} + \underline{g})$; this is determined by the translational symmetry of the region travelled by the scattered electrons.

The directions of the diffracted beams are determined by the wave-vector of the diffracted electrons, $\underline{k}'$, and hence by $\underline{k}_{||}$, $\underline{g}$ and E. This is illustrated in Fig. 2.8. For given values of E and $\underline{k}_{||}$, the diffraction pattern is determined by $\underline{g}(hk)$. For certain values of $\underline{g}(hk)$, $\underline{k}'_{\perp}$ is imaginary and corresponds to evanescent, or surface waves, which cannot escape from the solid. By collecting the diffracted electrons on a spherical fluorescent screen with the crystal at its focus the beams appear as spots, one for each value of $\underline{g}(hk)$. The spot produced by a beam with parallel component of momentum

$$\underline{g}(hk) = h\underline{s}_1^* + k\underline{s}_2^* \qquad (2.9)$$

is referred to as the (hk) spot or beam, the indices of (2.7-2.9) being used to label the diffracted beams. The beam labelling scheme appropriate to the Cu(111) LEED pattern of Fig. 2.7(a) is shown as Fig. 2.7(b).

Thus the (00) beam is made up of electrons which have interacted with the surface without momentum transfer and is called the specularly reflected beam. This specular beam is easily recognised as its direction remains constant as E changes as long as the electrons move in field-free space and the direction of the incident beam does not change. As the incident energy is increased, the perpendicular component of momentum increases, the angle of diffraction decreases and the beams

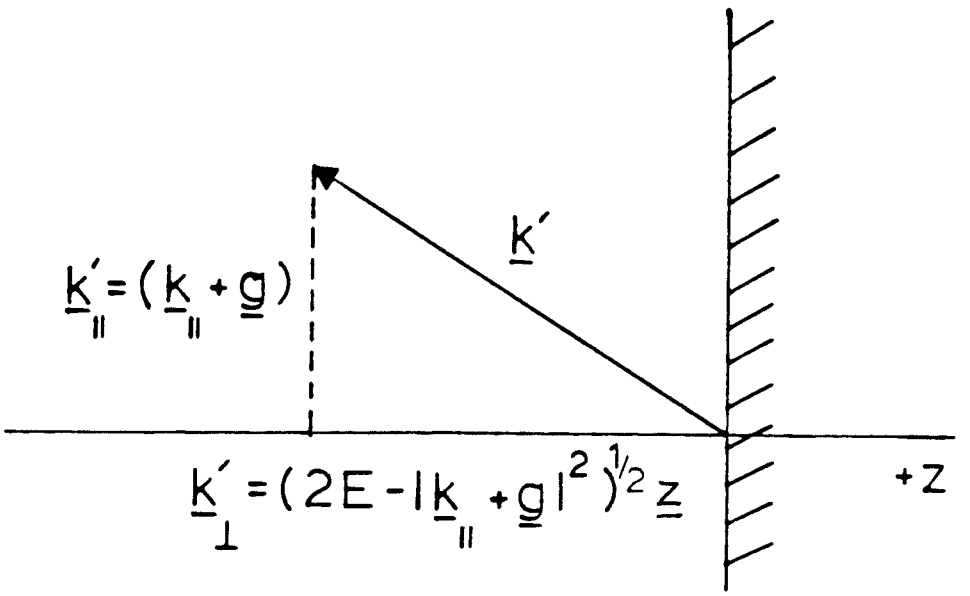

Figure 2.8 The direction of a diffracted beam is determined by the allowed values of $\underline{k}'$ and E.

crowd in towards the specular beam.

The diffraction pattern displayed on the usual fluorescent screen of a LEED apparatus provides a direct picture of the reciprocal net of the surface and hence the sides of the unit mesh of that net are easily determined, $\underline{s}_1^*$ and $\underline{s}_2^*$. The unit mesh of the real net is then obtained by inversion of equations (2.3) :

$$\underline{s}_1 = 2\pi (\underline{s}_2^* \times \underline{z}) / (\underline{s}_1^* \cdot \underline{s}_2^* \times \underline{z})$$

$$\underline{s}_2 = 2\pi (\underline{s}_1^* \times \underline{z}) / (\underline{s}_2^* \cdot \underline{s}_1^* \times \underline{z}) \qquad (2.10)$$

Although equation (2.9) gives the most fundamental designations of diffracted beams, for surfaces that reconstruct or contain adsorbed molecules it is often convenient that the diffracted beams are indexed with respect to the reciprocal lattice vectors of the substrate ($\underline{b}_1^*$ and $\underline{b}_2^*$), since the substrate is the initially known structure. This relation is

$$\begin{pmatrix} \underline{s}_1^* \\ \\ \underline{s}_2^* \end{pmatrix} = \begin{pmatrix} P_{11} & P_{12} \\ \\ P_{21} & P_{22} \end{pmatrix} \begin{pmatrix} \underline{b}_1^* \\ \\ \underline{b}_2^* \end{pmatrix} \qquad (2.11)$$

$$\text{or} \quad s^* = Pb^* \qquad (2.12)$$

The matrix P for a particular structure can often be obtained directly by comparing the LEED pattern of the surface with that calculated for the substrate. Matrix manipulation of equation (2.12) yields

$$s = \tilde{P}^{-1} b \qquad (2.13)$$

which defines the relation of the mesh vectors of the actual surface with those of the substrate. The matrix $\tilde{P}^{-1}$ provides the most general way of expressing this relation [32], but when the angle between $\underline{s}_1$ and $\underline{s}_2$ is equal to that between $\underline{b}_1$ and $\underline{b}_2$ a more compact designation is often used [29]. Then the relation between s and b can be specified by

$$(\underline{s}_1/\underline{b}_1) \times (\underline{s}_2/\underline{b}_2)\,\delta \qquad (2.14)$$

in terms of the lengths of the unit mesh sides and the angle of rotation (δ) between s and b (omitted when $\delta = 0$).

This notation is probably best illustrated by examples. In the simplest case, the surface structure is given by the termination of the bulk structure along a given plane. The surface unit mesh in such cases is briefly referred to as (1x1) in the Wood convention [29], indicating that the surface net vectors are identical to those of the underlying substrate e.g. Rh(100)-(1x1). In more general cases the surface periodicities will differ from those of bulk substrates. This is especially so for the deposition of foreign atoms (adsorbates) on the substrate material. (Such adsorbed overlayer stuctures will in general have a periodicity different from that of the substrate).

Another case more relevant to this thesis concerns the reconstructions of the surface regions of chemically clean materials such as occur for many semi-conductors and metals [14]. The (100) face of gold [33] for example yields a diffraction pattern shown schematically in Fig. 2.9(a). This is designated as a (5x1) LEED pattern and is associated with a (5x1) unit mesh relative to that of the bulk substrate. A model assuming an hexagonal arrangement of surface gold atoms on the underlying (100) substrate has been proposed to account for this pattern [33] as shown in Fig. 2.9(b) and (c). The actual LEED pattern observed in this case is a superposition of two patterns, as in Fig. 2.9(a), related by a 90° rotation. These correspond to the existence of two equivalent orientations, or domains, related by a 90° rotation of the surface layer on the

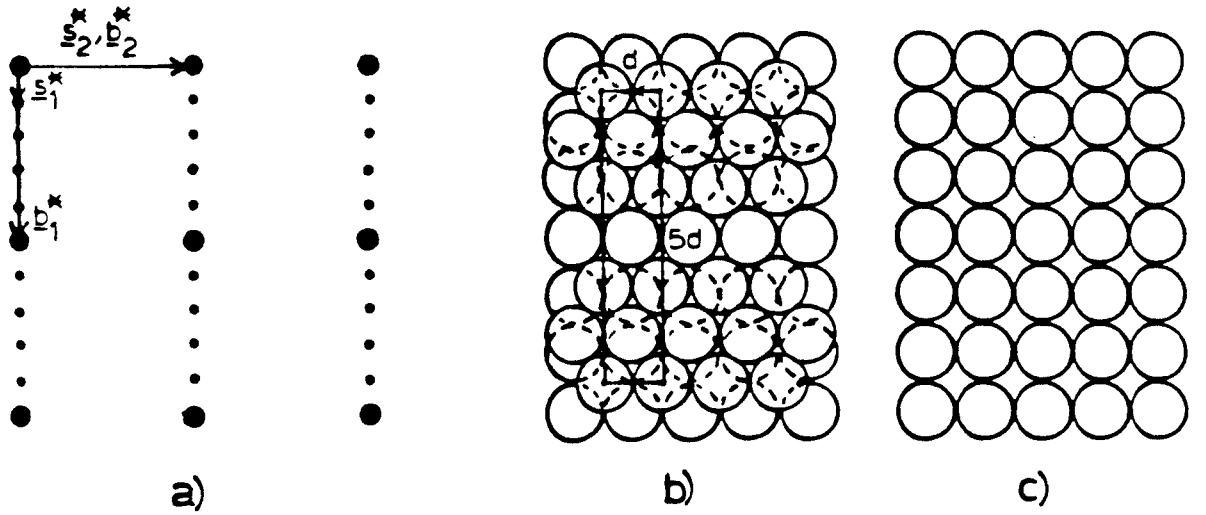

Figure 2.9 a) Schematic diffraction pattern from one domain of Au(100)-(5X1) reconstructed surface; b) Model structure of coincidental hexagonal gold layer superimposed on the underlying (100) substrate, c), (after Palmberg and Rhodin [33]).

underlying substrate

2.3 Intensities Of LEED Beams

The positions of the diffraction spots in the LEED pattern yield the size and symmetry of the surface unit mesh but no further information on the locations of the atoms in the unit mesh. This information is contained in the intensities of the LEED beams

Intensities are most usually measured at constant polar, θ, and azimuthal angle, ϕ, see Fig. 2.4, as a function of energy. Plots of intensity against energy, I(E) curves or "intensity profiles", are the usual form of data presentation although "rotation diagrams", $I(\phi)$ for const θ and E, and "rocking curves", $I(\theta)$ for constant ϕ and E, remain as neglected

alternatives. Fig. 2.10 shows typical I(E) curves for the specular beams diffracted from Cu(100) and Ni(100) surfaces for $\theta = 3^{o}$ [34].

Such curves show considerable structure exhibiting a number of maxima and minima as the energy is varied. Also, as noted in Section 2.1(a), electron reflectivities are low for elastic scattering. We can attempt to use the kinematical (or single-scattering) model, valid for low scattering cross-sections, to understand such I(E) curves. This model has been used with success to interpret X-ray diffraction intensities. However, low energy electron scattering cross-sections are much larger, by as much as 10^{6}, and so we cannot expect this theory to be much more than a rough guide for LEED intensities.

2.3(a) kinematical theory

In the kinematical theory only the incident wave is considered to produce scattered waves whilst double and multiple-scattering are ignored. For an incident plane wave

$$\psi_{\underline{k}} = \exp(i\underline{k}.\underline{r}) \qquad (2.15)$$

the kinematical expression for the total wave (corresponding to wave-vector $\underline{k}_{s}$) scattered to the point of observation (denoted by vector $\underline{r}$) by an assembly of scatterers is

$$\psi_{s} = A_{o}\sum f_{j}(E,\theta_{s}) \exp[i\underline{k}|\underline{r}-\underline{r}_{j}|]/|\underline{r}-\underline{r}_{j}| \exp(i\underline{k}.\underline{r}_{j}) \qquad (2.16)$$

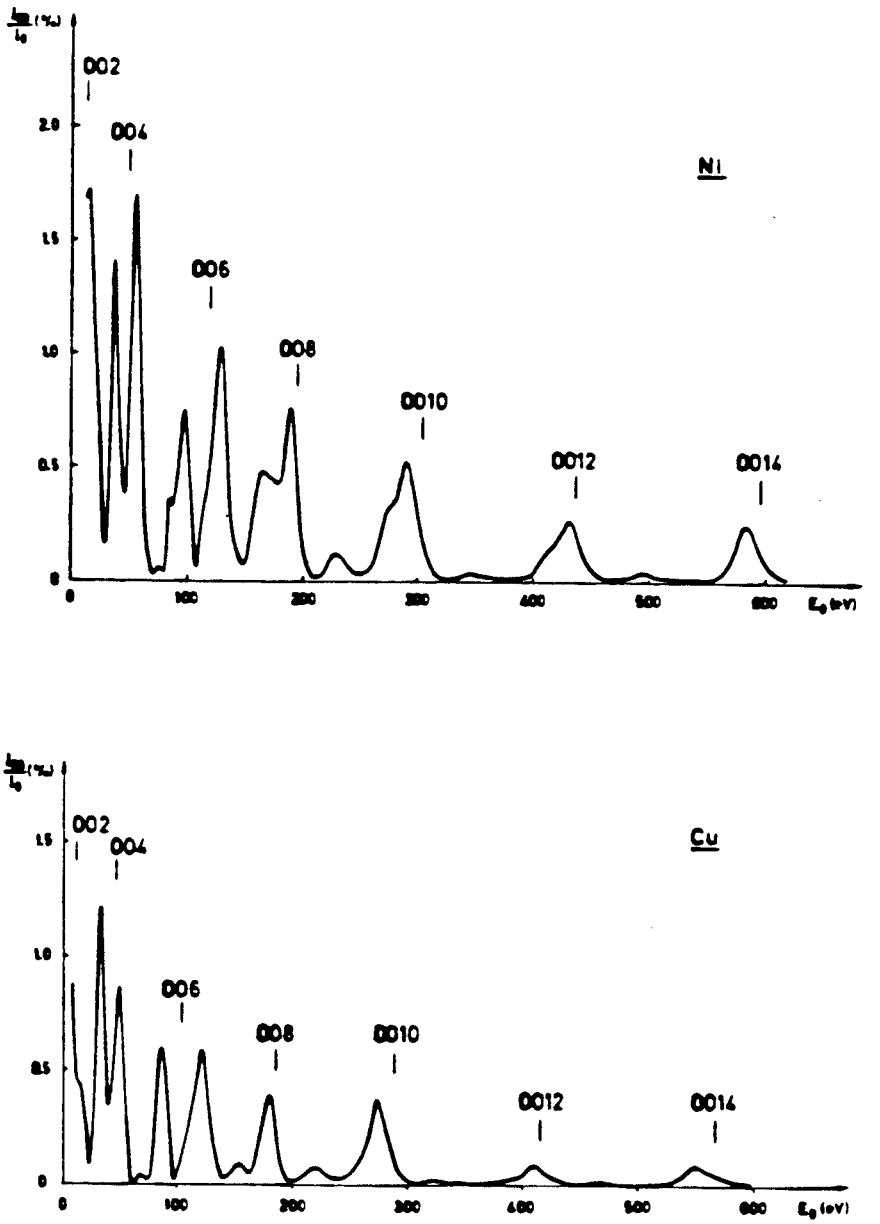

Figure 2.10 I(E) curves for the specular beam from Ni(100) and Cu(100), $\theta = 3°$. The bars denote kinematical Bragg conditions (after Anderson and Kasemo [34]).

where the summation is over the set of spherical waves produced at the scattering centres $\underline{r}_j$. The factor f_j is the atomic scattering factor for the atom j for elastic scattering of electrons of energy E through the angle θ_s (as defined by $\underline{k} \rightarrow \underline{k}_s$). The final term denotes the phase shifts for the incident waves at the scattering atoms. A_0 is a constant whose value is fixed by the density of atoms in the incident beam.

If the scattered electrons are detected at a long distance from the scattering region and if this region is small, so that $|\underline{r}-\underline{r}_j|$ can be approximated by r for the purpose of assessing the effect of distance on scattered amplitude, then equation (2.16) can be re-expressed as

$$\psi_s = A_0 \sum f_j(E,\theta_s) \exp[i(\underline{k}-\underline{k}_s).\underline{r}_j] \exp(ik_s r)/r \qquad (2.17)$$

In general $\psi\psi^* d\tau$ gives the probability that an electron represented by a wave-function ψ is to be found in a volume element $d\tau$; therefore the number of electrons received in unit time by a detector of solid angle $d\Omega$ is

$$dn = u\, A_0^2\, |B^2|\, d\Omega \qquad (2.18)$$

where u is the velocity of the electrons and B is the scattering amplitude

$$B = \sum_j f_j(E,\theta_s) \exp(i\underline{S}.\underline{r}_j) \qquad (2.19)$$

for the collection of atomic scatterers and

$$\underline{S} = \underline{k}_s - \underline{k} \qquad (2.20)$$

is the scattering vector. The number of electrons crossing unit area perpendicular to the direction of $\underline{k}$ per unit time is

$$I_o = u\, A^2_o \qquad (2.21)$$

and, on introducing the relation

$$dn = I_o\, d\sigma \qquad (2.22)$$

such that $d\sigma$ is the value of dn when I_o is unity, we obtain the differential scattering cross-section

$$d\sigma/d\Omega = I(\underline{S}) = |B|^2 \qquad (2.23)$$

where $I(\underline{S})$ corresponds to the flux, for scattering vector $\underline{S}$, scattered per unit solid angle from an incident beam of unit flux per unit area.

The equations (2.23) and (2.19) represent the general basic equations for kinematical scattering of a plane wave by any assembly of scatterers whose dimensions are small compared with the distance of observation of the scattered electron from the scattering region.

One of the interesting consequences of the elastic scattering being confined by strong inelastic scattering to the

vicinity of the surface is that the full three-dimensional periodicity of the crystal is not experienced by a scattered electron. We can proceed via two limiting cases, depending upon the strength of the inelastic scattering. The pure two-dimensional limit corresponds to very strong inelastic scattering, and the pure three-dimensional to very weak inelastic scattering.

The former is rather easier to follow; we consider a two-dimensional net defined by mesh vectors $\underline{s}_1$ and $\underline{s}_2$ such that net points are situated at points $\underline{r}$

$$\underline{r}_j = m\,\underline{s}_1 + n\,\underline{s}_2 \qquad (2.24)$$

in this case the atomic scattering factors f_j can be replaced by the scattering factor of the unit mesh, F (structure factor), which depends on the f_j and the atomic positions within the unit mesh. The scattered amplitude becomes

$$B = F(\underline{k}\rightarrow\underline{k}_s) \sum_j \exp\ (i\underline{S}.\underline{r}_j) \qquad (2.25)$$

and the differential cross-section is

$$d\sigma/d\Omega = |F(\underline{k}\rightarrow\underline{k}_s)|^2 \sum_{ij} \exp\ [\,i\underline{S}.(\underline{r}_i-\underline{r}_j)\,]$$

$$= |F(\underline{k}\rightarrow\underline{k}_s)|^2\ G(\underline{S}) \qquad (2.26)$$

The interference function $G(\underline{S})$ has maxima when the scattering vector $\underline{S}$ satifies the Laué conditions

$$\underline{S}.\underline{s}_1 = 2\pi h \quad \text{and} \quad \underline{S}.\underline{s}_2 = 2\pi k \qquad (2.27)$$

for integral h and k. These conditions can be rewritten as

$$\underline{S} = \underline{g}(hk) \qquad (2.28)$$

where the $\underline{g}(hk)$ are defined by equation (2.8); the Laué conditions are equivalent to the condition expressed earlier in equation (2.7) as

$$\underline{k}'_{||} - \underline{k}_{||} = \underline{g}(hk) \qquad (2.29)$$

That is, diffracted waves occur only in certain directions determined by equation (2.29) to produce the LEED pattern described in Section 2.2.

The interference function does not tell us anything about the energy dependence of the intensity of a spot. The structure factor is however energy-dependent through the energy dependence of the atomic scattering factors f_j. The form of this variation and hence the intensity variation of a diffraction spot with energy, an I(E) curve, in the two-dimensional kinematical approximation is shown in Fig. 2.11(a) to be monotonic.

In the pure three-dimensional kinematic limit the effect of the surface can be ignored and the electron will move in predominantly the full three-dimensional potential of the bulk crystal. Whereas in the two-dimensional limit the perpendicular component of the wave-vector $\underline{k}_\perp$ was free to assume a continuum

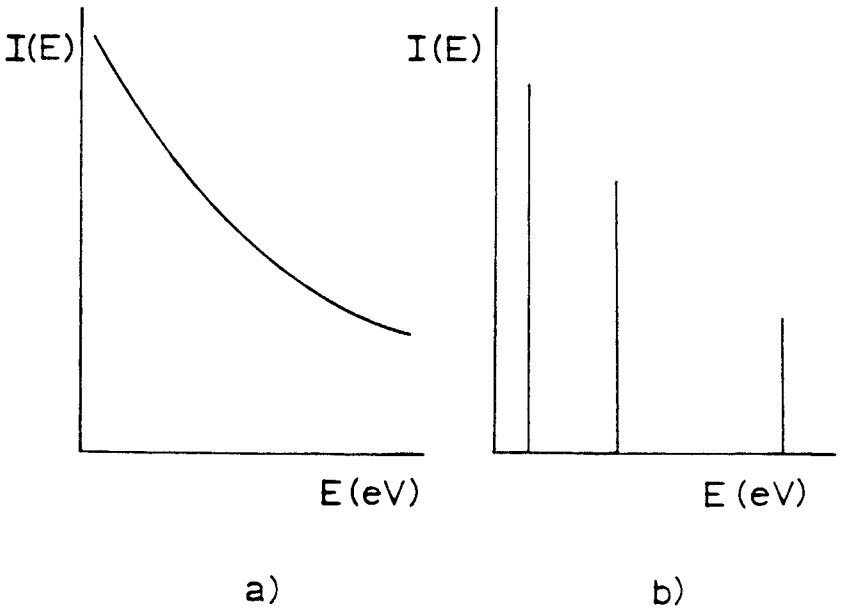

Figure 2.11 Intensity of a diffracted LEED beam as a function of energy in a) the pure two-dimensional limit and b) the pure three-dimensional limit (after Somorjai and Farrell [7]).

of values (that is only $\underline{k}$ is a good quantum number), in the three-dimensional limit it is constrained to only certain values due to the periodicity in the perpendicular direction

$$\underline{k}'_{\perp} = \underline{k}_{\perp} + \underline{g}_{\perp} \qquad (2.30)$$

where $\underline{g}$ is a reciprocal lattice vector perpendicular to the surface. Hence in the pure three-dimensional limit the diffracted intensity of a beam will be zero except where equations (2.29) and (2.30) are simultaneously satisfied, producing a variation of the form shown in Fig. 2.11(b) . These two equations can be combined into

$$\underline{k}' = \underline{k} + \underline{g}(hkl) \qquad (2.31)$$

where $\underline{g}(hkl)$ is a reciprocal lattice vector of the bulk three-dimensional lattice.

2.3(b) characteristics of I(E) curves

Re-examining Fig. 2.10 we find that real I(E) curves show characteristics intermediate between the two extremes of the pure two-dimensional and the pure three-dimensional kinematical limits. The curves are not monotonic and do exhibit maxima and minima; however, there are more peaks than are predicted by equation (2.31), at least at lower energies. The bars on Fig. 2.10 mark the positions of "primary Bragg peaks" where equation (2.31) is satisfied for various values of l. In general, maxima fall close to these values but subsidiary maxima can be seen. Such extra structure must be associated with the multiple-scattering events neglected in the simple kinematical treatment.

Three energy regions are often identified in I(E) curves according to the magnitude of beam intensities, degree of structure and peak widths [35,12]. These are, referring to Fig. 2.10:

(i) the low-energy region, typically below 20eV, where peaks are numerous and narrow with widths of 1-2eV and high diffracted intensities (sometimes >10% of the incident beam intensity);

(ii) the intermediate-energy range (20-150eV) has wider (up to 10eV) peaks of lower intensity. Structure is simpler though there are still more maxima than

predicted by equation (2.31);

(iii) the high-energy region, usually above 150eV, has wider (20-30eV) peaks of still lower intensity in positions that are broadly consistent with equation (2.31).

The kinematical theory, in the form presented earlier, does not provide information on peak widths. In order to account for peak widths, removal of electron flux by inelastic scattering must be introduced into the model (see Ch. 3). It is precisely the high inelastic scattering cross-sections for low-energy electrons that make them surface sensitive.

In general, diffracted beam intensities decrease with increasing temperature [36], often in an exponential manner. Consequently, attempts have been made, within the kinematical theory, to relate such dependencies to Debye-Waller factors in order to extract mean-square vibrational amplitudes of surface atoms [7]. However, the derived Debye temperatures show some variation (e.g. ±20%) from beam to beam and with the energy and direction of the incident beam.

Generally, the kinematical theory, even when modified to include inelastic scattering and temperature effects, and even double diffraction events [37], is not able to reproduce experimental I(E) curves successfully. An exception to this rule is the (111) surface of xenon, for which I(E) curves are essentially kinematical over most of the LEED energy range [38]. The much more successful multiple-scattering theories are discussed in Chapter 3.

2.4 Auger Electron Spectroscopy (AES)

Some of the electrons observed as small features on a slowly varying background in the medium-energy range of the secondary electron distribution (Section 2.1) are called Auger electrons, after Pierre Auger who first saw their tracks in a Wilson cloud chamber in 1925 and correctly explained their origin [39]. These electrons are particularly useful in LEED experiments as they allow the atomic composition of the surface to be monitored under the same conditions as which LEED experiments are carried out. Several reviews of such applications have been published e.g. [40-44,10].

The Auger effect is a two-stage radiationless transfer of energy to an electron following ionisation of a core electron. Fig. 2.12 shows a schematic representation of the process for a solid. Initially, Fig. 2.12(a), a core electron is ionised by the primary electon beam, of usually 1-10keV. For elements other than hydrogen, helium, lithium atoms or the Li^+ ion in solids, an electron from a higher energy level is able to drop down to the inner vacancy, Fig. 2.12(b). The surplus energy is released either as an X-ray photon (X-ray fluorescence), or is available to a third electron that is ejected as an Auger electron, Fig. 2.12(c). If the original ionisation is from a level with a binding energy of less than about 2keV then Auger emission is more probable than X-ray production [45]. Auger electrons appear as small peaks in the medium-energy range of the secondary electron distribution and are readily distinguished from energy-loss peaks as their energies are

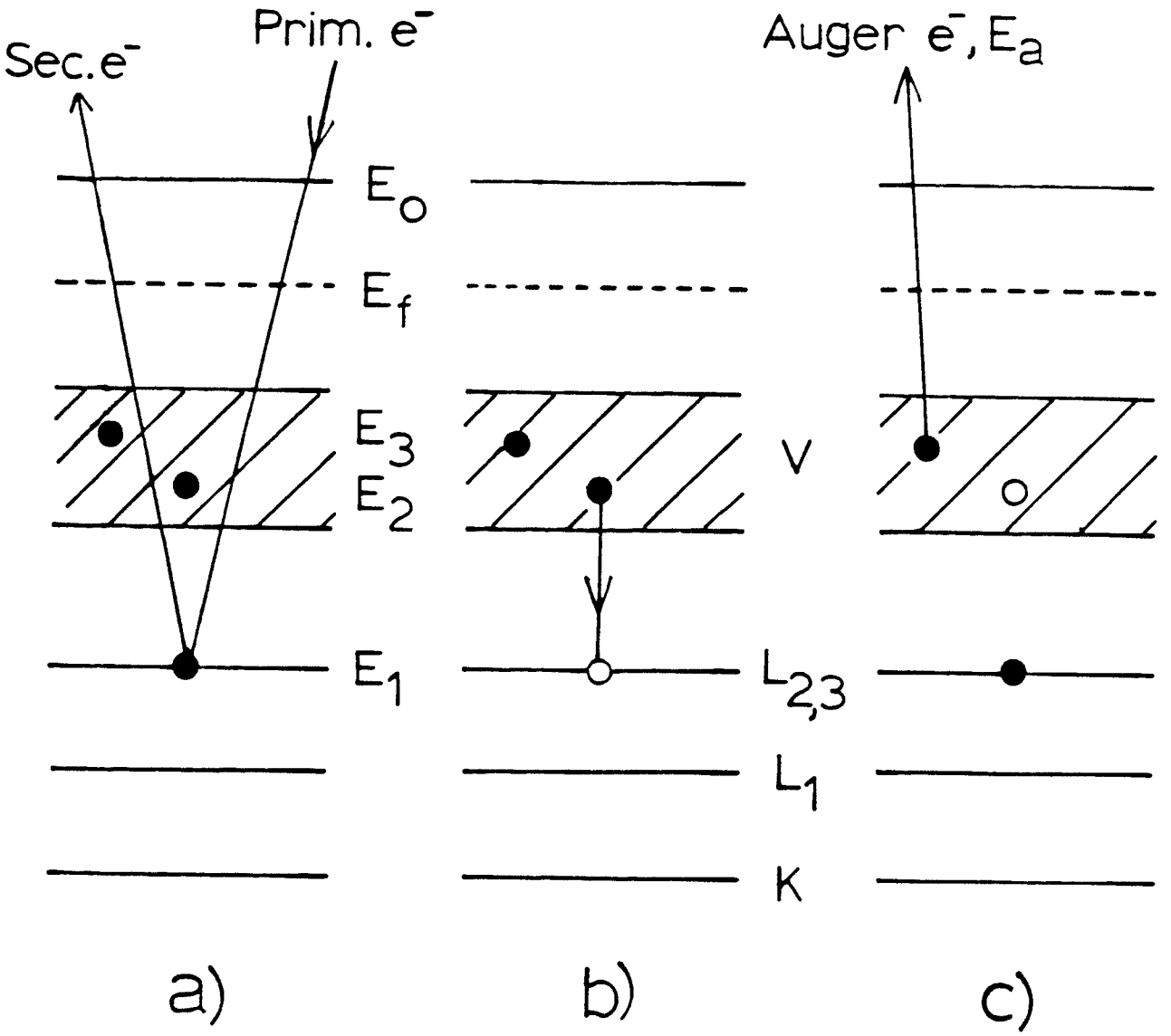

Figure 2.12 Schematic representation of the $L_{23}VV$ Auger transition: (a) ionisation of a core level, (b) filling of the core hole, (c) emission of the Auger electron.

independent of the primary beam energy, whereas loss peaks, due to e.g. plasmon excitation, shift with changes in the incident beam energy.

Auger electrons are labelled by the notation ABC, where these symbols indicate respectively the initial hole, the final hole, and the level from which the emitted electron leaves. For solids, the valence band is denoted by the letter V, but the inner levels, being quasi-atomic in nature, are assigned using the conventional X-ray notation K,L,M... according to the principal quantum number. Subscripts are used to denote the quantum numbers l and j; thus 1 for s states (l=0, j=1/2), 2 or 3 for p states (l=1, j=1/2,3/2) etc. With this notation the Auger electron of Fig. 2.12 would be designated as an $L_{2,3}VV$ electron.

The kinetic energy of that electron is approximately

$$E_A = E_1 - E_2 - E_3 \qquad (2.32)$$

The energy levels can be readily evaluated using X-ray [46] or ESCA [47] energy level energies, but this simple formula is inadequate in that it fails to take into account the different degrees of ionisation and the extra energy needed to remove the second electron from an already ionised atom. The formula has been modified by Jenkins and Chung [48]

$$E_A(Z) = E_1(Z) - 1/2[E_2(Z) + E_2(Z+1)] - 1/2[E_3(Z) + E_3(Z+1)] \qquad (2.33)$$

where Z is the atomic number of the chemical species involved. For atoms this formula has a typical accuracy of about 5eV.

The discrete levels in atoms are replaced by energy bands in solids. The quasi-atomic inner levels in solids may be shifted relative to the free atoms and the density of states in the valence band is sensitive to chemical environment. While the complete assignment of Auger transitions can be difficult, the use of AES for qualitative analysis depends only on the ability to assign peaks to a particular element. This type of assignment is generally unambiguous and the identity of surface atoms can be readily found using the tabulated Auger energies [49] and representative spectra [50] now available.

Unfortunately, quantitative assessments are not so easily made. The intensity of Auger emission is governed not only by the elemental cross-sections but also by the distribution of the element on the surface and into the crystal. Quantification therefore requires independent calibration experiments, usually employing known quantities of deposited material and assumptions of uniform distribution [51-52]. Auger spectra collected with a retarding field analyser based on LEED optics (see Ch. 4) allow impurities to be detected to approximately 1% of a monolayer for most elements.

A typical example of an Auger spectrum from the present work is shown in Fig. 2.13. This shows an Auger spectrum of a Rh(110) surface that is heavily contaminated with sulphur, and to a lesser extent, carbon and phosphorus. The spectrum is presented in the second derivative form $dN(E)/dE$ to enhance the otherwise weak Auger features and was taken with an incident beam current of about 10 microamps at 1.5keV. The Auger

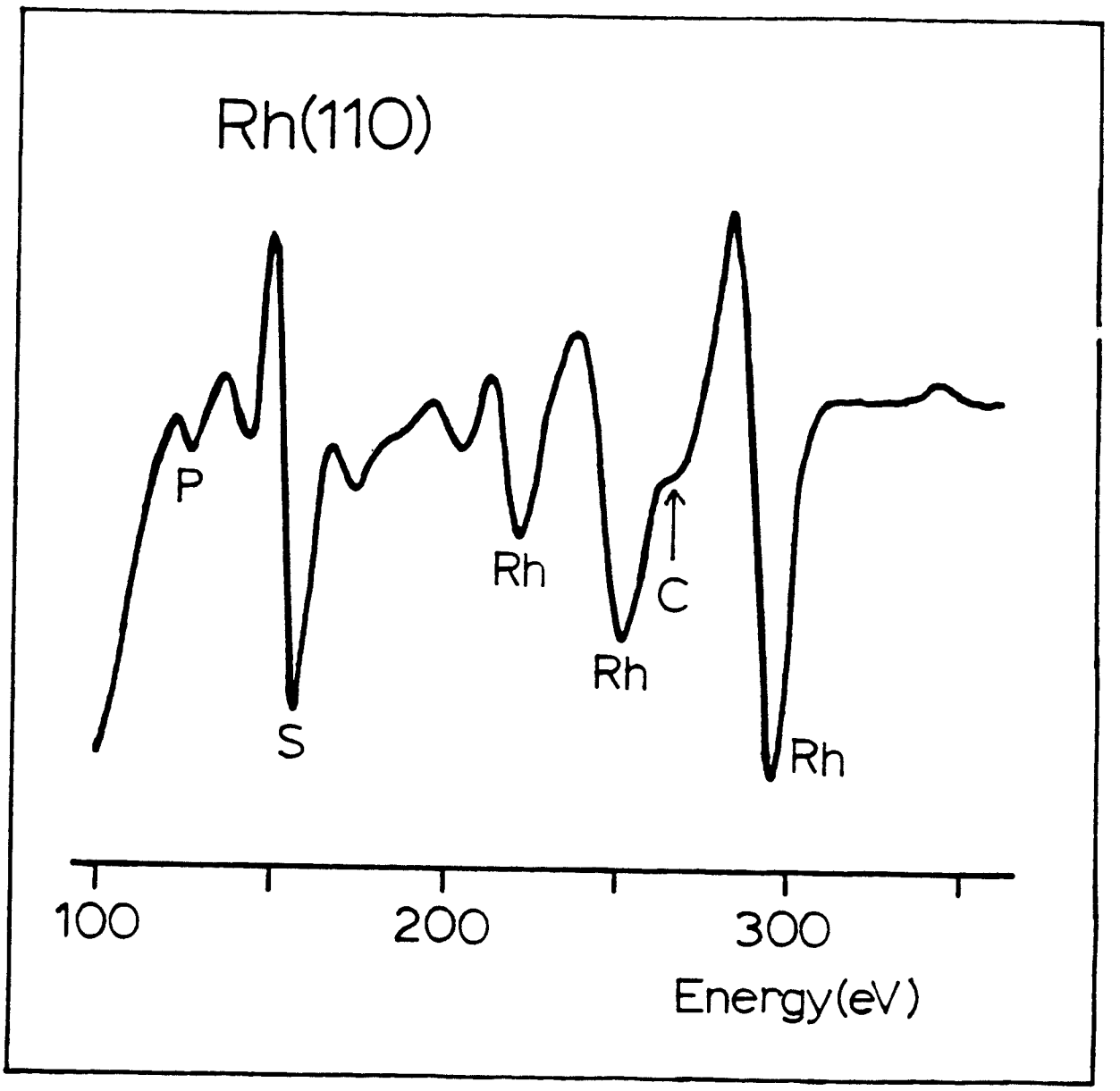

Figure 2.13 Auger spectrum of a heavily contaminated Rh(110) surface. Ep=1.5KeV, Ip=10 microamps.

transition energy is traditionally taken as the maximum negative excursion of the derivative peak [50].

CHAPTER 3

MULTIPLE-SCATTERING CALCULATIONS

3.1 Parameters For Theories Of LEED

In the last chapter we saw that intensities of LEED beams depend upon characteristics of the incident beam, such as energy and direction, and also on the geometry, scattering power, and dynamics of the surface atoms. Moreover, we also saw that the simple kinematical theory did not predict I(E) curves with any real measure of success and that any theory that is to be used to determine surface geometries, which is the primary object of the experiments, must therefore include multiple-scattering of the slow electrons. Such theories are called "dynamical" theories. In this section, the more important features that must be included in such theories are considered briefly; full details are given by Pendry [12].

3.1(a) the scattering potential

In a typical LEED experiment, only about 1% of the incident electrons are elastically backscattered, whereas the remainder are removed from the elastic flux by various inelastic scattering processes, particularly plasmon excitation [13]. While such inelastic scattering involves the valence electrons of the solid, the elastic backscattering arises from interactions with regions of high potential close to the nucleus; such regions involve the tightly bound core-state electrons or "ion-cores". The "muffin-tin" approximation is a convenient model of the solid that accommodates these two important features of the scattering process. As indicated in Fig. 3.1 the solid is modelled as non-overlapping regions of

spherically symmetric potential centred on each atom of the solid with a constant potential V_o in the intersphere region.

The intersphere region is mainly occupied by the valence electrons of the solid and therefore is the principal site for inelastic scattering. Inelastic scattering of all kinds can be treated in terms of a lifetime, τ, defined as the average time an incident electron spends in the crystal before it loses energy by inelastic scattering. Following Pendry [12], we can define the temporal variation of wavefunction amplitude for an electron with energy E, as $\exp(-iEt)$ in vacuo (for atomic units $h/2\pi=1$). In the region of constant potential V_o, this becomes $\exp[-i(E-V_o)t]$. If we allow V_o an imaginary component

$$V_o = V_{or} - iV_{oi} \qquad (3.1)$$

then the intensity of the wavefunction decays with time as $\exp(+2V_{oi}t)$, as V_{oi} is conventionally taken to be negative, and

$$V_{oi} = -1/2\tau \qquad (3.2)$$

Hence attenuation of the elastically scattered beams due to inelastic scattering can be simulated by adding an imaginary component to the potential, iV_{oi}, which can be estimated, via the time-energy uncertainty principle, from peak widths in I(E) curves. The peak width satisfies

$$\Delta E_w \geq 2|V_{oi}| \qquad (3.3)$$

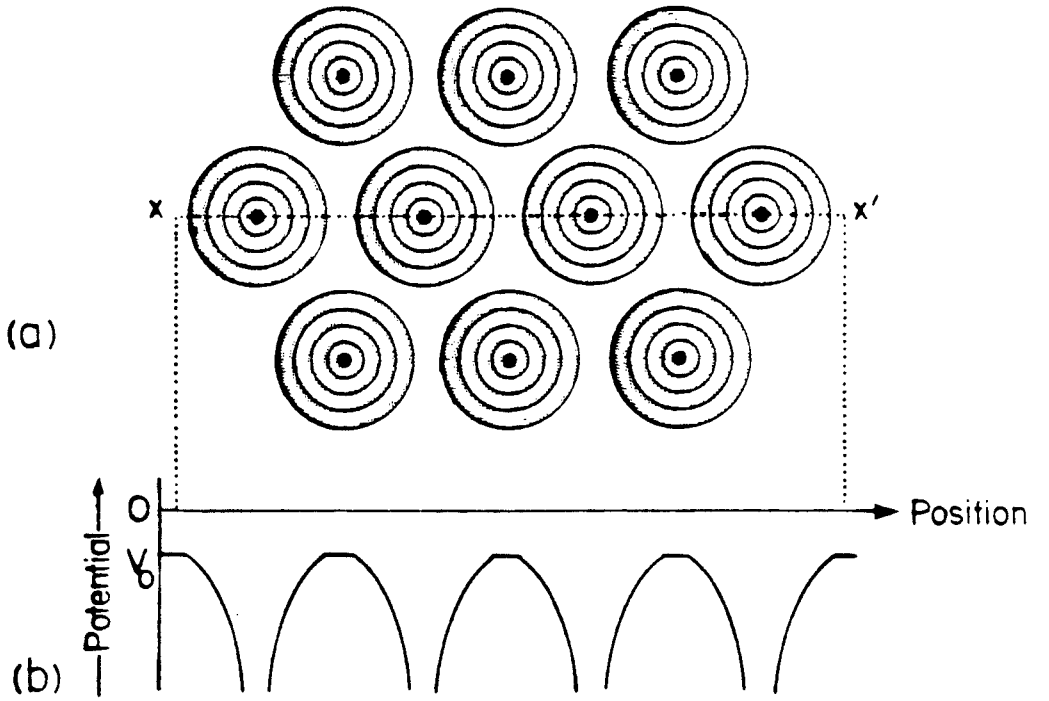

Figure 3.1 Muffin-tin potential (a) in cross-section as contours, (b) along XX'. Vc is the constant intersphere potential.

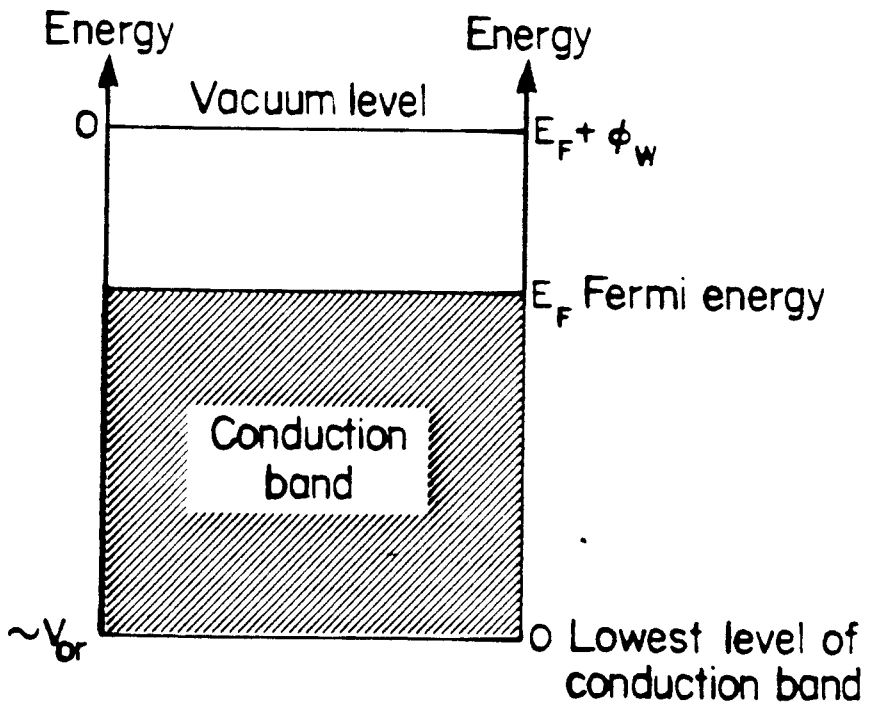

Figure 3.2 Illustration of the relationship between energies measured with respect to the vacuum level and those measured with respect to the lowest level of the conduction band.

V_{oi} is typically about -5eV and weakly energy-dependent [11]. In this work, V_{oi} was estimated from a primary Bragg type peak in an I(E) curve according to equation (3.3) and was allowed an energy-dependence of the form

$$V_{oi} = -i\beta(E) \qquad (3.4)$$

where $$\beta(E)=\alpha E^{1/3} \qquad (3.5)$$

according to the empirical relationship established by Demuth et al [11]. For copper α was set to 0.89 and to 1.12 for rhodium.

The real part of the intersphere potential, V_{or} in equation (3.1), accounts for the increase in energy experienced by an electron entering the crystal. This is usually called the inner potential. Typical values for this quantity are -10 to -20 eV and are, in principle at least, energy-dependent. This dependence appears, from experience, to be slight, and is usually ignored. Often V_{or} is approximated as the sum of the Fermi energy E_F and the work function ϕ_w, as shown in Fig. 3.2. In practice, V_{or} is usually estimated a priori and then empirically refined by visual or numerical comparison of calculated and experimental I(E) curves ; changing V_{or} amounts, to a good approximation, to a rigid shift in the energy scale. This topic is explored in more detail in Chapter 5. In this work V_{or} was set initially at -9.5eV for copper [65] and -12.0eV for rhodium [68,69].

The part of the potential that gives the backscattering in LEED is the spherically-symmetric potential within the muffin-tins; the ion-core potential. Various methods are available to

construct such potentials. In general, LEED calculations have used either full self-consistent band structure potentials or, more simply, the potential generated by a linear superposition of atomic charge distributions, as originally suggested by Mattheis [53]. Recently, a study of different prescriptions for ion-core potentials [54] has suggested that the simple muffin-tin linear superposition, with the $X\alpha$ approximation of Slater for the exchange potential [55], provides a suitable potential for LEED calculations, and that the full self-consistent band structure calculations do not lead to significant improvements in the degree of agreement of calculations with experiment (in that instance).

In the initial stages of this work a band structure potential for rhodium was not available. Hence interest centred on generating ion-core potentials by the superposition of charge densities method. In co-operation with Dr. L. Noodleman, a method was used that employed some of the initial routines of the scattered-wave $X\alpha$ programs developed by Johnson [56].

The method is as follows:

(i) using the tables of Herman and Skillman [57], the charge distribution for an isolated atom was calculated;

(ii) using the MOLPOT and ENERGY routines of the scattered-wave $X\alpha$ programs, the atomic charge densities of a cubo-octahedral M_{13} cluster (corresponding to an FCC crystal) were superimposed, Fig. 3.3. The charge distribution of the central atom was used to generate an electrostatic potential

including an exchange term using Slater's approximation [55].

$$V_{ex}(\underline{r}) = -6\alpha [(3p(\underline{r})/8\pi]^{1/3} \qquad (3.6)$$

Here $p(\underline{r})$ is the charge density, with α values taken from the tabulations of Schwarz [58,59].

The validity of this method was checked by comparing the scattering factors, Section 3.1(b), and I(E) curves, Section 3.2, produced by a Cu_{13} cluster superposition potential, V_{Cu13}, with those from the band structure potential of Burdick-Chodorow [60,61], V_{Cu}^{BC}. This potential had previously been used in a successful LEED analysis of the Cu(100) surface [65]. A rhodium superposition potential, V_{Rh13}, was also generated; the data used for the two potentials is given in Table 3.1. At a later stage a band structure potential became available for rhodium V_{Rh}^{WJM} [64]. Atomic phase shifts calculated for a cluster of 13 silver atoms were also shown to correspond closely to those used by Marcus et al [104].

3.1(b) phase shifts

LEED intensity calculations can be conveniently broken down into two parts (i) the determination of a single ion-core potential, and (ii) the solution of the behaviour of an incident electron multiply scattered by a lattice made up of these single ion-core potentials. The first step in performing part (ii) is to express the elastic scattering of an incident electron by a

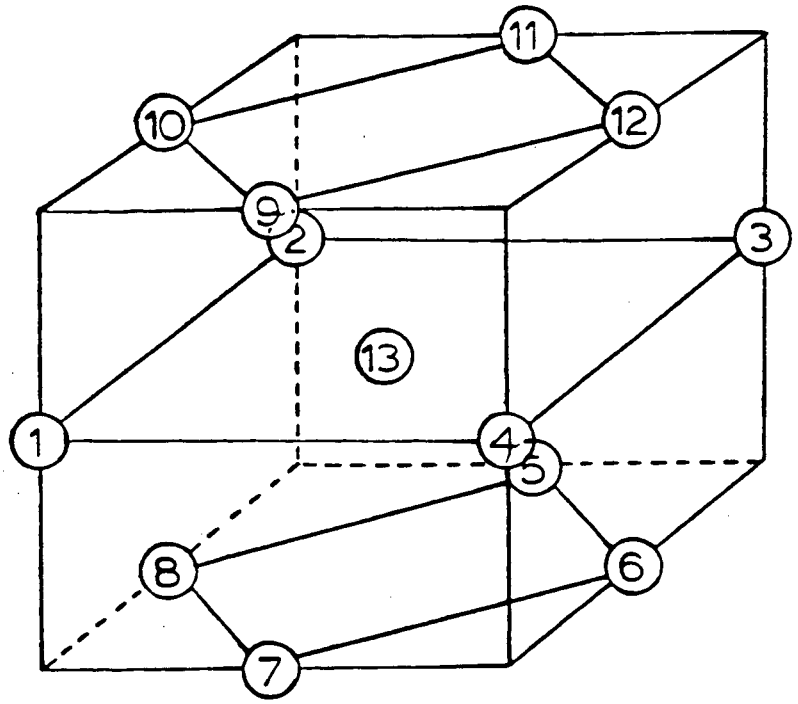

Figure 3.3 The cubo-octahedral M_{13} cluster used to model the ion-core potential for FCC crystals.

	Cu	Rh	
a_o	3.6150	3.8031	Å
r_{MT}	1.2780	1.3449	Å
α	0.70697	0.70214	

Table 3.1 Data used for construction of superposition potentials for M_{13} clusters. The crystal cube side a_o and muffin-tin radius r_{MT} are from [62,63] and the α values from [58,59].

single ion-core potential.

Assuming that the core-electrons are not polarised by the incident electron, the wavefunction of an incident electron inside a muffin-tin sphere is obtained by solving the Schrodinger equation

$$[\ -1/2\nabla^2 + V_s\ ]\psi = E\psi \qquad (3.7)$$

where V_s is the ion-core potential. For an incident plane wave, scattered waves correspond to solutions of equation (3.7). The intensity scattered to a particular point depends only on the modulus of the wave vector, k, the scattering angle θ^s, and the distance r of the point of observation from the scattering region, as depicted schematically in Fig. 3.4. At large r the solutions to equation (3.7) have the form [12,66,67];

$$\psi(r,\theta_s) \propto \exp(ikr\cos\theta^s) + f_k(\theta^s)\exp(ikr/r) \qquad (3.8)$$

where the first term is the incident wave at the point of observation and the second is an outgoing scattered spherical wave. The atomic scattering factor f_k is usually expanded as [12,66,67];

$$f_k(\theta^s) = (1/k)\sum_{l=o}^{\infty}(2l+1)\exp(i\delta_l)\sin(\delta_l)P_l(\cos\theta^s) \qquad (3.9)$$

in terms of the Legendre polynomials $P_l(\cos\theta^s)$, and the phase shifts δ_l which characterise the ion-core scattering for each value of the angular momentum quantum number l.

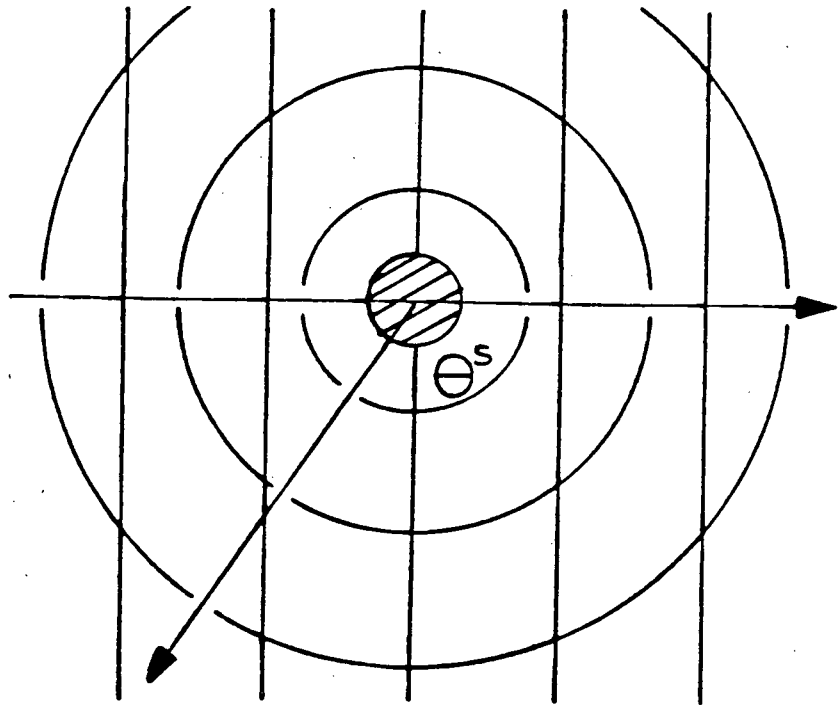

Figure 3.4 An ion-core immersed in a plane wave inducing scattered spherical waves whose intensities are functions of k, θ^s and r. After Pendry [12].

The scattering properties of an ion-core are thus contained in the energy-dependent phase shifts. For the potentials described in Section 3.1(a) the relevant phase shifts were found by numerical integration of the Schrodinger equation inside the muffin-tin sphere and joining the large r asymptotic forms of the solutions smoothly to the solution of the Schrodinger equation outside the sphere. Whilst in principle the expansion of equation (3.9) is over all values of l, it does converge quite rapidly and for calculations up to 250eV or so, 8 phase shifts (l=0-7) are usually sufficient [15] and were used in all the calculations presented here.

Plots of the energy-dependence of the phase shifts for the

two copper and two rhodium potentials are shown in Fig. 3.5 and Fig. 3.6. For copper, the band structure V_{Cu}^{BC} and superposition V_{Cu13} potentials produce very similar phase shifts which agree well with those given previously [35]. The rhodium shifts show somewhat greater differences. For example, the curves for l=0 and l=1 show corresponding features at lower energies for V_{Rh}^{WJM} compared with V_{Rh13}; also there are significant differences in the slopes of the two sets of phase shifts e.g. for l=2 at 5Ry (1Ry=13.6eV).

3.1(c) temperature corrections

In Section 2.3(b) it was noted that LEED beam intensities have a substantial temperature dependence and that such effects suggest that lattice motion should be included in the model used to calculate I(E) curves. The larger atomic displacements that occur as the temperature is raised increase the incoherent scattering and therefore decrease the intensities of scattered beams compared with those from an idealised stationary scattering lattice. In many instances, the experimental temperature-dependence of beam intensities is described quite well by a kinematical model [72].

Detailed treatments within the multiple-scattering theory have been produced [70,71]. Although atoms are effectively stationary on the time-scale of the diffraction process, their motion is sufficiently rapid for the detector to register intensities that have been averaged over the atomic displacements. The LEED measurement averages over many atoms at

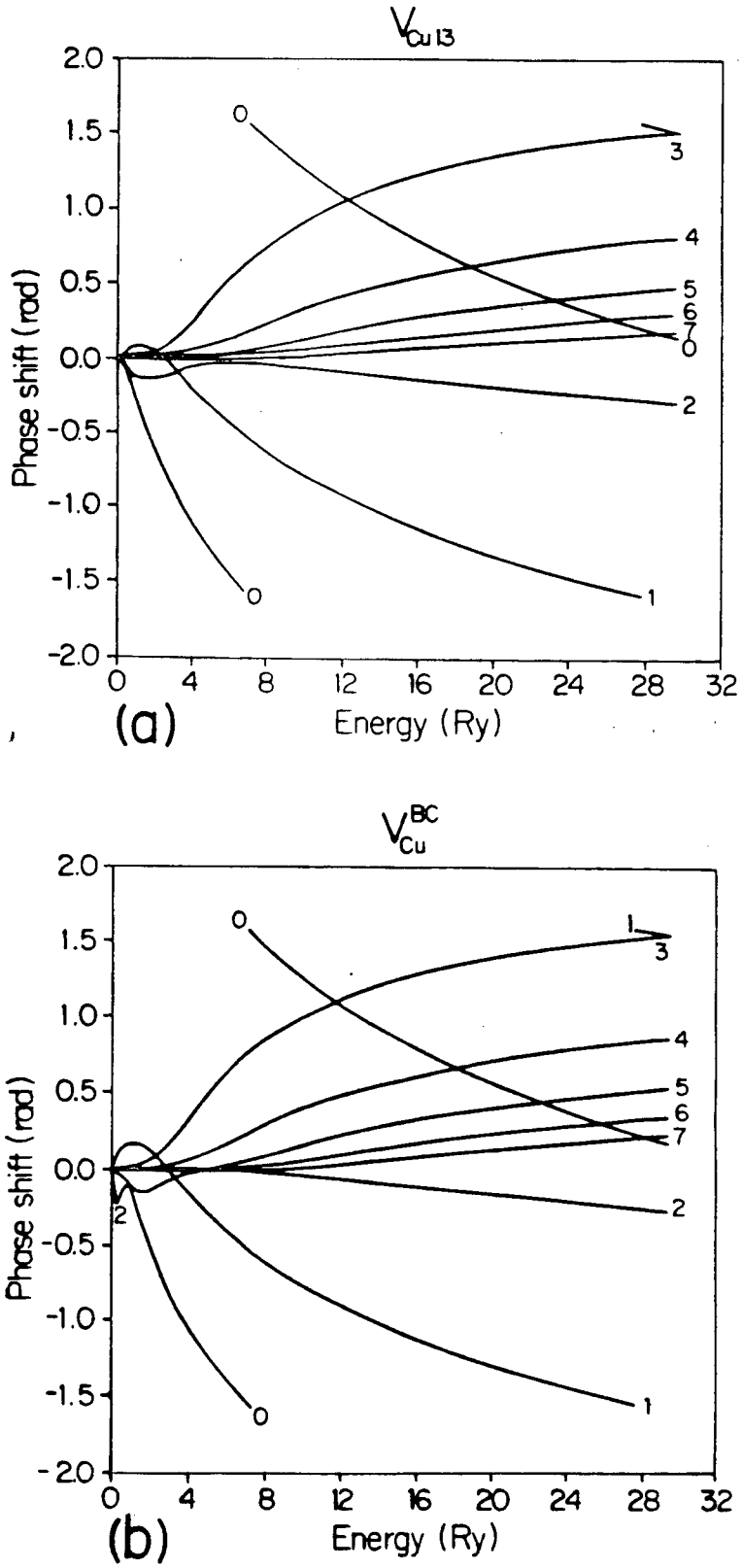

Figure 3.5 Energy dependence of copper phase shifts (l=0-7) for the potentials: (a) $V_{Cu\,13}$ and (b) V_{Cu}^{BC}.

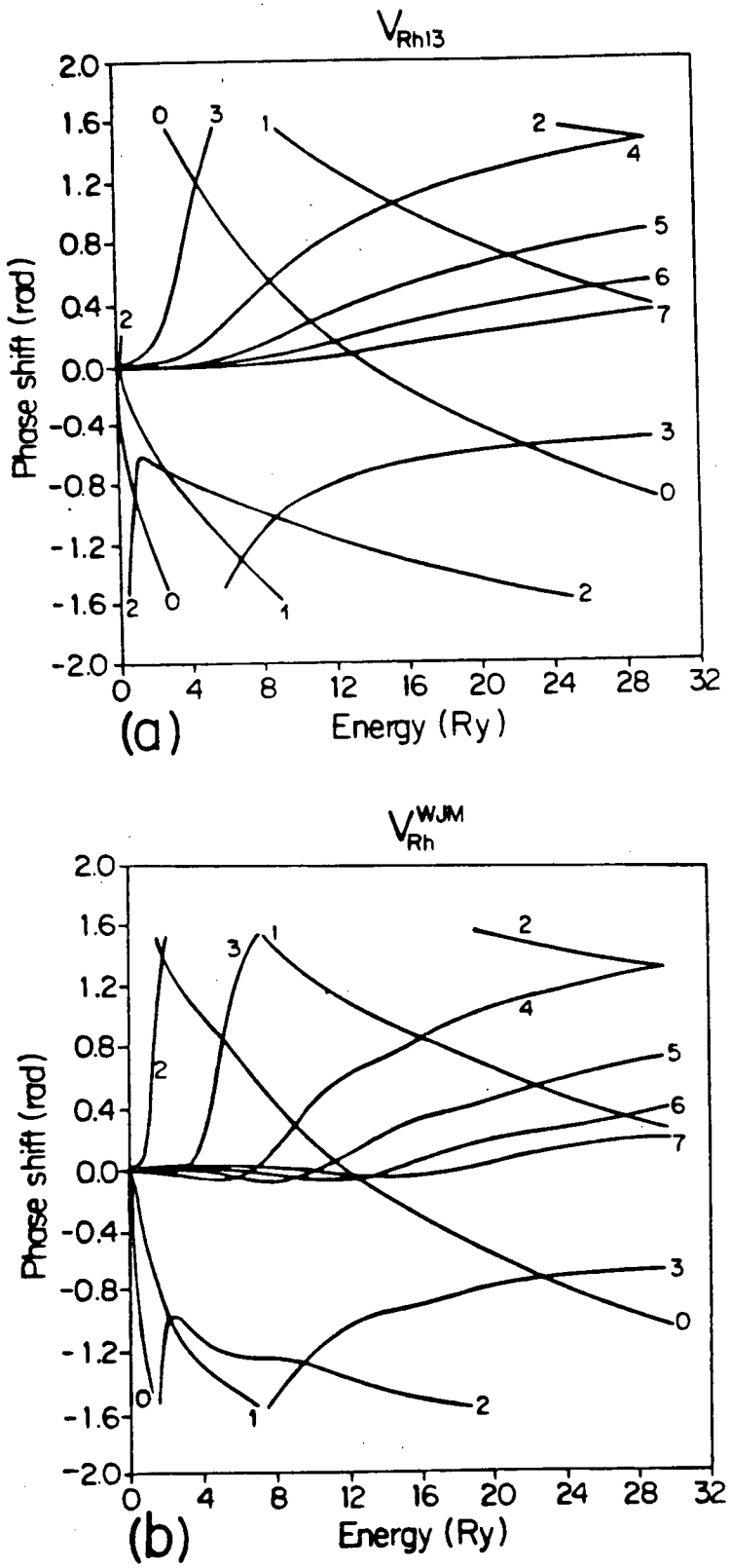

Figure 3.6 Energy dependence of rhodium phase shifts (l=0-7) for the potentials: (a) V_{Rh13} and (b) V_{Rh}^{WJM}.

any one moment. Thus the scattering of each atomic potential is averaged over the atomic motions. If we assume that the motions are uncorrelated [12] then we obtain a temperature-dependent atomic scattering factor that is related to that of the rigid lattice but with modifications in the phase shifts, which become complex. These temperature-dependent phase shifts must interfere in the correct fashion to produce strong forward, and weak back-scattering. In the back-scattering case there must be strong cancellation between contributions from different phase shifts. The higher the temperature, the more this is so, hence more shifts are needed to avoid truncation of the series of equation (3.9).

$$f_k(\theta^s, T) = \exp(-M_\chi)\, f_k(\theta^s) \qquad (3.10)$$

In the case of isotropic vibrations,

$$\exp(-M_\chi) = \exp(-\alpha|\underline{k}-\underline{k}'|^2) \qquad (3.11)$$

and α can be approximated, for large T, as a Debye-Waller type of factor

$$\alpha = 3\hbar^2 T/2mk_\beta\theta_D^2 \qquad (3.12)$$

where k_β is Boltzmann's constant, m the atomic mass of an ion-core and θ_D the Debye temperature.

In this work, surface atomic vibrations were assumed to be isotropic and layer-independent. An experimental value of the surface Debye temperature was used for copper (viz. 275K [73]) and, following van Hove and Tong [74], a value of $\sqrt{0.7}$ times the bulk value of 480K [75] was used for rhodium.

3.2 General Schemes Of Calculation

Having computed a suitable ion-core potential, with temperature-dependent phase shifts to describe the scattering from vibrating atoms, the other, and most difficult, task is to solve for an incident electron multiply scattered by the crystal lattice of scattering potentials.

Many methods have been developed for performing multiple-scattering, or dynamical, calculations; they differ considerably in their range of applicability, speed and computer memory requirements. All the useful methods start with the calculation of the scattering matrices $M_{\underline{g}\underline{g}'}$ that describe the electron flux multiply scattered, by one plane of the crystal parallel to the surface, from an incoming wave labelled by the reciprocal vector $\underline{g}$ (or angular momentum component l, depending on the particular method) to a scattered wave labelled by $\underline{g}'$ (or l'). Once this intralayer scattering matrix is known, the amplitude of beams diffracted from an assemblage of n layers, approximating an infinite crystal, can be found. A number of methods of doing this are available; they take into account the removal of electron flux by inelastic scattering processes and allow for interplanar multiple-scattering events.

Between any pair of layers in the crystal is present a set of plane waves [12]

$$\sum_{\underline{g}} U_{\underline{g}}^{\pm} \exp[i(\underline{k}+\underline{g})\cdot\underline{r}] \qquad (3.13)$$

or beams, that have been formed by diffraction of the incident

beam. Each of these has a different parallel component of momentum $(\underline{k}_{o_{\parallel}}+\underline{g})$, and travels either forwards or backwards $(\pm)$. Forward travelling beams

$$\sum_{\underline{g}} U_{\underline{g}}^{+} \exp(\underline{K}_{\underline{g}}^{+} \cdot \underline{r}) \qquad (3.14)$$

where

$$K_{\underline{g}}^{\pm} = [(\underline{k}_{o_{\parallel}}+\underline{g})_{x,y} \pm (2E-2V_{or}) - |\underline{k}_{o_{\parallel}}+\underline{g}|^2)^{1/2}] \qquad (3.15)$$

are incident upon the next layer as in Fig. 3.7. This set of beams is multiply-scattered by the plane of ion-cores as described by the layer matrix $M_{\underline{g}\underline{g}'}^{\pm\pm}$ (the $\pm$ signs referring to forward or backscattering) to give

$$\sum_{\underline{g}} \sum_{\underline{g}'} M_{\underline{g}\underline{g}'}^{\pm\pm} U_{\underline{g}}^{+} \exp(i\underline{K}_{\underline{g}}^{+} \cdot \underline{r}) \qquad (3.16)$$

with [12]

$$M_{\underline{g}\underline{g}'}^{\pm\pm} = (8\pi^2 i/Ak_o K_{\underline{g},z}^{\pm}) \sum_{LL'} Y_L(\underline{K}^{\pm}(\underline{g})) [1-X]_{LL'}^{-1} Y_{L'}(\underline{K}^{\pm}(\underline{g})) e^{i\delta_{L'}} \sin\delta_{L'} \qquad (3.16a)$$

In the sum over angular momentum components are included spherical harmonics Y_L and temperature-dependent phase shifts, δ_L, while multiple-scattering is accounted for by the inverse matrix term [12].

The evaluation of $M_{\underline{g}\underline{g}'}^{\pm\pm}$ is complicated and need not concern us here; however, it is worth noting that it is essentially composed of a stucture factor, dependent only on the positions of the ion-cores in the layer, and a scattering factor that describes the multiple-scattering within the layer in terms of phase shifts. Full details have been given by Pendry [12].

It is in the manner of assembling a stack of layers into a crystal and computing the reflectivity of the crystal that the various calculational schemes differ. They can be divided into

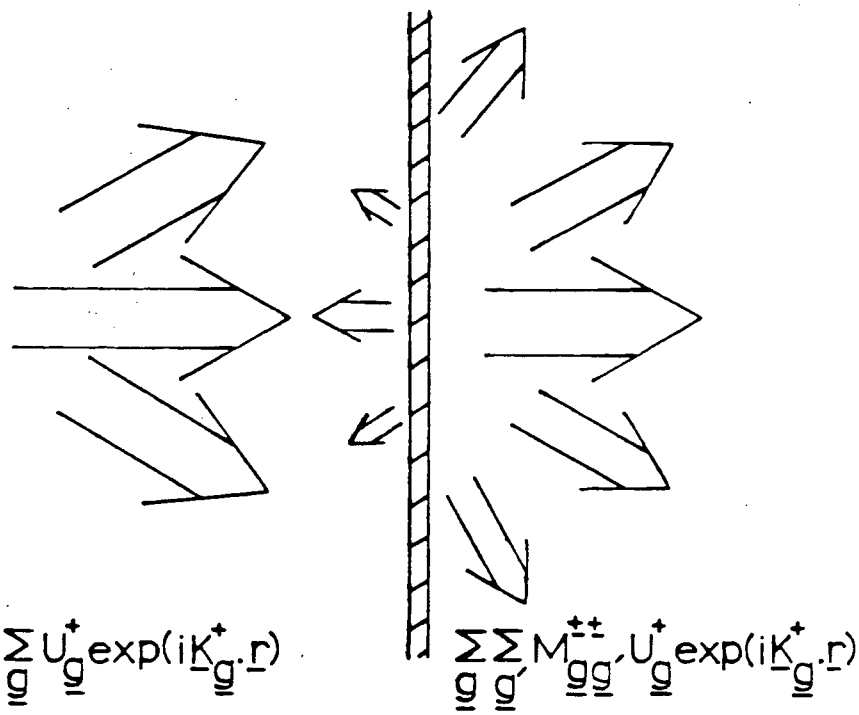

Figure 3.7 Schematic representation of a set of plane waves incident from the left multiply scattered by a plane of ion-cores.

a) "exact" methods

(i) Bloch wave methods

(ii) exact T-matrix method [76]

b) perturbative approximations

(i) T-matrix expansions [77]

(ii) layer doubling [12,78]

(iii) renormalised forward scattering (RFS) [12,79]

In this work the last two methods were used and will be discussed in a little detail. The other schemes will be

discussed in only the briefest outline and the interested reader is referred to individual references and to the review of Tong [15].

The "exact" methods are exact in that multiple-scattering is treated exactly both within and between layers. In the Bloch wave method the scattering matrices for a layer are found and the wave amplitudes between two layers calculated allowing for interplanar multiple-scattering. The scattered wavefield is then expressed as a combination of Bloch waves, or normal modes of the crystal. At the surface the scattered wavefunctions are matched to those of the incident wave to give the reflected amplitudes. In the most developed version of these methods, the layer KKR method [65], intralayer scattering is treated by the Korringa-Kohn-Rostoker (KKR) method of band theory. This method is accurate but slow as one has to solve a (2nX2n) matrix eigenvalue problem, where n is the number of waves used. Consequently, the layer KKR method has only been used to any great extent by the group at IBM [65] because of the vast computer time and storage requirements involved.

The exact T-matrix method [76] expresses the layer scattering matrices as so-called $\uparrow$ matrices in angular momentum, rather than reciprocal, space. A layer-dependent T-matrix is then computed, which includes contributions to the scattered wavefield from one layer due to waves already scattered from other layers. In order to do this, the crystal must be approximated as an N layer slab (N typically about 5). The total reflectivity of the N layer slab is then found. This involves solving N equations each having matrices of dimensions

$(l_{max}+1)^2 X (l_{max}+1)^2$. This method is accurate in the presence of inelastic scattering if enough phase shifts and layers are used, but is rather slow and is difficult to extend to complicated surfaces.

The T-matrix expansion method [77] is an extension of the last method in which a limit is placed upon the order of multiple-scattering (inter- and intraplanar) allowed. This little-used method is cumbersome above third order and can fail with strong scatterers or weak absorption.

3.2(a) layer doubling and RFS methods

These two convergent perturbative methods, pioneered by Pendry, Van Hove and Tong [12,78,79], are among the most popular in use today. Their iterative form makes them flexible, relatively easy to use in a routine manner, fast and conservative in core space requirements.

The layer doubling method starts with the multiple-scattering matrix for a single layer; in Fig. 3.8 these are marked as R (reflection) and T (transmission) matrices for two layers A and B. The interplanar multiple-scattering is then solved exactly for the pair to produce a composite layer C. The resulting matrices R_C and T_C are then used to solve for 4 layers, thus doubling the number of layers in the crystal. This process of doubling the thickness of the slab is then repeated until the reflected intensities converge, typically in 8 or 16 layers. This method involves matrix inversions and products of dimension n, the number of beams used, that converge even for

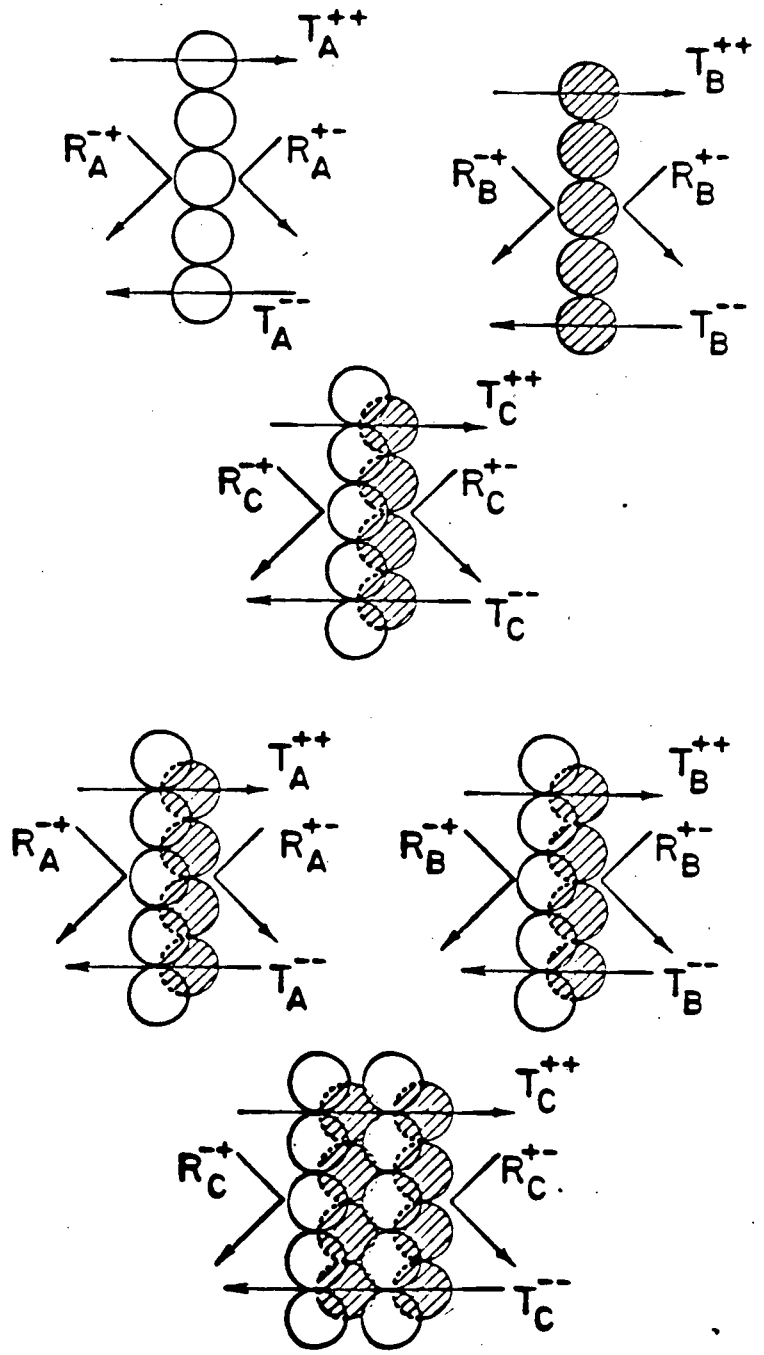

Figure 3.8 Building up subplanes by the layer doubling process. Individual subplanes are marked A and B; the resultant composite is marked C. After Tong [15].

small interplanar spacings.

The renormalised forward scattering, or RFS, method once more starts from the single layer multiple-scattering matrices of equation (3.16). Electrons are propagated through the crystal with forward scattering being evaluated exactly; backscattering is treatedly perturbatively. Referring to Fig. 3.9 , following Tong [15], we can define a column vector $A^{i}_{\alpha}(\underline{g})$ of length n, whose elements represent the amplitudes in each of the n beams (labelled by $\underline{g}$) propagating into the crystal, at the α^{th} layer. The index i denotes the number of times electrons are propagating into the crystal and is also the iteration order. Outside the crystal we have

$$A^{1}_{o}(\underline{g}) = \begin{pmatrix} 1 \\ 0 \\ 0 \\ 0 \\ \cdot \\ \cdot \end{pmatrix} \qquad (3.17)$$

The coefficients $A^{i}_{\alpha}(\underline{g})$ are evaluated midway between planes and can be found by iteration, assuming all layers are identical, thus

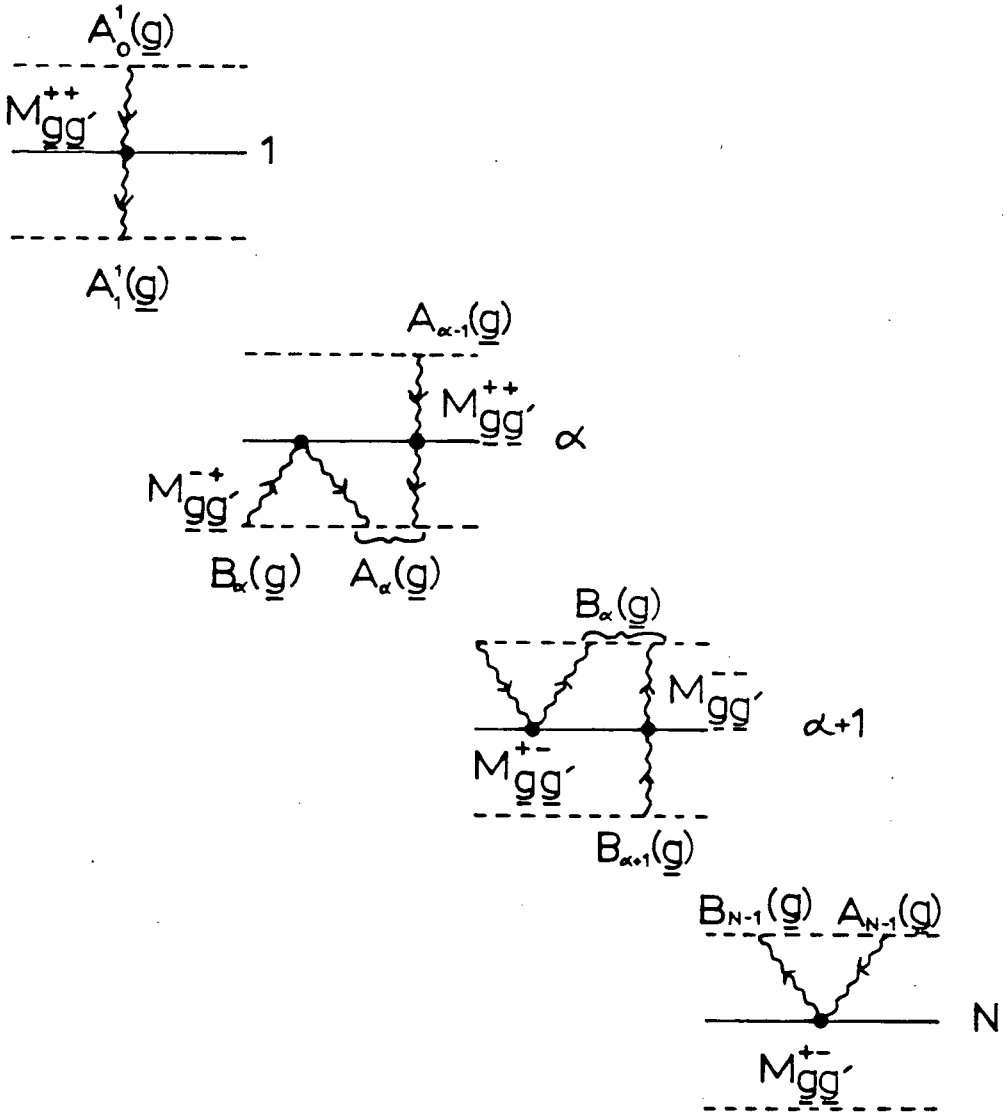

Figure 3.9 Diagramatic representation of the renormalized forward scattering (RFS) process. Inward amplitudes $A^{\uparrow}_{\alpha}(g)$ propagate from vacuum through the 1st layer to the Nth layer where they are turned around. The electrons are then propagated to the 1st layer with outward amplitudes $E^{\downarrow}_{\alpha}(\underline{g})$.

$$A^1_1(\underline{g}) = \sum_{\underline{g}'} M^{++}_{\underline{g}\underline{g}'} A^1_0(\underline{g}) \qquad (3.18)$$

and

$$A^1_\alpha(\underline{g}) = \sum_{\underline{g}'} M^{++}_{\underline{g}\underline{g}'} A^1_{\alpha-1}(\underline{g}) \qquad (3.19)$$

This is carried on until at the N^{th} layer the electrons are damped such that a negligibly small elastic flux reaches the $(N+1)^{th}$ layer, typically 7-14 layers.

The electrons are then turned around and we form a set of $B^i_\alpha(\underline{g})$ for amplitudes of electrons going back out. The set $B^1(\underline{g})$ are amplitudes for each $\underline{g}$-beam after passing in and outwards through the crystal once. Therefore, referring again to Fig. 3.9 we have

$$B^1_{N-1}(\underline{g}) = \sum_{\underline{g}'} M^{+-}_{\underline{g}\underline{g}'} A^1_{N-1}(\underline{g}) \qquad (3.20)$$

For $B^1_\alpha(\underline{g})$ there are contributions from backscattering of $A^1_\alpha(\underline{g})$ from the $(\alpha+1)^{th}$ plane, and transmission of $B^1_{\alpha+1}(\underline{g})$ thus

$$B^1_\alpha(\underline{g}) = \sum_{\underline{g}'} M^{+-}_{\underline{g}\underline{g}'} A^1_\alpha(\underline{g}) + \sum_{\underline{g}'} M^{--}_{\underline{g}\underline{g}'} B^1_{\alpha+1}(\underline{g}) \qquad (3.21)$$

Each set of coefficients is thus obtained from sets previously evaluated.

The electrons are eventually scattered by the first layer back into the crystal; i=2. Again the coefficients $A^2_\alpha(\underline{g})$ and, after reaching a deepest layer $N^1 \leq N$, the reflection coefficients $B^2_\alpha(\underline{g})$, are evaluated. Eventually the reflected amplitudes

converge and are summed to yield the reflected intensities.

The RFS method is very fast, usually requiring 3-5 passes to converge, but can fail to converge if the inelastic damping is too weak or the interlayer spacing too small. In such cases the layer doubling method, though slower, is to be preferred.

In the calculations reported here the RFS method was used in the main. Occasionally, at small interlayer spacings the layer doubling method was used; where the two methods overlapped, it was found that the intensities produced by both methods were numerically very similar.

3.2(b) uses of symmetry

Considerable savings in computer storage and time can be made by exploiting the symmetry among plane waves present when the electron beam is incident on the crystal surface along an axis or a plane of symmetry of the surface structure. Group theory allows us to consider only the symmetrical linear combinations of symmetry-related plane waves, as detailed by van Hove [81]. Therefore, in the list of $\underline{g}$ vectors that is input to the program, as explained shortly in Section 3.2(c), only one vector $\underline{g}$ for each set of symmetry-related vectors is read, together with a code-number that informs the programs about the omitted symmetry-related vectors. This code number instructs the programs to use the appropriate symmetrical wavefunctions (rather than the simple plane waves labelled by $\underline{g}$) and to assign only one row and one column in diffraction matrices for each symmetrical wavefunction (rather than one for

Surface	Max. g vector	Symm. axis	Number of beams no symm.	Number of beams with symm.
Rh(100)	{62}	4	69	13
Rh(111)	{43}	3	55	13
Rh(110)	{42}	2	55	18

Table 3.2 Reduction, due to symmetry, in the number of beams needed at normal incidence for the three simple faces of rhodium. The maximum g vector corresponds to the beam set with the largest (hk) values needed to cover the energy range 40-250eV.

each of the various symmetry-related plane waves). The savings of core storage and time can be considerable. This is illustrated in Table 3.2 where the reduction, due to symmetry, in the number of beams needed at normal incidence to cover the energy range up to about 250eV is shown for the Rh(100), (111) and (110) surfaces.

3.2(c) program flow

The flow-chart of Fig. 3.10 summarises the sequence of events that occur in a multiple-scattering calculation. The programs start by reading in all the relevant physical and potential data, and also a list of diffracted beams with their symmetry code-numbers. The multiple-scattering within a layer, described by equation (3.16) involves sums over reciprocal vectors $\underline{g}$, that is, over the diffracted beams. At any particular energy E, only certain beams with $\underline{g}$ vectors that permit $\underline{k}'_{\perp}$ to remain real, Section 2.2, can leave the crystal. In addition there are evanescent waves that propagate without emerging because of the potential step at the surface. The program automatically includes in the sums over the reciprocal

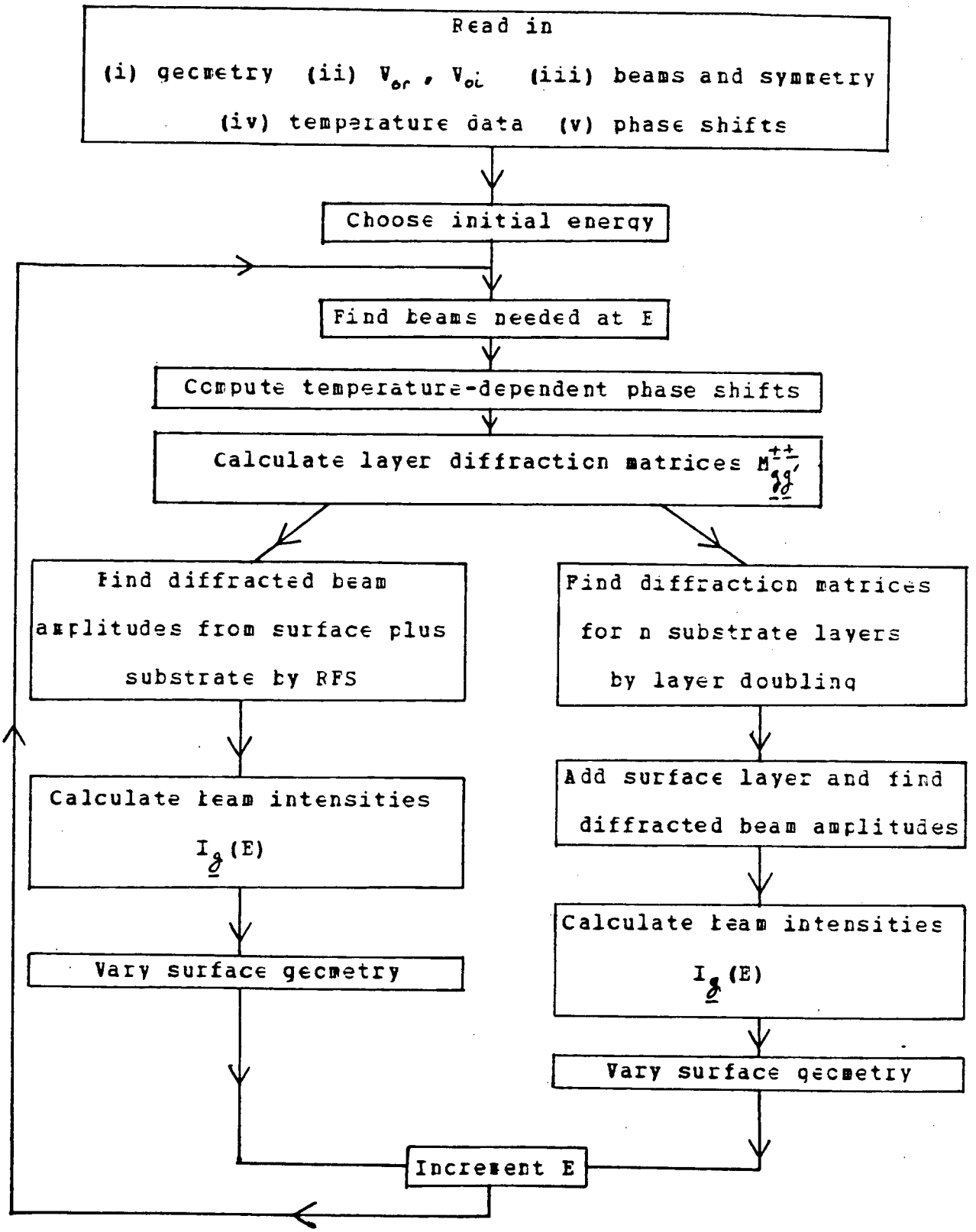

Figure 3.10 Flowchart showing principal steps in a multiple-scattering LEED calculation, using the RFS or layer doubling programs.

vectors only those waves that, from one layer to the next, do not decay to less than 0.002 of their amplitude.

Having incorporated temperature effects into the phase shifts, the layer diffraction matrices are calculated. The reflected amplitudes, and subsequently intensities, are then found by the layer doubling or RFS routines. Each method has the facility to include a surface layer that has a different geometry from that of the substrate. In the case of clean metal surfaces, the surface layer could be distinguished by a lateral reconstruction relative to the bulk structure or by a simple change in the topmost layer spacing. The two methods differ slightly in that the layer doubling method calculates reflection and transmission matrices for the substrate once only and then these are used repeatedly for as many surface geometries as desired by adding the surface layer as the final step. Using RFS, the whole substrate plus surface layer system must be rebuilt for each geometry as the surface layer is involved in the initial step of the calculation of the interlayer scattering.

The intensities $I_{\underline{g}}(E)$ of each beam are stored before incrementing the energy and repeating the whole process. Generally, the calculations were performed over an energy range of approximately 40 to 250eV. These limits are set at the low end by the lack of experimental data, and at the high end by the expense of the calculations and by doubts as to whether 8 phase shifts are sufficient to ensure convergence of the atomic scattering factors. An energy increment of 2eV was used for the range 40 to 100eV, and the increment was doubled for the range

above 100eV. For the latter range, intensity values were then interpolated back onto a 2eV grid using a cubic spline interpolation method [80]. All calculated intensities were stored on magnetic tape and subsequently the data could be transferred to paper tape for plotting by the Nova 2 minicomputer in the laboratory.

In order to check that the programs were running correctly, I(E) curves were calculated for surfaces that had previously been studied theoretically; careful checks were made for discrepancies before any calculations were performed on the unknown rhodium surfaces. These tests were made against

(i) the calculations of Laramore [20] for Cu(111) and Cu(100);

(ii) the calculations of Demuth et al [11] for Ni(100) and Ni(110), using nickel phase shifts supplied by M.A. Van Hove

In all cases comparison with the previous calculations showed that the programs used here produced essentially identical I(E) curves. This gave us confidence for using these programs for determining the unknown structures of rhodium surfaces.

These type of calculations were developed to investigate surface structures, and it is gratifying that significant changes can occur in calculated I(E) curves for only minor changes in the assumed surface geometry. For example, in Fig. 3.11 we see I(E) curves calculated for a Cu(111) surface at normal incidence, using both the Burdick-Chodorow, V_{Cu}^{BC}, and superposition, V_{Cu13}, potentials discussed earlier. The

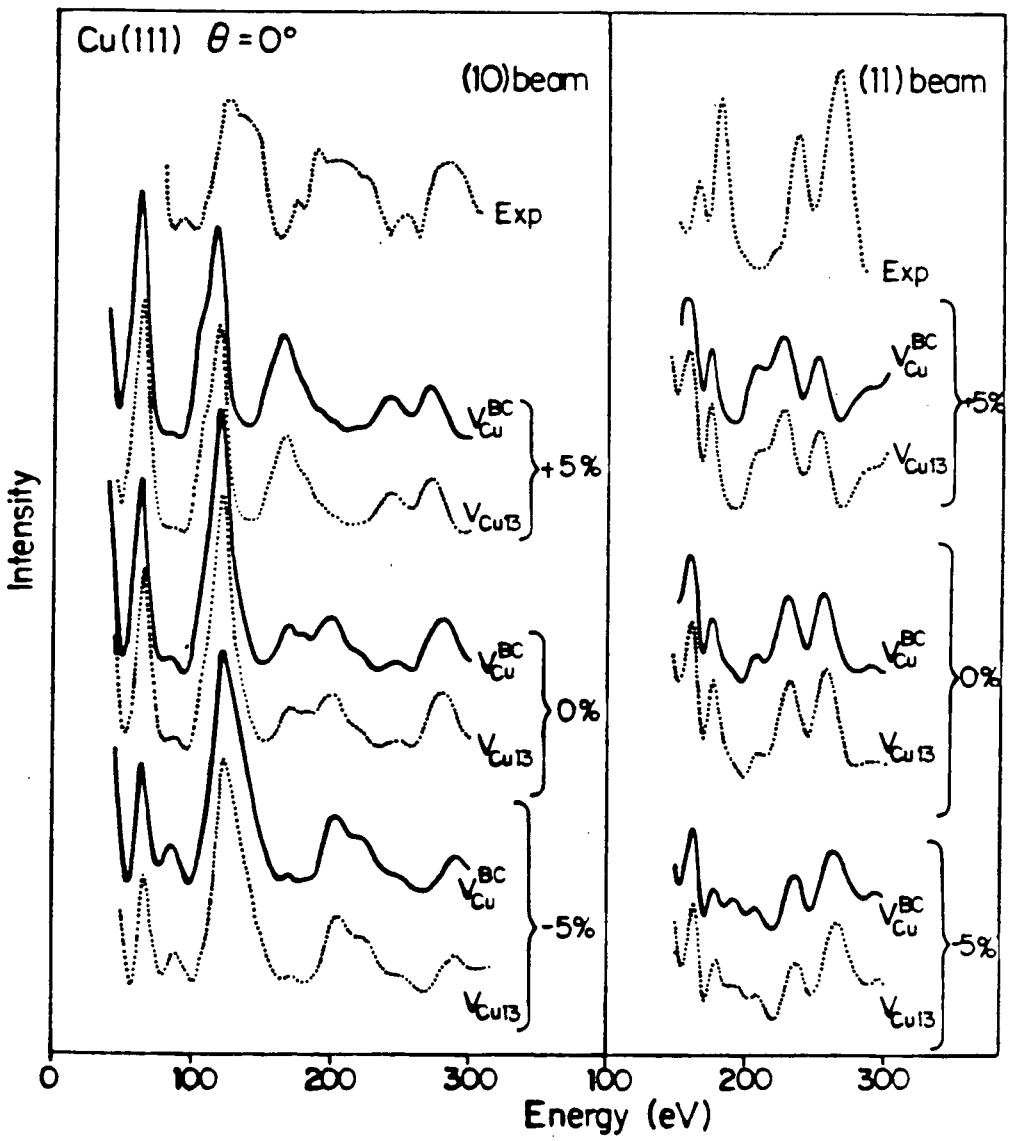

Figure 3.11 Comparison of experimental I(E) curves for Cu(111) at normal incidence with curves calculated for the V_{Cu13} and V_{Cu}^{BC} potentials for V_{or} = -9.5eV and three different values of $\Delta d\%$.

calculations are for the (10) and (11) beams for a range of values of the topmost interlayer spacing d expressed as a percentage change from the bulk value d_o, in steps of 5%,

$$\Delta d\% = [d-d_o/d_o] \times 100\% \qquad (3.22)$$

but assuming no other geometry changes. In this example, as the surface is contracted, relative intensities of peaks change significantly. New structure is introduced, e.g. a new peak grows at about 200eV for the (10) beam, and the relative intensities of the peaks at about 230 and 260eV in the (11) beam become reversed.

CHAPTER 4

EXPERIMENTAL ASPECTS

In order to deduce surface structures via a LEED analysis several experimental prerequisites must be fulfilled. The first problem is to prepare the surface of interest in as precise a fashion as possible. This involves accurately cutting a single crystal to expose the desired crystallographic plane and polishing the face obtained to a high degree of perfection. Having obtained a well-oriented surface we must be able to clean and maintain its state of cleanliness, at the level of small fractions of a monolayer of contamination. Diffraction of low energy electrons only occurs from well-ordered surfaces so the crystal must be treated in such a way as to possess a clean and well-ordered surface before the LEED experiment can begin. Finally, we are faced with the problem of performing the actual LEED experiment which, as we shall see, centres around problems of data collection and analysis.

4.1 Crystal Preparation

The samples used in this work were typically discs of about 1mm thickness and 6mm diameter. In some cases, precut slices on loan from other laboratories were used initially but the experiments were repeated on new discs cut here. Table 4.1 lists the sources of the crystals used.

The single crystal rods were carefully oriented using the Laué back-reflection technique [82] such that the desired crystallographic plane was perpendicular to the X-ray beam. Vertical cuts parallel to the plane were made on a spark erosion cutter ("Agietron", AGIE, Switzerland). The crystal rod was

Source	Treatment	Faces used
ROC-RIC	Cut and polished at UBC	(111), (100), (110)
Berkeley	As received	(111)
GE	Cut and polished at UBC	(100)

Table 4.1 Sources of rhodium crystals

1. ROC-RIC = Research Organic/Inorganic Chemicals Corp.
2. Berkeley = Courtesy of Prof. G.A.Somorjai, Lawrence Berkeley Laboratory, U. of California, Berkeley, Ca.
3. GE = Courtesy of Dr. C.W.Tucker, General Electric Research and Development Centre, Schenectady, N.Y.

left in place on the goniometer during this operation in order that the crystallographic orientation would not be compromised. The resulting disc was carefully mounted in acrylic resin ("Quickmount", Fulton Metallurgical Products Corp., USA) and polished by hand to a mirror-finish (0.05 micron alumina).

Whilst great care was taken during the polishing process to ensure that the orientation of the desired face was not lost, it is important to check afterwards that an error has not occurred. A simple technique was devised to check that the optical polished face was in fact parallel to the desired crystal plane. This involved re-orienting the crystal slice on the X-ray diffractometer such that the desired plane was once again perpendicular to the X-ray beam. The whole goniometer and crystal ensemble was then removed to an optical bench where the orientation of the optical face relative to the crystal plane could be checked, as shown in Fig. 4.1, by measurement of the angle of reflection of the beam from a small He-Ne laser.

This method can easily detect misorientations of $\pm 1/2^{o}$,

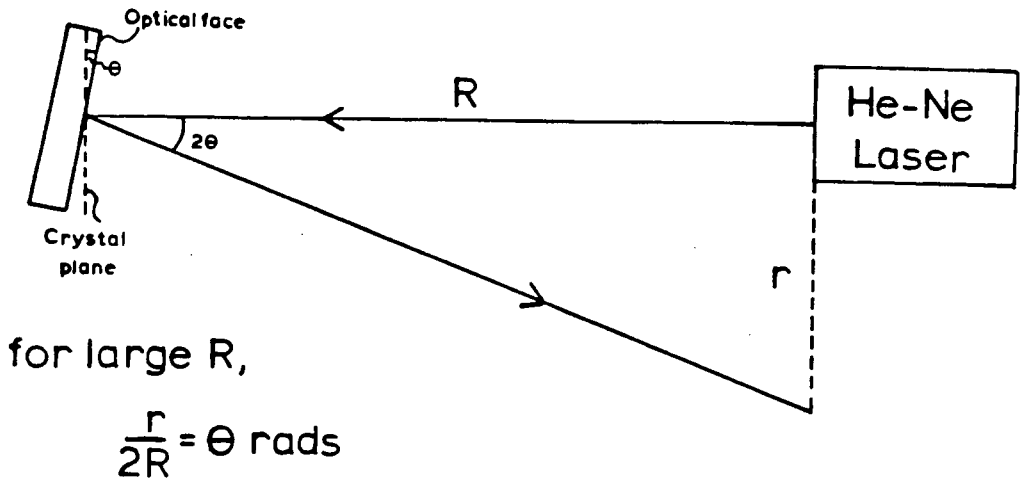

Figure 4.1 Laser alignment method to check the coincidence of the optical face and desired crystal plane.

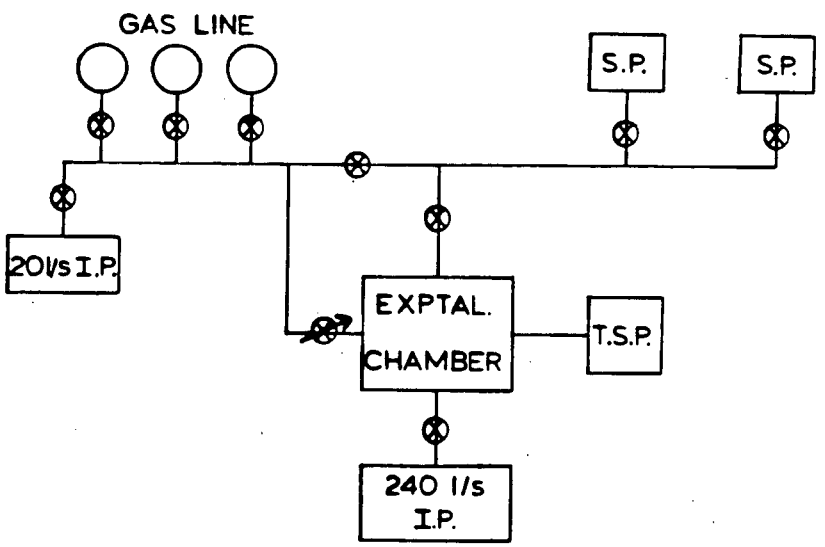

Figure 4.2 Diagrammatic representation of the pumping system: IP = Ion pump; TSP = titanium sublimation pump; SP = sorption pump.

although they can range up to ±2°, even with careful polishing. In the event of such a misorientation the crystal was repolished until it was within 1/2° of the desired crystal plane.

4.2 Ultra High Vacuum (UHV) Apparatus

Once having prepared a well-defined crystal surface it must be kept in an environment in which it will not become contaminated to any great extent before the experiments are completed. Simple consideration of the kinetic theory of gases shows that a contaminant with unit sticking probability will form a monolayer on the surface in about 1 second at 10^{-6} Torr. Therefore, it is necessary to work in the UHV pressure region i.e. in the 10^{-10} Torr pressure range, or better, in order to have sufficient time to perform an experiment without the crystal surface becoming seriously contaminated. The crystal slice is, therefore, mounted inside a UHV chamber. In this work two such systems were used, a Varian 240 and a Varian FC12 chamber. The former was only used for a short time in the early stages so further discussion will centre around the latter system. A schematic diagram of this apparatus is shown in Fig. 4.2.

The stainless steel chamber can be roughed out to a pressure of approximately 1 micron by two sorption pumps containing molecular sieve chilled by liquid nitrogen. The main 240 l/s ion pump can then be started and will attain a base-pressure of $<10^{-10}$ Torr following an overnight bake-out at 200°C to remove adsorbed gases from the chamber walls.

During crystal cleaning it is often necessary to admit gases into the chamber e.g. argon for ion-bombardment or oxygen for chemical cleaning. These gases are stored in glass bulbs on a gas line connected to the main chamber through a variable leak valve. The gas line can be baked separately from the chamber and is pumped by its own small ion-pump(20 l/s). Thus, the amount of extra background impurities from the gas line in the admitted gases can be kept to a few parts per million. When the chamber is flooded with argon for ion-bombardment, the main ion-pump can be throttled off by a gate valve and the titanium sublimation pump used to further lower the partial pressures of active gases in the chamber.

Fig. 4.3 shows a schematic representation of the FC12 chamber. On the various ports are fitted:

i) a manipulator on which is mounted the sample. The external controls of the manipulator allow the sample to be translated in all three perpendicular directions, together with variation of the polar angle of incidence, θ, and the "flip angle" in the vertical plane, as indicated in Fig. 4.3. Electrical feedthroughs to permit heating of the sample and a thermocouple monitor are also provided;

ii) a "nude" ion gauge to monitor the system pressure;

iii) a hypodermic gas doser, after Joyner and Somorjai [83], connected to the variable leak valve. This permits relatively high pressures of e.g. a chemical cleaning agent, at the crystal surface

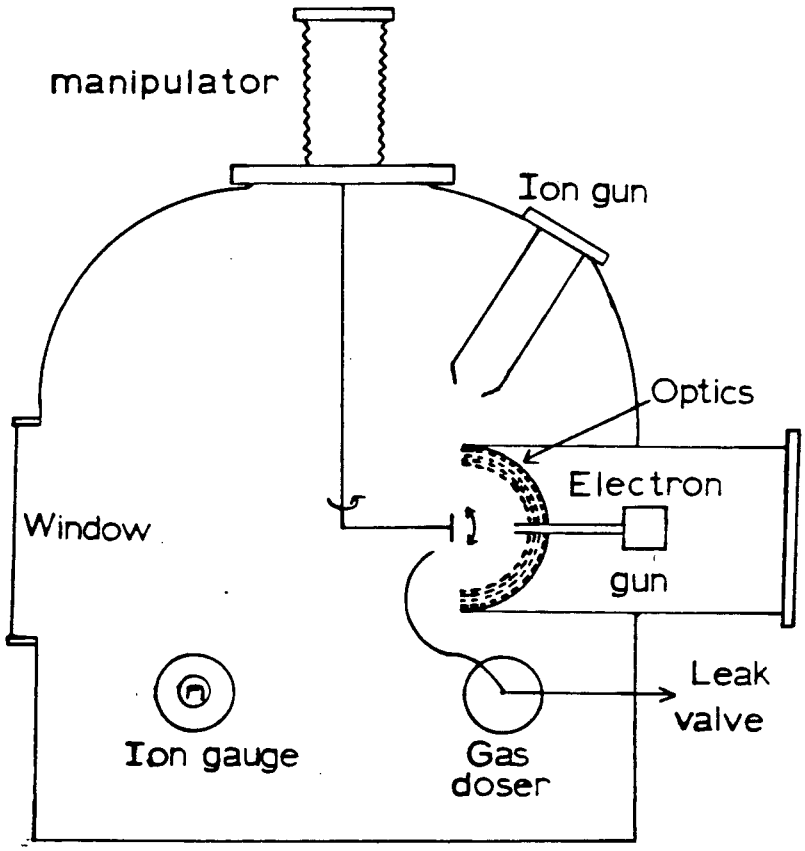

Figure 4.3 Schematic of the Varian FC12 UHV chamber.

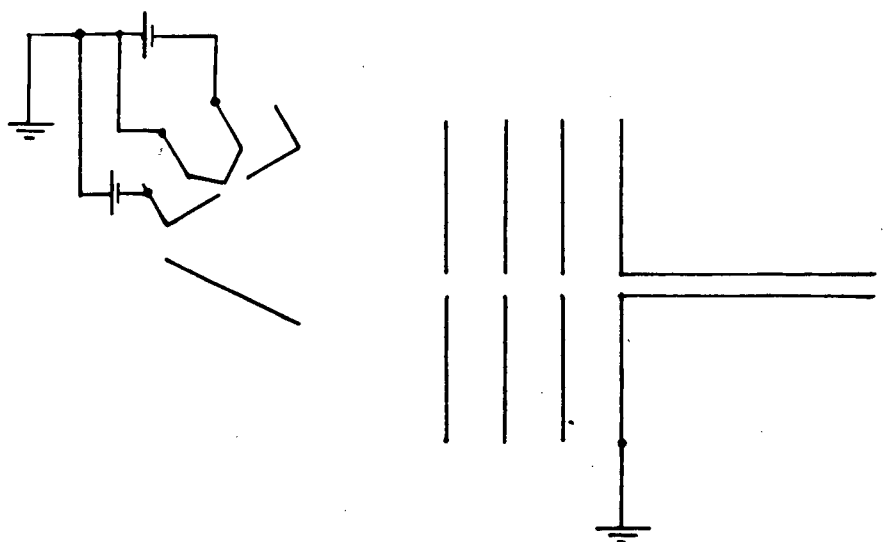

Figure 4.4 Simplified diagram of an off-axis electron gun with deflection electrode and drift tube.

while keeping the total system pressure relatively low;

iv) an ion-bombardment gun for crystal cleaning;

v) the LEED/Auger electron optics and electron gun. The principle of the construction of the gun is shown in Fig. 4.4. The off-axis tungsten filament emits electrons that are deflected into a collimating lens system and drift tube. The off-axis geometry prevents contamination of the surface by evaporation of cathode material. The electrons leave the drift tube, which is maintained at the same potential as the sample, and traverse field-free space as long as no stray magnetic fields are present. The beam diameter is about 1mm and has typically an energy spread of about 0.75eV. Secondary and Auger electrons are filtered by the system of grids, and the elastically scattered electrons are displayed on a fluorescent screen;

vi) a window to observe the sample and diffraction pattern on the fluorescent screen.

The chamber is surrounded by three orthogonal sets of square Helmholtz coils to reduce the residual magnetic field of the earth, ion-pumps, etc. to a level which will not interfere with the motion of slow electrons (about 20 mGauss for 50eV electrons [84]). Although this geometry does not satisfy the optimum Helmholtz condition the cubic arrangement is adequate

and experimentally more convenient. Satisfactory neutralisation was achieved using the criterion that the specular beam in the LEED pattern should remain stationary for all incident energies. The effectiveness of this cancellation was also checked by examining I(E) curves for symmetrically equivalent beams; for example, the (00) beam at equivalent angles of incidence on either side of the surface normal or non-specular beams of the same order at normal incidence.

4.3 Crystal Cleaning

4.3(a) Procedures

When the sample is first mounted in the UHV chamber its surface, in which we are interested, will be contaminated not only by adsorption of atmospheric gases but also by bulk impurities present in the original single crystal rod and by impurities introduced onto the surface by the polishing process. The surface must also be annealed in order to smooth the irregularities remaining in the surface and thereby produce a well-ordered surface that exhibits a sharp LEED pattern.

In this work a combination of two treatments was used to clean the crystal surfaces:

(a) cycles of argon ion-bombardment and vacuum anneals;

(b) heat treatments in oxidising or reducing

atmospheres.

Ion-bombardment was achieved by flooding the chamber to between 10^{-5} and 10^{-6} Torr of argon and operating the ion-bombardment gun, a device in which a heated filament generates argon ions which are accelerated on to the surface of interest. The impact of these ions sputters material from the surface thereby removing impurities. However, the host atoms are also removed and the surface may become too rough to produce a good LEED pattern; it must then be annealed by heating.

Several methods of heating the sample were employed. Fig. 4.5 displays these methods:

(a) the crystal was spot-welded to Rh or Pt foil and resistively heated. Typically a 50A current would produce a surface temperature of about 1200K. The main disadvantage of this method is that the supporting foil and manipulator legs heat up and can cause severe outgassing problems;

(b) the crystal was physically clamped to a commercial Varian conductive heater. This heater is limited in the temperature it can produce mainly due to the difficulty of achieving good thermal contact between the crystal and the main heater block;

(c) the crystal was spot-welded to thin Rh or Pt strips attached to a support ring and heated by electron bombardment from a filament behind the crystal which is floated to typically +1.5kV. This method leads

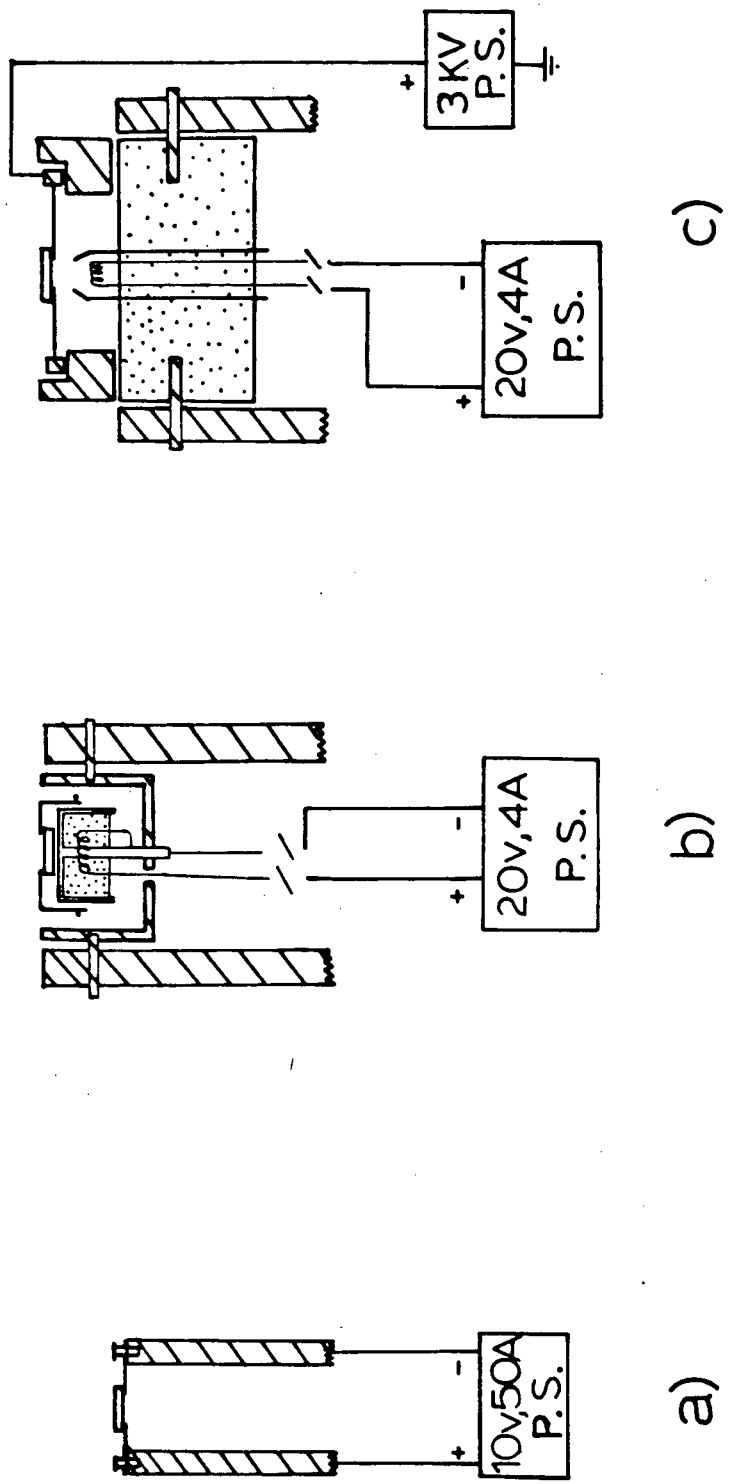

Figure 4.5 Three methods of heating a crystal sample: (a) direct resistive heating, (b) using a Varian conductive heater, (c) by electron bombardment. Hatched lines represent stainless steel and stipple ceramic insulators. Other materials generally Rh, Pt, W or Ta.

to very rapid heating of just the sample to high temperatures. However, a corollary of this is that the crystal cools down very slowly due to the poor thermal conduction that allows the selective heating.

Temperatures were measured by alumel-chromel or Pt/13%Rh-Pt thermocouples attached to the crystal or by an optical pyrometer (Hartmann and Braun, Frankfurt).

Chemical cleaning most often consisted of heating the sample in about 10^{-5} Torr of oxygen, a particularly useful procedure for removing surface carbon, which is only poorly sputtered by argon ions. The oxygen remaining on the surface could then usually be removed by ion bombardment and/or heating in hydrogen.

Details of the actual heating procedures used for the individual crystal faces of rhodium studied are given in the chapters dealing with each surface.

4.3(b) Monitoring surface composition

The discussion so far has assumed that we have some method of knowing when the surface is, in fact, clean and when it is contaminated. Fortunately, such a surface composition monitor exists in the form of Auger electron spectroscopy(AES), the elements of which were presented in Chapter 2.

The electron optics were used as a retarding-field analyser for AES , as shown in Fig. 4.6. The Varian electron gun

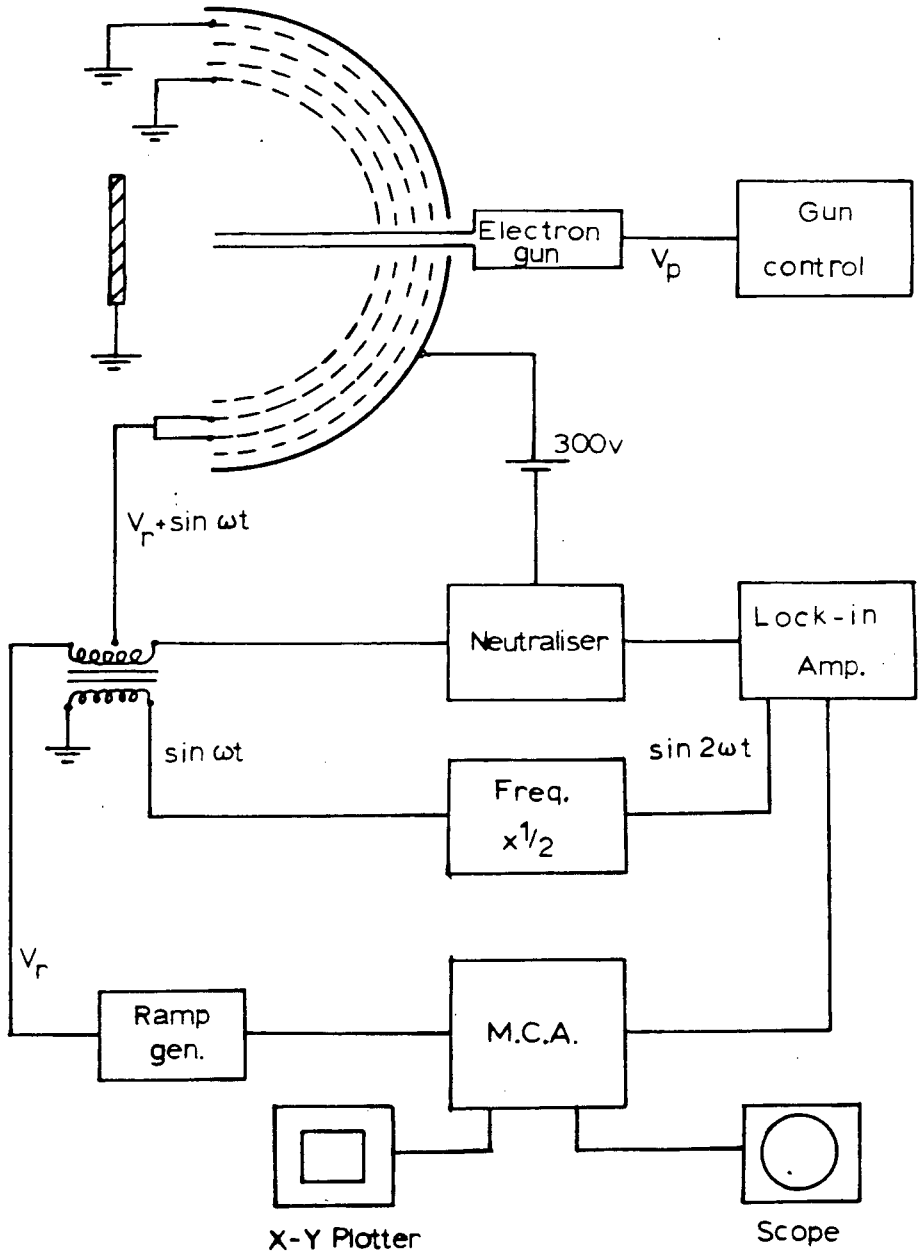

Figure 4.6 Schematic diagram of LEED optics used as a retarding field analyser for Auger electron spectroscopy: MCA = multichannel analyser.

operating in the Auger mode typically produces a beam of 10-15 microamps for a 1.5-2.5 kV primary beam voltage(V_p). The first grid of the optics is grounded to allow the electrons to move in field-free space, as is the fourth grid to prevent field penetration from the positively biased fluorescent screen behind it, here simply used as a collector. In order to extract the Auger electrons, the 2nd and 3rd grids are modulated by sinωt about the retard voltage V_r ($V_r \leq V_p$), which is ramped typically from about 30 to 400eV. The ramp is controlled by a multichannel analyser (Fabritek 1062) linked to a programmable power supply (Kepco OPS2000).

The frequency doubled modulation sin2ωt was used as a reference for a PAR HR-8 lock-in amplifier tuned to detect the second derivative of the signal collected by the screen. A simple circuit based on that of Nathan and Hopkins [85] was used to neutralise the capacitive coupling between the retard grids and the collector. The output of the lock-in amplifier was stored in the multichannel analyser and the spectrum swept until the signal-to-noise ratio was acceptable, at which point it could be plotted on an X-Y plotter (Hewlett-Packard 7004B).

4.4 LEED Intensity Measurements

The arrangement of the electron optics for operation in the LEED mode is sketched in Fig. 4.7. The inner grids are now set to be at the primary beam voltage V_p minus (usually) a small offset voltage V_s (typically about 5eV). This arrangement allows the whole of the "pseudo-elastic" peak (Section 2.1) to be displayed on the fluorescent screen, now biased at +5keV, with the optimum contrast between the diffracted beams and the background. The first and fourth grids are grounded, as before for the measurement of Auger spectra, to provide field-free drift space and to prevent field penetration of the screen voltage respectively. In this mode the electron gun is usually run in the range 20 to 300eV and supplies a maximum current of about 5 microamps. Unfortunately the beam current output is a function of the beam energy as depicted in Fig. 4.8. The curve shows a steady rise from very low current at low beam energies until a plateau is reached at about 100eV where the beam current stays constant to within 0.01 microamps. This variation is important for the measurement of I(E) curves since unless measured intensities are normalised to unit beam current, the beam intensities will appear artificially reduced at low energies because of the low beam currents.

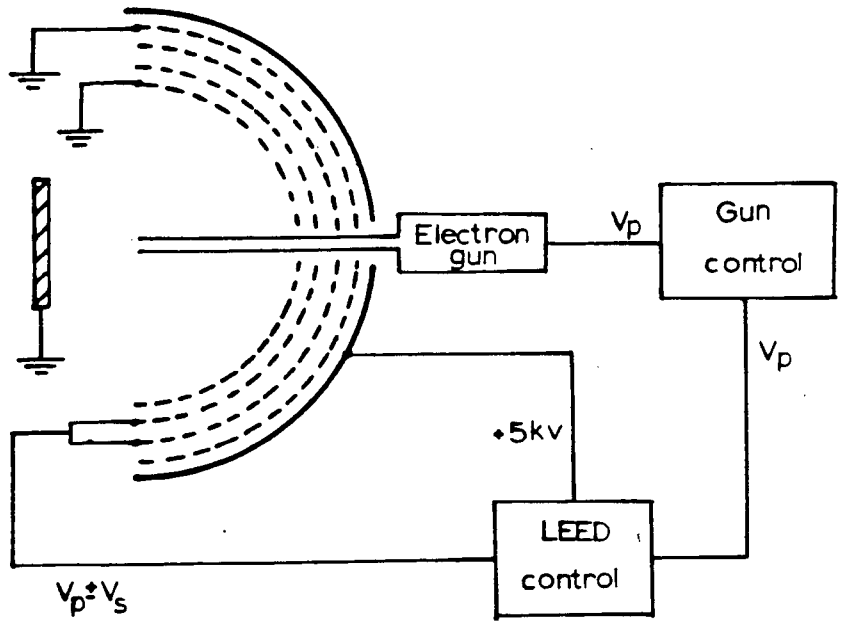

Figure 4.7 Schematic diagram of the electron optics used for LEED experiments.

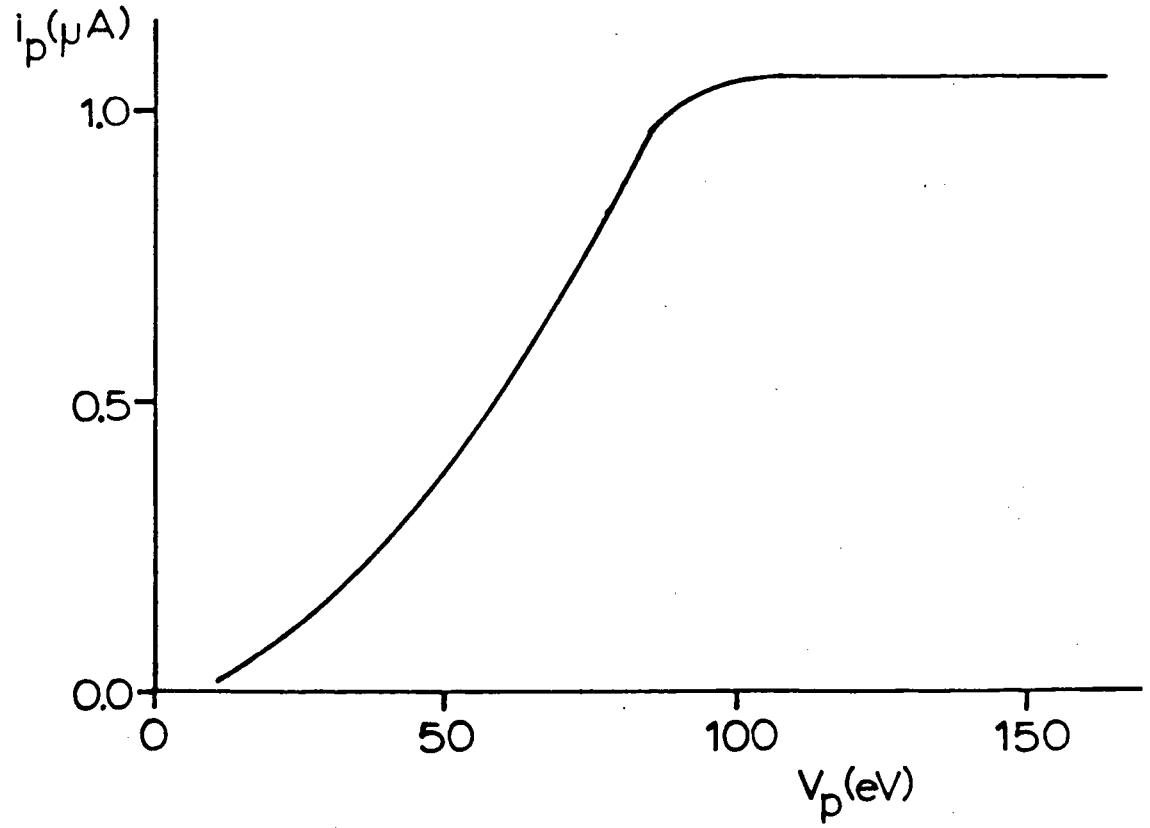

Figure 4.8 Typical variation of electron gun beam current Ip against beam voltage Vp in the LEED mode.

4.4(a) previous methods

LEED intensity measurements in the past have usually been made by measuring the diffracted beam current either directly with a Faraday cup collector inside the chamber, or indirectly by external measurement, with a calibrated spot-photometer, of the brightness of the spots on the fluorescent-display screen. A number of comparisons have indicated that both methods can provide reliable intensity data [86,19]. However, both methods possess some distinct disadvantages:

(i) in either method it is difficult to ensure that the detector is measuring the whole of the diffraction spot (in the angular sense) due to the finite aperture size of the detector. This is especially a problem when beams appear to shrink and grow as they vary in intensity;

(ii) allied to (i) is the problem of performing adequate background subtraction; usually particular values are taken which may, or may not, be representative of the true average background around a diffraction spot;

(iii) both methods are time-consuming and become awkward to use for complex LEED patterns. Non-specular beams move with incident energy and therefore the detector must be moved to track the beams. Hence collecting a large amount of data for a lot of beams becomes a very clumsy process, requiring frequent

re-calibration and re-cleaning of the surface to overcome problems from contamination or beam-surface interactions [87].

Recently Stair et al [88] investigated the procedure of photographing the diffraction spots and determining the relative intensities by scanning the negatives with a mechanically-driven microdensitometer. This method has the advantage of speed of data collection, thus helping to preserve the integrity of the surface. The large amount of experimental data present on the photographs can be subsequently analysed at leisure. The main disadvantage of this approach however, is in the analysis. The whole of each frame is scanned and the intensity of each point on the film, defined by the aperture of the microdensitometer is recorded on computer magnetic tape. The output of each frame is then examined by a large computer to deduce the location of diffraction spots and their integrated intensities. Possible problems associated with losing spots in the background, false identification of, for example, dust particles as diffraction features means that the output from each frame has to be checked visually. The analysis procedure is thus rather slow and it makes large demands on computer storage and time.

The next stage of development is to combine the attractive features of the photographic procedure with a more efficient and flexible method of analysis, thereby speeding up the process, cutting down on sources of error, and reducing the computer requirements to the point where the analysis could be done on-

line on a mini-computer in the laboratory. With the advent of computer-controllable Vidicon T.V. cameras, such an analysis of photographs of LEED patterns became feasible and was developed in this laboratory in collaboration with Dr.F.R.Shepherd.

4.4(b) Vidicon measurement of I(E) curves

The LEED patterns displayed on the fluorescent screen were photographed through the window of the vacuum chamber using a Nikon F2 35mm camera with an 85mm f1.8 lens and a K2 extension ring. Photographs were taken generally in the 20 to 250eV range at 2eV intervals in the incident beam energy using a fixed exposure of 1 sec at f4, the incident beam current (typically 0.75 microamp) and energy being recorded for each photograph. Using a motor drive unit and a 250 exposure film back, LEED patterns for this type of energy range could be recorded easily within five minutes. The surface condition was routinely checked with Auger electron spectroscopy after measurements to ensure that no detectable contamination had occurred during data collection.

A Kodak No. 2 calibrated step density wedge was also photographed on the same length of film. Standard Kodak Tri-X emulsion was used and the film processed in a continuous length in Acufine developer at 73°F for 7 minutes.

The photographic method depends on a knowledge of the detailed response curve of the emulsion (optical film density versus log exposure) so that measurement of the integrated optical density (D) of a diffraction spot on the film provides a

direct measure of the amount of light which caused the darkening of the film in that region of the negative [89]. In turn, it is assumed, as in the spot-photometric method, that the luminance [89] of the screen is directly proportional to the impinging electron flux so that D is related to the corresponding diffracted beam current (i) by

$$D = Ki \qquad (4.1)$$

where K is a proportionality constant. Dividing equation (4.1) throughout by the incident electron beam current (i_o) gives

$$(D/i_o) = K(i/i_o) = kI_{abs} = I_{rel} \qquad (4.2)$$

where the distinction is made between the absolute diffracted beam intensity I_{abs} and the relative diffracted beam intensity I_{rel}. The latter quantity is measured in the present work.

Fig. 4.9 shows a schematic diagram of the apparatus used to analyse the photographic negatives of LEED patterns. The Vidicon camera and associated electronics comprise part of the Computer Eye System (Spatial Data Systems Inc., Galeta, California) which was interfaced to a mini-computer (Data General Nova 2). The film held on the light table is scanned continuously by the camera, and the image displayed on the T.V. monitor in a 512x480 (xy) array. The intensity (z-value) of any element of the image may be sampled by triggering the digitiser with appropriate instructions from the computer. A profiler shows directly on the monitor the variation of intensity along

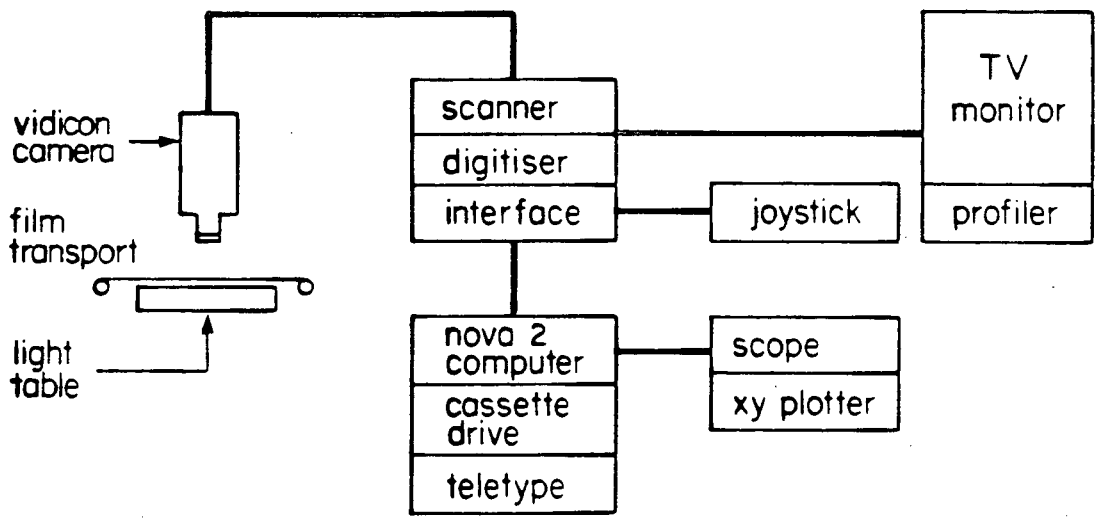

Figure 4.9 Schematic diagram of the apparatus used to analyse the photographic negatives of LEED patterns.

any selected vertical line of the image; this may correspond, for example, to a line through a diffraction spot on the film. The profiler also assists in setting the range of optical density covered by the digitiser; the latter can resolve 256 z-values over a maximum span of about 2.5 density units (corresponding to a change in absolute intensity by a factor of about 300). Another useful feature of this system is the "joystick". This controls the position of a flashing spot on the T.V. monitor, and may be used to "point" to any element of the image whose coordinates within the array are then available to the computer.

In order to check the performance of the Vidicon camera, a number of tests were made. The Kodak step density wedge was placed on the light table and scanned. Fig. 4.10 shows the digitiser output plotted against the calibrated values on the density wedge, and it seems that the camera response is linear to a good approximation over a range of at least 1.6 density units. After a preliminary warm-up, a number of scans of the density wedge demonstrated that the readings from the digitiser show good stability over periods of several hours. The presence of flare [89] in the camera optics could be observed visually on the monitor when very intense light levels were focussed on the Vidicon detector (e.g. with the aperture of the lens fully open). Under normal operating conditions a series of direct comparisons of readings from the Vidicon camera and a conventional fine-spot microdensitometer were made from scans of the density wedge and some typical LEED patterns; excellent agreement was found within the linear portion of Fig. 4.10, indicating that flare is not a

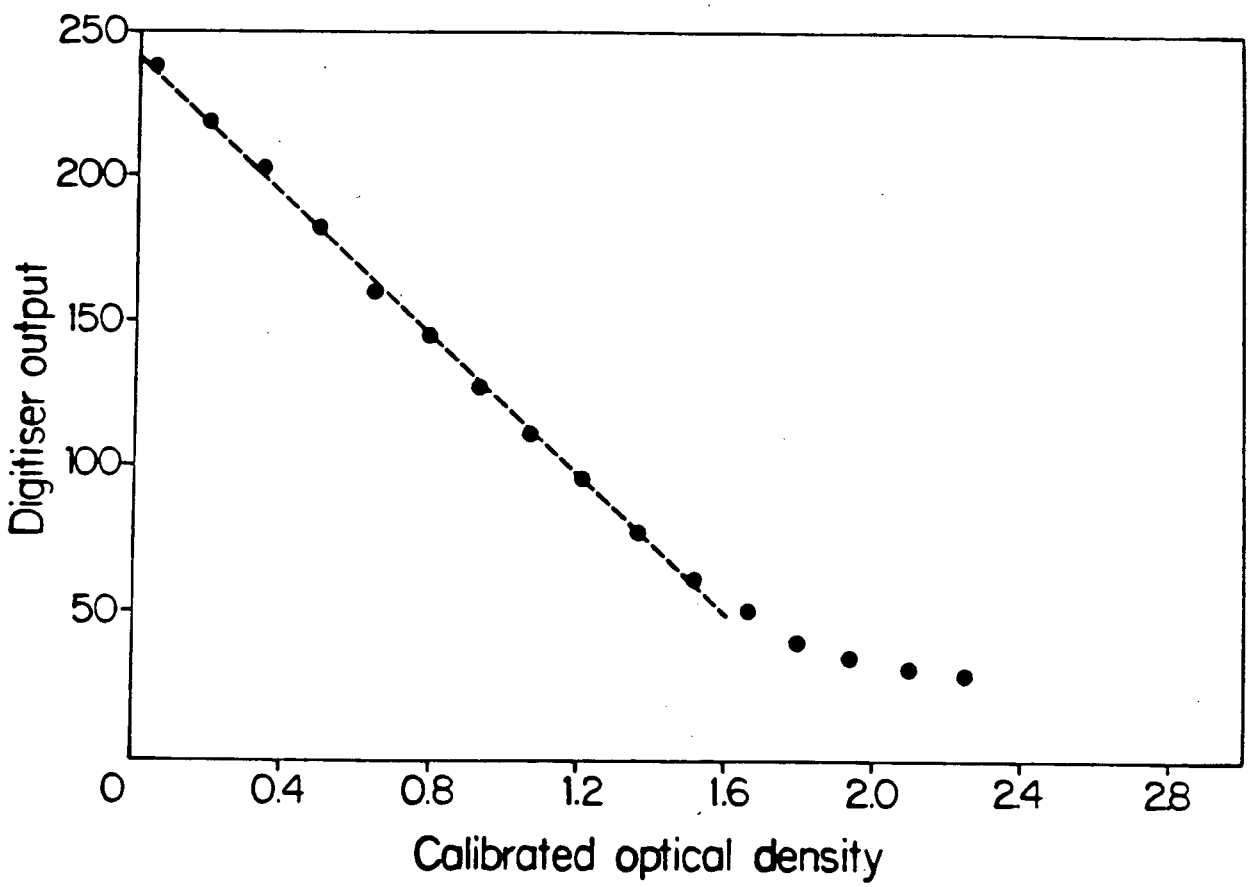

Figure 4.10 Digitiser output measured for different regions of a Kodak No. 2 step density wedge and plotted against the corresponding calibrated optical densities.

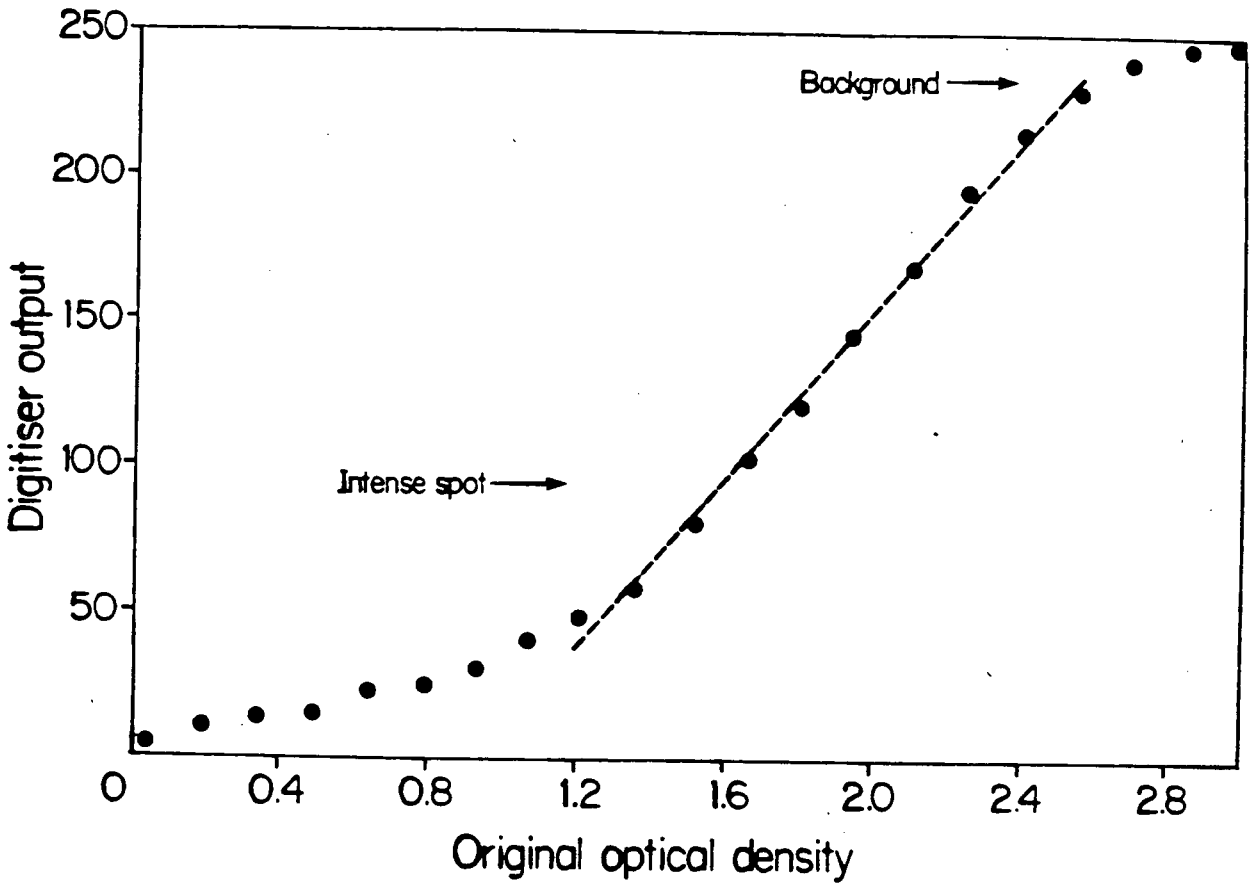

Figure 4.11 Digitiser output measured for different regions of a photographic negative of the step density wedge in Figure 4.10, plotted against the original calibrated optical density of the wedge. The arrows note the points on the plot which correspond to the minimum background and the maximum density observed on photographs of the LEED patterns from Cu(111).

significant problem in these measurements.

Fig. 4.11 shows the results of scanning the negative image of the density wedge which was photographed along with the diffraction patterns; this indicates the response of the 35mm film emulsion to a series of stepped exposures controlled by the density wedge. In the intermediate region of the plot the response of the film is a linear function of the original optical density, but in the extremes of high and low densities the linear relation is lost owing to reciprocity failure [89]. It is also noted on Fig. 4.11 that the maximum range of density of diffraction spots observed on the photographs lies well within the linear part of the response curve, thereby simplifying the conversion of digitiser output to optical density.

A simplified flow chart of the computer program, written by Dr. F. R. Shepherd, controlling the scanning process is given in Fig. 4.12. Under 'program interrupt', control characters issued from the teletype can direct the program to perform the various operations as required. For a given frame, the analysis of a particular diffracted beam proceeds by entering the energy and current of the incident electron beam through the teletype, and the joystick is used to point to the spot viewed on the T.V. monitor. A signal from the teletype initiates a routine which scans and digitises an area which is centred on the joystick coordinates and is somewhat larger than the spot. This is repeated and the array of averaged z-values is stored in the computer memory; after a two-dimensional smoothing operation, the coordinates of the maximum are determined and a new array

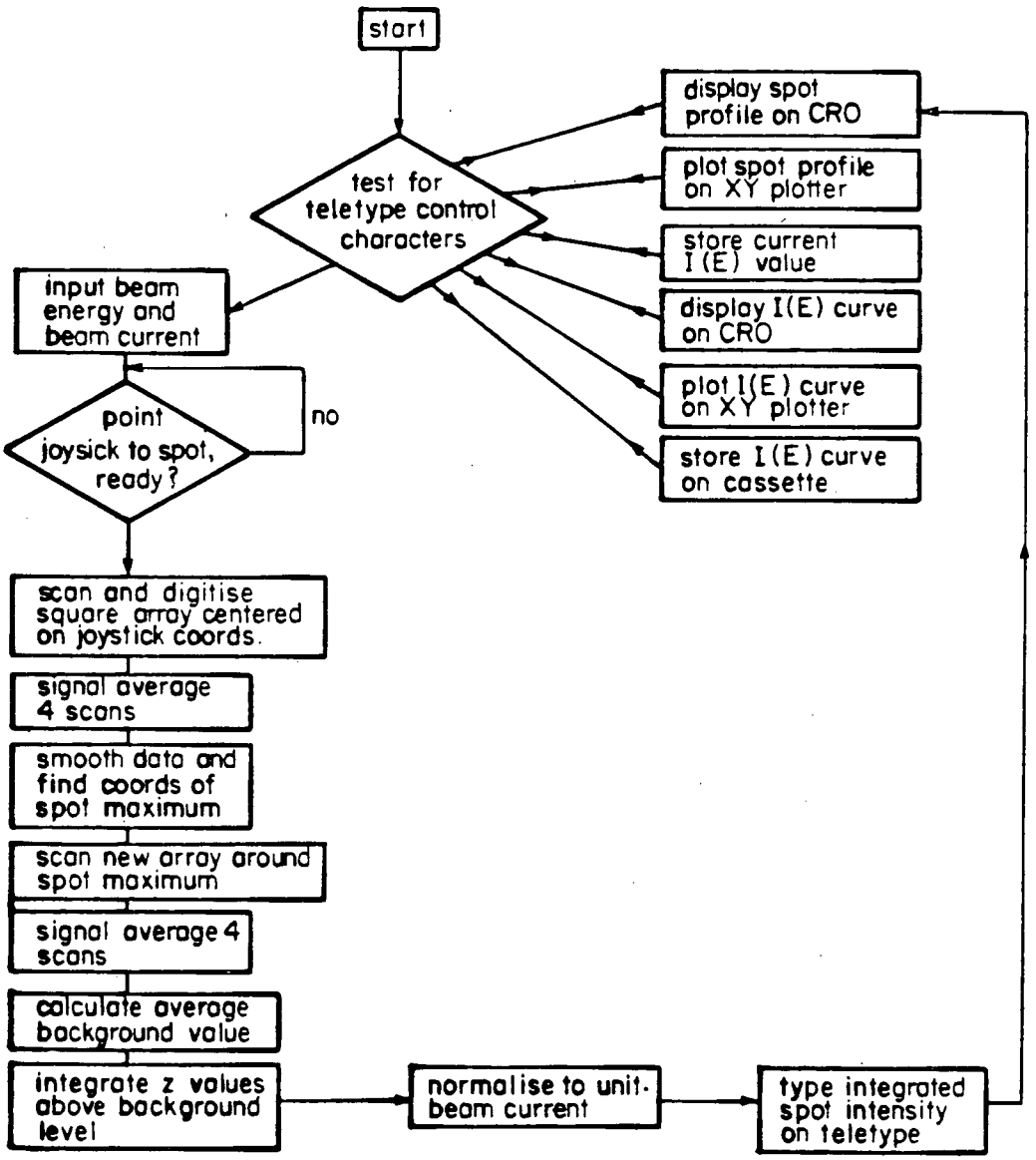

Figure 4.12 Flow chart of the computer program which controls the scanning of the photographs.

centred on these coordinates is scanned and digitised. In order to measure the background level, this distribution is displayed on the T.V. monitor using the profiler, and the extremities of the diffraction spot are fixed visually and marked using the joystick. Assuming a Gaussian profile, the standard deviation is found by determining the full width of the distribution at half its maximum value above the line joining the marked extremities. The average of the z-values of all elements lying on a thin annulus of mean radius 2σ is taken as the background level z_{back}. Experience has shown that a preprogrammed value of σ can be inserted into the program in order to automate the background determination without degrading the quality of the analysis.

The integration procedure involves summing all the values of $(z-z_{back})$ within the circle of radius 2σ, and dividing by the incident beam current to give a measure of the diffracted beam intensity (I_{rel}). This normalisation is important to avoid distortion of intensity values at low energies where the variation of incident beam current with beam energy is substantial, as was seen in Fig. 4.8.

The analysis of one spot takes only a few seconds. By studying successive frames for one diffracted beam, a complete I(E) curve is generated and stored on digital cassette and may be displayed on the oscilloscope and plotted on the XY recorder. After the initial frame, the coordinates of the diffraction spots are stored in the computer so that when the next frame is positioned in approximately the same place under the camera using a marker, the analysis of this next frame can start

without respecifying the positions of the spots via the joystick. The movement of the beams for a 2eV energy increment is sufficiently small that the initial search for the new diffraction spot using the coordinates of the spot on the previous frame is always successful. This results in substantial savings in analysis time so that a complete set of I(E) curves for perhaps 10 beams can be produced in a few hours.

4.4(c) Measurements of I(E) curves for Cu(111)

The Cu(111) surface was used as a test of the reliability of the Vidicon version of the photographic method for measuring experimental I(E) curves. This surface was convenient as some previous experimental [19] and theoretical studies [20] were available.

Figure 4.13 shows I(E) curves measured for two non-specular beams at normal incidence where the beam energy is expressed relative to the vacuum level. All the features in the figure are reproducible from one set of measurements to the next and reanalysing a particular strip of film suggests that uncertainties in measuring optical densities (and hence diffracted beam intensities) are typically less than 5%. This slight variation must be ascribed to a degree of uncertainty in applying the background correction. Nevertheless the associated errors are probably less than those involved, for example, with some inevitable variability in surface conditions.

At normal incidence the LEED pattern from Cu(111) shows three-fold symmetry, see Fig. 2.7, and so the same intensity

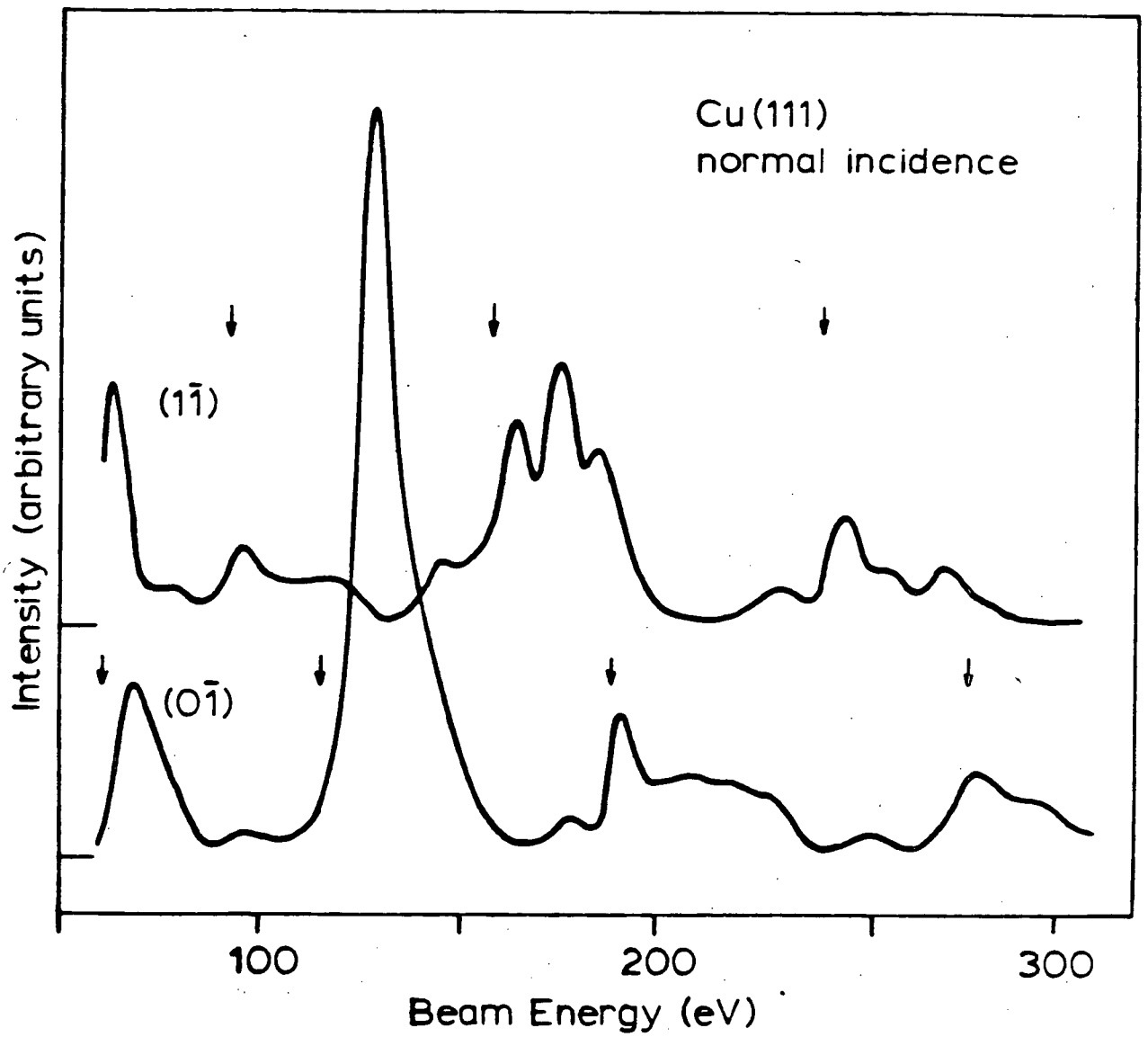

Figure 4.13 I(E) curves for the (1$\bar{1}$) and (0$\bar{1}$) beams from Cu(111) at normal incidence.

variation is expected within each group of symmetrically-related beams, such as the $(10, 0\bar{1}, \bar{1}1)$ and $(1\bar{1}, \bar{1}0, 01)$ groups. This is illustrated in Fig. 4.14 where the measured intensities of the $(1\bar{1})$ and $(0\bar{1})$ beams are closely similar to the $(\bar{1}0)$ and (10) beams respectively. Such behaviour is consistent with the screen phosphor responding in a uniform way to these different, but equivalent, beams and this represents an essential requirement for both the photographic and spot photometric methods. Off normal incidence, the three-fold symmetry in the non-specular beams is lost and beam intensities depend on both the polar and azimuthal angles of incidence.

In Fig. 4.15 are shown two I(E) curves measured from photographs with the Vidicon camera for the specular beam with (a) $\theta = 12^{\circ}, \phi = 186^{\circ}$ and (b) $\theta = 12^{\circ}, \phi = 6^{\circ}$; (c) reproduces the experimental intensity data reported by Woodruff and McDonnell [19] with a Faraday cup collector for $\theta = 12^{\circ}, \phi = 7^{\circ}$. Although the azimuthal angle does differ by one degree in this comparison the data reported in reference 19 showed that the I(E) curves for the specular beam vary slowly with ϕ around these values.

Some differences in peak shapes between the two angles in (a) and (b) are apparent although peak energies are reproduced very well. However, the curves (a) and (b) in Fig. 4.15 should be exactly equivalent because of time reversal symmetry [90]. The slight differences in shape observed must therefore be attributed to a degree of experimental uncertainty. To some extent this could be due to the beam energy being increased in fixed increments of 2eV, even where the intensity is changing

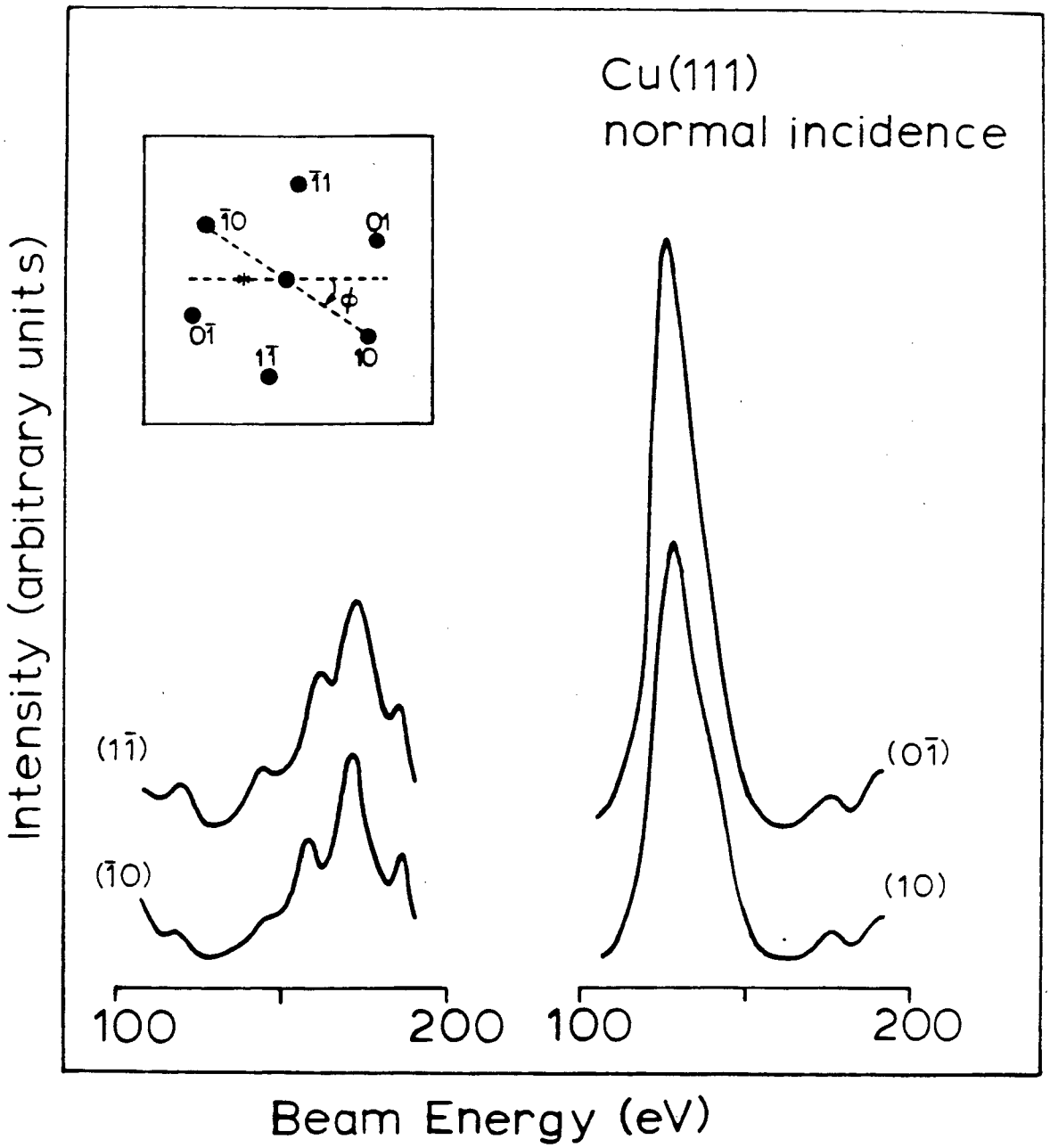

Figure 4.14 I(E) curves of symmetrically equivalent beams for normal incidence on Cu(111). The inset indicates the beam notation and a specification of the azimuthal angle ϕ; the asterisk illustrates the position of the electron gun for the non-normal incidence case.

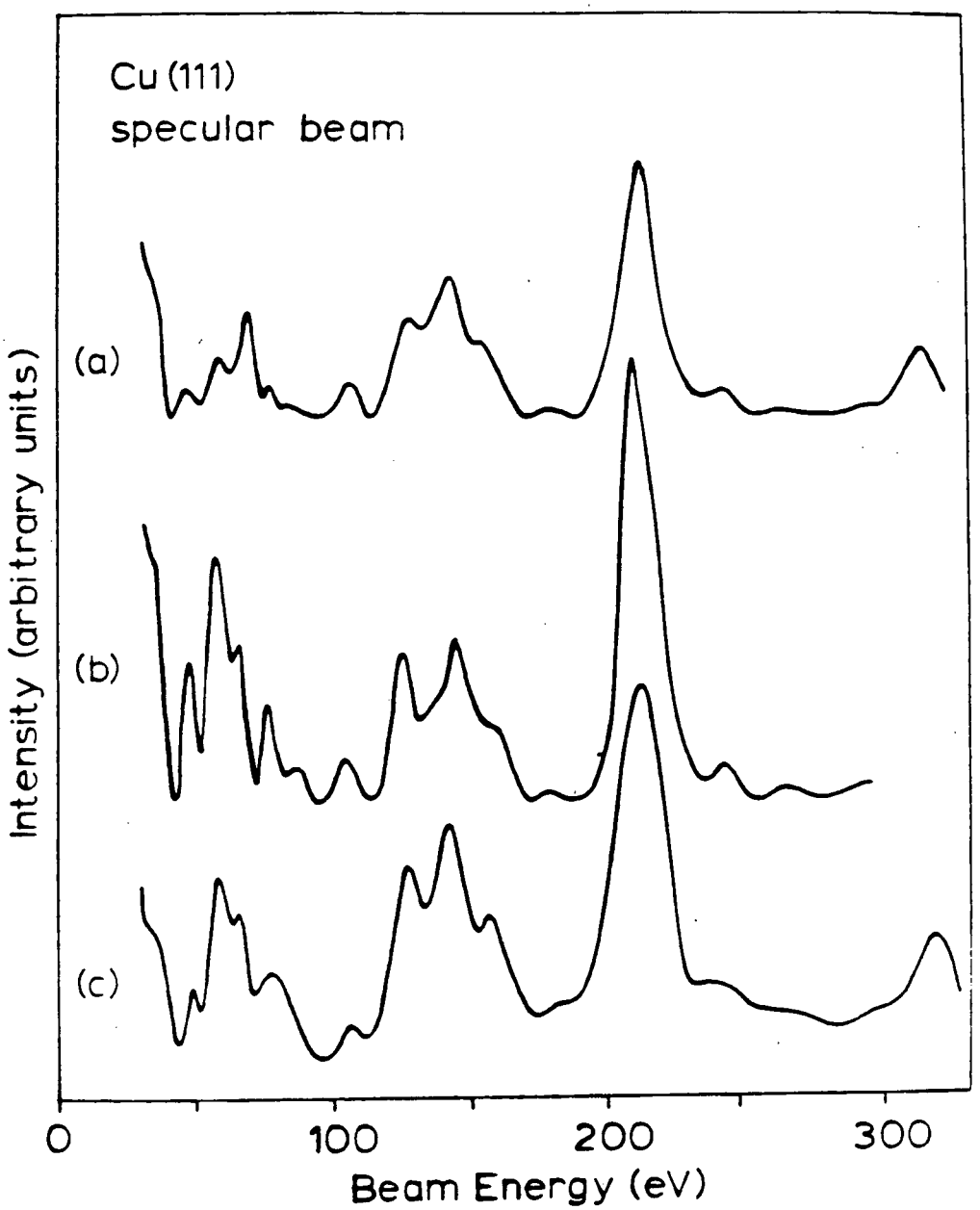

Figure 4.15 I(E) curves for the specular beam for Cu(111): (a) $\theta = 12^{\circ}$, $\phi = 186^{\circ}$; (b) $\theta = 12^{\circ}$, $\phi = 7^{\circ}$. The first two were measured by the method described in this paper, and (c) represents measurements made by Woodruff and McDonnell [19] with a Faraday cup collector.

relatively rapidly with energy, but other possible factors include uncertainties in the angles of incidence (to the order of one degree in each set of measurements) and in surface conditions.

The point of special significance is that all three curves exhibit the same features at the same beam energies to within our 2eV uncertainty. This encourages us to believe that the method described here is able to approach the reliability of the Faraday cup method for measuring relative beam intensities. In contrast, Stair et al compared intensity data from the photographic and spot photometric methods on the same surface, but since these methods have a number of assumptions in common, the comparison made here, although it is of limited extent, may perhaps be seen as being the more stringent.

In this method of measurement there is no physical aperture to define the angular size of a spot; the size is fixed by the background subtraction procedure which is sufficiently flexible that the effective aperture can be made large enough to include the whole of the spot above background to a good approximation and, if neccessary, can be redefined during the analysis. Background subtraction is handled in an accurate manner using an averaged value of many elements in an annulus surrounding the spot. This seems a preferable procedure to the more common practice of averaging only a restricted number of arbitrary background values. The short data collection times limits complications due to contamination or beam-surface interactions. The convenience of a "hard-copy" record, which may be subsequently reanalysed at leisure, represents another

attractive feature of the photographic method.

4.4(d) Future developments

Further improvements in the collection of intensity data are needed. As Jona [138] has emphasised, the ideal solution will not only be fast, but be on-line i.e. intensity data will be available while the experiment is in progress. The present Vidicon system in use here has shown under test that it is not sensitive enough to record beam intensities direct from the fluorescent screen. However, it is certain that the next generation of such cameras will have increased sensitivity. Indeed, shortly after the first set of measurements, Heilmann et al [91] reported the successful use of a different make of Vidicon camera to make such direct measurements; these authors required about 5 minutes to collect intensity data for 10 beams to 200eV.

Many present Vidicon cameras would be adequate for direct measurements if the brightness of the diffraction spots seen by the camera could be increased. In principle this can be achieved either externally with the use of an image-intensifier, or internally with a channel plate electron multiplier. The latter method has been used to measure photoemission angular distributions [92], and for the production of visible LEED patterns with very weak (nanoamp) beam currents [137]. An attractive aspect of possible future reductions in incident beam currents is the associated possibility of reduced beam-surface interactions.

One of the problems of any image analysing device is the amount of time spent in digitising unwanted background portions of the LEED pattern. At normal incident energies the area of the screen occupied by the diffracted beams is only a small fraction of the total. We have avoided this problem by recording the data in a hard-copy form and then only analysing the features of interest in a semi-interactive manner. The provision of a fast on-line recording system, at a reasonable cost, that automatically records only significant features, and yet can differentiate true diffraction spots from spurious events, is still a major task.

CHAPTER 5

LEED CRYSTALLOGRAPHY

5.1 General Considerations

We have seen that the intensities of experimental LEED beams contain information on the structure of the surface in both the parallel and perpendicular directions. Fortunately, I(E) curves calculated for trial structures are quite sensitive to changes in the surface geometry as we saw in Section 3.2(c). Changes in non-structural parameters such as the inelastic damping, vibrational properties etc. produce uniform small changes in intensity or position for all the peaks in an I(E) curve [12].

The usual procedure followed to obtain structural information with LEED has been a trial and error process consisting of three steps:

(i) experimental data is collected for a number of diffracted beams at several angles of incidence;

(ii) a theoretical set of data is produced for the same beams by postulating a structural model and choosing a number of non-structural parameters;

(iii) structural (and preferably, but by no means often, non-structural parameters) are varied in the calculations until an agreement is found between the experimental and theoretical data.

Agreement between the experimental data and the calculations for a particular structural model is usually accepted as the proof for the correctness of the postulated

model. Underlying this is the assumption that such agreement, especially if it involves a large data base, cannot be accidental. Small discrepancies between the theoretical and experimental sets of data are usually attributed to such factors as experimental errors in setting the incidence angle, poor preparation of the crystal surface or slightly incorrect values of the poorly known non-structural parameters that enter into the calculations, such as the surface Debye temperature.

Therefore determining the quality of fit between the calculations and experiment is crucial. In general, this evaluation has been performed visually. While the eye is able to make fine distinctions between closely similar data, it is impossible to objectively evaluate the large data base needed if one is to have confidence in the final result. For example, let us suppose that we have experimental data for 10 diffracted beams and have calculated the corresponding I(E) curves for 7 different structural models, as would be the case for a typical range of expansions and contractions of the surface layer relative to the bulk. Visual examination would then involve 70 different comparisons to be synthesised into one final result. If a non-structural parameter such as the inner potential is then also allowed to vary, the total number of comparisons to be made rapidly becomes unmanageable in a visual analysis, even when obvious misfits are discounted. The difficulties are further increased if, as is often the case, a change in one parameter improves the correspondence with experiment for some curves but worsens those of others. The consequence of these difficulties is an unknown uncertainty in the values of the

"correct" parameters.

Therefore, there is a real need in LEED crystallography for a numerical factor which ideally can both select the best structure from the experimental and calculated intensities and can give some measure of the reliability of that result. Such a reliability-factor or index is necessarily complex because a whole set of features has to be evaluated in the comparison beween calculations and observations. These features include:

(i) the general shape of the I(E) curves ,regardless of the absolute intensities;

(ii) the number and energies of maxima, minima, shoulders etc.;

(iii) the presence of portions of curves with marked peculiarities e.g. narrow peaks, deep troughs.

Several attempts have been made to construct reliability-indices that take regard of some or all of the above points and they are outlined in the next section. The most complete index is that of Zanazzi and Jona [23] which is discussed in detail.

5.2 Reliability-indices

Several authors have attempted to construct simple reliability-indices to complement visual evaluations. One of the most straightforward involves calculating the mean value of the difference in corresponding peak postions in the theoretical and experimental curves

$$\overline{\Delta E} = (1/N) \sum_{i=1}^{N} |E_i^{cal} - E_i^{obs}| \qquad (5.1)$$

where the E_i are the energies at which the i^{th} peak occurs in the calculated and observed curves and N the number of peaks in the beam under study [93,94]. The most important defect of the $\overline{\Delta E}$ criterion is that it completely disregards the peak intensities and weighs exclusively their positions. Other disadvantages are possible ambiguities in the choice of peaks to be matched and degrees of subjectivity in positioning poorly-resolved features and deciding whether a minor peak should, or should not be considered.

Recently Van Hove et al [95], combining the experience of earlier attempts, have proposed the use of five separate reliability-indices, each of which tend to pick out different features of I(E) curves. The first two are similar to those employed in structure determinations by X-ray crystallography [96,97]

$$R1 = \sum_{E_{1i}}^{E_{2i}} |c_i I_{i,cal} - I_{i,obs}| / \sum_{E_{1i}}^{E_{2i}} I_{i,obs} \qquad (5.2)$$

and

$$R2 = \sum_{E_{1i}}^{E_{2i}} |c_i I_{i,cal} - I_{i,obs}|^2 / \sum_{E_{1i}}^{E_{2i}} [I_{i,obs}]^2 \qquad (5.3)$$

where c_i is a scaling factor that places the observed and calculated intensities on the same scale for an energy range E_{1i} to E_{2i}. The factors R1 and R2 tend to emphasise the match in positions, heights and widths of peaks and valleys whilst ignoring shoulders and bumps within a peak. A third, R3, evaluates the fraction of the energy range for which the slopes of I(E) curves have different sign. This can measure, better than R1 or R2, differences in minor structure. The factors

$$R4 = \sum_{E_{1i}}^{E_{2i}} |c_i I'_{i,cal} - I'_{i,obs}| / \sum_{E_{1i}}^{E_{2i}} I'_{i,obs} \qquad (5.4)$$

and

$$R5 = \sum_{E_{1i}}^{E_{2i}} |c_i I'_{i,cal} - I'_{i,obs}|^2 / \sum_{E_{1i}}^{E_{2i}} [I'_{i,obs}]^2 \qquad (5.5)$$

where the primes indicate derivatives, match in greater detail the slopes of the theoretical and experimental I(E) curves. In principle, when experiment and theory match closely, all five R-factors should simultaneously attain their minimum values. However, if the proposed surface structure is wrong, then the various factors could be expected to show a scattering of minima at various spacings.

The most complete reliability-index proposed so far that attempts to include all the features mentioned above is that of Zanazzi and Jona (ZJ) [23]. This index has been used in this

work to determine the structures of rhodium surfaces.

5.2(a) the reliability-index of Zanazzi and Jona (ZJ)

The ZJ index compares directly the shapes of the two curves under scrutiny by comparing their derivatives, and at the same time takes into account the features described in Section 5.1. Thus the reliability-index for a single beam [23] is

$$r_i = \int_{E_{1i}}^{E_{2i}} w(E)\,|c_i I'_{i,cal} - I'_{i,obs}|\,dE \;/\; \int_{E_{1i}}^{E_{2i}} I_{i,obs}\,dE \qquad (5.6)$$

The notation follows that above; the scaling constant c_i again allows for an arbitrary intensity scale in the experimental curves:

$$c_i = \int_{E_{1i}}^{E_{2i}} I_{i,obs}\,dE \;/\; \int_{E_{1i}}^{E_{2i}} I_{i,cal}\,dE \qquad (5.7)$$

The weight function w(E)

$$w(E) = |c_i I''_{i,cal} - I''_{i,obs}| \;/\; |I'_{i,obs}| + \varepsilon \qquad (5.8)$$

emphasises the extrema of the observed curve through the inverse dependence on $I'_{i,obs}$, as well as those prominent features with high curvature in both sets of curves through the use of second derivatives. The difference function in the numerator prevents w(E) from vanishing at inflection points, unless both curves have an inflection point at the same energy. A possible disadvantage of equation (5.8) is that w(E) vanishes if the two

curves have straight portions in the same energy range, even if of opposite slope. The factor ε prevents divergence of the integral for small $|I'_{i,obs}|$ and is chosen [23] to be

$$\varepsilon = |I'_{i,obs}|_{max} \qquad (5.9)$$

This choice ensures that w(E) is independent of the scale of both the experimental and theoretical intensities.

As equation (5.6) stands, the index r_i has no theoretical upper limit. For a given pair of curves it has a specific value; the smaller this value, the better the match between the two curves. Thus it is convenient to introduce the reduced r-factor [23]

$$(r_f)_i = r_i/0.027 \qquad (5.10)$$

where 0.027 is an average value of r_i for random pairs of curves [23]. Random pairs of curves thus give values of $(r_f)_i$ of the order of unity.

ZJ applied this reliability-index to many examples of single beams and made a direct association between values of $(r_f)_i$ and degrees of fit assessed visually by a number of individuals. This enabled ZJ to produce a correspondence between visual evaluations and $(r_f)_i$ values which is reproduced in Table 5.1.

The determination of a surface structure involves more than one beam, either at the same or different angles of incidence. The concept of a single beam reduced r-factor was therefore

Visual match for a single beam	Good	Mediocre	Bad
Single beam index $(r_f)_i$ or many-beam index R	0.20	0.35	0.50
Reliability of structure	Very probable	Probable	Doubtful

Table 5.1 Correspondence between visual match and $(r_f)_i$ for a single beam (first and second row), and between R for a structural model and its reliability (second and third row). After Zanazzi and Jona [23].

extended by ZJ to a set of beams

$$\bar{r}_f = \sum_i (r_f)_i \Delta E_i \Big/ \sum_i \Delta E_i \qquad (5.11)$$

where $\Delta E_i = E_{2i} - E_{1i}$

The quantity $\bar{r}_f$ satisfies many of the requirements for a reliability-index in LEED crystallography. However, LEED structural analyses have been performed on data bases of varying degrees of completeness. Structural models could be proposed on the basis of only a few beams at one angle of incidence, or, preferably from a much larger range of experimental data. To accommodate these considerations, ZJ proposed an overall R-factor

$$R = [(p/n) + q]\, \bar{r}_f \qquad (5.12)$$

where p and q are constants, and n is the number of beams tested. This form was used so that the bracketed term should decrease with increasing n but should never become smaller than

some asymptotic value q. This avoids the situation in which a "wrong" model for which a very large number of beams were tested could produce a small value of R.

The numerical values of p and q are determined by establishing a relationship between the numerical value of R and the reliability of the corresponding structural model. For simplicity ZJ found it convenient to maintain the assignment that was established for single beams in the first two rows of Table 5.1. Thus, by using the denominations of "very probable" etc. for a given structure, they arrived at the R value assigments shown in the second and third rows. This assignment then suggests possible values for p and q in equation (5.12). The asymptotic value q must be such that, where the $(r_f)_c$ values are of the same order as those obtained from comparing random curves, the corresponding structure R-factor must remain worse than "doubtful" regardless of the number of beams used in the analysis. The value of q was therefore set to 2/3. Also, the value of the bracketed function in equation (5.12) should increase rapidly for n<3, so that structural models will not be judged as very probable on the basis of less than 3 beams. The overall R-factor proposed by ZJ is

$$R = [\,(3/2n) + (2/3)\,]\,\bar{r}_f \qquad (5.13)$$

The choice of p=3/2 has the advantage that the numerical value of R does not change much beyond n=10. R remains almost constant for structures that are determined with 10,15 or 20

beams.

The details of the numerical evaluation of equation [5.6] are given in the original paper of ZJ [23]. To avoid instability problems with the integrals involved, all the experimental and theoretical data are put onto a finely-spaced common linear energy grid. Noise and scatter in the experimental data must be removed prior to the calculation of the reliability-index to eliminate abrupt changes in the derivatives. The programmed index was used as supplied by the authors with only minor modifications to accommodate input-output requirements.

5.3 Structural Analysis Using The ZJ Reliability Factor: The Cu(111) Surface As An Example

Results from a Cu(111) surface will be used to illustrate the use of the ZJ reliability-index and the refinements and additions made to it during the course of this work. Referring to Fig. 3.11 and Fig. 5.1, we can see I(E) curves for a total of four beams at two angles of incidence, together with the corresponding curves calculated for an unreconstructed surface using the V_{Cu13} and $V_{Cu}^{\beta<}$ potentials. The calculations were performed for an initial inner potential of -9.5eV and for a range of top layer spacings from $\Delta d\% = -10\%$ to $+10\%$ of the bulk spacing in steps of 2.5% (0.052Å). The curves shown in the figures are only for three values of $\Delta d\%$ to avoid overcrowding. The I(E) curves calculated for Cu(111) from the two potentials are almost identical, consistent with the similarities noted for

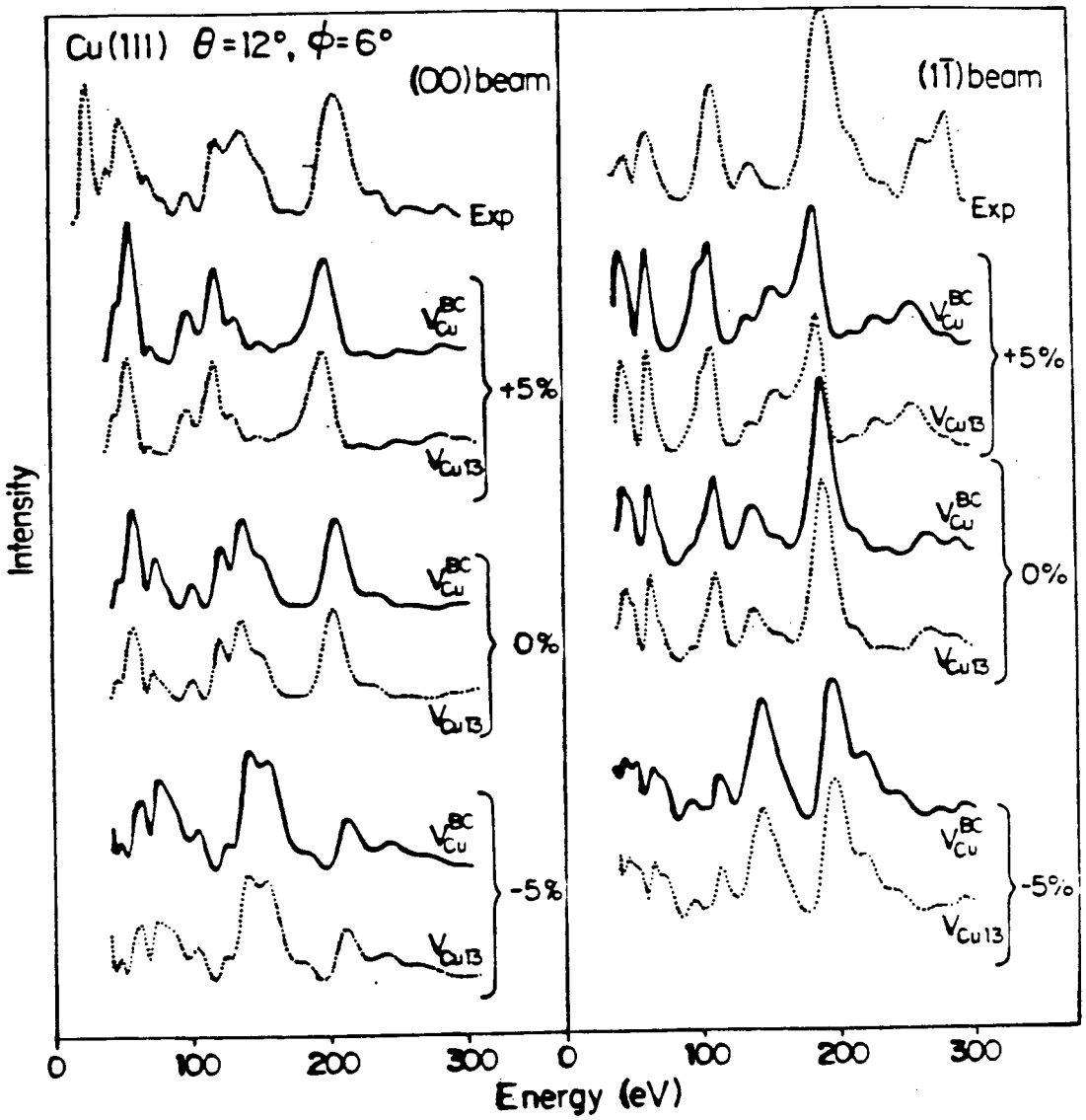

Figure 5.1 Comparison of some experimental I(E) curves for Cu(111) with calculations for the potentials V_{Cu}^{BC} and V_{Cu13} at $\theta=12°$, $\phi=6°$; $V_{or}=-9.5$eV and $\Delta d\%=+5$, 0 and 5%.

the phase shifts in Section 3.1(b).

In a surface structure analysis, the final matching of calculated and experimental I(E) curves involves not only a variation of $\Delta d\%$ but also a variation of the inner potential. This latter parameter is fixed a priori for the calculations but is a poorly known quantity. The inner potential is clearly an important quantity since, in a structural analysis, it is necessary to distinguish its effects from those associated with $\Delta d\%$. To a good approximation, a change in the inner potential results in a translation of the calculated curve along the energy axis. A visual estimation of the "best-fit" value of $\Delta d\%$ therefore also involves a simultaneous determination of the "best-fit" value of the inner potential. This delicate procedure was attempted for all 16 beams measured from the Cu(111) surface and these results are shown, for each potential, as the lower rows of Table 5.2.

This type of comparison is very difficult to make as a visual estimation of the degree of fit may vary from very good for some beams e.g. the (00) beam of Fig. 5.2 at $\Delta d\%=-5\%$, to quite poor for others, e.g. the (10) beam of Fig. 3.11 at $\Delta d\%=+5\%$. Balancing good fits against bad fits for so many pairs of experimental and calculated curves is difficult and the uncertainty in V_{or} and $\Delta d\%$ are inevitably appreciable. Moreover this analysis shows the two potentials to be indistinguishable. The overall visual estimate suggests best-fit values of $V_{or}=-9\pm2$eV and $\Delta d\%=-2.5\pm2.5\%$.

The equivalent operation using the ZJ reliability-index is as follows: (i) an I(E) curve is calculated with a reasonable

	Extent of Comparison			Conditions of best agreement		
Pot.	n	E(eV)	Analysis	$\Delta d\%$	V_{or}	R
V_{Cu13}	16	2382	R-factor	-4.1±0.6	-9.8±0.6	0.132
			visual	-2.5±2.5	-9 ±2	
V_{Cu}^{bc}	16	2342	R-factor	-4.2±0.6	-9.0±0.6	0.136
			visual	-2.5±2.5	-9 ±2	

Table 5.2 Summary of structural determinations of the Cu(111) surface.

value of V_{or}; (ii) the values of $(r_r)_i$ are computed for a number of pairs formed by the observed curve on one hand and the calculated curve translated by various amounts ΔV_{or} on the other. The minimum value of $(r_r)_i$ indicates the best match, and the corresponding "best" inner potential for the calculated curve is $V_{or}+\Delta V_{or}$. For a number of beams, $\overline{r_r}$ is calculated from the single-beam data and the minimum in $\overline{r_r}$ found. The process can then be repeated for other models e.g. a change in $\Delta d\%$.

In their original analysis ZJ plotted the results of such a procedure as $\overline{r_r}$ (the energy-weighted mean of the individual beam r-factors $(r_r)_i$), as in equation (5.11), against V_{or} or $\Delta d\%$ and the best combination of minima was chosen by inspection. An example of this method of presentation is shown for the Cu(111) data in Fig. 5.2. This analysis uses the V_{Cu13} potential, a total of 16 beams and experimental I(E) curves over a total energy range of 2342eV. The minimum value of $\overline{r_r}$ is estimated by this method to be for $\Delta d\%=-4\pm2\%$ and $V_{or}=-9\pm2$eV.

We can note two points from such plots. First, the estimates of the position of $\overline{r_r}$ along the $\Delta d\%$ and V_{or} axes are subject to error owing to the large spacing between points along

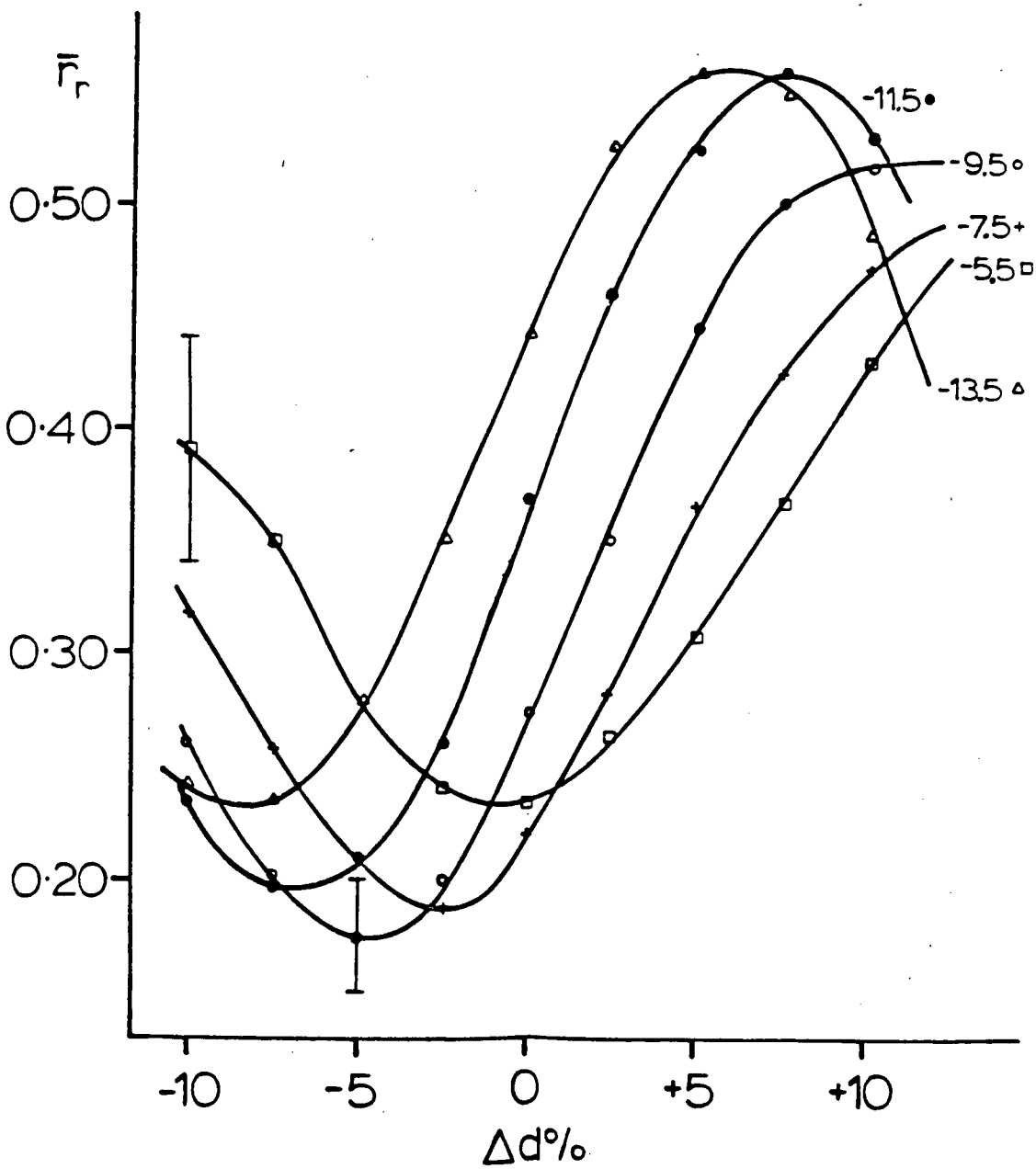

Figure 5.2 Plot of $\bar{r}_r$ against Δd% for various values of V_{or} for Cu(111) with the V_{Cu13} potential. Error bars are standard errors in the weighted mean.

the $\Delta d\%$ axis (2.5%) and the V_{or} axis (2eV). A finer grid, particularly of $\Delta d\%$ values, would however be rather costly in terms of computer time.

Second, each point on one of the curves in Fig. 5.2 is a weighted mean over the 16 beams available for analysis. The standard error on the weighted mean is [98]

$$\varepsilon_r = [\sum_i \Delta E_i ((r_r)_i - \bar{r}_r)^2 / (n-1) \sum_i \Delta E_i]^{1/2} \qquad (5.13)$$

where n is the number of beams and the other symbols are as before. Some typical values of ε_r are indicated by bars on Fig. 5.2 and can be substantial. This opens up the question of why the curves shown in Fig. 5.2 are so smooth, given that the errors can be so large.

A rationalisation of this apparent anomaly is suggested by Fig. 5.3 where values of $(r_r)_i$, for individual beams from Cu(111), are plotted as a function of $\Delta d\%$ for V_{or}=-9.5eV. Of the 16 beams available only 9 are shown for clarity, the others have a combined weighting of less than 20%. Also shown in Fig. 5.3 , as the dashed curve, is a plot of $\bar{r}_r$ whose minimum value of 0.173 corresponds to $\Delta d\%$=-4.1%. The degree of agreement in the individual curves varies from $(r_r)_i$=0.057 to $(r_r)_i$=0.240 with a standard error ε_r=0.047. The mean (dashed) curve at $(\bar{r}_r)_{min} \pm \varepsilon_r$ (for 68% probability) indicates a contraction with the topmost interlayer spacing corresponding to -4±3%. However, it is apparent that the minima of all the individual curves in Fig. 5.3 lie well within these limits, and this suggests that the error in the value of $\Delta d\%$ that

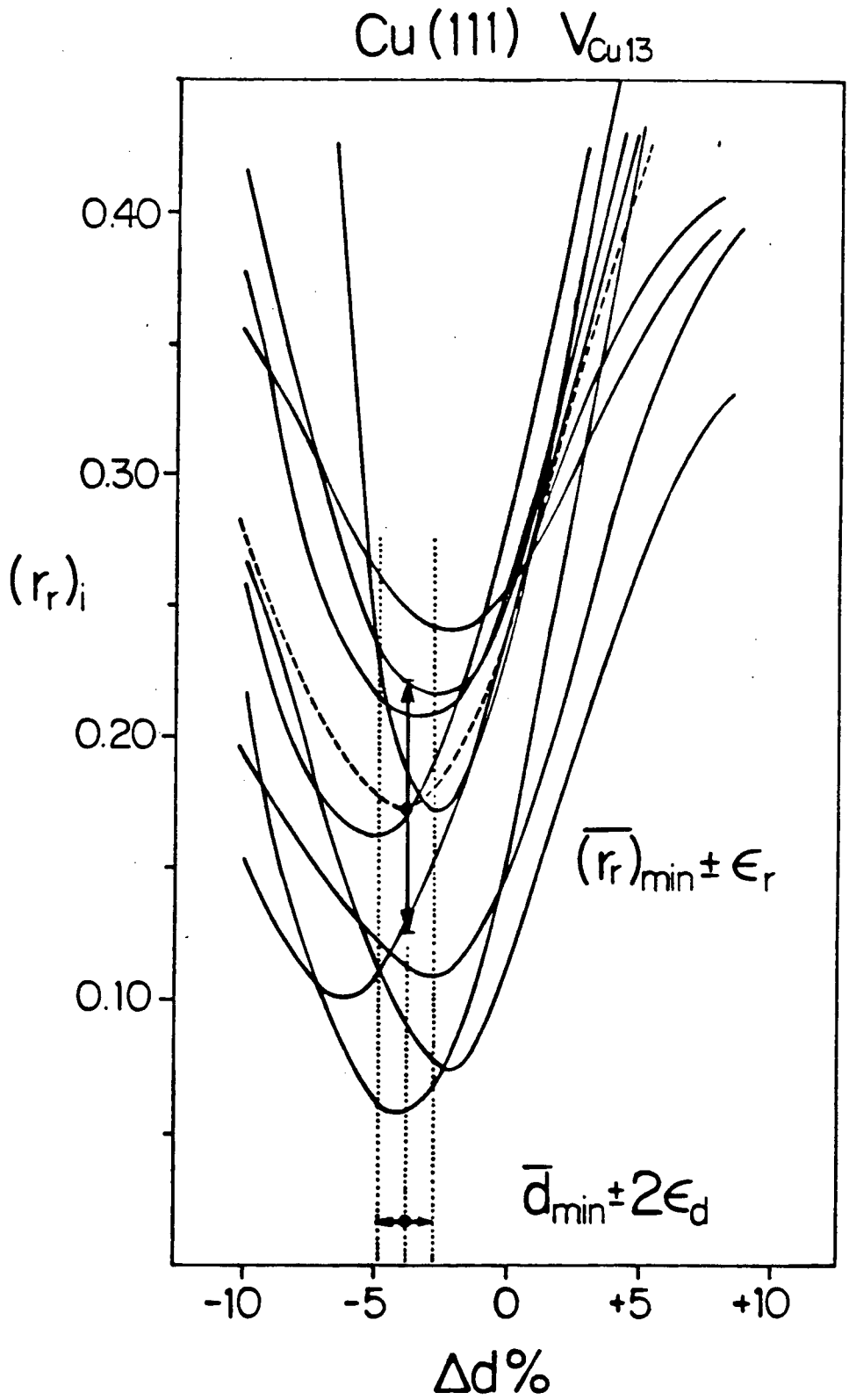

Figure 5.3 Plots for Cu(111) of $(r_r)_i$ for 9 individual beams versus $\Delta d\%$ for the V_{Cu13} potential with V_{or}=-9.5eV. The dashed line shows the dependence of the energy weighted mean $\bar{r}_r$ versus $\Delta d\%$.

corresponds to a best fit for a particular value of V_{or} should perhaps be evaluated from the set of interlayer separations (Δd^{i}_{min}) corresponding to the minimum in each of the individual curves. Accordingly we can define

$$\overline{\Delta d_{min}} = \sum_{i} \Delta E_i \Delta d^{i}_{min} \Big/ \sum_{i} \Delta E_i \qquad (5.14)$$

$$\varepsilon_d = \Big[\sum_{i} \Delta E_i (\Delta d^{i}_{min} - \overline{\Delta d_{min}})^2 \Big/ (n-1) \sum_{i} \Delta E_i \Big]^{1/2} \qquad (5.15)$$

where the Δd^{i}_{min} are determined after extra points have been fitted to the curves by interpolation; $\overline{\Delta d_{min}} \pm 2\,\varepsilon_d$ (for 95% probability) corresponds to $-4.1 \pm 1.2\%$. This range is indicated in Fig. 5.3 and it points to a much smaller, and apparently more representative, error in the geometry than that suggested above. It is also clear from Fig. 5.3, provided the individual curves for $(r_f)_i$ show similar variations with $\Delta d\%$, that the mean curve $\overline{r}_f$ will be a smooth function of $\Delta d\%$ even though the $(r_f)_i$ individually exhibit varying degrees of fit.

Since the $\overline{r}_f$ are functions of at least two important variables, namely $\Delta d\%$ and V_{or}, a more informative method of presenting the data is in the form of a contour plot or diagram; this is depicted in Fig. 5.4 for both the potentials. These plots were constructed by taking the original grid of $\overline{r}_f$ values and interpolating separately along lines of constant V_{or} and constant $\Delta d\%$ to obtain an expanded grid of about 900 points; the error involved in not using a true two-dimensional interpolation is small compared with other errors already present in the data. The position of the minimum in r that

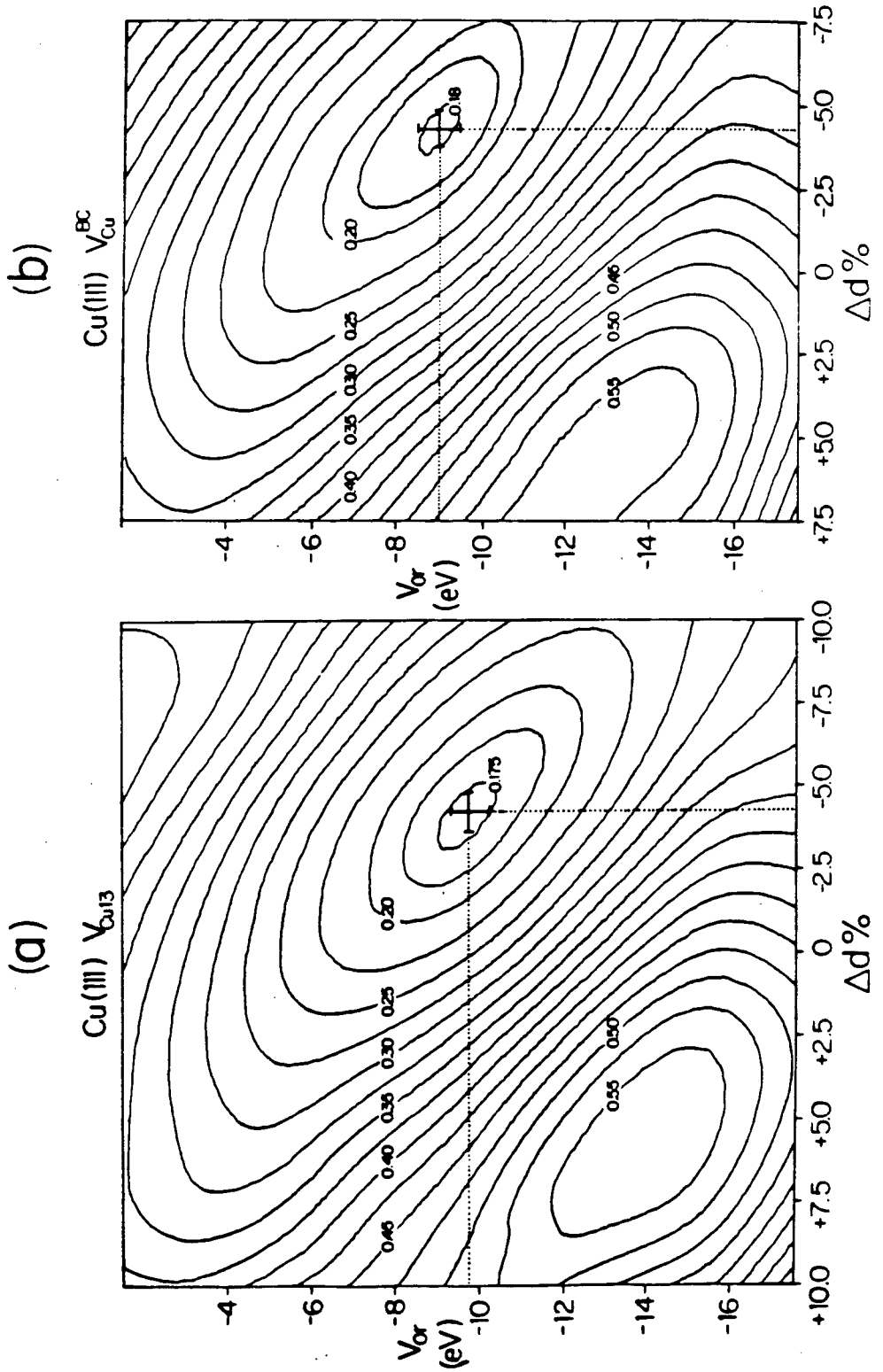

Figure 5.4 Contour plots for Cu (111) of $\bar{r}_f$ versus Δd% and V_{or} for the potentials (a) V_{Cu13} and (b) V_{Cu}^{BC}.

determines the best fit values of V_{or} and $\Delta d\%$ is found by inspection. Also shown in Fig. 5.4 are the error bars corresponding to $\pm \epsilon_d$ and $\pm \epsilon_v$ (the standard error in the minimum for the inner potential, defined analogously to ϵ_d) which places 68% confidence limits on the location of the minimum of $\overline{r}_r$; these are evaluated at the nearest grid point and provide estimates of the errors in the location of the actual minimum.

The plots of Fig. 5.4 illustrate the value of the reliability-index approach in analysing LEED data; with such displays the values of parameters giving best-fit with experiment can be selected immediately. Each of these contour plots provides an immediate assessment of 784 curves of the type shown in Fig. 5.1 (that is I(E) curves for 16 beams at 7 different values of $\Delta d\%$ and 7 different values of V_{or}).

The values of $\Delta d\%$ and V_{or} corresponding to minimum $\overline{r}_r$ are identical to within one standard error for the two potentials, Table 5.2. Both potentials indicate a contraction in the topmost interlayer spacing of $-4.1 \pm 0.6\%$ and $V_{or} = -9.4 \pm 0.6$eV. The low values of the overall ZJ reliability factor, R, (0.132 and 0.136 for V_{c13} and $V_c^{\beta c}$ respectively) and the small error in the best-fit values of $\Delta d\%$ and V_{or} suggest that this represents a rather well-defined structure.

Previous studies of the (111) surfaces of FCC metals with LEED have indicated no large expansions or contractions of the surface layer, see Section 5.5. For aluminium, one study [11] has suggested an expansion of 5% while other studies [11,120] indicate the topmost spacing is equal to the bulk within 5%. For both nickel [11,120] and platinum [122], LEED analyses

indicate this spacing is within 2.5% of the bulk value; studies on Pt(111) with ion-channeling [123] now suggest an expansion of about 2%.

The one previous structural determination of Cu(111) by Laramore [20] concluded that the surface is not dilated but that a small contraction between 0 and 5% is possible. The contraction determined here for Cu(111), namely -4.1±0.6%, is consistent with this and is the largest yet reported for a close-packed surface, although larger contractions are known for more loosely packed surfaces, e.g. 10% for Al(110) [101,110,111] and 7% for Ag(110) [101,106,107].

5.4 Other Methods Of Obtaining Surface Structural Information From LEED Data

While most surface structural determinations by LEED have been performed by comparisons of experimental and calculated I(E) curves for various structural models, there have been attempts to find data inversion procedures that will produce a surface structure directly from experimental data. This procedure would avoid the inevitably lengthy and expensive trial and error process associated with conventional multiple-scattering calculations.

Two approaches have been proposed so far; both are based on the kinematical theory, although neither can yet be considered to be well-established. One method attempts to manipulate the experimental data so as to enhance the single-scattering structure and concomitantly diminish the multiple-scattering

features. If successful, this would allow analysis with the comparatively simple kinematical theory; this is the philosophy of the data-averaging (DA) approach [102,103]. The alternative approach uses the Fourier transform (FT) method [99,100], in analogy with the approach in X-ray structure analysis of generating a Paterson map of the scattering centres. Because of difficulties associated with each method, and a reluctance on the part of LEED practitioners to discard data of multiple-scattering origin, these methods have suffered some criticism. However, there is a continuing hope that they can become useful, at least in the sense of restricting the volume of "parameter space" that must be searched in a typical full multiple-scattering analysis.

5.5 Bibliography Of Surface Structures Of Clean Metals

In this section is compiled a bibliography of surface structure determinations of clean metals by LEED. It is not intended to be an exhaustive list of every paper published about clean metal surfaces. Many early papers contained experimental data or calculations now recognised to be of dubious quality or of such a limited scope as to be of little use. In such cases the more recent and complete studies are quoted, although some early work of high quality is given. A few structures are now being investigated by techniques such as medium-energy electron diffraction (MEED), ion-channeling (IC) and medium-energy ion scattering (IS) and have been included for completeness.

The metals are listed alphabetically and by face. The

crystal habit is also listed as investigations of phase changes are now being carried out. The methods used to determine the surface stucture is listed as visual (V), reliability-index (RI), Fourier transform (FT) or data averaging (DA). The surface spacing is characterised by $\Delta d\%$ and is supplied with the estimated errors. In some cases doubts are raised by severely limited ranges of either the calculated or experimental data. The list is current as of Aug. 1978.

In all these cases the metal surfaces do not reconstruct in a lateral sense but do show varying degrees of contraction or expansion of the surface layer. In general, the close-packed (111) faces of FCC metals can be seen to show very small differences of the surface layer spacing from that of the bulk, with possibly a slight preference for contractions. The situation seems to be similar for the (100) surfaces of FCC metals while (100) surfaces of BCC metals appear in general to show contractions of the order of 5 to 10%. The interesting example of Co, which has a phase change from HCP to FCC at about 800°C behaves unexceptionally in either phase. The HCP metals have been little studied but the basal planes of Ti and Zn are unremarkable. The only higher index face studied so far, that of Cu(311) shows a contraction of similar magnitude to the FCC (110) faces.

Several of the notable omissions from this list e.g. Pt(100), Au(100) show by their complex LEED patterns that they are laterally reconstructed; their surface structures have not yet been solved by LEED intensity analyses using multiple-scattering calculations.

Metal	Face	Crystal habit	Method	Δd%	Ref.
Ag	(100)	FCC	V	0±?	104
	(111)	FCC	V	0±?	105
	(110)	FCC	FT	-7±5	101
			RI	-10±1	106
			MEED	-5±5	107
Al	(100)	FCC	V	0±1?	108
			V	0±?	109
			V	0±5	110
	(111)	FCC	V	0±5	110
			V	+5±5	111
			V	0±5	112
			FT	-3±5	99
	(110)	FCC	FT	-4±5	101
			V	-10±5	110
			V	-10±5	111
			V	-10±1	108
			V	-12±3	112
Co	(0001)	HCP	V	0±5	113
	(111)	FCC	V	0±5	113
Cu	(100)	FCC	FT	0±1	99
			DA	0±1	114
			V	0±5	20
	(111)	FCC	V	-2.5±2.5	20
			RI	-4.1±0.6	this work
	(311)	FCC	RI	-5.0±1.5	115
Fe	(100)	BCC	V	-1.5±2.5	116
Ir	(111)	FCC	V	-2.5±5	117
Mo	(100)	BCC	V	-11±5	118
Na	(110)	BCC	V	0±5	119
Ni	(100)	FCC	FT	0±1	99
			V	+5±5	11
			V	0±5	120
			DA	0±4	121
	(111)	FCC	V	-1±1	11
			V	0±5	120
	(110)	FCC	V	-5±1	11
			FT	-5±5	101
			IS	-4±?	135

Metal	Face	Crystal habit	Method	Δd%	Ref.
Rh	(100)	FCC	RI	0±2.5	this work
	(111)	FCC	RI	-1±3	this work
	(110)	FCC	RI	-2.7±2.0	this work
Pt	(111)	FCC	V	+2.5±2.5	122
			IC	+2±1	123
			IS	+1.5±1	136
Ti	(0001)	HCP	V	-2±1	124
W	(100)	BCC	V	-11±5	125
	(110)	BCC	V	0±5	126
Zn	(0001)	HCP	V	-2±2	127

CHAPTER 6

THE (111) SURFACE OF RHODIUM

Previous LEED studies on this single crystal face are limited to that of Grant and Haas [130], which concentrated mainly on Auger spectroscopy, and a recent chemisorption study by Castner et al [18]. Both these authors reported a (1X1) LEED pattern for the clean surface but did not perform any intensity measurements. An as yet unpublished LEED study of this surface which centres especially on the vibrational properties of the surface atoms, but which does report some intensity data, has been recently undertaken [131].

6.1 Experimental

Experimental data for the Rh(111) surface were taken from two crystals (see Table 4.1): one was a pre-cut slice loaned by Prof. G. A. Somorjai (Berkeley), and the second was cut and polished here. Despite the different prehistories of these crystals, they behaved identically within experimental error.

Auger electron spectroscopy of both the (111) surfaces as mounted in the vacuum chamber revealed appreciable amounts of carbon(272eV) and sulphur(152eV) contaminants as shown in the Auger spectrum of Fig. 6.1(a). Argon ion bombardment removed S from the surface but the C Auger signal showed a relative increase, Fig. 6.1(b). This appears to be a common situation caused by the low sputtering cross-section of carbon. Sputtering tends to leave islands of C or a surface layer enriched in carbon. Annealing at about 1300K reduces the level of carbon contamination on the surface by back-diffusion into the bulk crystal, but will induce the re-appearance of sulphur

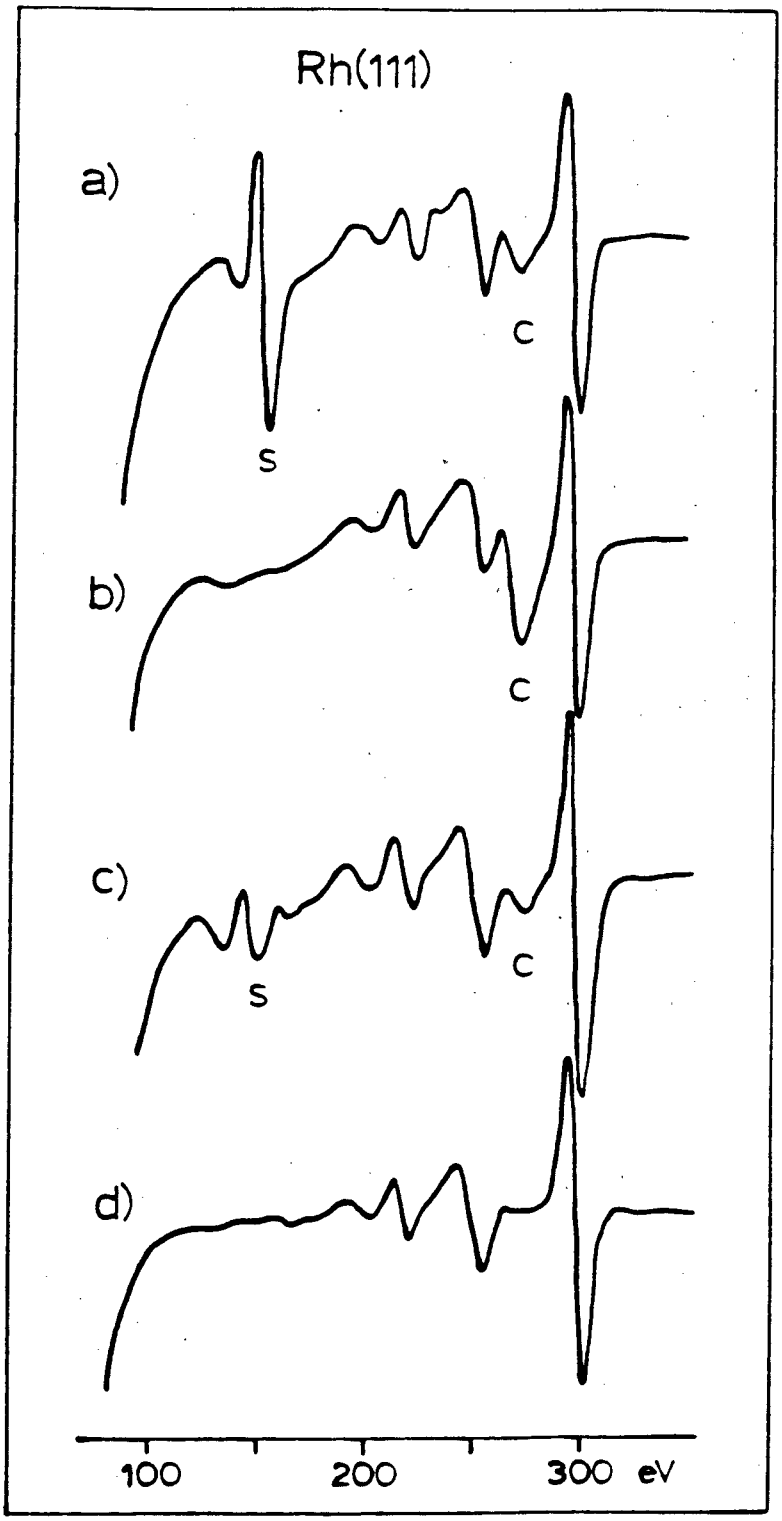

Figure 6.1 Auger spectra of Rh(111) surfaces with a 1.5keV, 10 microamp beam:
(a) as mounted, considerable S(152eV) and C(282eV) contamination;
(b) after argon-ion bombardment, reduced S, increased C;
(c) after annealing, reduced C, increased S;
(d) cleaned surface.

as is shown in Fig. 6.1(c). The level of S and C contamination subsequent to bombardment can be regulated by careful temperature control. A clean surface showing very low C and S Auger signals could be produced by many cycles of hot ion-bombardment (about 1 microamp at 2kV for 10 minutes with the crystal at 1000K) followed by a 10 minute anneal at 1300K. After several such cycles the sulphur content of the surface region of the crystal becomes depleted, and cleaning is made easier; often only a short anneal is then required to remove surface carbon.

The spectrum of the cleaned surface is shown in Fig. 6.1(d). The rhodium peak energies and relative intensities are listed in columns 1 and 5 of Table 6.1. The results of the other experimental studies of this surface are listed for comparison in columns 2 to 4. Some variation in reported peak energies is obvious; in part this must be attributed to difficulties in establishing a strictly linear energy scale and to contact potential differences. Also estimation of the position of weak peaks is probably subject to several eV error, especially if the signal to noise ratio of the spectrum is not very good, which may account for the relatively large spread in the quoted energies of the weak features below 220eV. The calculated energies and assignments of Packer and Wilson [49] are also listed in the final two columns. These calculations are for free atoms with an ionisation correction but nevertheless are in reasonably good agreement with the experimental data.

No significant amount of boron (Auger peak at 180eV) could

OBSERVED				REL. INT. %	CALC.	ASSIGNMENT
a)	b)	c)	d)	a)	d),e)	e)
139		145		5	141	$L_2L_3N_{45}$
170	174	175	170	5	175	$M_5N_1N_{23}$
203	208	210	200	5	208	$M_2M_4N_{45}$
225	226	227	222	15	225	$M_5N_1N_{45}$
257	260	259	256	30	258	$M_5N_{23}N_{45}$
302	306	303	302	100	303	$M_5N_{45}N_{45}$

a) this work, b) reference 130, c) reference 131, d) reference 18, e) reference 49

Table 6.1 Observed and calculated Auger transitions for rhodium.

be detected in the contaminated or clean surfaces. This is in contrast to another study [18] in which a bulk boron contaminant diffused to the surface during cleaning procedures and proved very difficult to remove. One of the crystals used in the work reported here was the same crystal as used in this earlier study. The difference in behaviour in relation to boron seems to be the result of these workers having removed nearly all the bulk boron contamination through many cleaning cycles (private communication). In the second case, the crystal was purchased from a different source from that of the first crystal; in this case we have to conclude that neither the manufacturing process, nor the polishing method employed, introduced any significant amounts of boron into the crystal.

After several cycles of bombardment and annealing, a sharp (1X1) LEED pattern was observed, in agreement with earlier work [18,130,131], with a low background and negligible Auger signals for species other than rhodium. Sample photographs of the LEED pattern and the beam labelling scheme are shown in Fig. 6.2. The intensities of diffracted beams were measured as described in Chapter 4 up to about 250eV at normal incidence and for $\theta = 10°, \phi = 109°$ in the angle convention of Jona [128]. Each set of experimental intensity measurements was repeated three times on separate occasions to assess the effect of small experimental variations on the structural analysis.

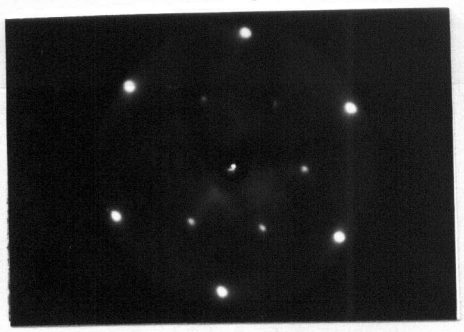

a)

b)

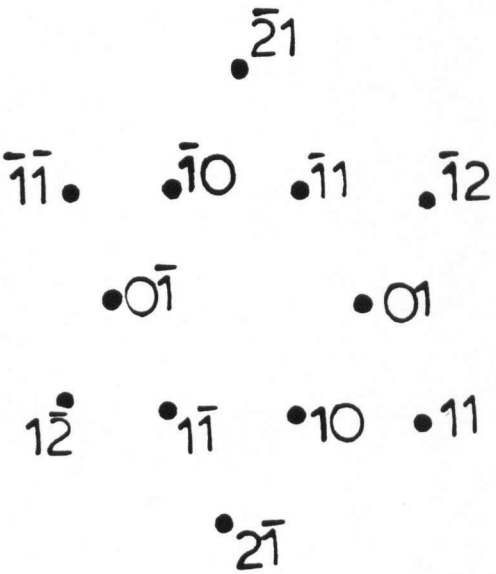

c)

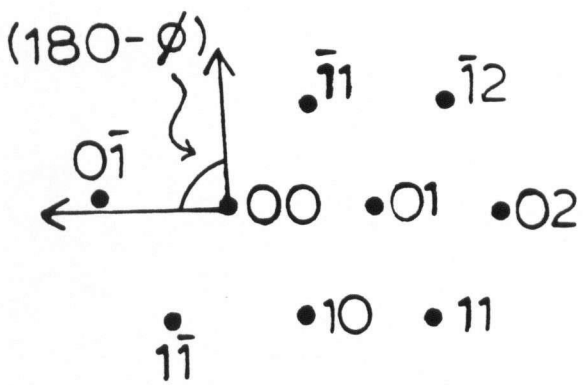

d)

Figure 6.2 Photographs of the (1x1) LEED pattern from the clean Rh(111) surface at (a) normal incidence (158eV), (b) $\theta = 10°$, $\phi = 109°$ (122eV) in the angle convention of Jona [128]. The labelling scheme is shown in (c) and (d).

6.2 Calculations

The (1x1) LEED pattern obtained indicates that the surface does not reconstruct in such a way as to change the surface symmetry from that of the bulk structure. However it is possible for the surface to reconstruct in such a way as to preserve the (1x1) pattern, that is by altering the registry of the surface layer with respect to those underneath. Such possibilities are shown in Fig. 6.3. If the surface does not reconstruct then the face-centred cubic stacking sequence is continued to the surface, as shown in (a) namely CBACBA...C. Two possible reconstructions are to a CBACBA...A sequence, (b), or to a CBACBA...B stacking, (c), the latter stucture possessing the hexagonal close packed seguence for the top three layers. This last surface reconstruction seems physically the more plausible and was the only reconstruction model that was investigated here with direct calculations.

Calculations were performed as detailed in Chapter 3 for both the V_{Rh}^{WJM} and V_{Rh13} potentials in the energy range 30-260eV; a total of 55 beams were available to determine the layer diffraction matrices depending upon the energy and angle of incidence.

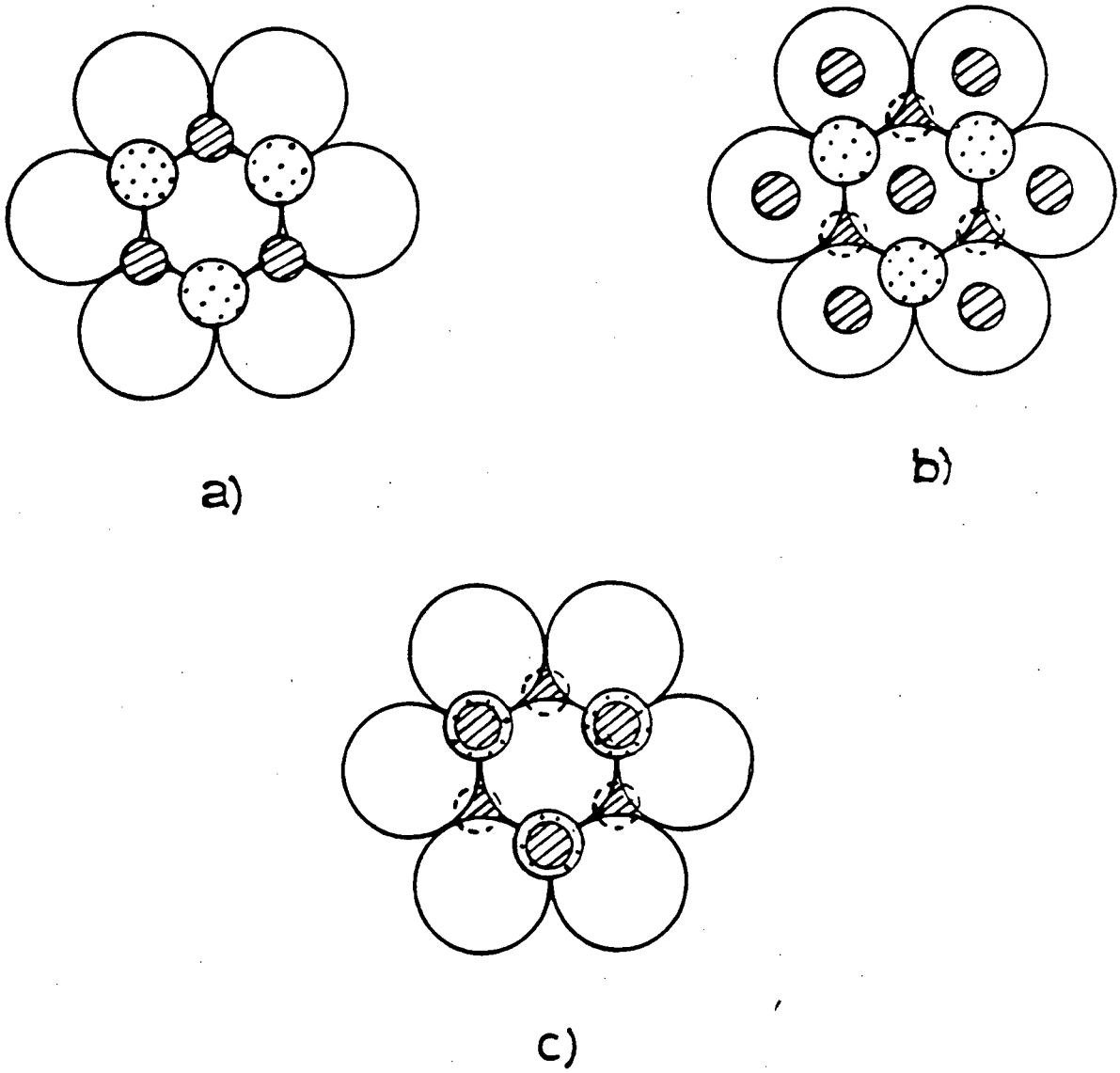

Figure 6.3 Possible reconstructions of the (111) surface that preserve the (1x1) symmetry of the LEED pattern:
(a) non-reconstructed, CBACBA...C FCC stacking;
(b) reconstructed, CBACBA...A stacking;
(c) reconstructed, CBACBA...B, HCP stacking.
The 4th layer C is indicated by small dashed barred circles, the 3rd layer B by large blank circles, the 2nd A by medium dotted circles, and
the 1st layer is indicated by small barred circles.

6.3 Results And Discussion

6.3(a) Normal incidence

Three independent sets of intensities were measured for normal incidence. Although these independent sets showed a good general agreement with each other, there were small differences in detail as, for example, in relative peak intensities and in structure such as shoulders (all the experimental data is shown in Appendices A1-A3). Within each set of data the measured intensities of the diffracted beams show closely the symmetry expected if the actual surface arrangement maintains the three-fold rotation axes which are perpendicular to (111) planes in the bulk (alternatively the symmetry in the LEED pattern could be associated with equal populations of appropriate domains). To minimise any artifacts in the comparison with calculated intensities, measured I(E) curves for sets of beams which are theoretically equivalent, on the above basis, were averaged and digitally smoothed (by two operations of a three point smoothing filter) prior to comparing with the calculations.

Figure 6.4 compares experimental I(E) curves for the (10) and (01) beams at normal incidence with I(E) curves calculated for two stacking sequences; a continuation of the bulk stacking sequence, Fig. 6.3(a), and the hexagonal reconstruction model, Fig.6.3(c), with the topmost layer spacing equal to the bulk value of 2.195Å. A detailed matching of peaks and troughs between the experimental and calculated curves could only be

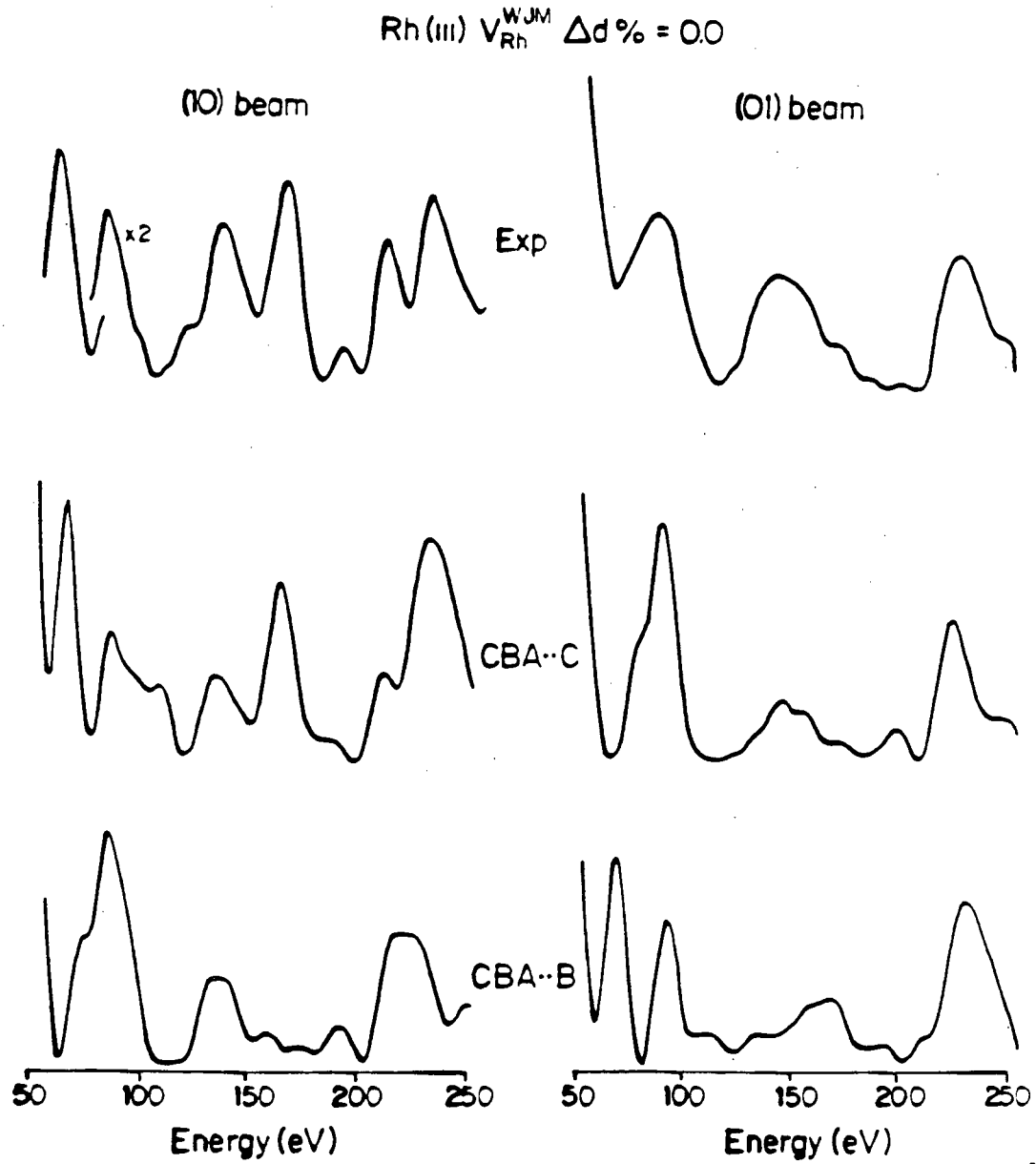

Figure 6.4 A comparison for the (10) and (01) beams of I(E) curves measured at normal incidence for Rh(111) with those calculated with the potential V_{Rh}^{WJM} for the normal FCC stacking sequence and for the HCP stacking sequence over the top three surface layers.

achieved for the normal face-centred cubic packing sequence; the other diffracted beams are similarly inconsistent with an HCP arrangement for the top three layers.

To determine the surface relaxation, calculations were performed for different values of the top interlayer spacing, expressed as in the Cu(111) case as percentage changes from the bulk value(Δd%). This quantity was varied from +10% (dilation) to -10% (contraction) in steps of 2.5% (0.055Å). Figure 6.5 compares I(E) curves for the (10) and (01) beams with those calculated for Δd%= -5,0 and +5% for the two ion core potentials. It is difficult even with this limited data set to assess visually which value of the surface relaxation best describes the experimental data, but Fig. 6.6 attempts a more complete assessment by showing contour plots of the mean reduced reliability index $\overline{r_r}$ as functions of Δd% and V_{or}, from one of the sets of independent data, as described in Chapter 5. With the averaging referred to above, the experimental data used in these contour plots for normal incidence involves the (10), (01), (11), (20) and (02) beams.

The minimum of $\overline{r_r}$ in Fig. 6.6(a) occurs for Δd% = -3.7±1.1% and V_{or} = -19.1±0.9eV, where the uncertainties in Δd% and V_{or} ($\pm \varepsilon_d$ and $\pm \varepsilon_v$ respectively) are the standard errors in the energy-weighted means deduced from the spread in values given by the minima of the reliability index $(r_r)_i$ for the various individual beams as detailed in Chapter 5. To the extent that these errors really do represent a gauge of the uncertainty in each result then there is a 68% probability that the actual minimum lies within the area defined by the error bars in

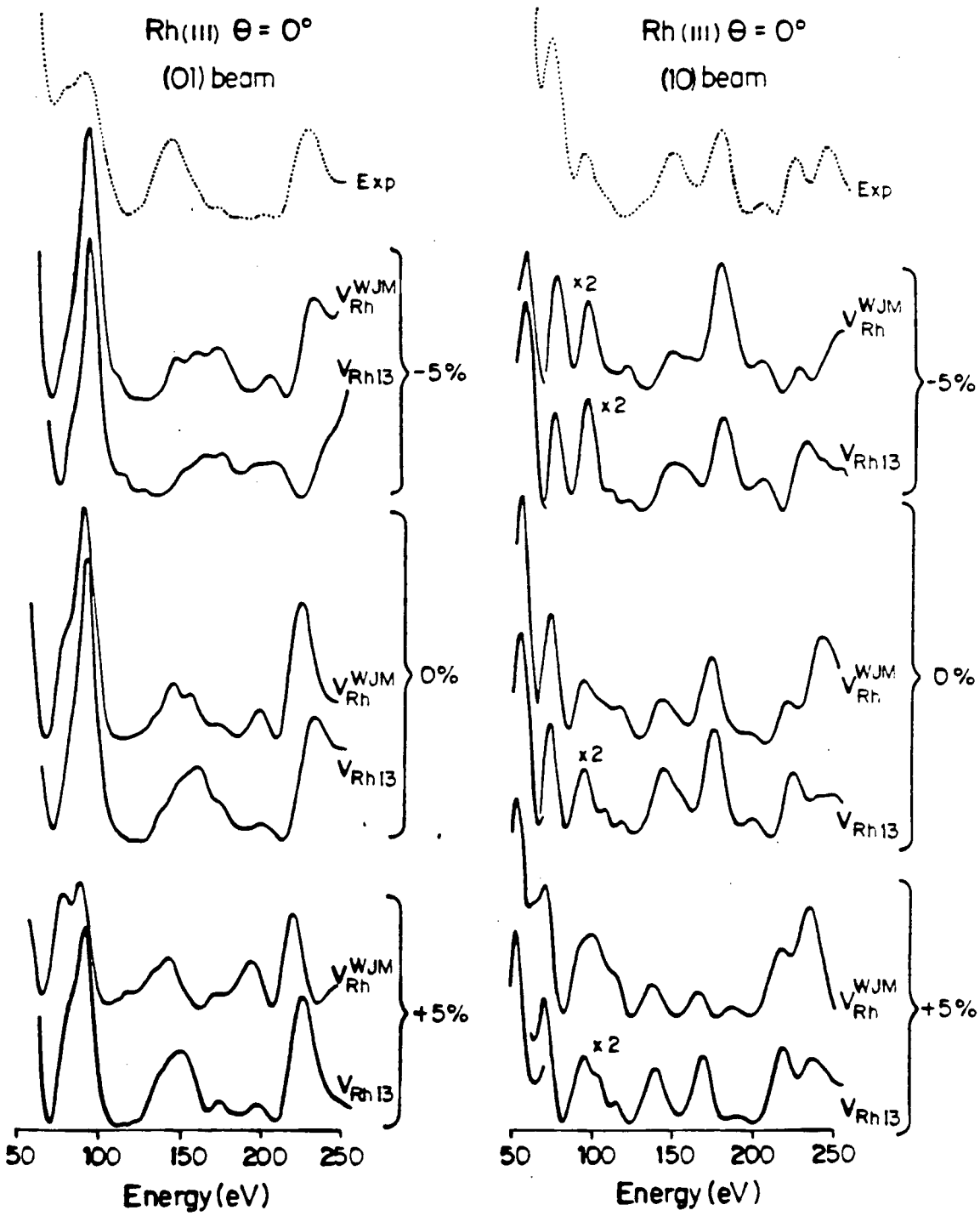

Figure 6.5 A comparison of experimental I(E) curves for the (10) and (01) beams at normal incidence for Rh(111) with intensity curves calculated for the potentials V_{Rh}^{WJM} and V_{Rh13} for three different values of $\Delta d\%$ assuming the normal FCC registry for the surface arrangement.

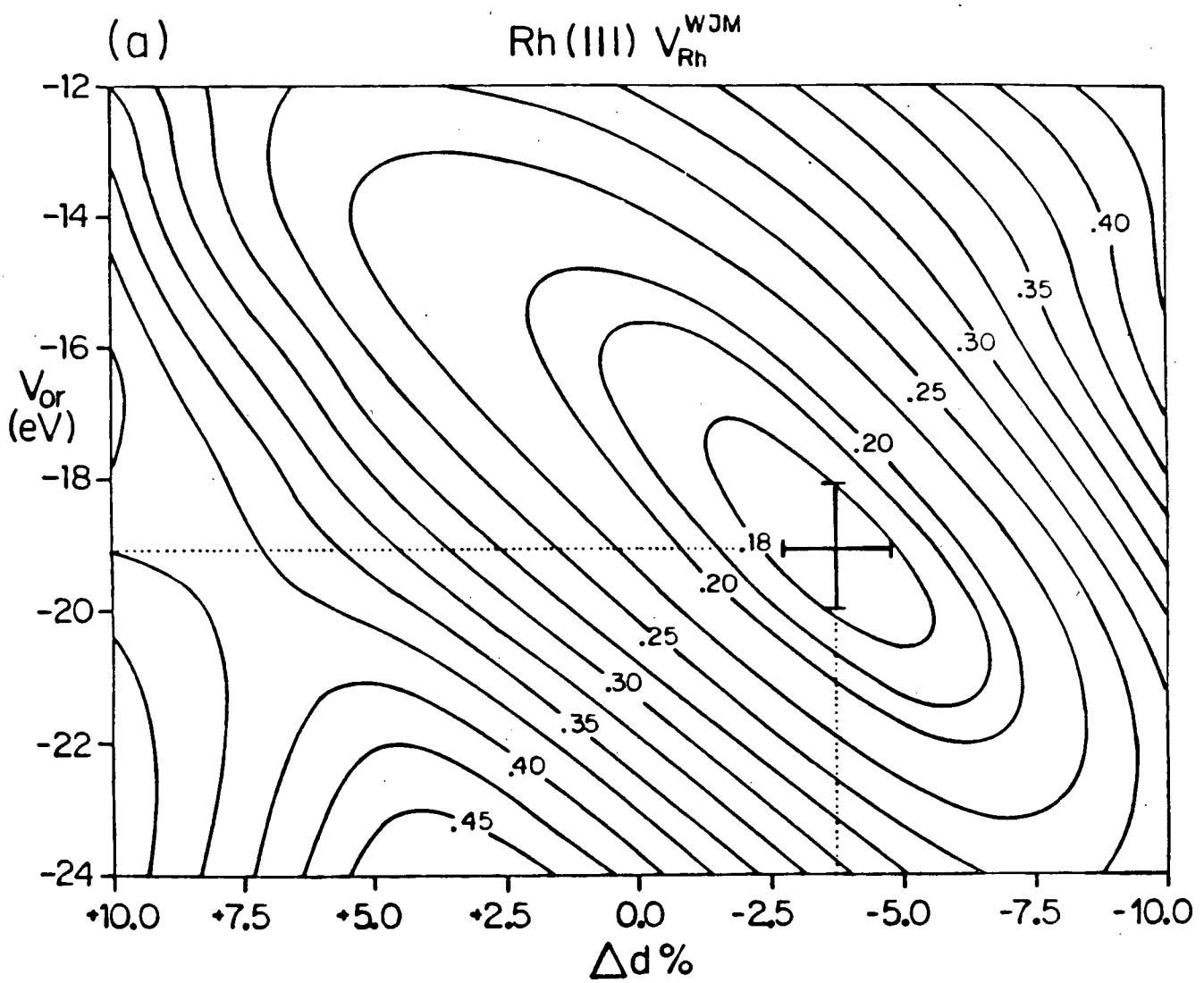

Figure 6.6 Contour plots for Rh(111) at normal incidence of $\overline{\Gamma}_r$ versus V_{or} and Δd% for the potentials (a) V_{Rh}^{WJM} and (b) V_{Rh13} starting from 54 eV.

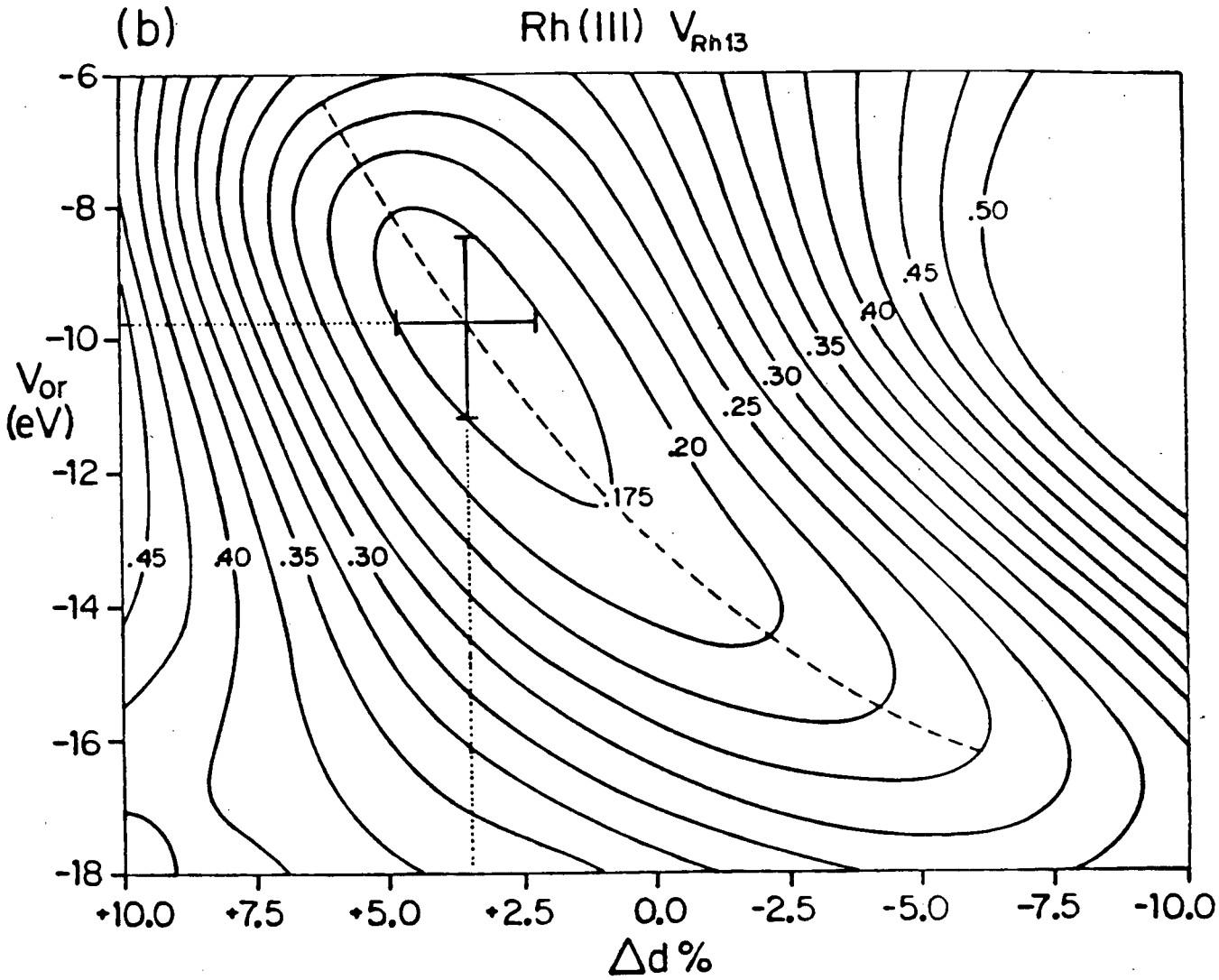
(b)
Rh(III) V_{Rh13}
-6
-8
-10
-12
-14
-16
-18
V_{or} (eV)
.50
.45
.40
.35
.30
.25
.20
.175
.45
.40
.35
.30
+10.0
+7.5
+5.0
+2.5
0.0
-2.5
-5.0
-7.5
-10.0
Δd %

Fig. 6.6(a). Figure 6.6(b) shows the corresponding contour plot which compares the experimental curves with those calculated from the superposition potential V_{Rh13} ; the minimum of $\overline{r}_f$ now occurs for $\Delta d\% = +3.5 \pm 1.2\%$ and $V_{or} = -9.7 \pm 1.2$eV. Although both sets of calculated curves are basically similar (see Fig. 6.5) the minima in the contour plots are at rather different values of the parameters $\Delta d\%$ and V_{or}.

We can see that the overall level of agreement, as judged by the value of $\overline{r}_f$, is very good within the Zanazzi-Jona (ZJ) framework. The values of the refined values of V_{or} differ by over 9eV for the two potentials. Part of this difference can be traced back to the difference in potential at the edge of the muffin-tin spheres. This amounts to about 6eV and results in an energy shift of the two sets of phase shifts relative to one another as was discussed in Chapter 3 (see Fig.3.6). Correspondingly, this will result in a relative shift in calculated I(E) curves as, for example, in Fig. 6.5 where the large peaks in the calculated curves at +5% for the (01) beam at normal incidence are displaced relative to one another. The extra shift of about 3eV, deduced from the reliability-index analysis, may reflect further differences in the two potentials.

The difference in the values of $\Delta d\%$ given by the two potentials appears more serious. The two minimum values of $\overline{r}_f$ given in Fig. 6.6 seem sufficient to preclude choosing either potential as giving the "best fit".

We can probe into the origins of the different values of $\Delta d\%$ from V_{Rh13} and V_{Rh}^{WJM} by noting that the contour plots in Fig. 6.6 exhibit elongated valleys running diagonally across the

diagrams; a similar effect can be seen in the analogous plots for Cu(111) in the discussion of Chapter 5 (see Fig.5.4). As a result of these valleys in the contour plots, relatively good agreement between experiment and calculations (as judged by $\overline{r}_r$) can be achieved for a number of combinations of V_{or} and $\Delta d\%$. For Fig. 6.6(b), all pairs of values which fall on the dashed line from V_{or} =-16eV, $\Delta d\%$=-6% to V_{or} =-6eV, $\Delta d\%$=+6% have $\overline{r}_r$ <0.25, and therefore give "good" agreement according the criterion of ZJ. Since the degree of fit worsens rapidly in directions perpendicular to the valley, it seems probable that any minor deficiencies in the calculated or measured I(E) curves would mainly move the location of the minimum of $\overline{r}_r$ along the valley. To see the extent of this for small changes in experimental intensities, the corresponding reliability-index calculations with the other two independent sets of experimental data were made. The results of the additional contour plots with V_{Rh}^{WJM} give values of $\Delta d\%$ equal to -5.6±1.3% and -4.8±0.8%, and therefore an overall mean value of -4.7%. The further plots with V_{Rh13} give $\Delta d\%$=+3.8±1.3% and +3.5±1.2%, and mean value of +3.6%. It seems clear that, while these mean values of $\Delta d\%$ are outside the 96% confidence limits ($\pm 2\epsilon_d$), this discrepancy in geometry from the two potentials is not primarily associated with small uncertainties in the experimental data.

Figure 6.7 shows plots of $(r_r)_i$ for the individual beams against $\Delta d\%$ for V_{Rh}^{WJM} in (a), and V_{Rh13} in (b); the dotted lines show the corresponding variations of $\overline{r}_r$. In accord with the above results, the minima of curves for the individual beams in Fig. 6.7(b) are generally shifted to more positive values of $\Delta d\%$

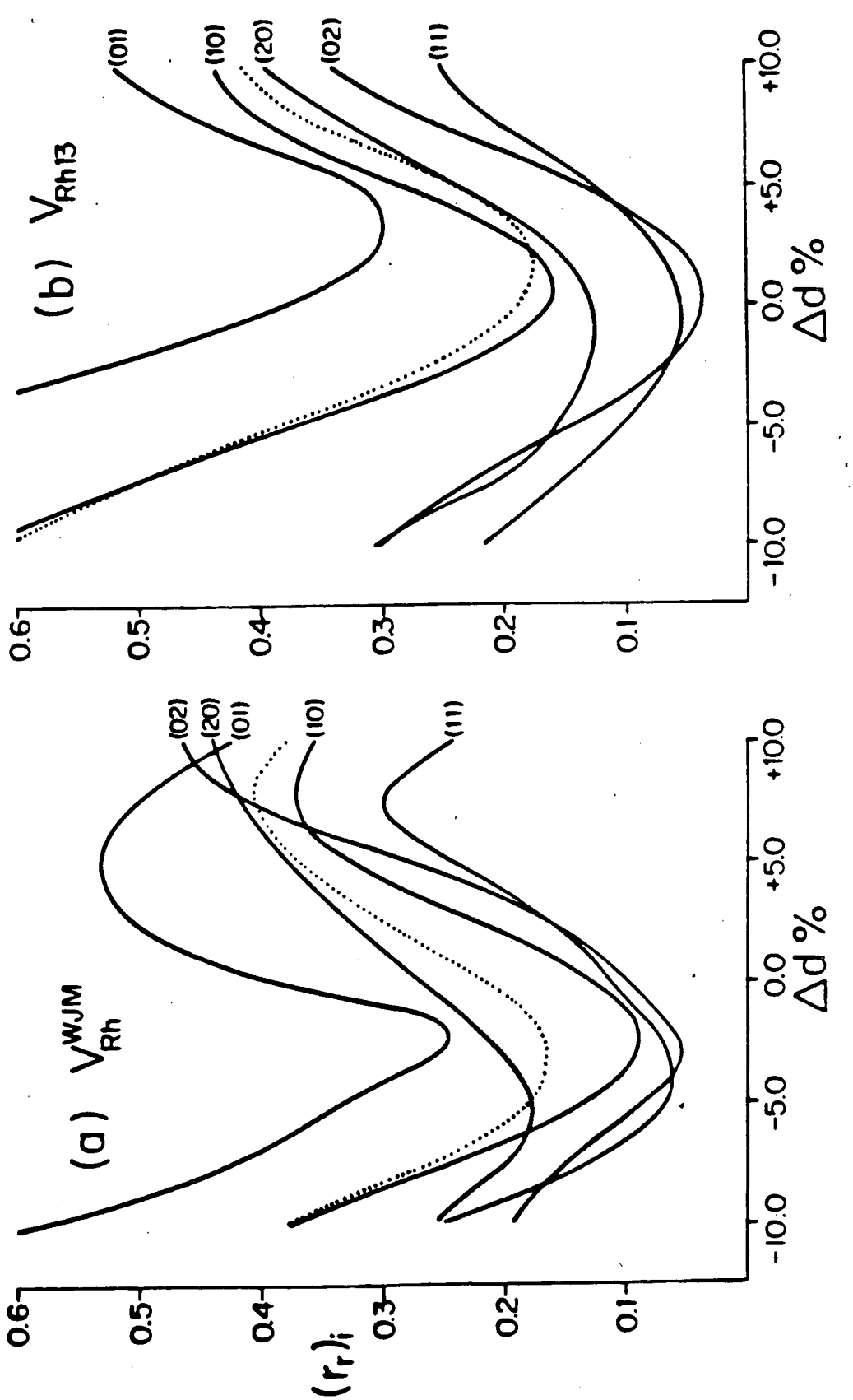

Figure 6.7 Plots for Rh(111) of $(r_r)_i$ for five independent beams at normal incidence versus Δd% for (a) V_{Rh}^{WJM} (V_{or} = 18eV) and (b) V_{Rh13} (V_{or}=-10eV). The dashed lines show the dependence of $\bar{r}_r$ versus Δd%.

compared with the corresponding values in Fig. 6.7(a). However, for the (10) and (01) beams there is a much steeper rise at negative values of $\Delta d\%$ in Fig. 6.7(b); in particular the degree of fit for the (01) beam appears to deteriorate much more rapidly in this region for V_{Rh13} (Fig. 6.7(b)) than for V_{Rh}^{WJM} (Fig. 6.7(a)). The origin of this behaviour in the reliability-index analysis may not be immediately obvious from a visual evaluation of the I(E) curves in Fig. 6.5, although this difference is ascribed here as being associated with the large peak in the calculated I(E) curves for the (10) beam at around 54eV. This peak is approximately twice as large at $\Delta d\% = -5\%$ for V_{Rh13} as for V_{Rh}^{WJM}, and is the dominant feature in both I(E) curves. The presence of such a strong feature right at the beginning of I(E) curves being compared with the reliability-index turns out to be undesirable. This is because the values of the scaling constant c_i can change substantially over the range of V_{or} shifts employed; this problem arises from the areas under the I(E) curves changing appreciably as the energy range is truncated at different points within this peak when the value of the inner potential is varied.

To avoid this problem, it was found necessary to start the comparison of the I(E) curves at a higher energy. Figure 6.8 shows contour plots for the same set of normal incidence data as in Fig. 6.6 when the comparison is started at 66eV instead of 54eV as was done earlier. By comparing these two figures we can see that the best fit of the inner potential is lowered by about 1eV for the band structure potential by this small energy range truncation, but little effect on V_{or} is discernable for the

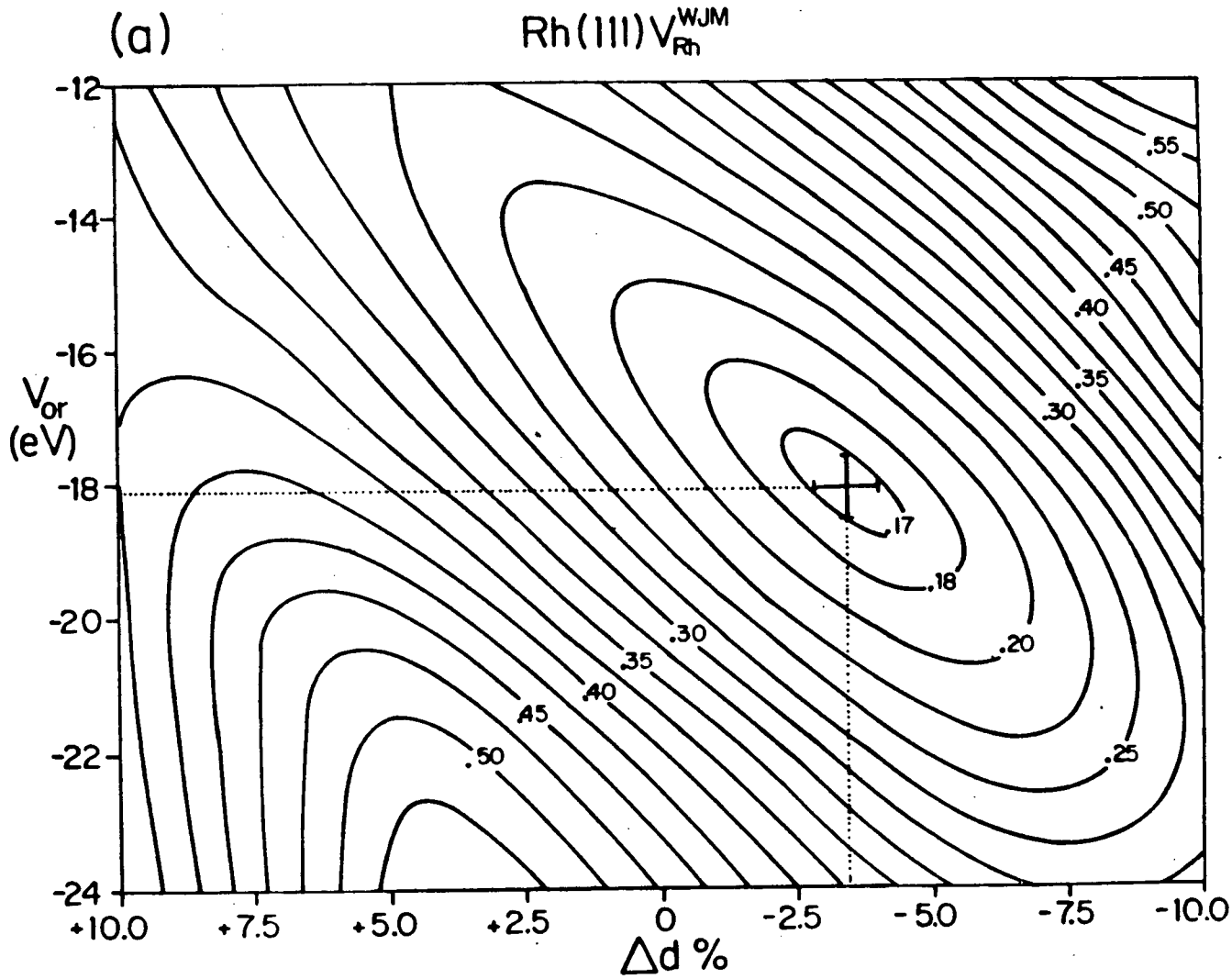

Figure 6.8 Contour plot of $\bar{r}_f$ versus V_{or} and Δd% for Rh(111) at normal incidence, using the data of Fig. 6.6 only from 66eV for the potentials (a) V_{Rh}^{WJM} and (b) V_{Rh13}.

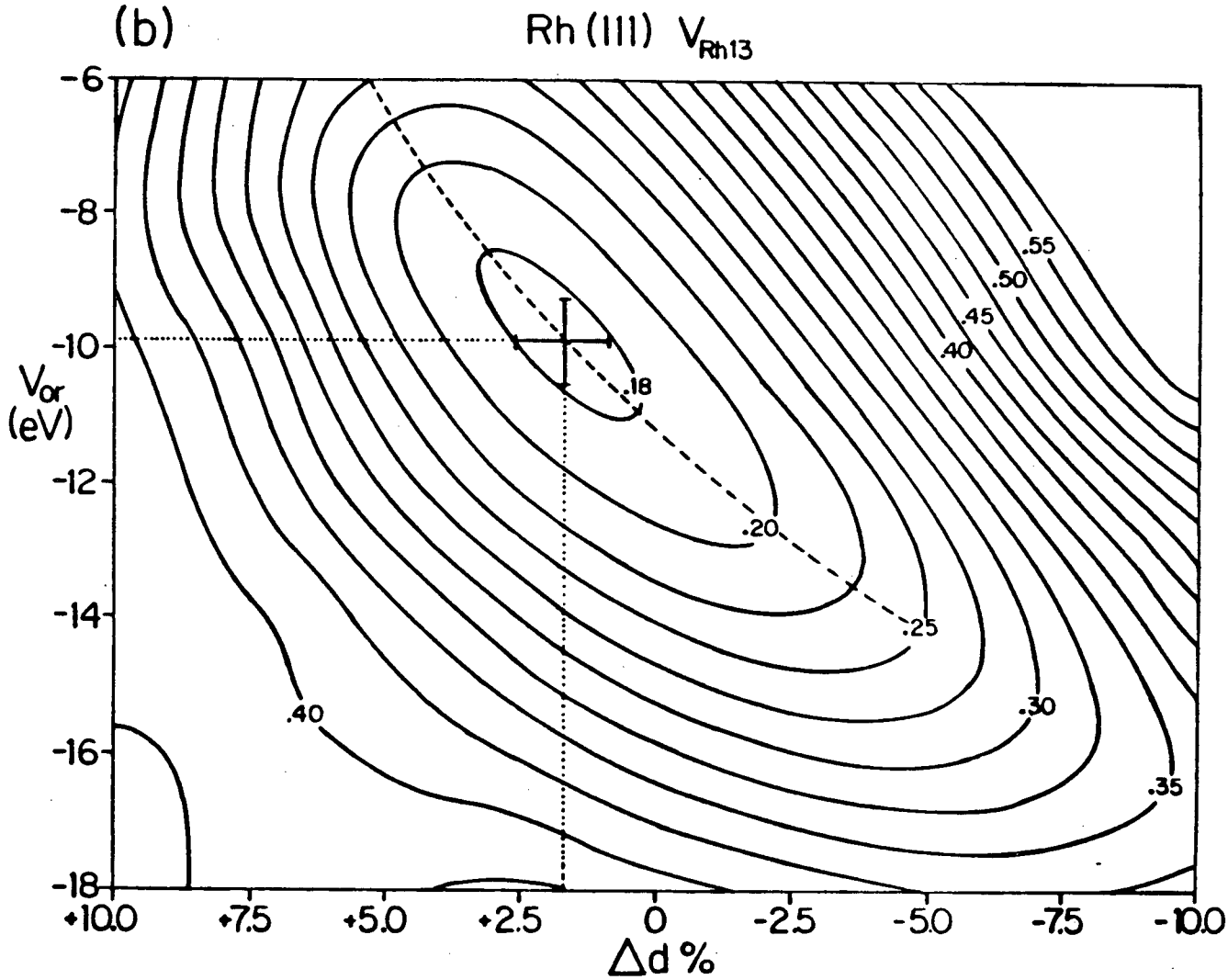
(b)
Rh (111) V_{Rh13}
-6
-8
-10
-12
-14
-16
-18
V_{or} (eV)
.55
.50
.45
.40
.18
.20
.25
.40
.30
.35
+10.0
+7.5
+5.0
+2.5
0
-2.5
-5.0
-7.5
-10.0
Δd %

superposition potential. The opposite appears to be true for $\Delta d\%$ however; in the V_{Rh}^{WJM} case, the minimum value of $\overline{r}_f$ occurs at a slightly smaller contraction after truncation, whereas for V_{Rh13} an appreciable change of almost 2% is seen. The results from the shortened energy range comparison are collected in Table 6.2. Starting at 54eV rather than 66eV adds only 1/2% to the total energy range, and yet this extension has a strong effect on results from the reliability index analysis for the potential V_{Rh13}. Thus while the value of $\overline{r}_f$ is increased between only 0.01 and 0.02, the value of $\Delta d\%$ shifts to more positive values by over 3% on average when the comparison is started from 54eV. For V_{Rh}^{WJM}, where the peak close to 54eV in the calculated I(E) curve is somewhat smaller than for V_{Rh13}, the change in the value of d% for the two energy ranges is only about 0.4%. The same problem with normalisation could arise when a large peak in an I(E) curve occurs close to the end of the energy range of the comparison.

To consider further the top layer registry, in Figure 6.9 is presented a contour plot of $\overline{r}_f$ showing the comparison of one set of the experimental data for normal incidence with calculations for V_{Rh}^{WJM} for the surface arrangement with the laterally shifted top layer (CBA..B). These contours contrast with the steep valley and localised minimum found in each of the plots in Figure 6.6 for the bulk stacking sequence (CBA..C); the contours for the HCP surface arrangement have a rather flat topography and much higher values of $\overline{r}_f$. Although other registries have not been investigated, these results point strongly to a continuation of the bulk stacking sequence at the

No. of Experiment	Potential	No. of beams compared	Energy range compared	Conditions for best agreement		
				$\Delta d\% \pm \varepsilon_d$	$V_{or} \pm \varepsilon_V$	$\bar{r}_r$
1	V_{Rh}^{WJM}	5	628 eV	-3.3±0.6%	-18.1±0.5 eV	0.17
2	V_{Rh}^{WJM}	5	620 eV	-5.3±0.8%	-19.6±0.6 eV	0.15
3	V_{Rh}^{WJM}	5	604 eV	-4.2±0.5%	-18.6±0.5 eV	0.10
Mean values:				-4.3±0.7%	-18.8±0.5 eV	
1	V_{Rh13}	5	628 eV	+1.7±0.9%	-9.9±0.7 eV	0.18
2	V_{Rh13}	5	620 eV	0.0±0.9%	-10.7±0.7 eV	0.17
3	V_{Rh13}	5	604 eV	-0.7±0.8%	-11.3±0.7 eV	0.12
Mean values:				+0.3±0.9%	-10.6±0.7 eV	

Table 6.2 Conditions of best agreement between experiment and multiple-scattering calculations for three sets of intensities measured at normal incidence on Rh(111).

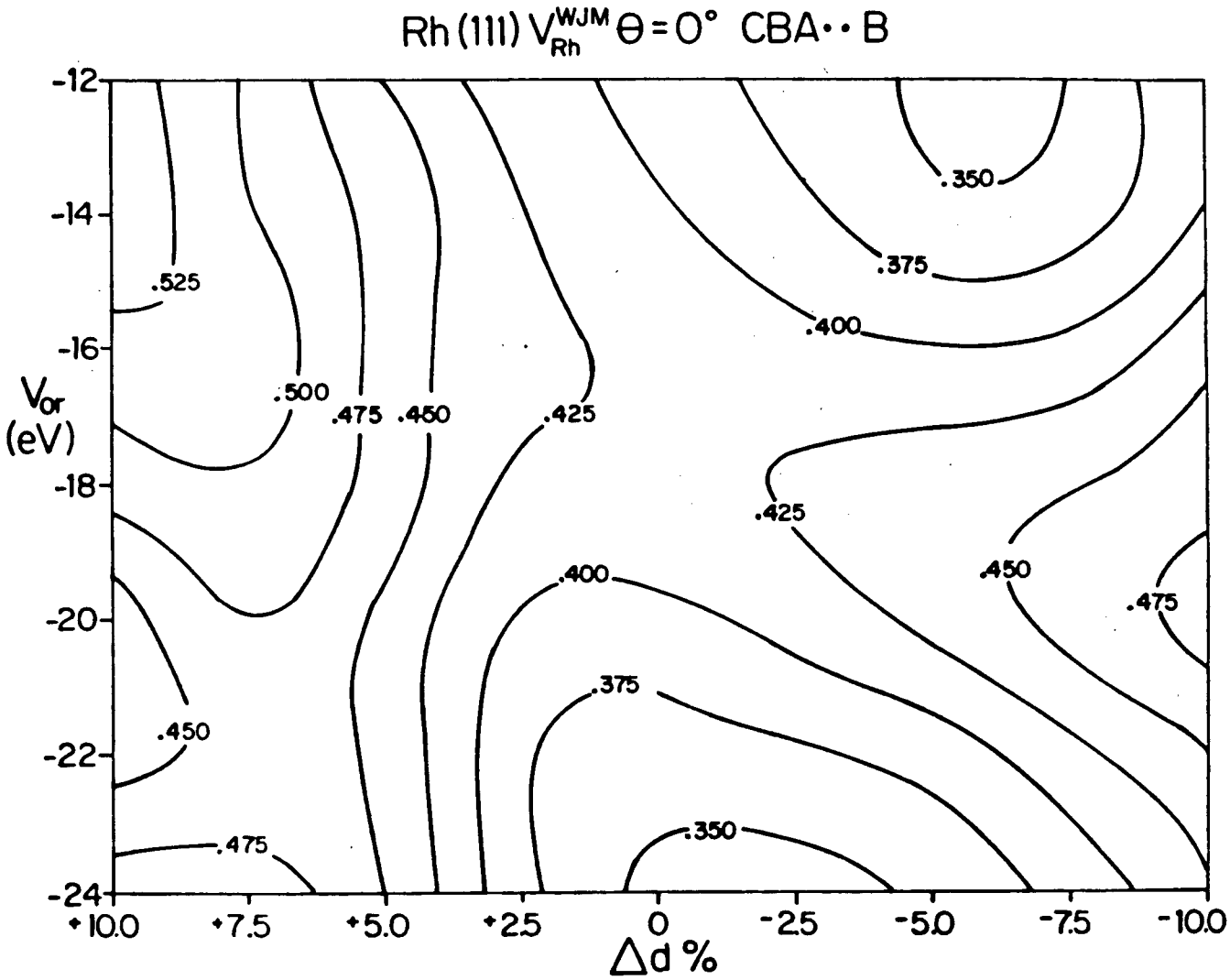

Figure 6.9 Contour plot of $\bar{r}_f$ versus V_{or} and Δd% for the potential V_{Rh}^{WJM} and the model of the Rh(111) surface in which the top three layers have the HCP stacking sequence.

Rh(111) surface, as suggested above with reference to Figure 6.4.

6.3(b) Direction of incidence $\theta=10°, \phi=10°$

Depending on the data set involved up to 16 individual beams were measured at this angle of incidence for the Rh(111) surface; these data are collected in Appendices A4-A6. A plot of experimental I(E) curves for the (11) and (10) beams with curves calculated for the two potentials is presented in Fig. 6.10, for the normal bulk stacking sequence.

Following on the previous experience, the comparisons of individual calculated and measured I(E) curves were closely checked to avoid misleading conclusions associated with dominant peaks in I(E) curves at the beginning or end of the considered energy range. For diffraction spots close to the edge of the curved LEED screen, our measured intensities are artificially diminished because both the solid angle subtended at the point of observation and the grid transmission [129] are lower compared with those for spots near the centre of the screen. To assess the influence of such additional factors, comparisons of experimental and theoretical I(E) curves were made with different energy ranges (and different numbers of beams) for the independently measured sets of data. Sample contour plots are presented in Fig. 6.11 and the results from the contour plots of $\bar{r}_f$ for these data at off-normal incidence are given in Table 6.3 as well as specifications of the extent of the comparisons made between multiple scattering calculations and each set of the

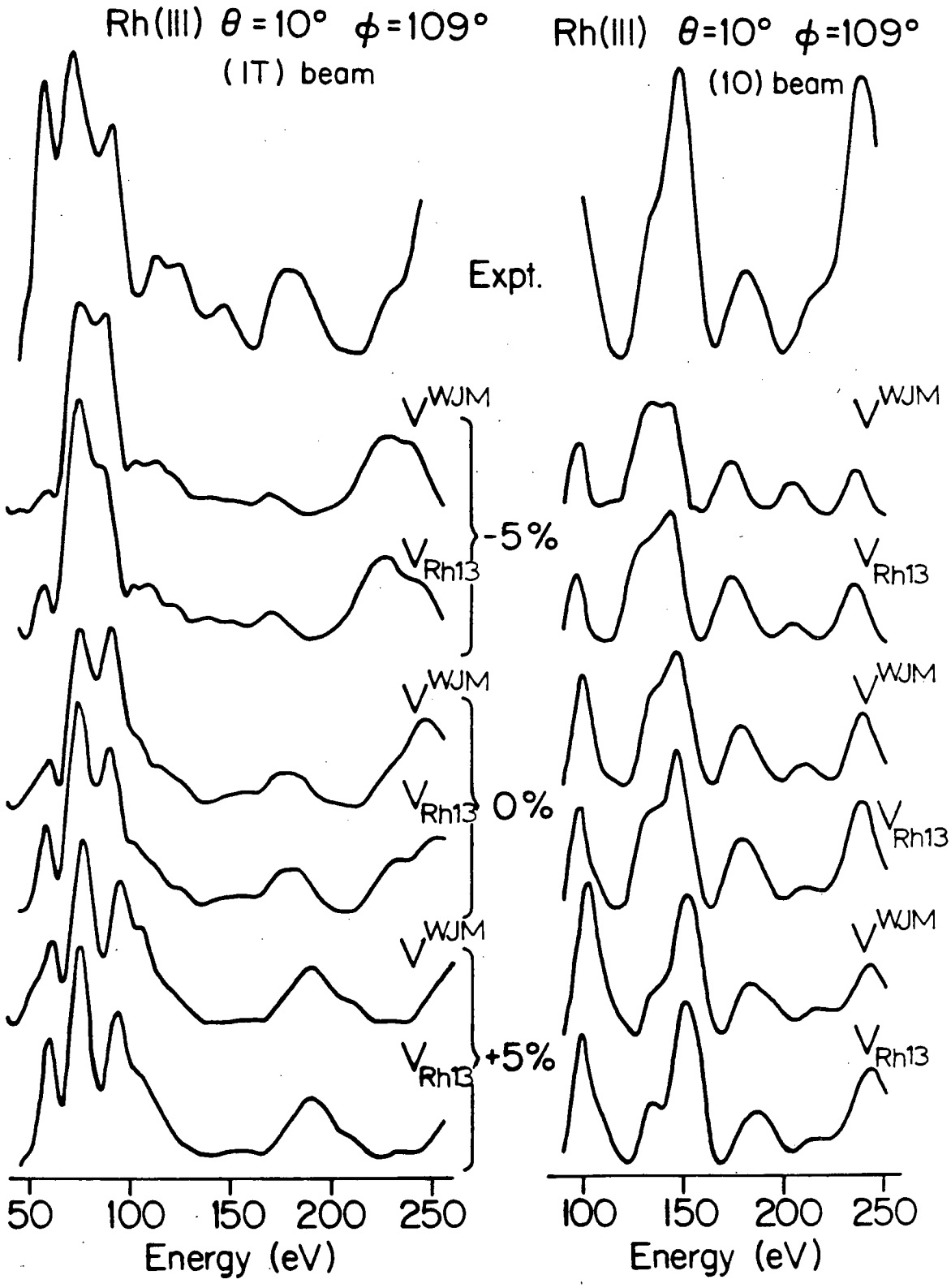

Figure 6.10 A comparison of experimental I(E) curves for the $(1\bar{1})$ and (10) beams at $\theta=10°$, $\phi=109°$ for Rh(111) with intensity profiles calculated for the potentials V_{Rh}^{WJM} and V_{Rh13} for three different values of $\Delta d\%$ assuming the normal FCC registry for the surface.

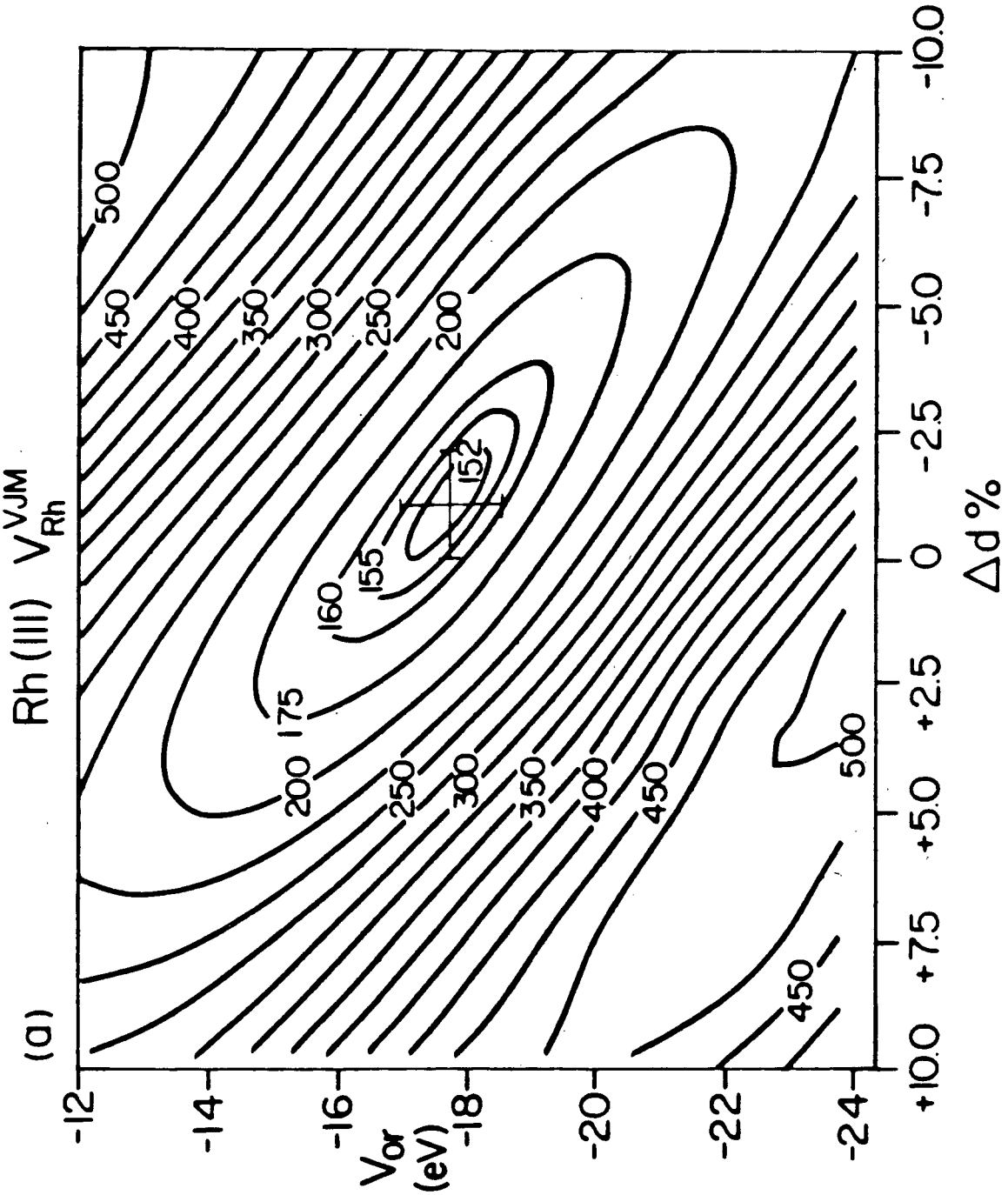

Figure 6.11 Contour plot of $\overline{r}_r$ versus V_{or} and $\Delta d\%$ for Rh(111) at $\theta = 10^{\circ}$, $\phi = 109^{\circ}$ for the potentials (a) V_{Rh}^{VJM} and (b) V_{Rh}^{LJ} .

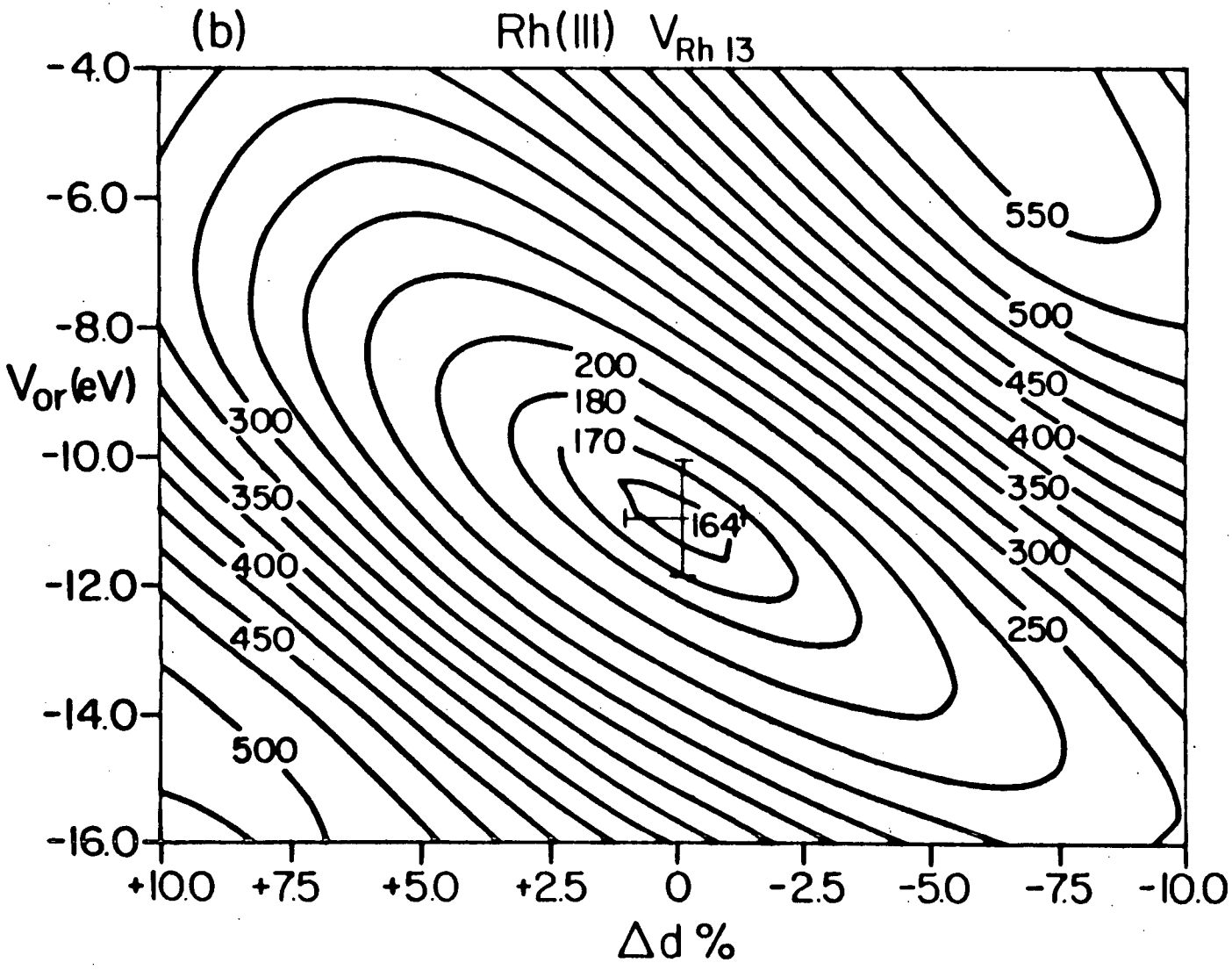
(b)
Rh(111) $V_{Rh\,13}$
-4.0
-6.0
-8.0
-10.0
-12.0
-14.0
-16.0
V_{or}(eV)
550
500
450
400
350
300
250
200
180
170
164
300
350
400
450
500
+10.0
+7.5
+5.0
+2.5
0
-2.5
-5.0
-7.5
-10.0
Δd %

experimental data.

All three independent sets of data measured at $\theta = 10°$, $\phi = 109°$ give consistent values of $\Delta d\%$ and V_{or}. Furthermore, for this direction of incidence, both potentials indicate a small contraction (about 1%) for the topmost layer spacing, in contrast with the data at normal incidence where a discrepancy was noted (Table 6.2). It is also interesting that the difference between the mean values of V_{or} in Table 6.3 for V_{Rh13} and V_{Rh}^{WJM} is very close to the 6 eV expected from the different potentials at the muffin-tin radius. By contrast the mean values of V_{or} in Table 6.2 are more negative (-18.8eV) and more positive (-10.6eV) than the values in Table 6.3 for V_{Rh}^{WJM} and V_{Rh13} respectively. The corresponding values of $\Delta d\%$ in Table 6.2 are more negative (-4.3%) and more positive (+0.3%) than the values in Table 6.3; in relation to the results for off-normal incidence, at normal incidence the minima in $\bar{r}_f$ have been displaced slightly in opposite directions along the valleys in the contour plots of Figure 6.6. Even though the mean values of $\Delta d\%$ and V_{or} for this off-normal angle of incidence correspond closely for the two potentials, the reliability index $\bar{r}_f$ does not indicate the overall agreement is any better than that achieved at normal incidence.

Although the minimum values of $\bar{r}_f$ in Table 6.3 indicate that the general level of agreement between calculated and measured I(E) curves diminishes as the comparisons are made over increased energy ranges (and for more beams), the corresponding values of $\Delta d\%$, and V_{or} are closely similar for each set of data. This suggests that the neglect of variations in the grid

No. of Experiment	Designation of calculation†	No. of beams compared	Energy range compared	Conditions for best agreement $\Delta d \pm \epsilon_d$	$V_{or} \pm \epsilon_V$	$\bar{r}_r$
1	V_{Rh}^{WJM}	9	1152 eV	-1.1±1.0%	-17.8±0.6 eV	0.15
2	V_{Rh}^{WJM}	13	1684 eV	-1.2±0.7%	-17.9±0.3 eV	0.16
3	V_{Rh}^{WJM}	16	2024 eV	-0.1±0.8%	-17.1±0.6 eV	0.22
Mean values:				-0.8±0.8%	-17.5±0.5 eV	
1	V_{Rh13}	9	1152 eV	-1.3±0.8%	-11.5±0.4 eV	0.13
2	V_{Rh13}	13	1616 eV	0.0±0.8%	-11.0±0.9 eV	0.16
3	V_{Rh13}	16	2144 eV	-0.4±0.6%	-10.8±0.5 eV	0.20
Mean values:				-0.5±0.7%	-11.0±0.7 eV	
3	V_{Rh}^{WJM} θ=8° ϕ=109°	16	2024 eV	-1.0±0.6%	-17.9±0.6 eV	0.22
3	V_{Rh}^{WJM} θ=12° ϕ=109°	16	2024 eV	-4.0±1.6%	-18.2±1.1 eV	0.34

† Unless otherwise stated the calculations have been made for θ=10° ϕ=109°.

Table 6.3 Conditions of best agreement between experiment and multiple-scattering calculations for three sets of intensities measured at θ=10°, ϕ=109° on Rh(111).

transmission and the angle subtended at the point of observation are not strongly affecting conclusions about surface geometry, although there may be reductions in the overall agreement. Another source of experimental uncertainty is in setting the angle of incidence. To assess this for the data of experiment 3, information is given in Table 6.3 comparing the level of agreement with experiment for additional calculations made with $\theta=8^{o}$, $\phi=109^{o}$ and $\theta=12^{o}$, $\phi=109^{o}$. The first of these additional angles of incidence does not improve the level of agreement achieved with $\theta=10^{o}$, $\phi=109^{o}$, as monitored by $\overline{r_f}$, but the second indicates a much poorer agreement. This suggests that the value $\theta=10^{o}$ is correct to within 1^{o}, and this experimental uncertainty does not seriously affect the determination of the topmost interlayer spacing.

6.4 Conclusions

By averaging the results of the reliability-index analysis for the three independent sets of measurements at each angle of incidence we find(Tables 6.2 and 6.3) the following values for the surface structural parameter $\Delta d\%$ and the inner potential V_{or}:

(i) from V_{Rh}^{WJM} $\Delta d\%=-4.3\pm0.7\%$ and $V_{or}=-18.8\pm0.5$eV at normal incidence

and $\Delta d\%=-0.8\pm0.8\%$ and $V_{or}=-17.5\pm0.5$eV at $\theta=10^{o}$, $\phi=109^{o}$

(ii) from V_{Rh13} $\Delta d\% = +0.3 \pm 0.9\%$ and $V_{or} = -10.6 \pm 0.7$eV at normal incidence

and $\Delta d\% = -0.5 \pm 0.7\%$ and $V_{or} = -11.0 \pm 0.7$eV at $\Theta = 10^{o}$, $\phi = 109^{o}$

As a final step, results from each potential need averaging over the two angles of incidence. This could be done by a direct superposition of the individual contour plots, after weighting them according to the appropriate energy range. This would be equivalent to the approach of ZJ. However, at this stage the overall results for Rh(111) can be gauged just as objectively by taking an energy-weighted mean of parameter values given for each angle of incidence. With the appropriate rounding of significant figures this yields a final result:

(i) from V_{Rh}^{WJM} $\Delta d\% = -2 \pm 2\%$ and $V_{or} = -18 \pm 1$eV

(ii) from V_{Rh13} $\Delta d\% = 0 \pm 2\%$ and $V_{or} = -11 \pm 1$eV

The final uncertainties quoted here appear to encompass the effects of small errors of an experimental nature, including minor differences in I(E) curves from independent measurements and errors in setting the angle of incidence.

The results from the V_{Rh}^{WJM} potential clearly indicate the necessity for including more than one angle of incidence in surface structural determinations; whether two angles of incidence necessarily provides sufficient data is still perhaps debatable. The reliability-index approach in this case does not allow a statement to the effect that one potential is right and the other is wrong. Within the present calculational scheme

both potentials describe the experimental data equally well, although some clarification of their relative merits may become apparent if further refinements are made e.g. including the energy dependence of V_{or} and better descriptions of the atomic vibrations in the calculations. This work does show that special care is needed when there are dominant features in I(E) curves at the beginning (or end) of the energy range considered.

The zero or small contraction found here for the Rh(111) surface is typical of the values found for other (111) faces of face-centred cubic metals. As was listed in Section 5.5 the (111) surfaces of Ag,Al,Co,Ir and Ni all show small to zero contractions while the work presented earlier on Cu(111) in Section 5.3 indicates a somewhat larger contraction of about 5%. As yet Pt remains the only FCC metal thought to show a dilation of its (111) surface, though the modification is of small proportions.

CHAPTER 7

THE Rh(100) SURFACE

The (100) surfaces of the transition metals have been intensely studied for their chemisorption properties [14] and for the fact that the most stable (100) surfaces of Pt, Ir and Au are reconstructed [25,26,33] at room temperature. As discussed in Section 2.2, these reconstructions of FCC metals are thought to essentially involve a hexagonal surface layer superimposed on the bulk (100) substrate.

Aside from the present work, the only other LEED studies of Rh(100) are those of Tucker [16,17] and of Castner et al [18], both concerned mainly with chemisorption properties, and neither of which reported any I(E) data. Tucker's results suffered from the lack of a surface composition monitor, but both sets of authors reported a (1x1) pattern for the clean surface. A stable reconstructed Rh(100) surface therefore appears unlikely; if such a reconstruction should occur, it would have to preserve the symmetry of the surface. Two possible reconstructions that fulfill this criterion by simple registry shifts of the surface layer are shown in Fig. 7.1. The normal bulk stacking sequence requires the surface atoms to occupy the A sites. Two other possible registries are with the top-layer atoms on the on-top C sites or on the bridge sites B.

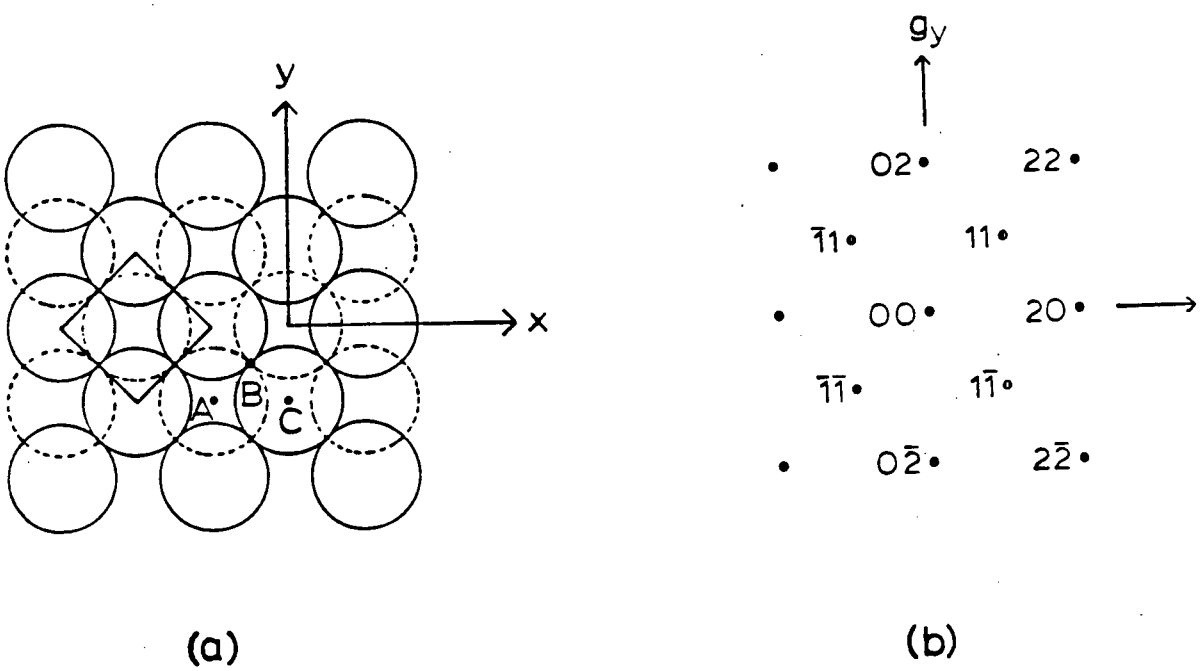

Figure 7.1 Schematic diagram of the Rh(100) surface (a) and the corresponding LEED pattern (b) in the notation of Jona [128]. The unit mesh is marked in (a). The complete circles are for atoms in the second layer, and the dashed circles correspond to a topmost layer with the registry belonging to the bulk i.e. atoms in the top layer are above the 4-fold sites such as A. Other registries considered are where atoms are over the 2-fold site (like B), or directly over atoms in the layer below (as for C).

7.1 Experimental

The first experiments were carried out on the same single crystal as used by Tucker [16,17]. The (100) slice was found, however, to be misoriented by some 4°, so the slice was carefully repolished to the correct (100) orientation.

Tucker reported sharp LEED patterns on heating to 1600K. In the present work with this crystal, Auger electron spectroscopy showed that prolonged heating at 1300K, the temperature limit of the heater used in this case, caused appreciable amounts of C and Si to accumulate on the surface as shown in Fig. 7.2(a). The Si could be removed by argon ion bombardment (500 eV, about 5 microamps/cm^2) for 10 minutes, Fig. 7.2(b). Annealing at 1000K in vacuum, or slightly lower temperatures in oxygen, reduced the C Auger signal to below the detectable limit, Fig. 7.2(b). However, depending upon the precise time and temperature of annealing, Si was sometimes found to reappear on the surface.

It was found that a sharp (1x1) LEED pattern, with low background intensity and minimal contamination as indicated by Auger electron spectroscopy, could be obtained from several cycles of argon ion bombardment and heat treatment in oxygen followed by a final annealing for a few minutes at 900K in vacuum. Heating at or below 600K in hydrogen (1×10^{-7} Torr) was found to be useful for removing any residual oxygen during the final stages of cleaning.

On several occasions during the cleaning and ordering procedures, faint fractional-order diffraction spots were found

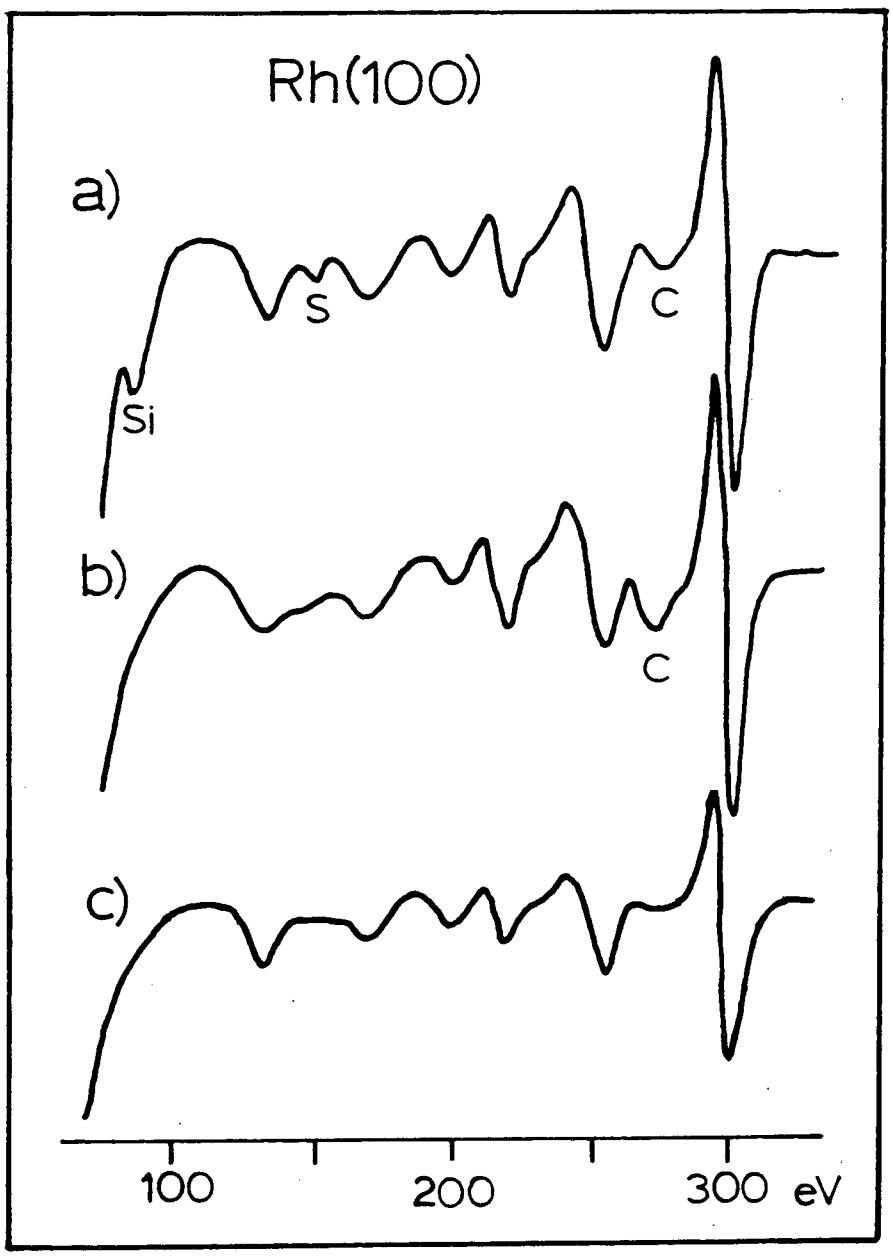

Figure 7.2 Auger spectra of Rh(100) surfaces for a .5KeV, 10 microamp beam:

a) surface after prolonged heating at 1300K showing substantial Si and C impurities

b) after argon ion-bombardment, showing reduced Si and increased carbon

c) clean surface spectrum after heating at 1000K in vacuo.

for limited energy ranges; this LEED pattern corresponded to a two-domain (3x1) surface structure (see Fig. 7.3). However, Auger electron spectroscopy indicated that this pattern was not simply due to a reconstructed top metal layer but rather was associated with the presence of Si impurity (Auger peak at 92eV) which had segregated to and ordered on the surface. It would be interesting to know the actual surface structure involved; a coincidence site superposition, perhaps involving a rhodium silicide layer, may seem more plausible than a 1/3 monolayer coverage of atomic Si.

Later experiments using slices cut from a crystal from a different source, see Table 4.2, failed to duplicate this (3x1) pattern. Auger electron spectroscopy did not reveal any Si impurity; hence the occurence of this (3 x 1) pattern does in fact seem to be associated with the presence of Si on the surface. When this second crystal was cleaned by the method described earlier, a surface exhibiting a sharp (1x1) LEED pattern and a "clean" Auger spectrum similar to those of the clean Rh(111) surface, Fig. 6.1(d), was obtained. For both crystals, it was noticeable that the low energy features at 170 eV and 139 eV were relatively intense for the (100) face compared with those from the (111) faces, see Fig. 6.1(d) and 7.2 (c).

A typical LEED pattern and the beam labelling scheme is depicted in Fig. 7.4. I(E) curves were measured at normal incidence and for $\theta=9^{0}$, $\phi=20^{0}$, in the angle convention of Jona [128]. The integrated beam intensities, normalized to unit incident current and corrected for background intensity, were

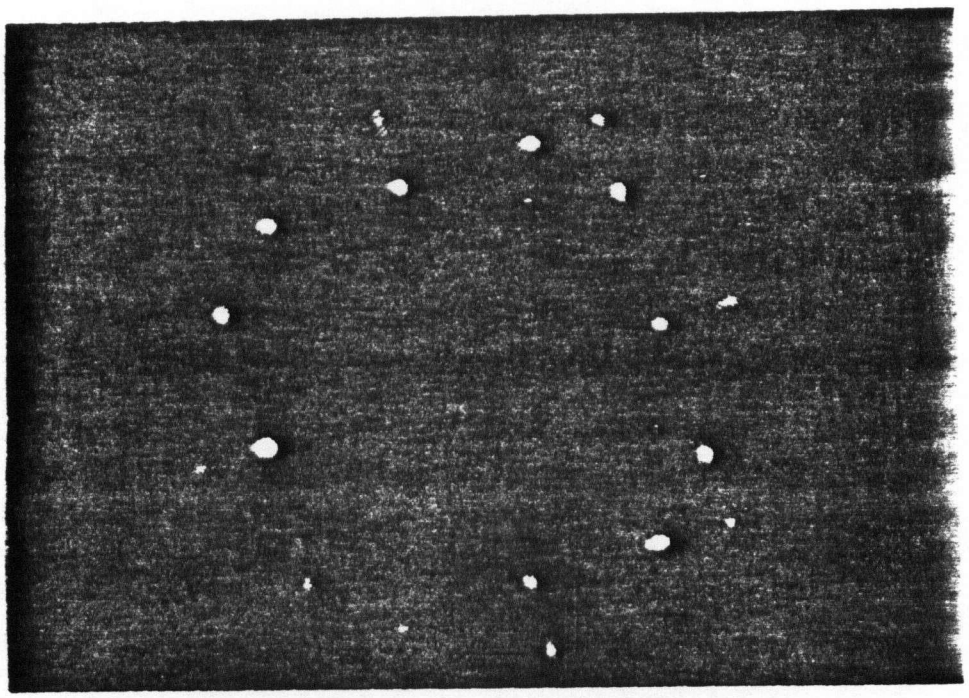

Figure 7.3 Two-domain (3X1) LEED pattern from the Rh(100) surface at 100eV, thought to be due tc the presence of silicon

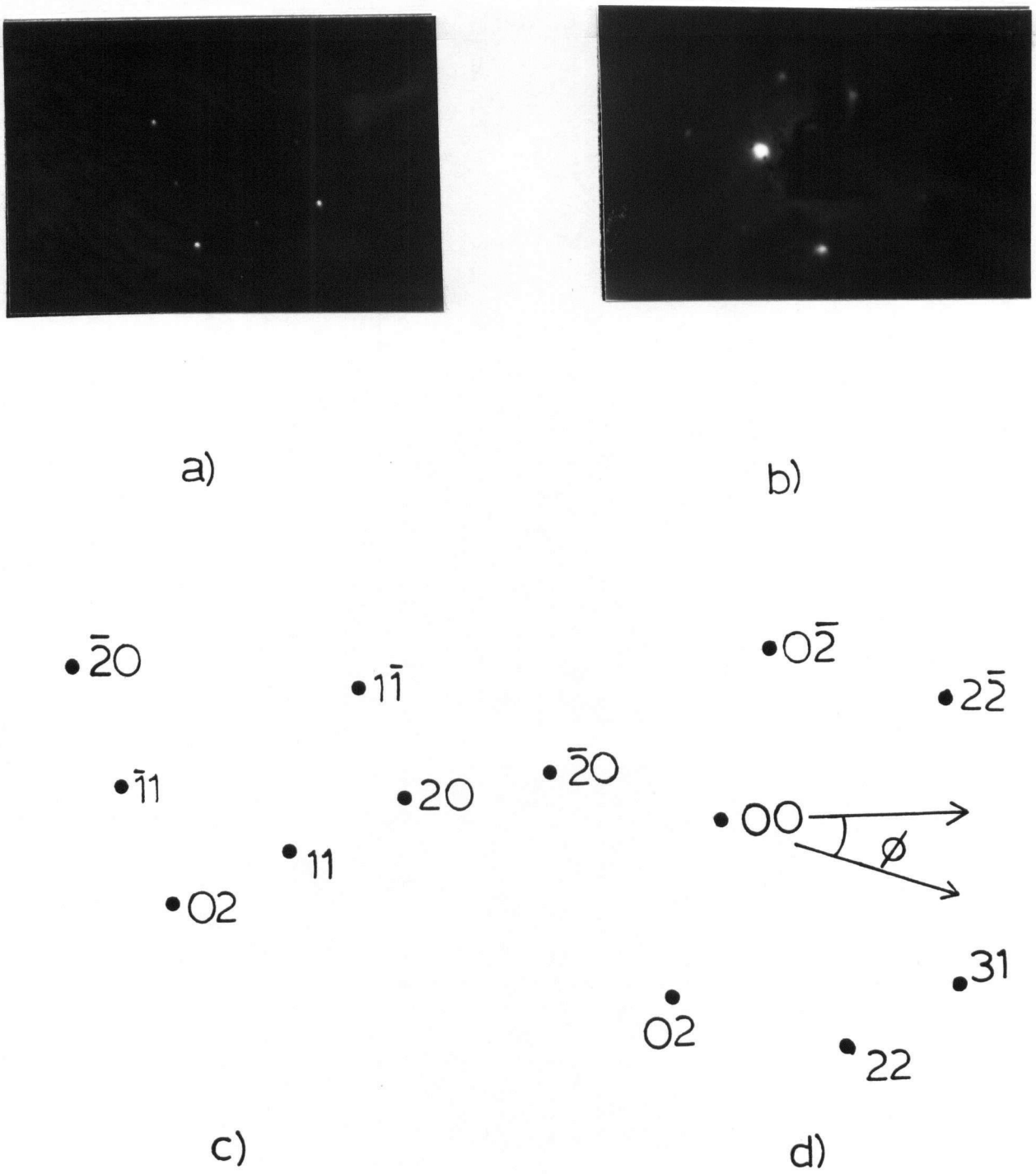

Figure 7.4 LEED patterns from the clean Rh(100) surface for (a) normal incidence (150eV), (b) for $\theta = 9°$, $\phi = 20°$ (94eV) and the beam labelling scheme (c) and (d).

stored on digital cassette prior to transfer to an IBM 370/168 computer for the reliability-index calculations. The experimental data are collected in Appendices A7-A9.

Experimental I(E) curves for beams that should be equivalent by symmetry at normal incidence were averaged, although the differences were small. The I(E) curves measured for the (11) set of beams, which should be equivalent at normal incidence, are shown in the upper half of Fig. 7.5; the same peak positions and overall intensity variation is observed for the (11), $(\bar{1}1)$ and $(1\bar{1})$ beams. Similarly, the (20), (02) and $(0\bar{2})$ beams have almost identical profiles. Small variations in the relative peak intensities for beams in the {11} set were always present in independent experiments at normal incidence, whilst the agreement between individual beams in the {20}, {22} and other beam sets was in general slightly better. Such variations have to be attributed to experimental errors (involving such factors as uneven response of the screen, imperfections in the crystal surface, and uncertainties in setting the angle of incidence), and they limit the level of agreement to be expected between calculation and experiment.

I(E) curves for all beams were smoothed by two operations of a three-point smoothing filter prior to the reliability-index calculations. To avoid spurious results in these calculations, background and scatter in the experimental data were eliminated.

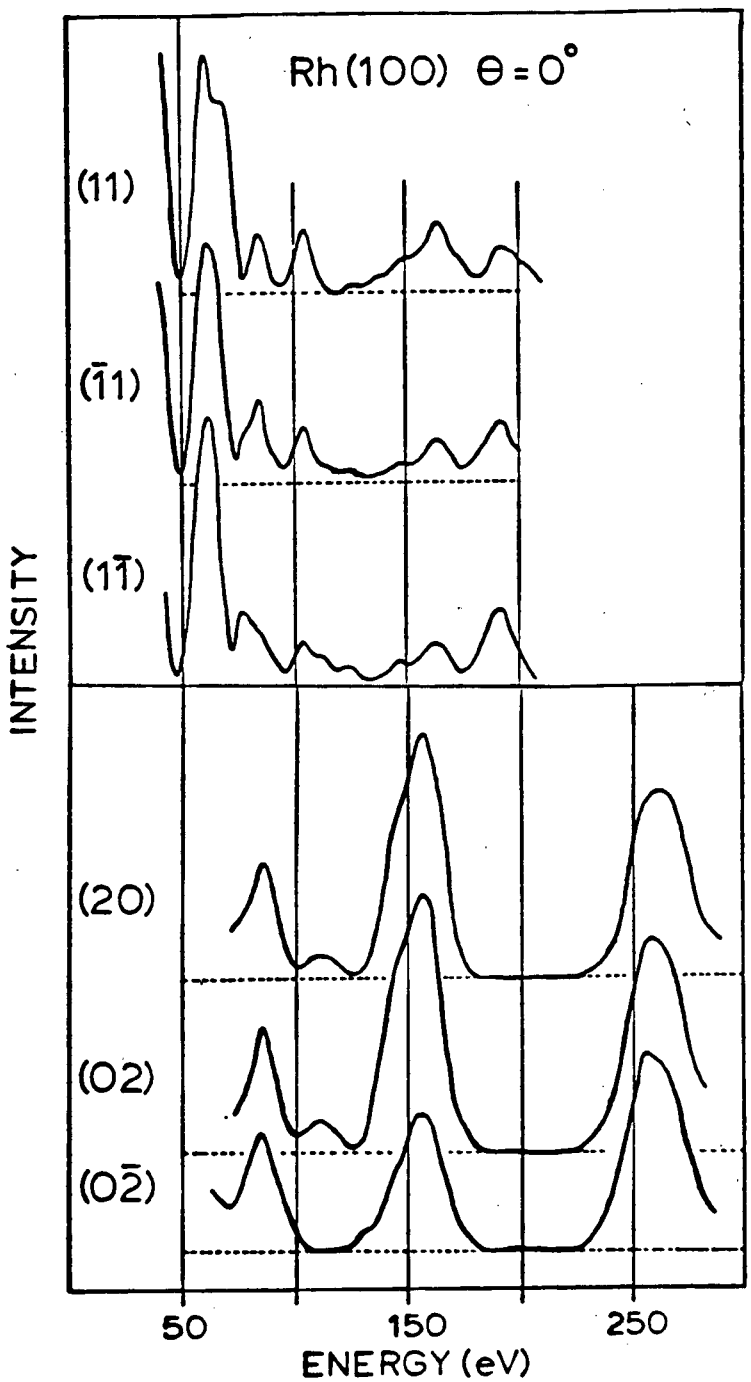

Figure 7.5 I(E) curves for two sets of beams that should be equivalent at normal incidence on the Rh(100) surface; the fourth member of each set is obscured by the sample manipulator.

7.2 Calculations

The calculations were performed as detailed in Chapters 3 and 5, for the two alternative registries shown in Fig. 7.1 as well as for a truncated bulk crystal; the topmost layer spacings ranged from a -10 to +10% change from the bulk value of 1.9022Å, in steps of 2.5% or 0.0475Å. Both the band structure potential V_{Rh}^{WJM} and the superposition potential V_{Rh13} were used with a total of 69 beams being available to determine the layer diffraction matrices for an energy range of 40-300eV.

7.3 Results And Discussion

Fig. 7.6 compares experimental I(E) curves at normal incidence for the (11) and (20) beams with those calculated for the different registries using the V_{Rh13} potential; In these calculations the top interlayer spacings are fixed by the hard-sphere model for atomic radii determined by the bulk structure of rhodium [62,63]. It is concluded from Fig. 7.6 that the theoretical curves for registries B and C do not agree as well as those for the bulk stacking sequence (registry A), although the level of agreement for the latter is by no means ideal. Consideration of other diffracted beams and other topmost interlayer spacings further preclude the registries B and C; it seems that the surface structure of Rh(100) is interpreted best by an unreconstructed packing sequence for the top layer.

Fig. 7.7 shows I(E) curves measured for six beams diffracted from the Rh(100) surface, together with curves calculated for an unreconstructed surface using both potentials,

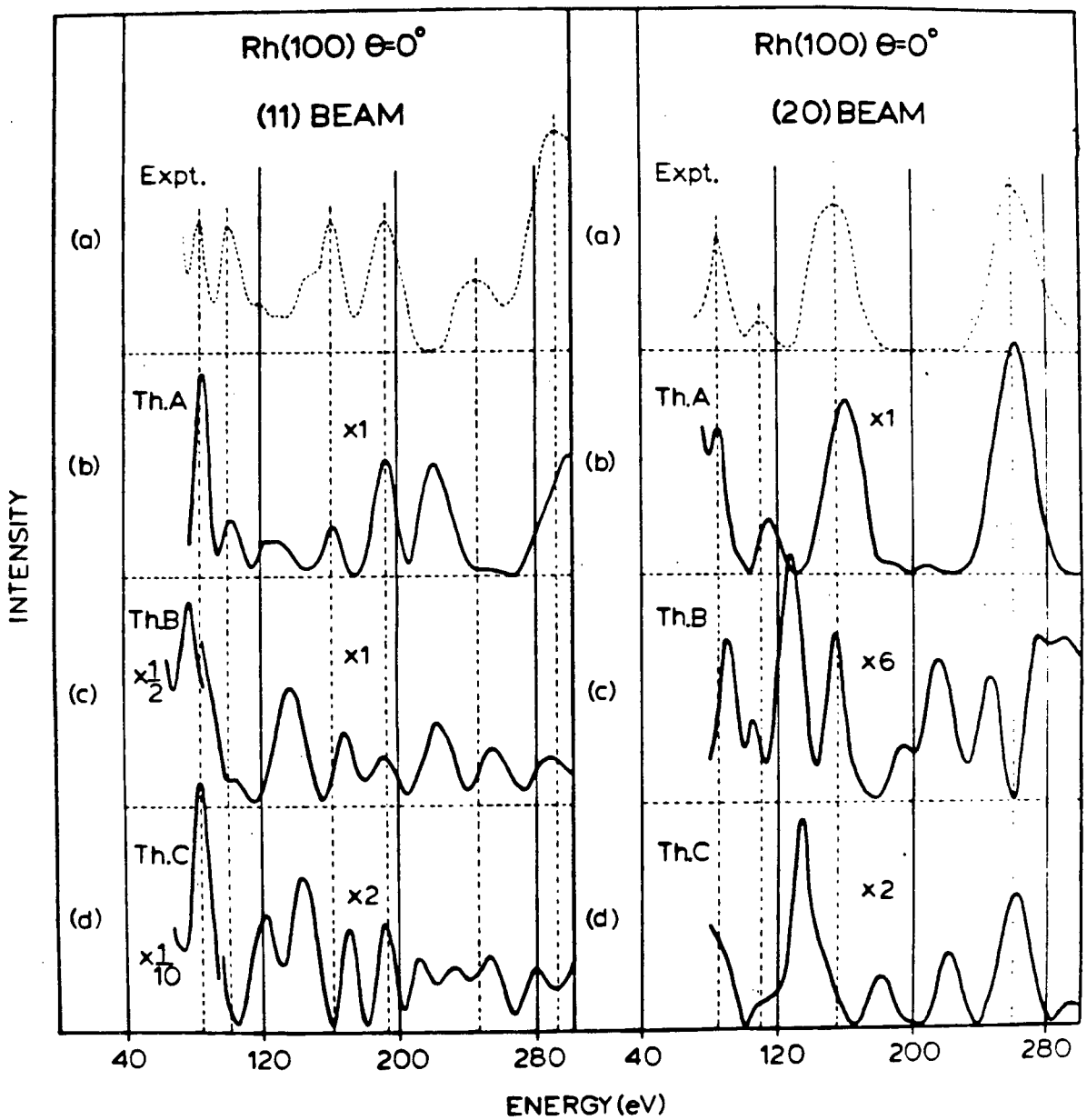

Figure 7.6 Comparison of experimental I(E) curves for the (11) and (20) beams at normal incidence on Rh(100) with calculations, for the V_{phs} potential, for the topmost registries defined by A, B and C in Fig. 7.1. The topmost interlayer spacings are 1.90, 2.33 and 2.69Å for the 4-fold, 2-fold and 1-fold sites respectively.

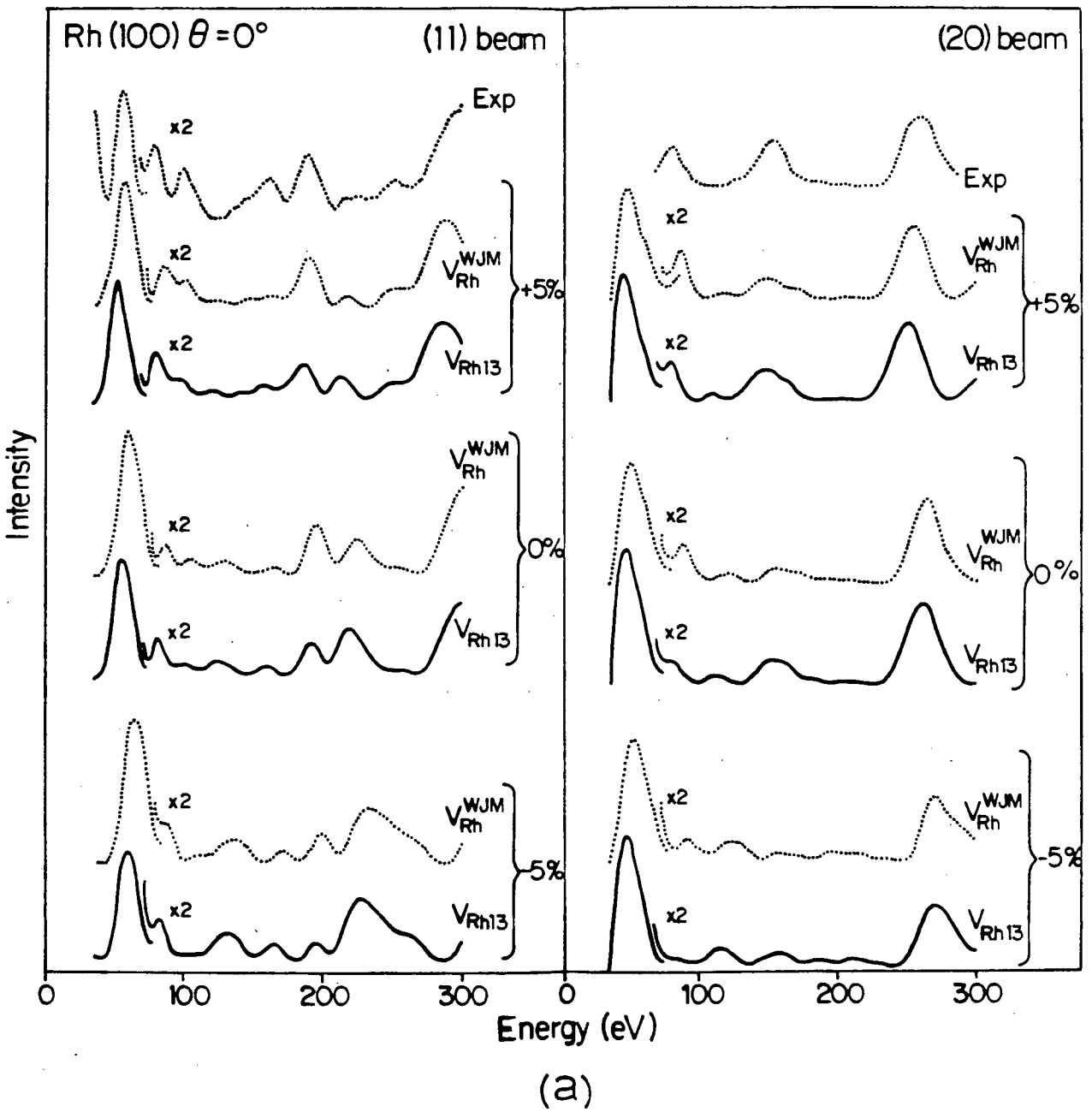

Figure 7.7 Comparison of some experimental I(E) curves for Rh(100) with calculations for the V_{Rh}^{WJM} and V_{Rh13} potentials. V_{or} = -12eV and $\Delta d\%$ = -5, 0 and +5% for (a) normal incidence and (b) at $\theta = 9^{o}$, $\phi = 20^{o}$.

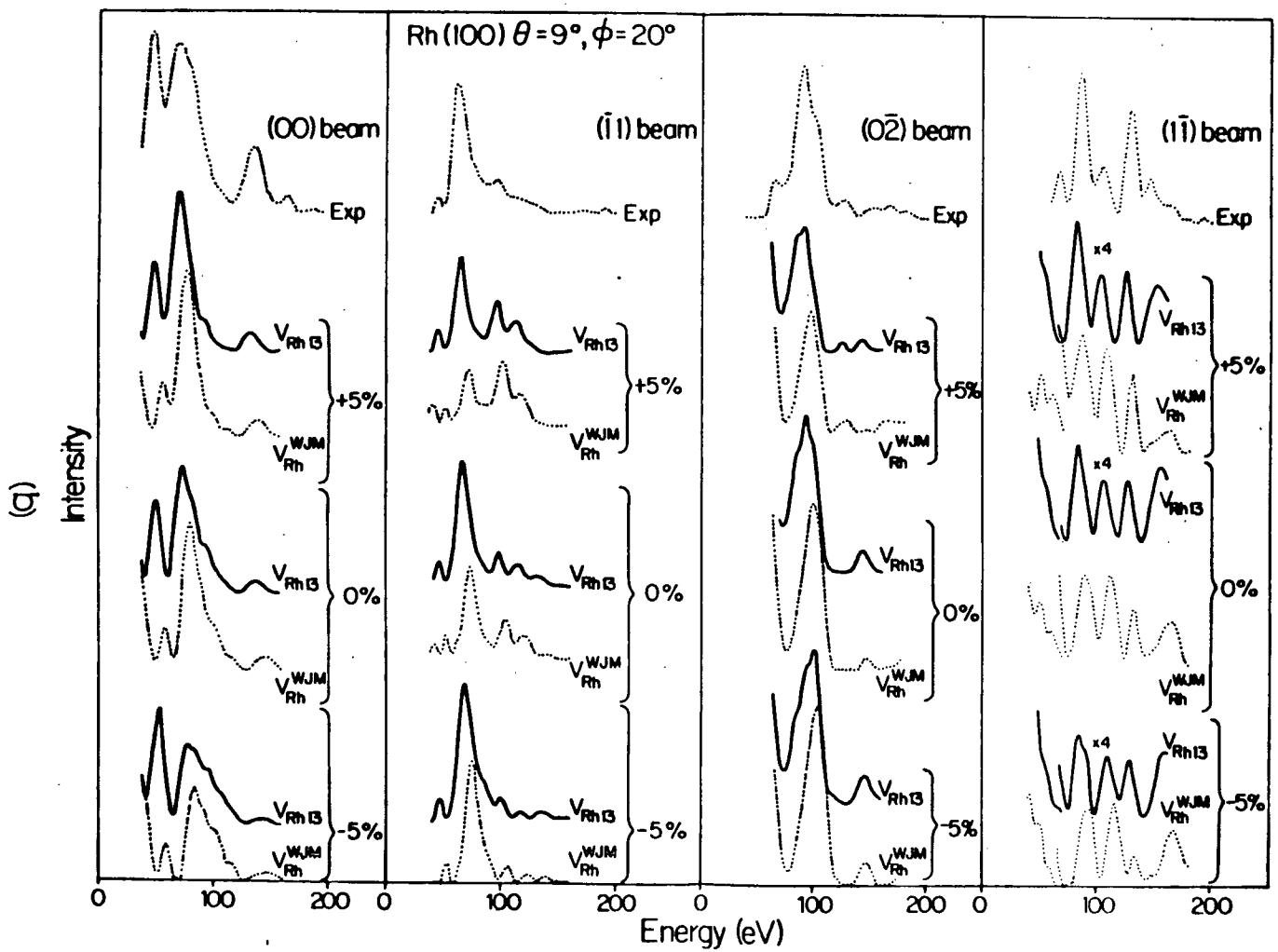
Rh(100) θ=9°, φ=20°
(00) beam
(ī1) beam
(0$\bar{2}$) beam
(1$\bar{1}$) beam
Exp
$V_{Rh\,13}$
V_{Rh}^{WJM}
+5%
0%
-5%
x4
Intensity
(a)
0
100
200
Energy (eV)

for $\Delta d\%=-5\%$, 0 and -5%. For each beam and spacing, the two sets of calculated curves are closely similar apart from a slight shift to higher energy for V_{Rh}^{WJM} relative to V_{Rh13}.

Otherwise the differences noted earlier in the behaviour of the phase shifts do not appear to have much visual effect on the calculated I(E) curves. The observed shift relates to the difference in potential at the radius of the muffin-tin spheres of about 6eV, as mentioned in Chapter 6, and assuming this provides the main difference in the potentials, the two sets of calculated I(E) curves would show peaks at the same energies if the real parts of the inner potential (i.e. V_{or}) are taken as -12eV for V_{Rh13} and -18eV for V_{Rh}^{WJM}. To a good approximation, making V_{or} more negative causes a rigid shift in the calculated I(E) curves to lower energy.

With these values of V_{or}, the agreement with experiment may be estimated by visual comparison to vary from very good for some beams (e.g. (11) beam at normal incidence, $\Delta d\%=-5\%$) to quite poor for others (e.g. (11) beam at $\Theta=9°$, $\phi=20°$, $\Delta d\%=-5\%$). A visual estimation of the overall degree of fit cannot distinguish between the two potentials, but it suggests that d% has a value betweem 0 and +5%. This estimate is included in Table 7.1.

The results of a reliability-index analysis for the total of 16 beams analysed at the two angles of incidence are tabulated in Table 7.1 and shown as contour plots in Fig. 7.8 for both potentials. Once again we notice a pronounced "valley of best fit" as noted in Chapter 6 for the (111) face. The precautions noted there concerning strong features at the

	Extent of Comparison				Conditions of best agreement		
Pot.	θ_D	n	E(eV)	Analysis	$\Delta d\%$	V_{or}	R-
V_{Rh13}	402	16	1548	R-factor	+2.5±0.9	-11.5±0.7	0.155
				visual	+2.5±2.5	-12 ±2	
V_{Rh}^{WJM}	402	16	1684	R-factor	-1.8±1.0	-19.6±0.8	0.167
				visual	+2.5±2.5	-17 ±2	
V_{Rh13}	250	16	1786	R-factor	+2.7±1.0	-11.0±0.9	0.188

Table 7.1 Summary of structural determination of the Rh(100) surface.

beginning or end of I(E) curves were taken into account.

Despite the similar degree of visual agreement between the experimental data and both sets of calculated curves, the contour plots exhibit minima at somewhat different values of $\Delta d\%$ and V_{or} (Table 7.1). From the discussion above, a 6eV shift in V_{or} is expected because of differences in potential at the edge of the muffin-tin sphere; the observed difference is 8eV, the extra 2eV presumably reflecting further differences in the potentials. The values of the surface relaxation predicted by the two potentials are outside the 68% confidence limits (1 standard error), although they are within 95% confidence limits (2 standard errors). The minimum value of R is slightly lower for V_{Rh13} (0.155) than for V_{Rh}^{WJM} (0.167).

As an experimental value of the surface Debye temperature (θ_D) was not available for rhodium, a further calculation using the potential V_{Rh13} was performed with θ_D=250K. The best fit values of $\Delta d\%$ and V_{or} have been changed only slightly (Table 7.1) although R has increased to 0.188 from 0.155 for θ_D=402K. All values of R quoted in Table 7.1 are below 0.20,

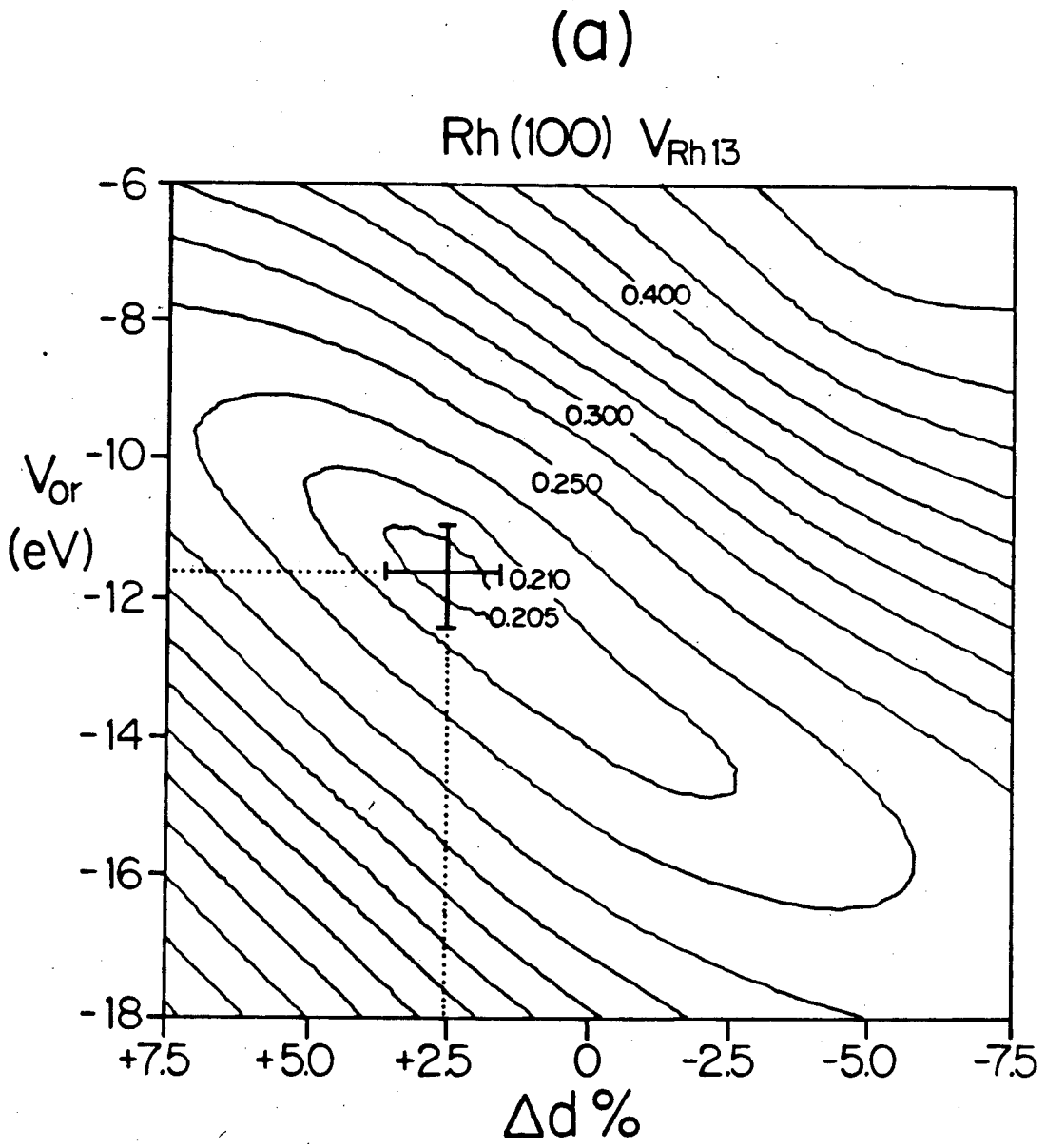

Figure 7.8 Contour plots for Rh(100) of $\bar{r}_f$ versus V_{or} and $\Delta d\%$ for (a) the V_{Rh13} and (b) the V_{Rh}^{WJM} potential. Error bars are the standard errors and defined in Chapter 5.

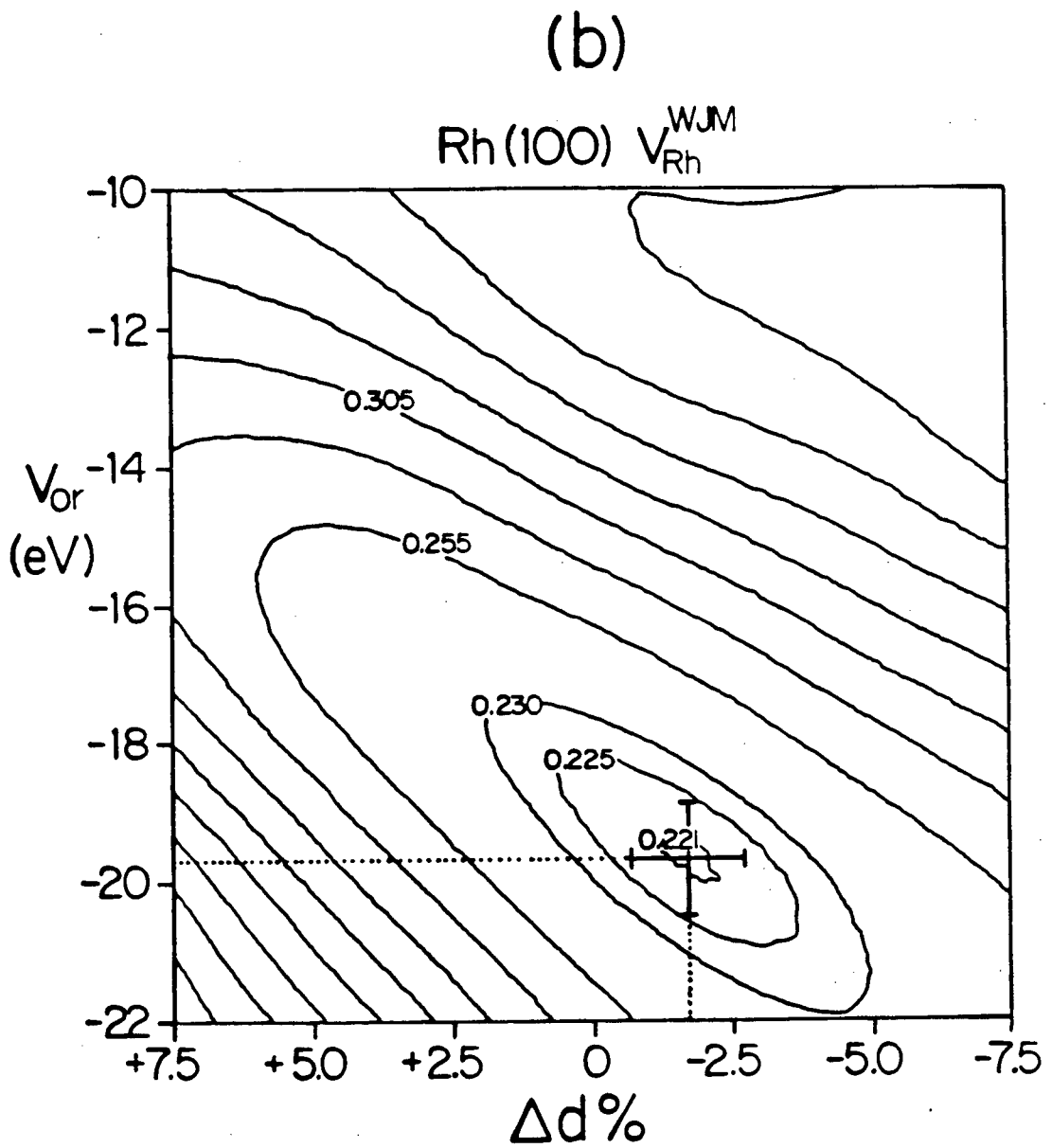
(b)
Rh(100) V_{Rh}^{WJM}
-10
-12
-14
-16
-18
-20
-22
V_{or}
(eV)
0.305
0.255
0.230
0.225
0.221
+7.5
+5.0
+2.5
0
-2.5
-5.0
-7.5
Δd%

and are therefore within the range for which Zanazzi and Jona proposed a structure is "very probable". The analysis here puts such considerations on a more quantitative basis. Further studies with contour plots for registries that are incorrect, on the basis of visual analysis, give high values of R at local minima as well as large uncertainties as measured by ϵ_d and ϵ_v.

Comparison of the determinations of $\Delta d\%$ from the two potentials, with both the visual and reliability-index analyses, as well as the slightly higher R value for the V_{Rh}^{WJM} potential, make it tempting to label the V_{Rh13} potential as the "better" potential and therefore to quote a more definite d% value. Unfortunately at present it is not possible to assess the full significance of the different values of R for the two potentials. Careful examination of the data did not produce any anomalies of the sort noted for the (111) surface where a relatively minor feature in an I(E) curve significantly interfered with the comparison between experiment and theory. Nevertheless that experience suggests caution in attaching uncertainties at this stage of LEED crystallography; we therefore believe that the value of $\Delta d\%$ for Rh(100) must be quoted as 0±2.5%.

7.4 Comparisons With Previous Studies

The bibliography of Section 5.5 shows that none of the (100) faces of face-centred cubic metals studied up till now show any substantial contraction or dilation. Thus far, no other reliability-index calculations have been performed for (100) surfaces although Fourier transform [99] and data averaging [114] analyses on data from Cu(100) claim low error margins with results of a surface contraction of 0±1%. As the results from the two potentials used here appear equally probable, we can see that the result of $\Delta d\% = 0 \pm 2.5\%$ is consistent with the conclusions reached for other FCC (100) surfaces.

CHAPTER 8

THE RH(110) SURFACE

The (110) surfaces of several FCC metals have been studied by LEED; the bibliography of Section 5.5 indicates that these surfaces often exhibit contractions for the surface layer of up to 10% from the bulk value. Studies of the Rh(110) surface appear to be confined to the early oxygen adsorption experiments of Tucker [16], a short infrared study of CO adsorption on (110) oriented Rh films [132] and, most recently, a detailed study of CO adsorption on the single crystal surface by Marbrow and Lambert [133]. In this latter work the authors found that the clean Rh(110) surface showed a simple (1x1) LEED pattern and hence was unlikely to be laterally reconstructed. A diagram of an ideal (110) surface is shown in Fig. 8.1, together with the associated LEED pattern. This surface possesses only a two-fold symmetry axis with 2 mirror planes and is relatively open compared with the (111) or (100) surfaces. The bulk interplanar spacing is correspondingly short, and this may account in part for the seemingly large contractions reported for the Ag(110) and Al(110) surfaces; thus the absolute contractions may be similar to those found on the less open surfaces but the shorter bulk interlayer distances lead to larger percentage changes.

A recurring question in the LEED studies of the (110) surfaces of Al and Ag involves the role of surface roughness. For Al [101,108,110-112] and Ag [101,106-107] only modest agreement between experimental and theoretical I(E) curves has been obtained. The discrepancies have been attributed to surface roughness, as evidenced by poor contrast in the LEED patterns in some cases, but a simple attempt to include roughness in the multiple-scattering calculations did not

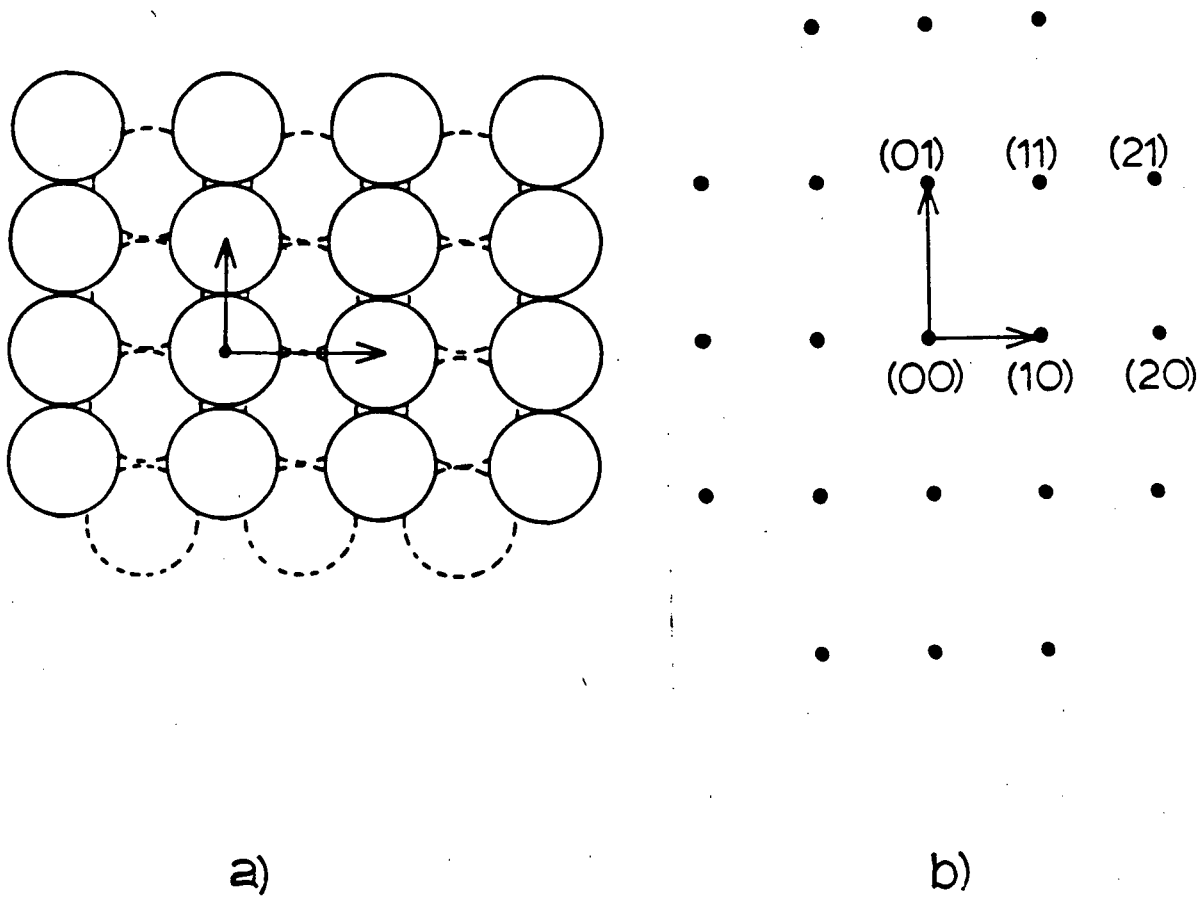

Figure 8.1 Diagram of a) a (110) surface and b) the associated LEED pattern.

substantially improve the agreement with experiment [108]. Most recently a UPS/XPS study [134] has shown that the angular dependence of photoemission from the clean Ag(110)-(1x1) surface is markedly altered by the nature of the crystal polishing. However, both chemically and non-chemically polished specimens gave apparently identical LEED patterns; unfortunately no I(E) curves were measured. The authors suggest that chemical cleaning does in fact produce a "smoother" surface and that incomplete removal of the disordered material induced by mechanical polishing may be responsible for some of the difficulties experienced in obtaining good agreement between experimental and theoretical LEED data.

8.1 Experimental

Experiments were performed on a single crystal slice cut from a rod purchased from Research Organic/Inorganic Chemicals Corporation. The initial heat treatments produced the Auger spectrum of Fig. 8.2(a). Peaks due to small amounts of C(272eV) and S(152eV) can be seen in addition to the main Rh peaks. A small peak at about 116eV is assigned to phosphorus; this element is usually found at 120eV but no other common contaminants have an Auger peak in this region. Rhodium does not have a calculated transition near this energy [49] and the peak is not apparent in the clean surface spectrum, Fig. 8.2(c).

Once again no trace of a boron peak at 180eV could be detected. This is in marked contrast to the results of Marbrow and Lambert [133] who obtained B signals almost as strong as the

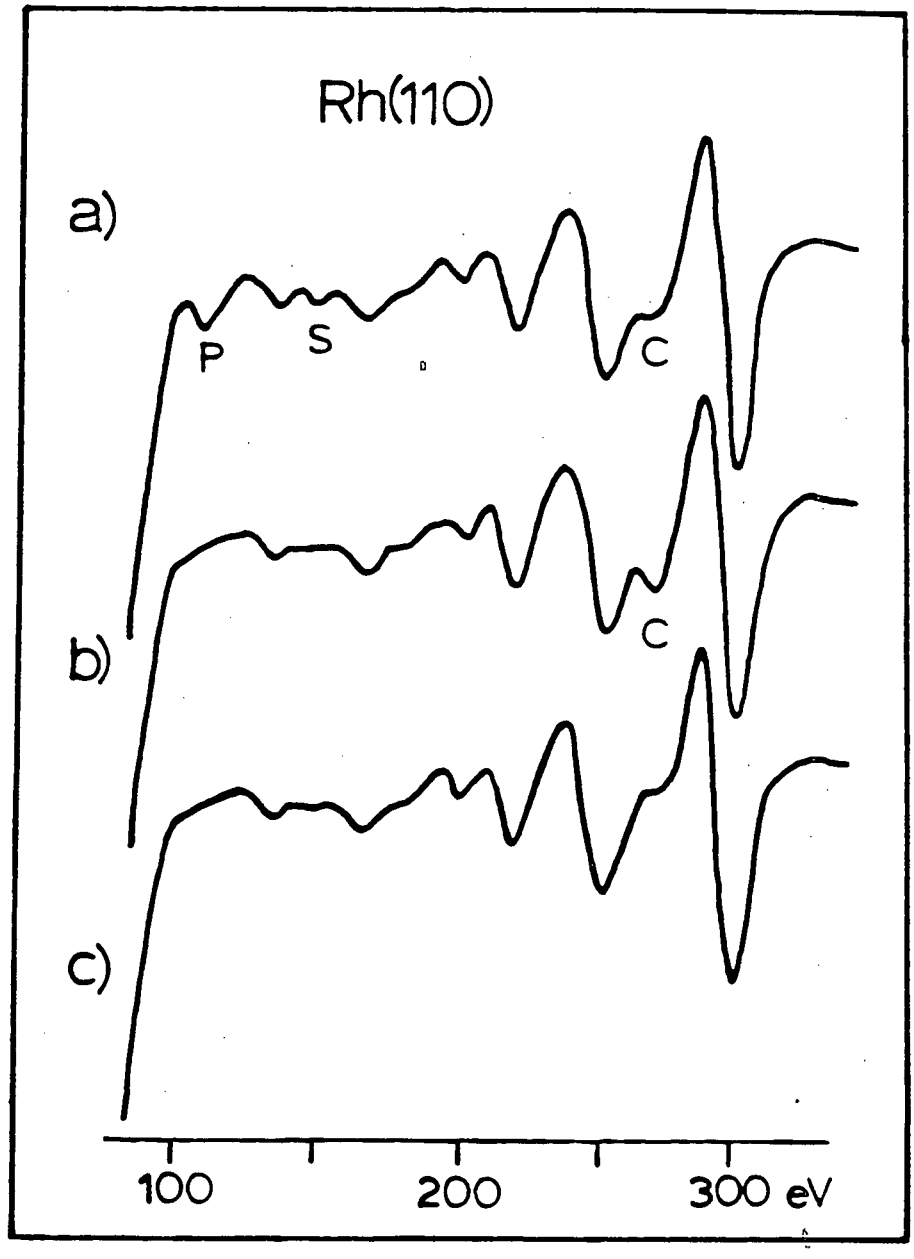

Figure 8.2 Auger spectra of the Rh(110) surface at a primary beam voltage of 1.5KeV and 10 microamp current:
a) after initial heat treatments showing S(152eV), P(120eV) and C(272eV) contamination on the surface
b) after argon ion-bombardment; P and S removed but C increased
c) clean surface spectrum.

main Rh peak at 302eV upon heating to 1300K. It can only be concluded again that these contrasting observations must originate in differences in manufacture or polishing procedures.

The S and P contaminants could be removed from the surface by argon-ion bombardment (1keV at 5 microamps for 20 minutes) but again only at the expense of increasing the surface concentration of C as shown in the Auger spectrum of Fig. 8.2(b). However, this surface carbon diffused back into the bulk on heating at 1000K. After several cycles of ion-bombardment and annealing an apparently clean surface was obtained having the Auger spectrum of Fig. 8.2(c) with a sharp (1x1) LEED pattern. The Auger spectrum of the clean surface is roughly intermediate in appearance between that of Rh(100) (Fig. 7.2) and that of Rh(111), Fig. 6.1. The major peaks remain very similar in all three cases. The minor peaks at 139 and 170eV appear to increase in relative intensity as (111)<(110)<(100).

A typical LEED pattern and the labelling scheme is shown in Fig. 8.3 for Rh(110). Intensity data were recorded for the range 50 to 250eV for two directions of incidence defined by $\theta=0°$, and $\theta=10°, \phi=135°$ in the angle convention of Jona [128]. I(E) curves that should be equivalent by symmetry at normal incidence were averaged prior to smoothing. Equivalent members of the {11} and {21} beam sets are depicted in Fig. 8.4. The similarity of each member of an equivalent set to the other members of that set is not as satisfactory as that typically found for the (111) and (100) surfaces. This may perhaps be associated with some degree of surface roughness of this (110)

a)

b)

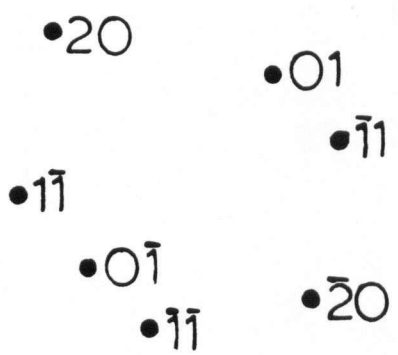

c)

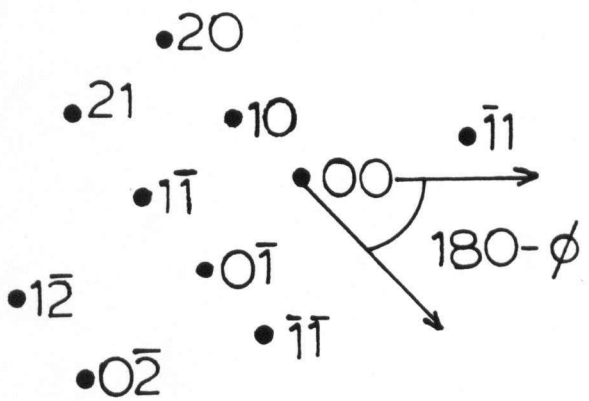

d)

Figure 8.3 LEED pattern from the clean Rh(110) surface at (a) normal incidence (88eV) and (b) $\theta = 10°$, $\phi = 135°$ (90eV). The beam labelling scheme is shown in (c) and (d).

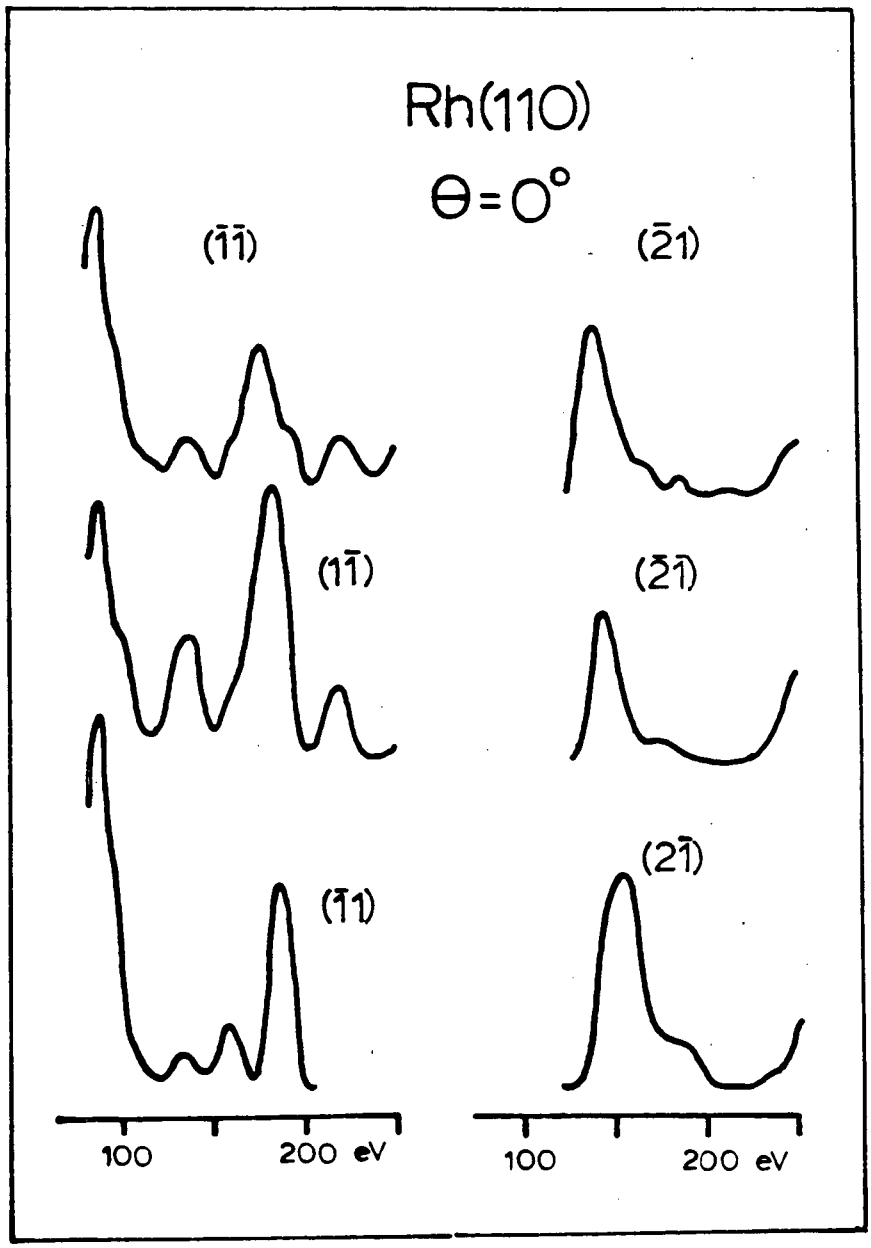

Figure 8.4 Experimental I(E) curves for the Rh(110) surface at normal incidence for the 4-fold equivalent {11} and {21} beam sets. The 4th member of each set is obscured by the sample manipulator.

surface. Two complete sets of independent experiments were performed for each angle of incidence, and the intensity data is gathered together in Appendices A10-A13, where the good agreement between the two sets can be seen.

8.2 Calculations

Due to the low symmetry of the (110) surface multiple-scattering calculations are relatively slow and costly. Hence it is desirable in this case to limit computational effort by taking note of several lessons learnt during the studies of the (111) and (100) surfaces. Firstly, different top-layer registries that preserve the symmetry of the surface, and hence a (1x1) LEED pattern, do in fact give clearly distinguishable calculated I(E) curves. It seems reasonable therefore that if the I(E) curves for a laterally unreconstructed surface are a good match to the experimental data then it is very unlikely that another registry will produce theoretical I(E) curves with a better fit. For Rh(110) the surface was initially assumed to have the registry of the appropriate bulk layer and calculations with alternative registry were deferred until the fit of the bulk stacking calculations with experiment had been assessed.

Secondly, the experience of the (111) and (100) surfaces reveals that neither the V_{Rh13} superposition potential nor the band structure potential V_{Rh}^{WJM} could be judged to be a more suitable potential for LEED; both gave essentially identical degrees of agreement of theory with experiment. As discussed previously, they did differ however in the inner potential

needed and in the value of surface contraction suggested.

Thirdly it appears that results derived from different directions of incidence can vary at least as much as results for the same angles but with a different potential.

Taking these points together, diffracted beam intensities were calculated using both the renormalised forward scattering and layer doubling formalisms for only the superposition potential V_{Rh13} as the use of the second potential seems unlikely to be very helpful at this stage. The same non-structural parameters used for the (111) and (100) surfaces were taken, and calculations were made assuming a truncated bulk structure for which the surface spacing was allowed to vary from a 15% contraction to a 5% expansion from the bulk value (1.345Å) in steps of 2.5%.

8.3 Results And Discussion

Sets of experimental and calculated I(E) curves are compared in Fig. 8.5 for the (11) beam at normal incidence and for the (00) beam at $\theta = 10°$, $\phi = 135°$. A visual comparison indicates a better fit for the (11) beam; values of the reliability indices for individual beams, $(r_r)_i$, are also given in Fig. 8.5. These values seem consistent with visual evaluations, especially for the (11) beam. The (00) beam at off-normal incidence is judged by the $(r_r)_i$ values to show a relatively poor fit, presumably because structure in the calculated I(E) curves between 50 and 100eV is not reproduced in the experimental data.

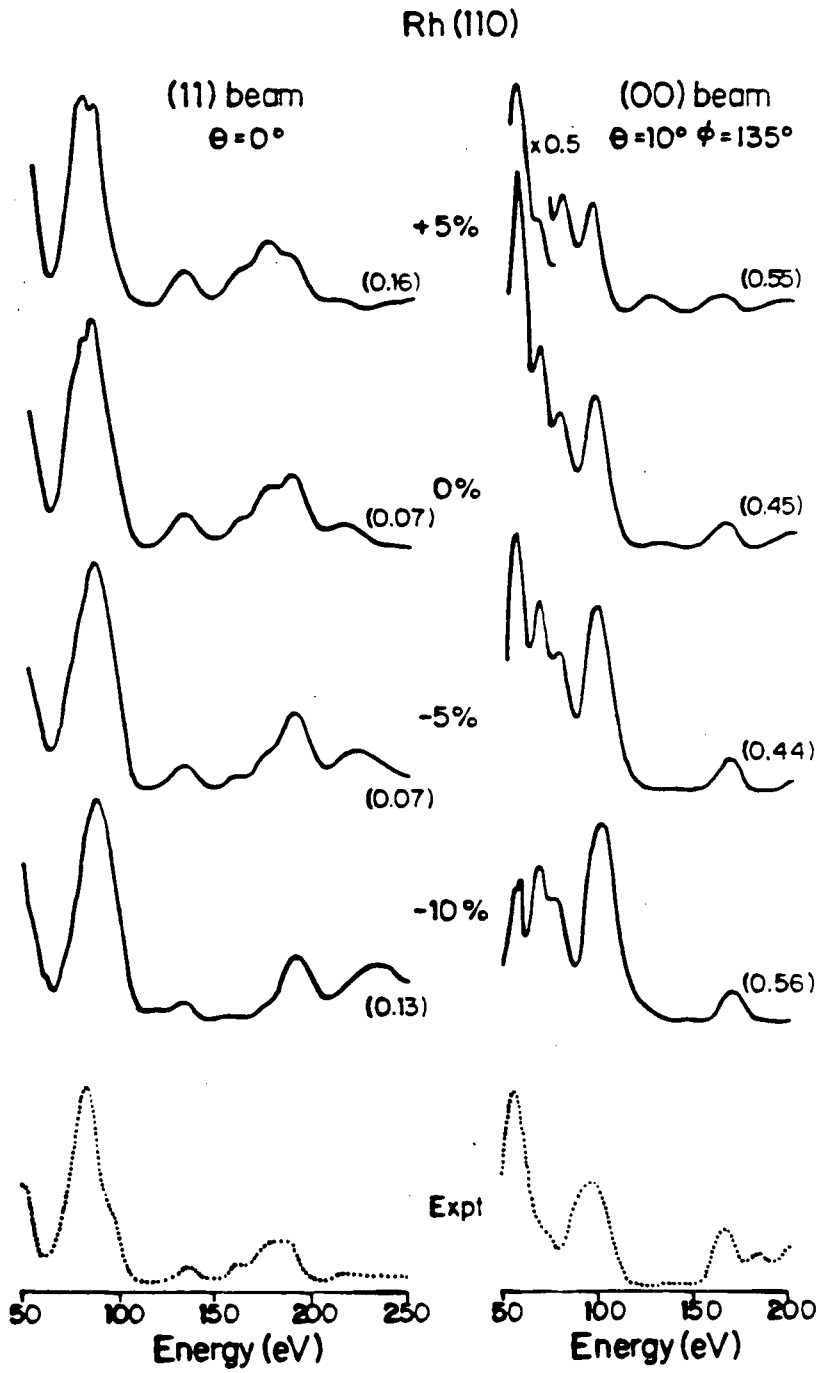

Figure 8.5 Comparisons of two experimental I(E) curves for the Rh(110) surface with calculations, using the V_{Rh13} potential for four values of $\Delta d\%$. The value of the individual beam reliability-index (r_p)$_i$ is given in brackets for each calculated curve.

Figure 8.6 shows a contour plot of the energy-weighted mean reliability-index $\overline{r_r}$, as a function of V_{or} and $\Delta d\%$ for a single set of data at normal incidence. As noted previously for the (111) and (100) surfaces and for Cu(111), there is a valley of "good fit" running diagonally across the plot and a pronounced minimum. The value of $\overline{r_r}$ at the minimum (viz. 0.10) indicates a close correspondence between the experimental and calculated I(E) curves for this set of data at normal incidence; in this case the conditions for the minimum are V_{or}=-11.2±0.6eV and $\Delta d\%$=-2.5±1.2%.

The results of the reliability-index analyses for the two independent sets of experimental data at the two angles of incidence employed are collected in Table 8.1. The agreement both between different angles of incidence and different experiments is at least as good as that found for the other faces of rhodium. As was found for Rh(111), the off-normal incidence data appear to show a greater percentage contraction than do the normal incidence data. For both angles the second experiment shows a smaller contraction than the first; again it appears that experimental error must limit the accuracy of a result at a particular angle to 1 or 2% of the bulk spacing.

The energy-weighted mean of the results in Table 8.1 yields a contraction of the topmost interlayer spacing of 2.7±2.0%, compared with the bulk spacing, and V_{or}=-10.7±1.0eV. This value of the inner potential compares rather well with those found with the same ion-core potential for the other rhodium faces (viz. -11.5±0.7 and -11.0±0.6eV).

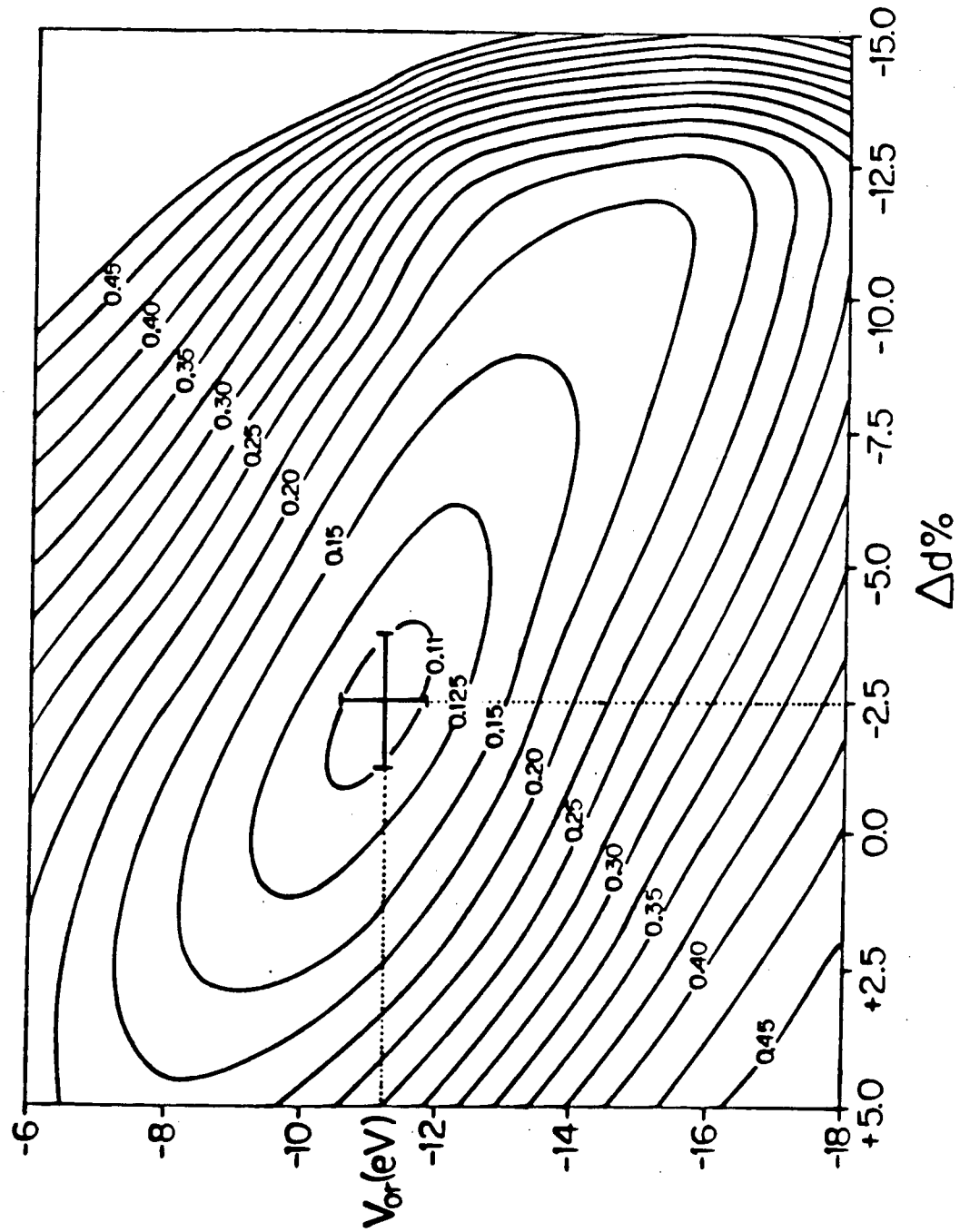

Figure 8.6 A contour plot for Rh(110) of $\overline{r_r}$ versus V_{or} and Δd% for data at normal incidence and a calculation for the V_{RAU} potential.

Direction of incidence	Experiment	No. of beams compared	Energy range compared	Conditions for best agreement $\Delta d\%$	V_{or}	$\bar{r}_r$
$\theta=0°$	1	5	894 eV	-2.5±1.2%	-11.2±0.6eV	0.10
$\theta=0°$	2	5	728 eV	-1.0±1.2%	-10.5±0.8eV	0.09
	mean values:			-1.8±1.2%	-10.8±0.7eV	
$\theta=10°$, $\phi=135°$	1	8	878 eV	-4.4±2.0%	-11.0±1.0eV	0.25
$\theta=10°$, $\phi=135°$	2	8	896 eV	-2.6±2.1%	- 9.9±1.0eV	0.25
	mean values:			-3.5±2.0%	-10.5±1.0eV	

Table 8.1 Conditions of best agreement between experiment and multiple-scattering calculations measured for two angles of incidence on Rh(110).

8.4 Comparisons With Previous Work

On a percentage basis, the Rh(110) surface appears to be slightly more contracted than the (111) or (100) surfaces. The contraction of about 3% for Rh(110) is to be compared with the contractions of 5% for Ni(110)[11,135], 5 to 10% for Ag(110)[106,107] and between 10 and 15% for the (110) surface of Al[108,110-112] reported previously with multiple-scattering calculations. Similar or slightly lower contractions have been indicated for the latter surfaces by the convolution-transform method [101]. However, with the exception of the latter approach and the latest work on Ag(110)[106], all the other comparisons of experimental and calculated intensities have been made visually and are therefore liable to unknown degrees of error associated with subjective evaluation of the data.

The question of surface roughness raised over Al(110)[108] and Ag(110)[106,134] cannot be conclusively refuted for Rh(110). The sharpness of the LEED patterns, the generally similar appearance of symmetrically related beams and the substantial agreement of theory and experiment argue against such a problem. On the other hand, there are significant differences between members of symmetrically-related beam sets and the experimental I(E) curves for the $\theta=10°, \phi=135°$ data do show poorer agreement with calculations than is the case for normal incidence. The assessment of the effect of surface imperfections on experimental I(E) curves requires detailed and careful studies of a type that have not yet been initiated.

REFERENCES

1. L. de Broglie, Phil. Mag. 47 (1924) 446

2. C. J. Davisson and C. H. Kunsman, Science 52 (1921) 522

3. H. E. Farnsworth, Phys. Rev. 25 (1925) 41

4. C. J. Davisson and L. H. Germer, Phys. Rev. 30 (1927) 705

5. C. Eckert, Proc. Nat. Acad. Amer. 13 (1927) 460

6. G. P. Thomson, Contemp. Phys. 9 (1968) 1

7. G. A. Somorjai and H. H. Farrell, Adv. Chem. Phys. 20 (1971) 215

8. K. A. R. Mitchell, Contemp. Phys. 14 (1973) 251

9. M. B. Webb and M. G. Lagally, Solid State Phys. 28 (1973) 301

10. G. Ertl and J. Kuppers, "Low Energy Electrons and Surface Chemistry", Monographs in Modern Chemistry 4, Verlag Chemie, Weinheim 1974, Ch. 9

11. J. E. Demuth, P. M. Marcus and D. W. Jepsen, Phys. Rev. B11 (1975) 1460

12. J. B. Pendry, "Low Energy Electron Diffraction", Academic Press, New York, 1974

13. C. B. Duke, Adv. Chem. Phys. 27 (1974) 1

14. G. A. Somorjai,"Principles of Surface Chemistry", Prentice Hall, Englewood Cliffs, New Jersey, 1972

15. S. Y. Tong, Progress in Surface Science 7 (1975) 1

16. C. W. Tucker Jr., J. Appl. Phys. 37 (1966) 3013, 4147

17. C. W. Tucker Jr., Acta Met. 15 (1967) 1465

18. D. G. Castner, B. A. Sexton and G. A. Somorjai, Surface Sci. 71 (1978) 519

19. L. McDonnell and D. P. Woodruff, Surface Sci. 46 (1974) 505

20. G. E. Laramore, Phys. Rev. B9 (1974) 1204

21. D. C. Frost, K. A. R. Mitchell, F. R. Shepherd, and P. R. Watson, J. Vac. Sci. Technol. 13 (1976) 1196

22. R. L. Park, in "Experimental Methods in Catalysis Research 3", ed. R. B. Anderson and P. T. Dawson,

Academic Press, 1976

23. E. Zanazzi and F. Jona, Surface Sci. 62 (1977) 61

24. H. P. Bonzel, C. R. Helms and S. Keleman, Phys. Rev. Letters 35 (1975) 1237

25. A. Ignatiev, A. V. Jones and T. N. Rhodin, Surface Sci. 30 (1972) 573

26. F. Jona and P. M. Marcus, Comment Sol. State Phys. 8 (1977) 1

27. G. C. Bond, "Catalysis by Metals", Academic Press, London, 1962

28. D. Pines, "Elementary Excitations in Solids", Benjamin, New York, 1964

29. E. A. Wood, J. Appl. Phys. 35 (1964) 1306

30. N. F. M. Henry and K. Lonsdale, eds. "International Tables for X-Ray Crystallography", Vol. 1 (1952), The Kynoch Press, Birmingham

31. P. J. Estrup and E. G. McRae, Surface Sci. 25 (1971) 1

32. R. L. Park and H. H. Madden Surface Sci. 11 (1968) 188

33. P. W. Palmberg and T. N. Rhodin, Phys. Rev. 161 (1967) 586

34. S. Andersson and B. Kasemo, Surface Sci. 25 (1971) 273

35. C. W. Tucker and C. B. Duke, Surface Sci. 15 (1969) 231

36. M. B. Webb and M. G. Lagally, Solid State Phys. 28 (1973) 301

37. E. G. McRae, J. Chem. Phys. 45 (1966) 3258

38. A. Ignatiev, J. B. Pendry and T. N. Rhodin, Phys. Rev. Letters 26 (1971) 189

39. P. Auger, J. Phys. Radium 6 (1925) 205

40. T. W. Haas, G. J. Grant, A. G. Jackson and M. P. Hooker, "A Bibliography of LEED and AES" in Progress in Surface Science Vol. 1 (1), Pergamon Press, Oxford, 1971

41. J. C. Tracy, in "Electron Emission Spectroscopy", ed. W. Dekeyser et al, Reidel Publishing Co., Dordrecht, 1973

42. D. T. Hawkins, "AES:A Bibliography, 1925-1975, IFI-

Plenum, New York, 1977

43. T. E. Gallon and J. A. D. Matthew, Rev. Phys. Technol. 3 (1972) 31

44. C. C. Chang in "Characterization of Solid Surfaces, ed. P. F. Kane, G. B. Larrabee, Plenum Press, New York, 1974

45. H. E. Bishop and J. C. Riviere, J. Appl. Phys. 40 (1969) 1740

46. J. A. Bearden and A. P. Burr, Rev. Mod. Phys. 39 (1967) 125

47. K. Sieghahn et al, "ESCA:Atomic, Molecular and Solid State Structure Studied by Means of Electron Spectrscopy", Almquist and Wiksells, Uppsala, 1967

48. M. F. Chung and L. H. Jenkins, Surface Sci. 22 (1970) 479

49. M. E. Packer and J. M. Wilson, "Auger Transitions", Institute of Physics, London, 1973

50. P. W. Palmberg et al, "Handbook of Auger Spectra", Physical Electronics Industries Inc., Minnesota, 1972

51. R. E. Weber and A. L. Johnson, J. Appl. Phys. 40 (1969) 314

52. M. Pedereau, Surface Sci. 24 (1971) 239

53. L. F. Mattheis, Phys. Rev. 133 (1964) A 1399

54. S. Y. Tong, J. B. Pendry and L. L. Kesmodel, Surface Sci. 54 (1976) 21

55. J. C. Slater, Adv. Quantum Chem. 6 (1972) 1

56. K. H. Johnson, Adv. Quantum Chem. 7 (1973) 143

57. F. Herman and S. Skillman, "Atomic Structure Calculations", Prentice Hall, Englewood Cliffs, N. J., 1963

58. K. Schwarz, Phys. Rev. B5 (1972) 2466

59. K. Schwarz, Theoret. Chim. Acta 34 (1974) 225

60. G. A. Burdick, Phys. Rev. 129 (1963) 138

61. M. I. Chodorow, Ph.D. Thesis, Massachusetts Institute of Technology, 1939

62. R. W. G. Wyckoff, "Crystal Structures", Vol. 1, Interscience, N. Y., 1963

63. J. D. H. Donnay, G. Donnay, E. G. Cox, O. Kennord, and M. U. King,"Crystal Data", Am. Crystallographic Assoc., 1963

64. V. L. Morruzzi, J. F. Janak and A. R. Williams, "Calculated Electronic Properties of Metals", Pergamon Press, New York, 1978

65. D. W. Jepsen, P. M. Marcus and F. Jona, Phys. Rev. B5 (1973) 3933

66. L. J. Schiff, "Quantum Mechanics", McGraw-Hill, New York, 1968

67. R. G. Newton, "Scattering Theory of Waves and Particles", McGraw-Hill, New York, 1966

68. D. E. Gray, ed. "American Institute of Physics Handbook", McGraw-Hill, New York, 1972

69. K. A. R. Mitchell, F. R. Shepherd, P. R. Watson and D. C. Frost, Surface Sci. 64 (1977) 737

70. G. E. Laramore and C. B. Duke, Phys. Rev. B2 (1970) 4783

71. B. W. Holland, Surface Sci. 28 (1971) 258

72. J. M. Morabito, R. F. Steiger and G. A. Somorjai, Phys. Rev. 179 (1969) 638

73. D. P. Woodruff and M. P. Seah, Phys. Status Solidi (a) 1 (1970) 429

74. M. A. Van Hove and S. Y. Tong, Surface Sci. 54 (1976) 91

75. K. A. Gschneider, Solid State Phys. 16 (1964) 275

76. S. Y. Tong and L. L. Kesmodel, Phys. Rev. B8 (1973) 3753

77. S. Y. Tong and T. N. Rhodin, Phys. Rev. Letters 26 (1971) 711

78. M. A. Van Hove and S. Y. Tong, J. Vac. Sci. Technol. 12 (1975) 230

79. J. B. Pendry, Phys. Rev. Letters 27 (1971) 856

80. See U.B.C. Computing Centre Manual "U.B.C. Curve".

81. M. A. Van Hove and J. B. Pendry, J. Phys. C8 (1975) 1362

82. N. F. M. Henry, H. Lipson and W. A. Wooster, "The Interpretation of X-Ray Diffraction Photographs", MacMillan, London, 1960

83. G. A. Somorjai, R. W. Joyner and B. Lang, Proc. Roy. Soc. London, 331 (1972) 1586

84. N. J. Taylor, "The Effect of Strong Magnetic Fields on the Operation of the LEED Instrument", Varian Vacuum Division, 1966

85. R. Nathan and B. J. Hopkins, J. Phys. E6 (1973) 1040

86. J. E. Demuth and T. N. Rhodin, Surface Sci. 42 (1974) 261

87. H. H. Madden and G. Ertl, Surface Sci. 35 (1973) 211

88. P. C. Stair, T. J. Kaminska, L. L. Kesmodel and G. A. Somorjai, Phys. Rev. B11 (1975) 623

89. A. Horder, "The Manual of Photography", Focal Press, London, 1971

90. D. P. Woodruff and B. W. Holland, Phys. Letters A31 (1970) 207

91. P. Heilmann, E. Long, K. Heinz and K. Muller, Appl. Phys. 9 (1976) 247

92. S. P. Weeks and J. E. Rowe, J. Vac. Sci. Technol. 15 (1978) 659

93. J. E. Demuth, D. W. Jepsen and P. M. Marcus, Solid State Commun. 13 (1973) 1311

94. P. M. Marcus, J. E. Demuth and D. W. Jepsen, Surface Sci. 53 (1975) 501

95. M. A. Van Hove, S. Y. Tong and M. H. Elconin, Surface Sci. 64 (1977) 85

96. "Critical Evaluation of Chemical and Physical Structural Information", Eds. P. R. Lide Jr. And M. A. Paul, National Academy of Sciences, Washington, D.C., 1974

97. L. V. Azaroff, "Elements of X-Ray Crystallography", McGraw-Hill, New York, 1968

98. J. Topping, "Errors of Observation and Their Treatment", Chapman and Hall, London, 1962

99. D. L. Adams and U. Landman, Phys. Rev. B15 (1977) 3775

100. S. L. Cunningham, C-M. Chan and W. H. Weinberg, Phys.

Rev. (in press)

101. C-M. Chan, S. L. Cunningham, M. A. Van Hove and W. H. Weinberg, Surface Sci. 67 (1977)

102. M. G. Lagally, T. C. Ngoc and M. B. Webb, Phys. Rev. Letters 26 (1971) 1557

103. M. G. Lagally, T. C. Ngoc and M. B. Webb, J. Vac. Sci. Technol. 9 (1972) 645

104. D. W. Jepsen, P. M. Marcus and F. Jona, Phys. Rev. B8 (1973) 5528

105. F. Forstman, Jap. J. of Appl. Phys., Suppl. 2, Part 2, (1974) 657

106. M. Maglietta, E. Zanazzi, F. Jona, D. W. Jepsen and P. M. Marcus, J. Phys. C10 (1977) 375

107. N. Masud, G. G. Kinniburgh and J. B. Pendry, J. Phys. C10 (1977) 1

108. Group d'Etude des Surfaces, Surface Sci. 62 (1977) 567

109. R. H. Tait, S. Y. Tong and T. N. Rhodin, Phys. Rev. Letters 28 (1972) 553

110. G. E. Laramore and C. B. Duke, Phys. Rev. B5 (1972) 267

111. D. W. Jepson, P. M. Marcus and F. Jona, Phys. Rev. B6 (1972) 3684

112. M. R. Martin and G. A. Somorjai, Phys. Rev. B7 (1973) 3607

113. B. W. Lee, R. Alsenz, A. Ignatiev and M. A. Van Hove, Phys. Rev. B15 (1978) 1510

114. G. G. Kleiman and J. M. Burkstrand, Surface Sci. 50 (1975) 493

115. R. W. Streater, W. T. Moore, P. R. Watson, D. C. Frost and K. A. R. Mitchell, Surface Sci. 72 (1978) 744

116. K. O. Legg, F. Jona, D. W. Jepsen and P. M. Marcus, J. Phys. C10 (1977) 937

117. C-M. Chan, S. L. Cunningham, M. A. Van Hove, W. H. Weinberg and S. P. Withrow, Surface Sci. 66 (1977) 394

118. A. Ignatiev, F. Jona, H. D. Shih, D. W. Jepsen and P. M. Marcus, Phys. Rev. B11 (1975) 4787

119. P. Echenique, J. Phys. C9 (1976) 3193

120. G. E. Laramore, Phys. Rev. B8 (1973) 515

121. W. N. Unertl and M. B. Webb, Surface Sci. 59 (1976) 373

122. L. L. Kesmodel, P. C. Stair and G. A. Somorjai, Surface Sci. 64 (1977) 342

123. J. A. Davies, D. P. Jackson and P. R. Norton, Proc. 7th Int. Vacuum Congress and 3rd Int. Conf. On Solid Surfaces, Vienna, 1977, p.2527

124. H. D. Shih, F. Jona, D. W. Jepsen and P. M. Marcus, J. Phys. C9 (1976) 1405

125. B. W. Lee, A. Ignatiev, S. Y. Tong and M. A. Van Hove, J. Vac. Sci. Technol. 14 (1977) 291

126. M. A. Van Hove and S. Y. Tong, Surface Sci. 54 (1976) 91

127. W. N. Unertl and H. V. Thapliyal, J. Vac. Sci. Technol. 12 (1975) 263

128. F. Jona, I.B.M. J. Res. Develop., 14 (1970) 444

129. K. O. Legg, M. Prutton and C. Kinniburgh, J. Phys. C7 (1974) 4236

130. J. T. Grant and T. W. Haas, Surface Sci. 21 (1970) 76

131. J. T. Yates, Jr., private communication

132. R. A. Marbrow and R. M. Lambert, Surface Sci. 67 (1977) 489

133. H. Eckstrom, G. G. Possley and S. E. Hannum, J. Chem. Phys. 52 (1970) 5435

134. D. Briggs, R. A. Marbrow and R. M. Lambert, Solid State Commun. 26 (1978) 1

135. W. C. Turkenburg, R. G. Smeenk and F. W. Saris, Surface Sci. 74 (1978) 181

136. J. F. van der Veen, R. G. Smeenk and F. W. Saris, Proc. 7th Int. Vacuum Congress and 3rd Int. Conf. On Solid Surfaces, Vienna, 1977, p.2515

137. M. D. Chinn and S. C. Fain, J. Vac. Sci. Technol. 14 (1977) 314

138. F. Jona, Surface Sci. 68 (1977) 204

APPENDICES

The following appendices contain all the experimental data from rhodium surfaces used during this work. In all cases except one, the data is as collected and has not been smoothed or manipulated in any way save for a correction to unit incident beam current. The exception (A7) shows data that has been averaged and smoothed; unfortunately the failure of a tape cassette has led to irrecoverable loss of the original data in this instance. The contents of the appendices are listed below.

APPENDIX	SURFACE	ANGLE	DATA SET
A1	(111)	$\theta = 0^o, \phi = 0^o$	1
A2			2
A3			3
A4		$\theta = 10^o, \phi = 109^o$	1
A5			2
A6			3
A7	(100)	$\theta = 0^o, \phi = 0^o$	1
A8			2
A9		$\theta = 9^o, \phi = 20^o$	1
A10	(110)	$\theta = 0^o, \phi = 0^o$	1
A11			2
A12		$\theta = 10^o, \phi = 135^o$	1
A13			2

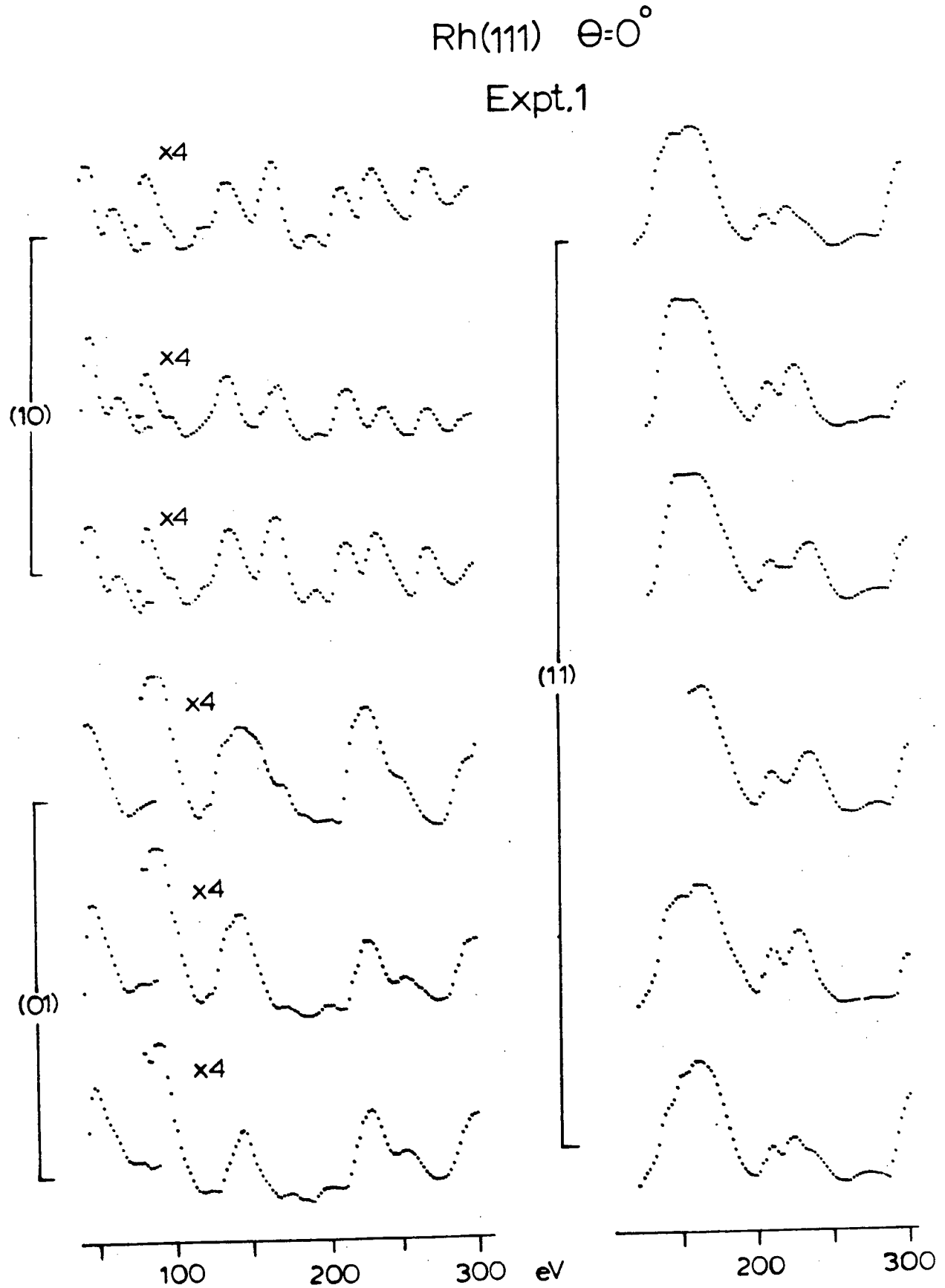

A1

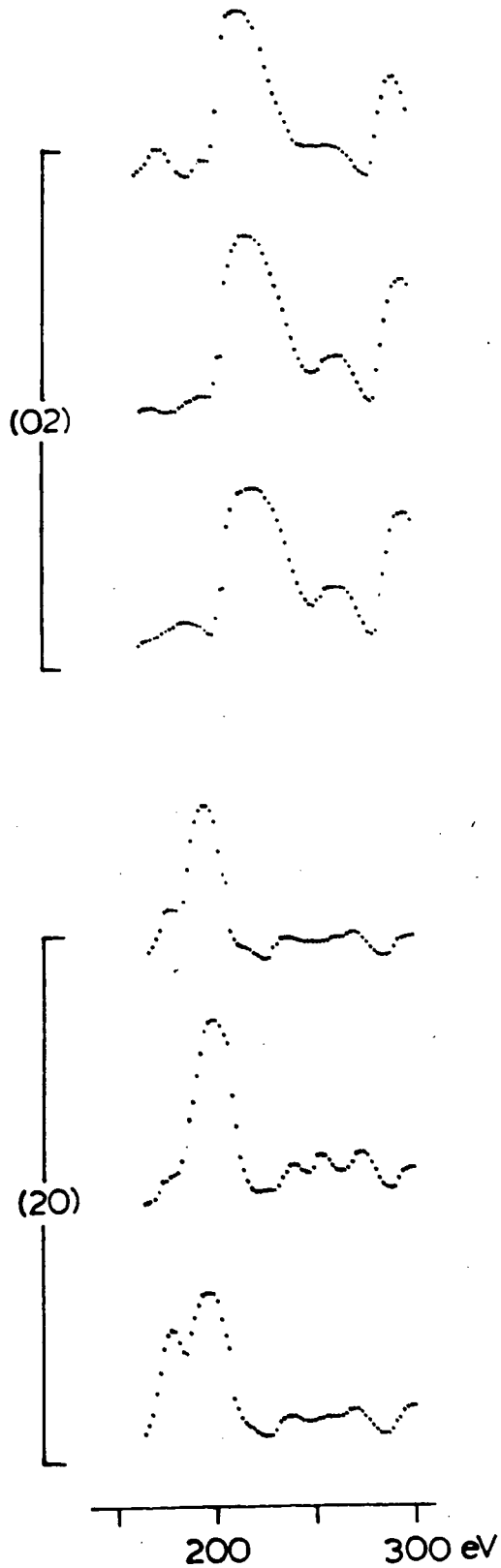

A1

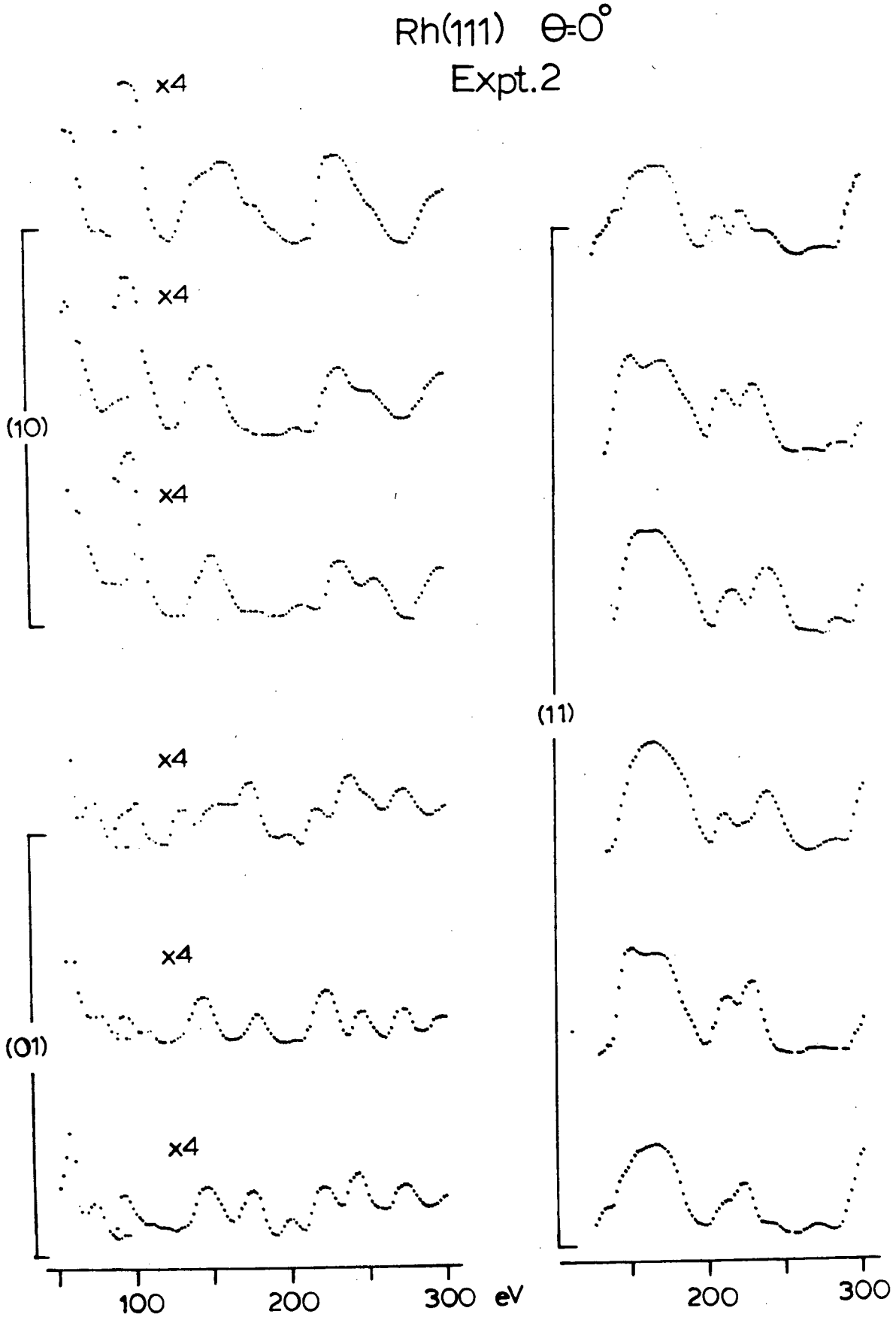

A2

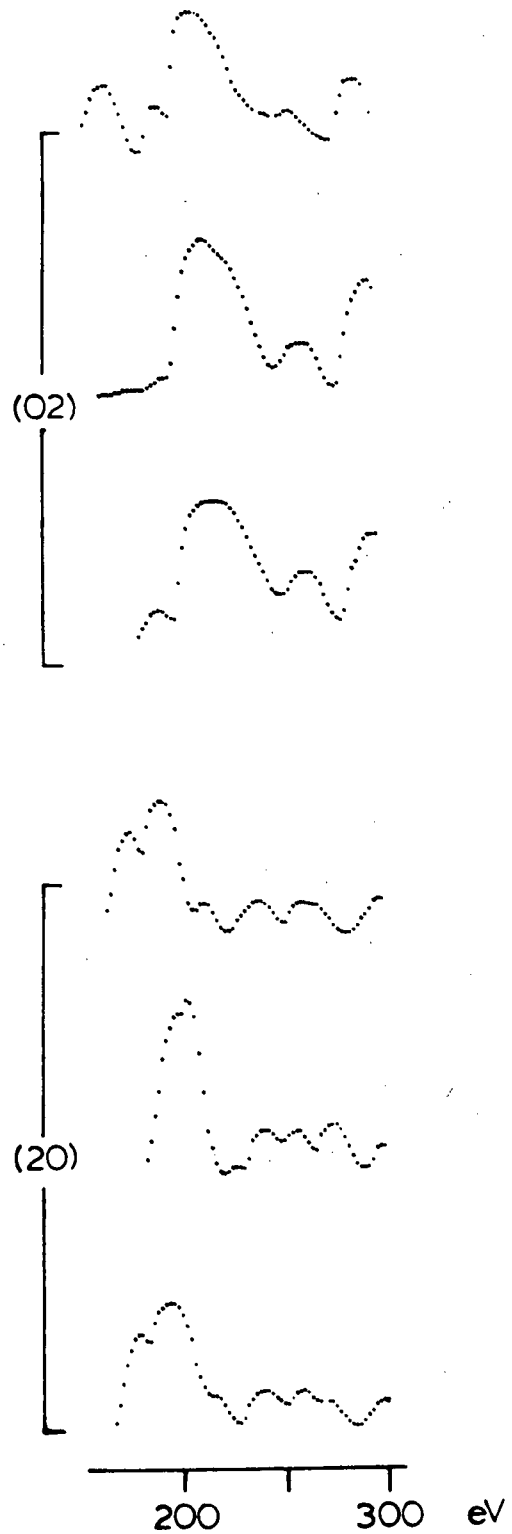

A2

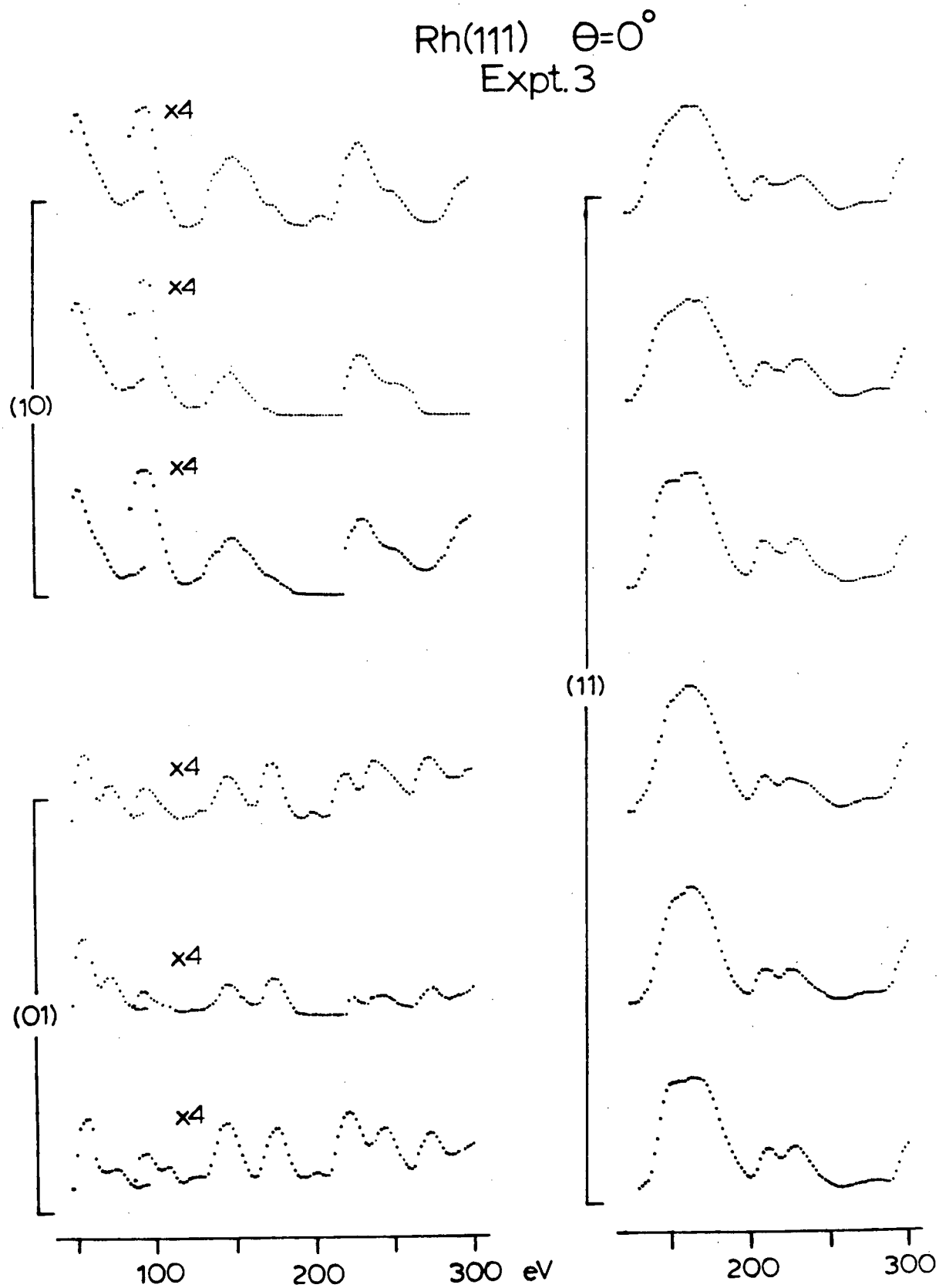

A3

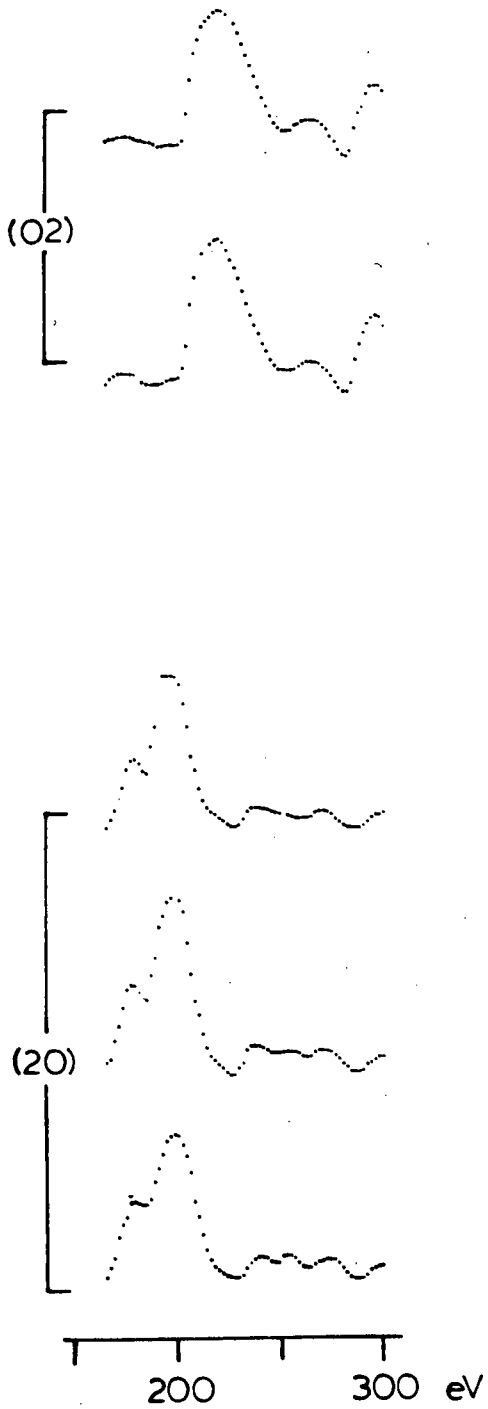

A3

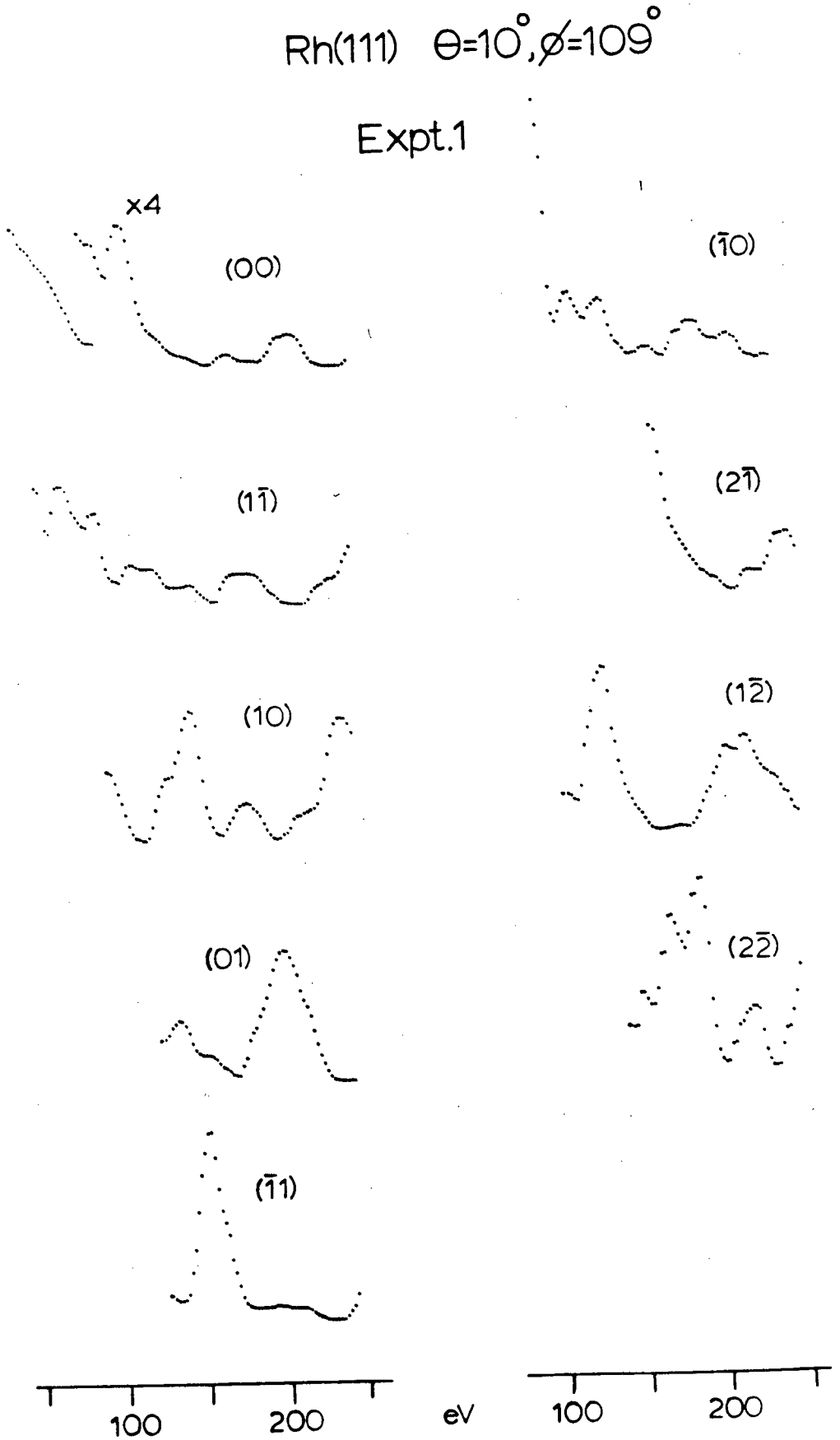
Rh(111) θ=10°,ø=109°
Expt.1
x4
(00)
(1̄0)
(1̄1̄)
(2̄1̄)
(10)
(1̄2̄)
(01)
(2̄2̄)
(1̄1)
100
200
eV
100
200

A4

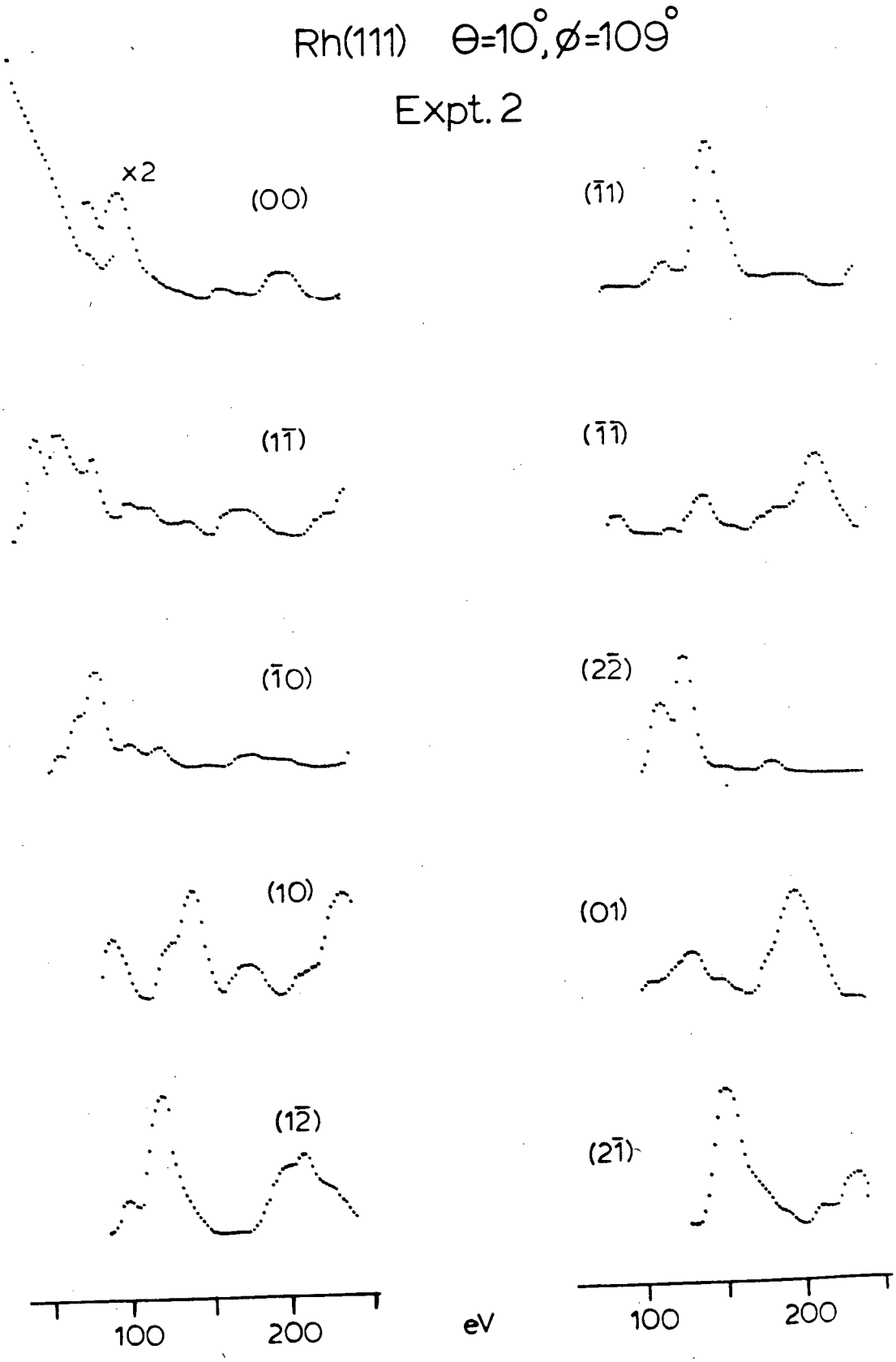
Rh(111) θ=10°, ø=109°
Expt. 2
x2
(00)
(1̄1)
(1 1̄)
(1̄1̄)
(1̄0)
(2 2̄)
(10)
(01)
(1 2̄)
(2 1̄)
100
200
eV
100
200

A5

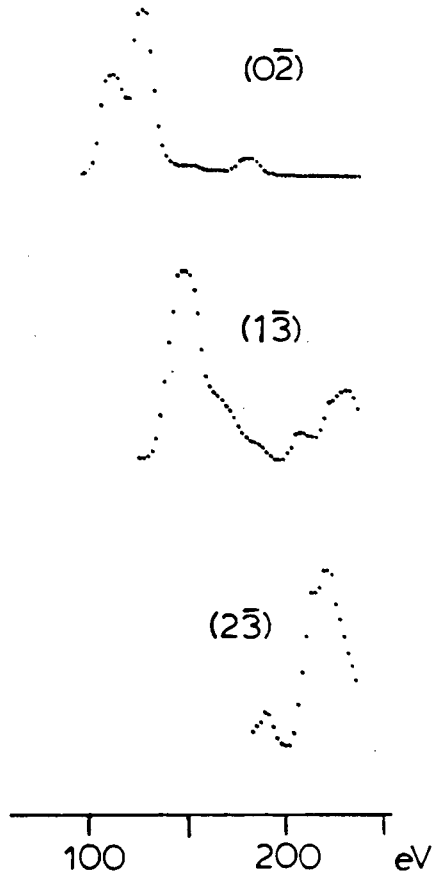

A5

Rh(111) $\theta=10^{\circ}, \phi=109^{\circ}$

Expt.3

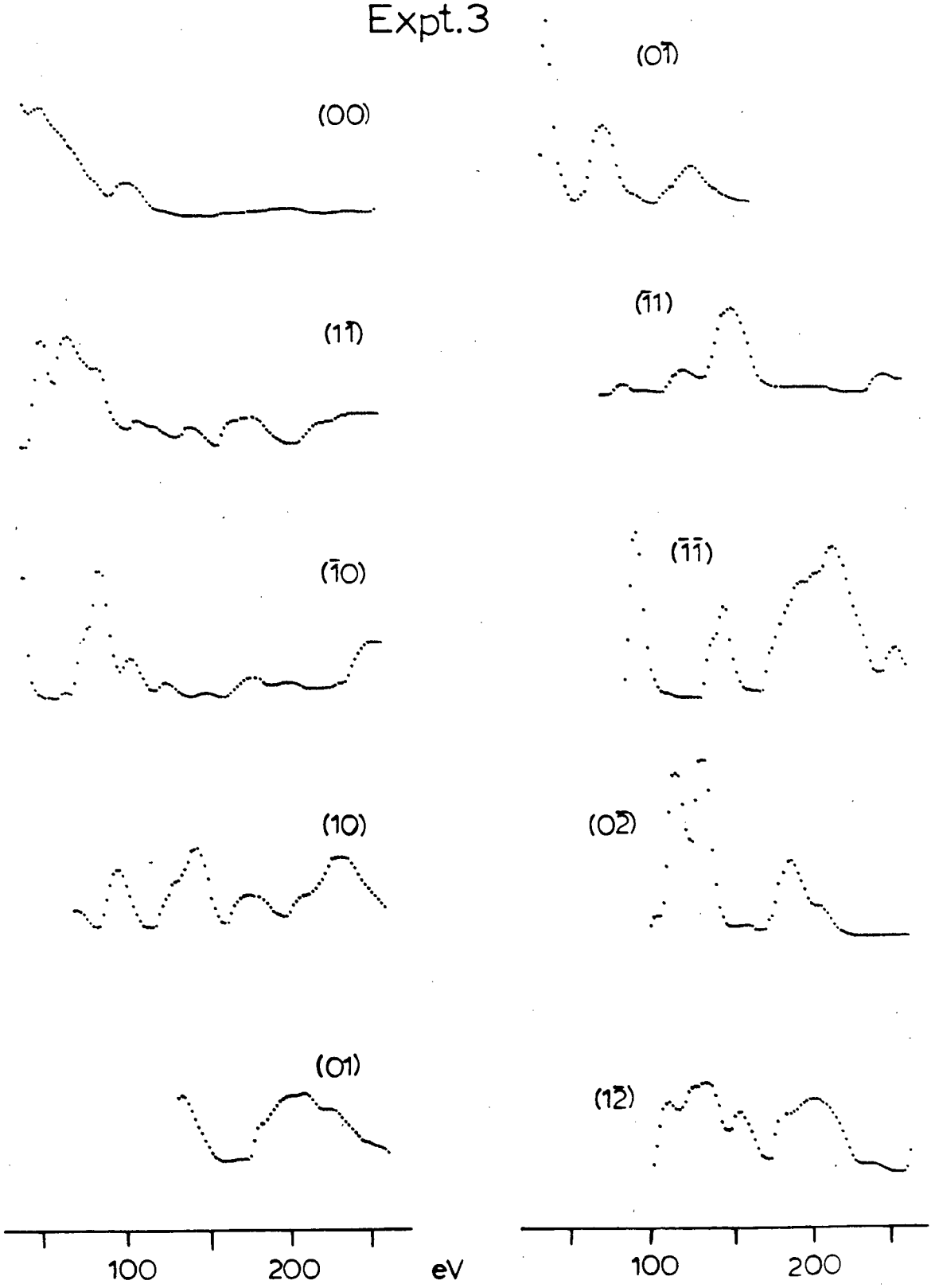

A6

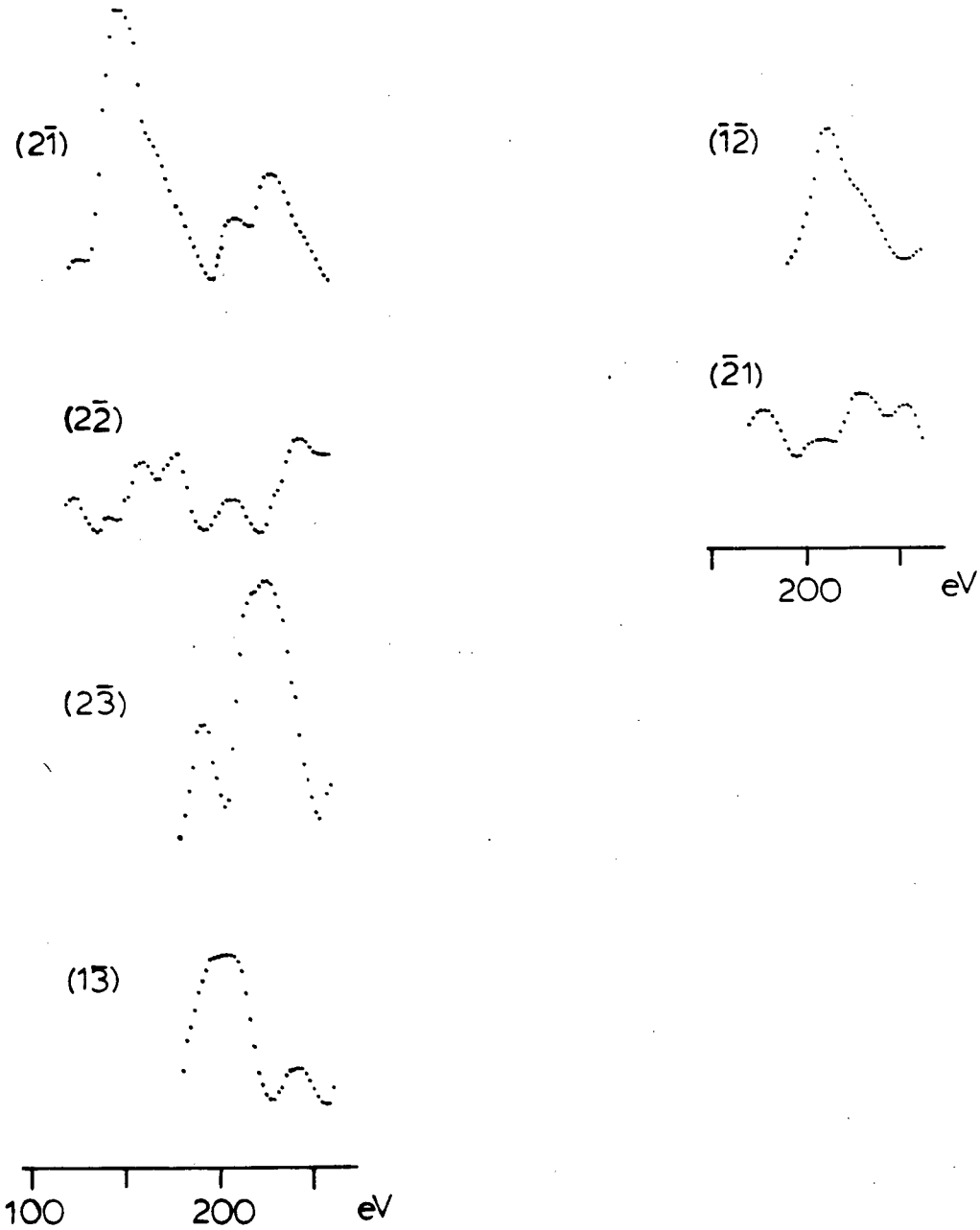

A6

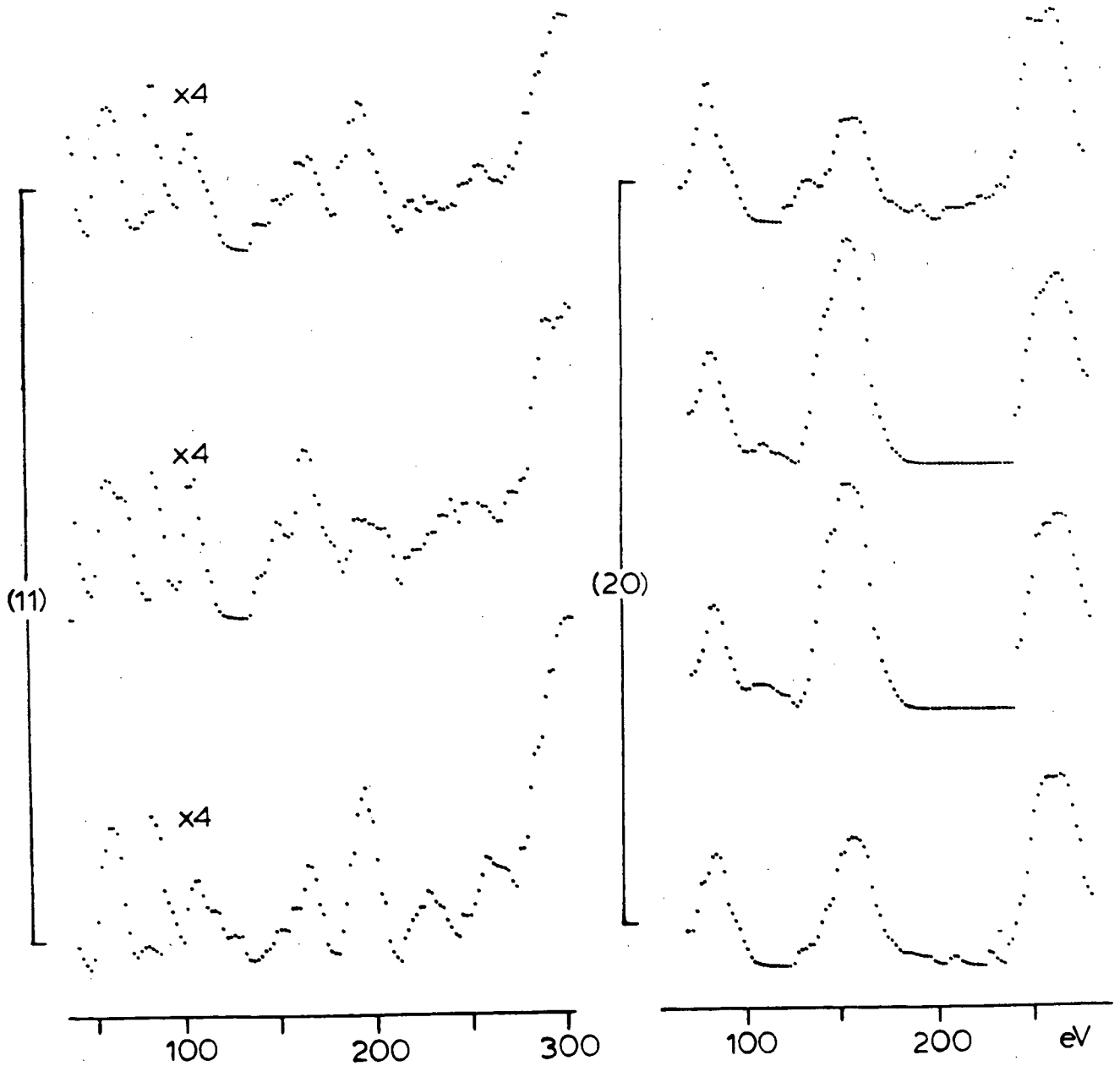

A7

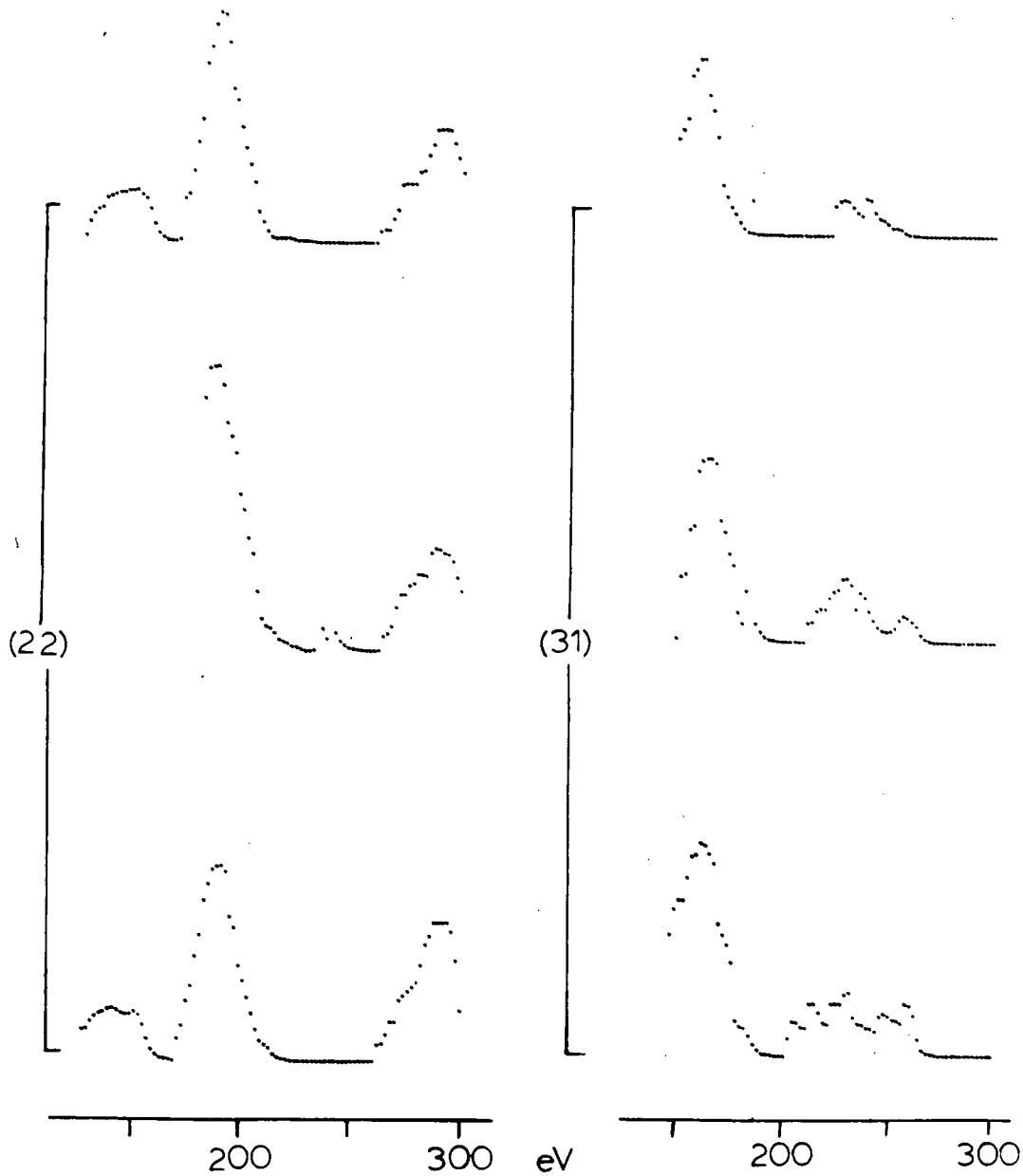

A7

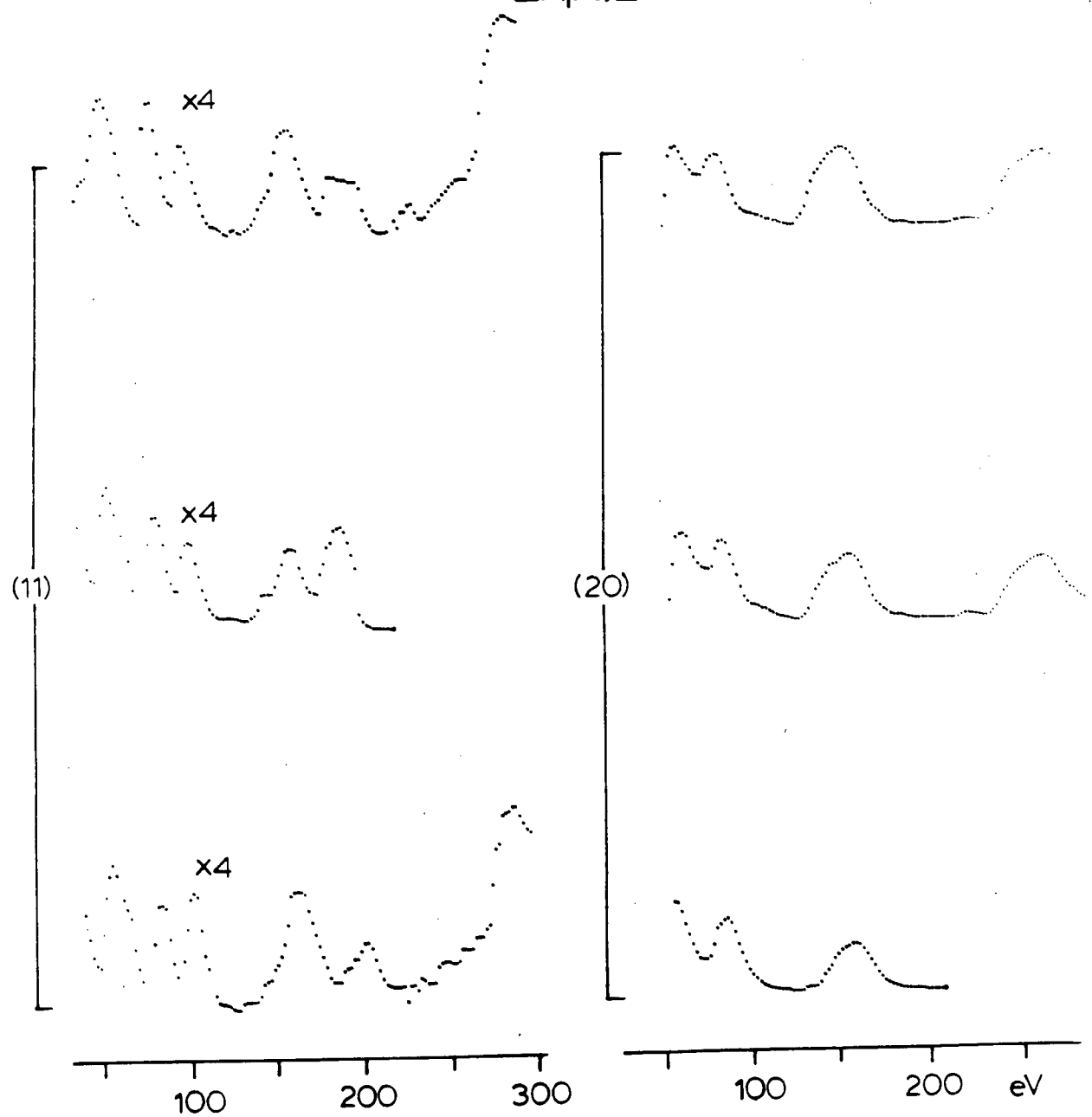

A8

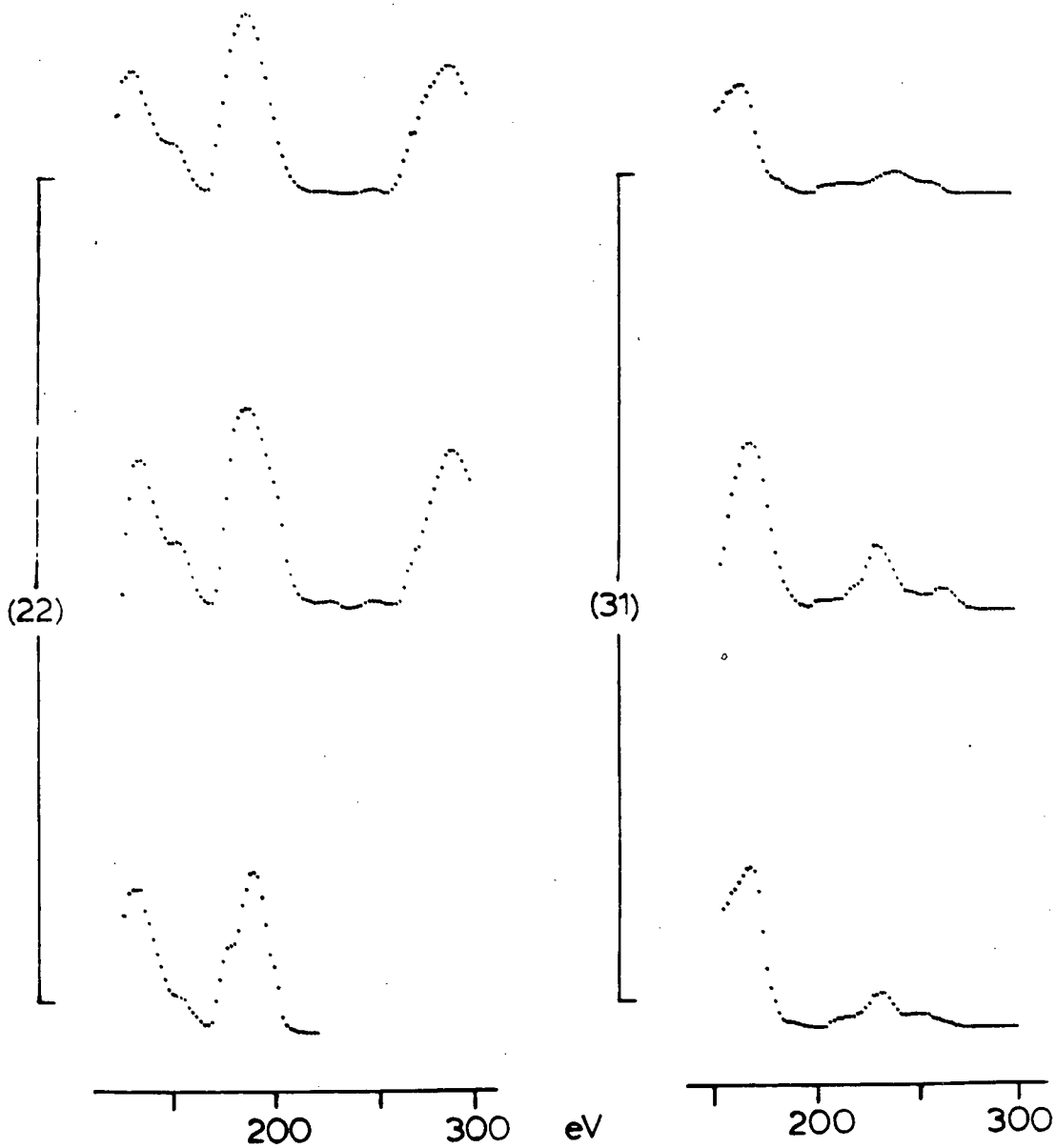

A8

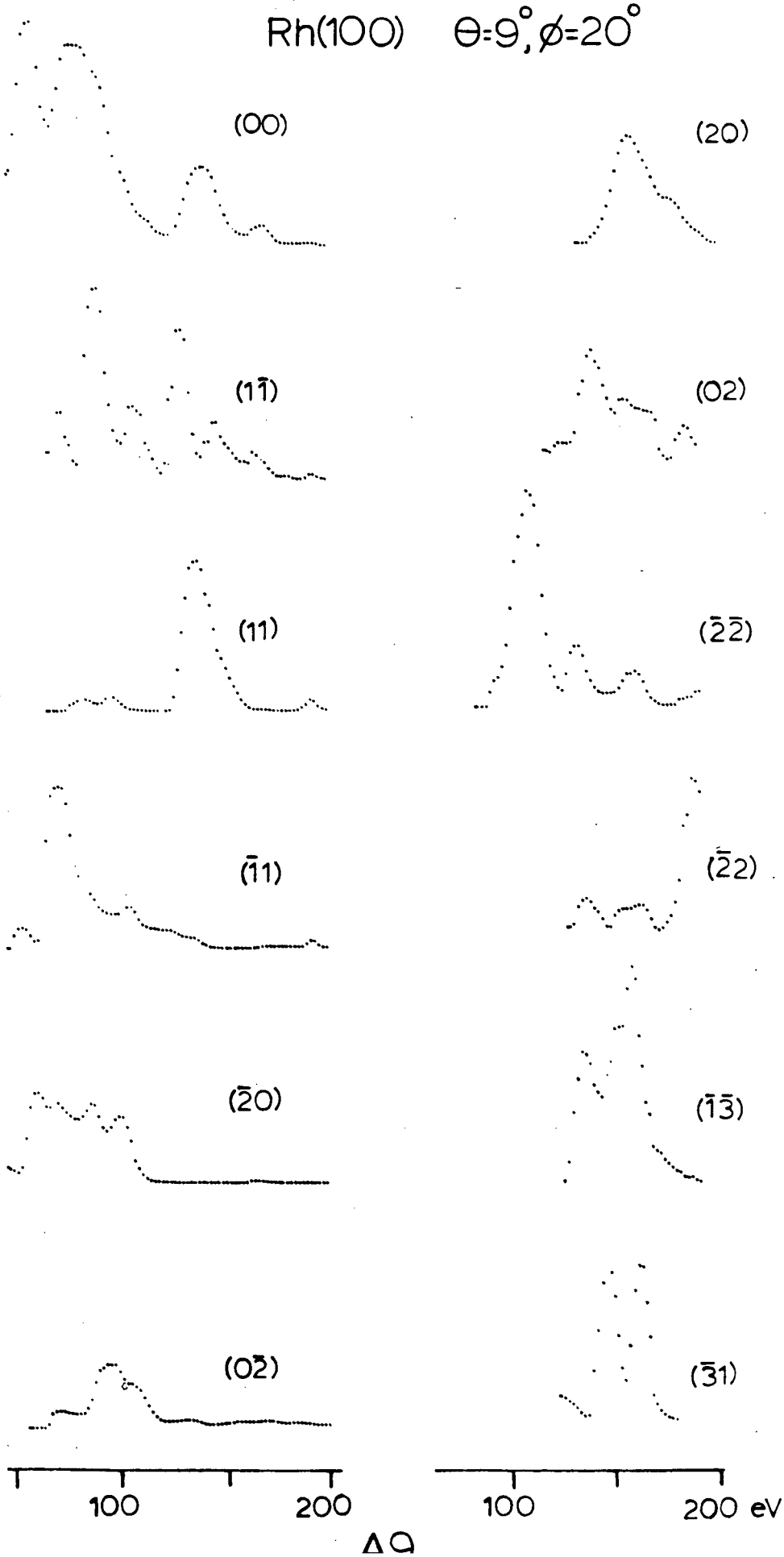
Rh(100) θ=9°, ø=20°
(00)
(20)
(1$\bar{1}$)
(02)
(11)
($\bar{2}\bar{2}$)
($\bar{1}$1)
($\bar{2}$2)
($\bar{2}$0)
($\bar{1}\bar{3}$)
(0$\bar{2}$)
($\bar{3}$1)
100
200
100
200 eV
ΔQ

Rh(110) $\Theta=0^\circ$

Expt.1

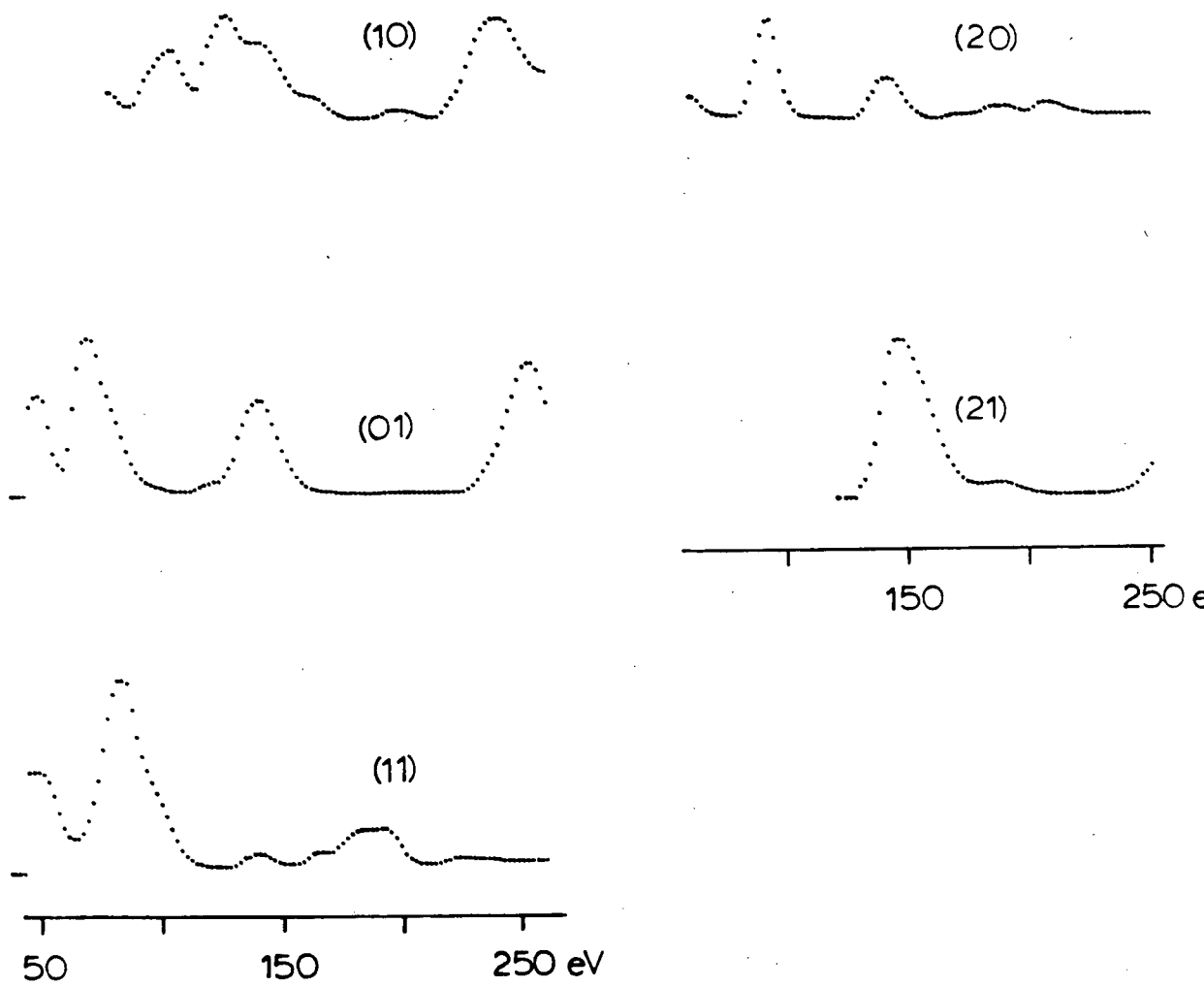

A10

Rh(110) $\theta = 0^\circ$

Expt. 2

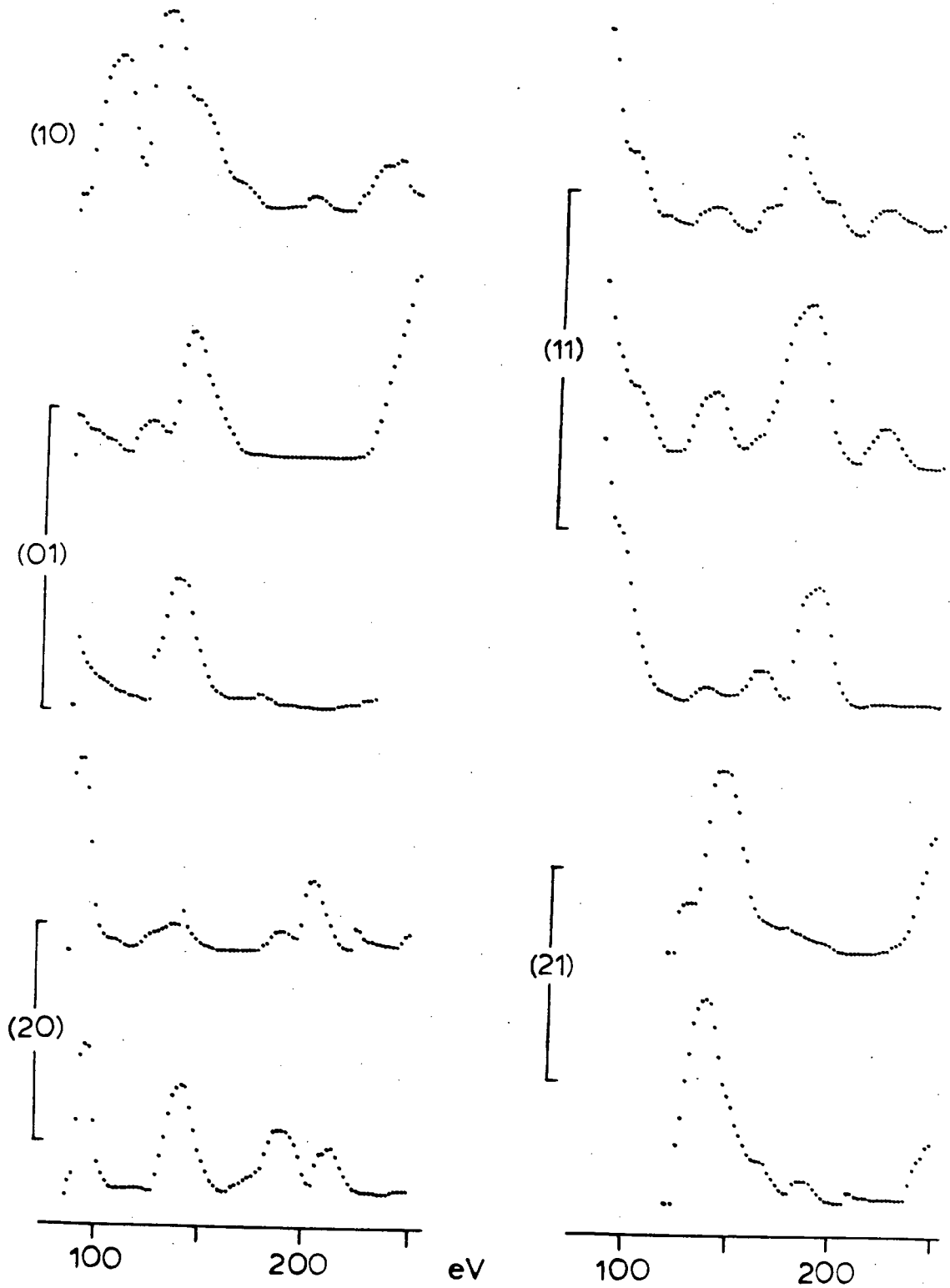

A11

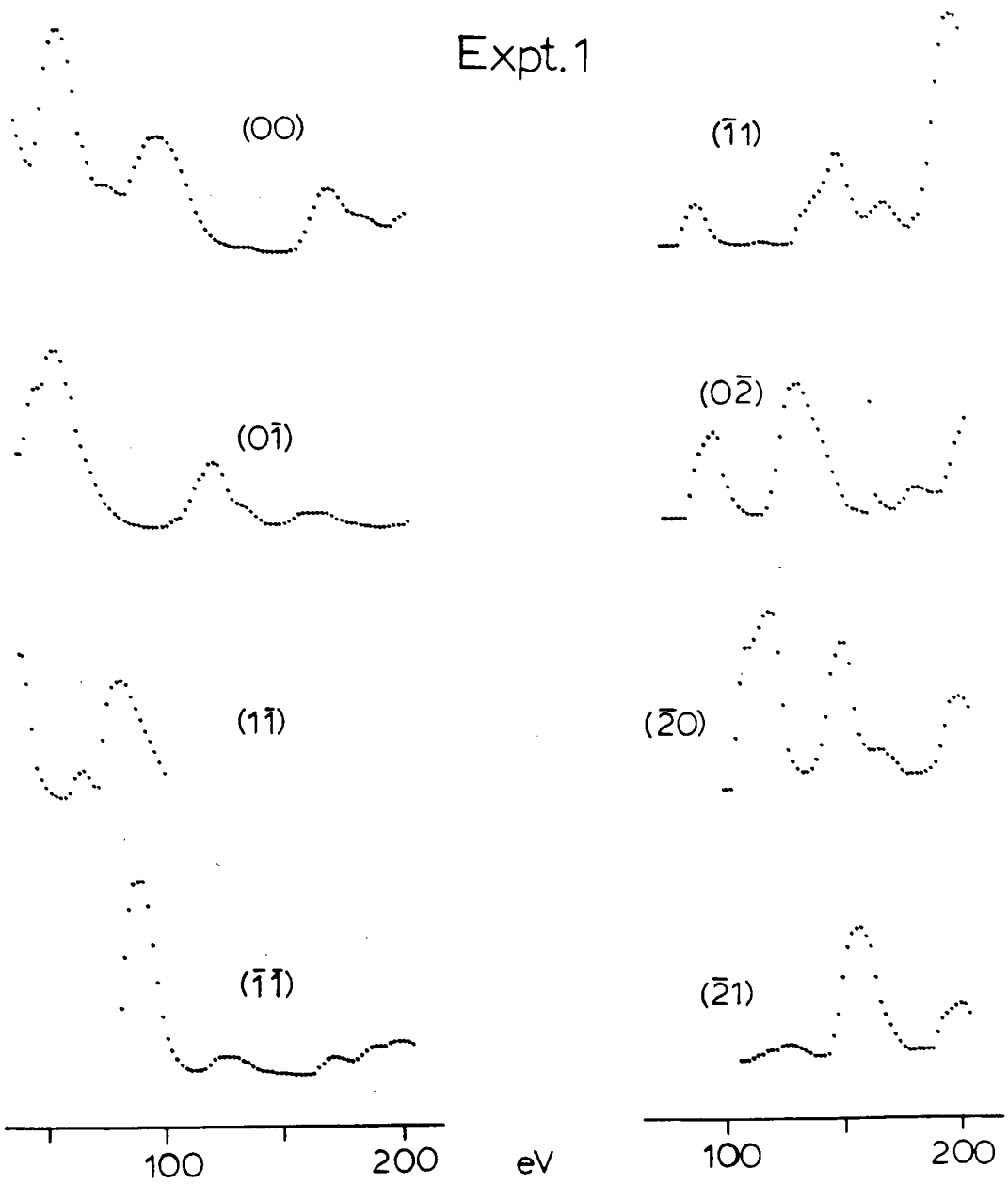

A12

Rh(110) $\Theta=10^{\circ}, \phi=135^{\circ}$

Expt. 2

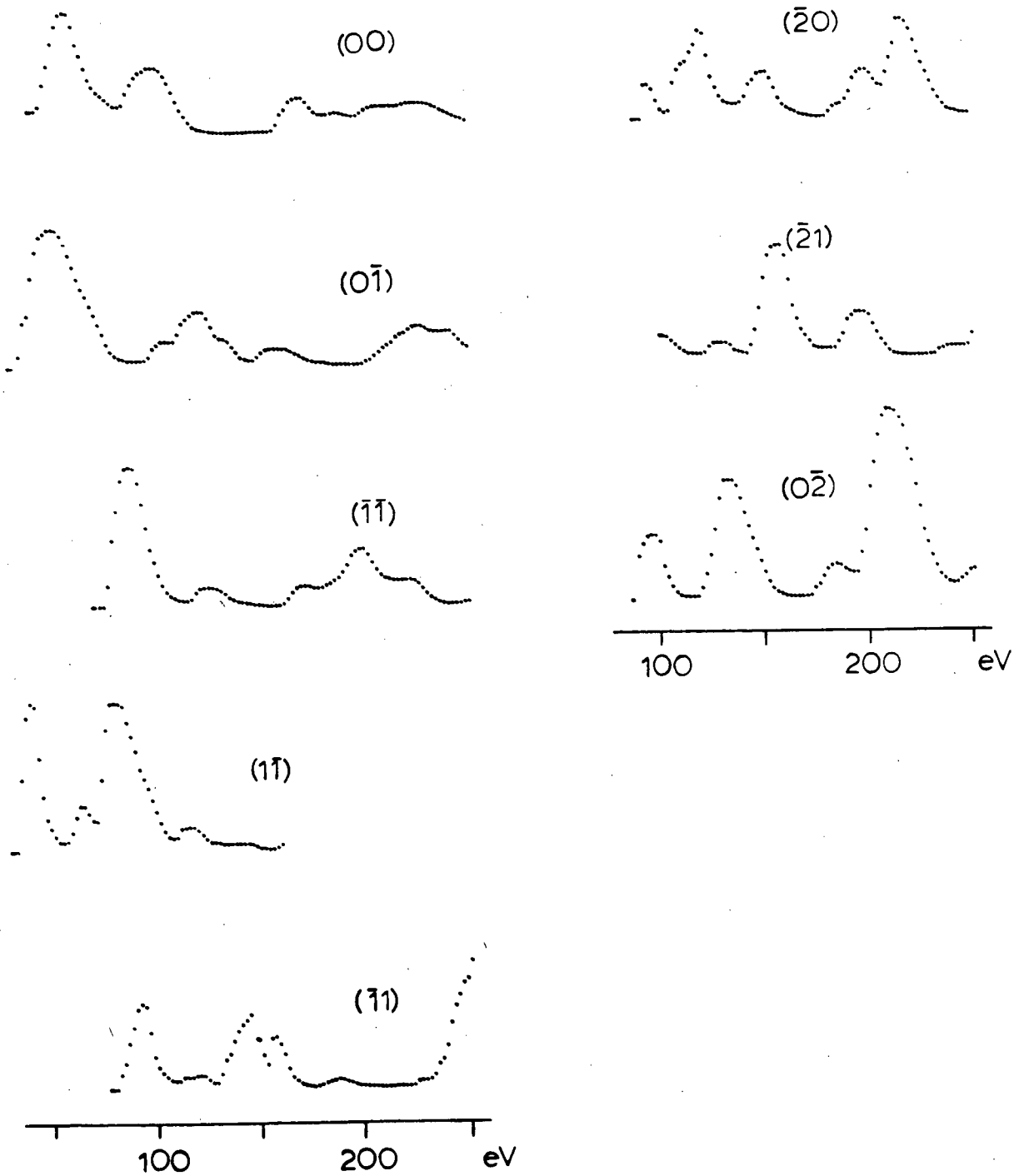

A13

PUBLICATIONS

"Use of a Vidicon camera for the measurement of LEED beam intensities by the photographic method," D.C. Frost, K.A.R. Mitchell, F.R. Shepherd and P.R. Watson, Journal of Vacuum Science and Technology, 13 (1976), 1196-98.

"Structure determination of the (100) surface of rhodium by LEED," K.A.R. Mitchell, F.R. Shepherd, P.R. Watson and D.C. Frost, Surface Science, 64 (1977), 737-750.

"Surface Structures of Rhodium Studied by LEED," D.C. Frost, K.A.R. Mitchell, F.R. Shepherd and P.R. Watson, Proceedings of the 7th International Vacuum Congress and 3rd International Conference on Solid Surfaces, Vienna, 1977, pA-2725 (Poster).

"LEED intensities from Cu(311) and Ni(311)," D.C. Frost, K.A.R. Mitchell, W.T. Moore, R.W. Streater and P.R. Watson, Ibid, p2403-2406.

"Applications of the reliability factor proposed for LEED by Zanazzi and Jona to structure determinations of the Rh(100) and Cu(111) Surfaces," P.R. Watson, F.R. Shepherd, D.C. Frost and K.A.R. Mitchell, Surface Science, 72 (1978), 562-576.

"The Structure of the (311) surface of copper as determined by multiple scattering calculations of LEED intensities," R.W. Streater, W.T. Moore, P.R. Watson, D.C. Frost and K.A.R. Mitchell, Surface Science, 72 (1978), 744-748.

"An investigation with LEED of the structure of the (111) surface of rhodium," F.R. Shepherd, P.R. Watson, D.C. Frost and K.A.R. Mitchell, Accepted for publication by Journal of Physics.

"The structure of the (110) surface of rhodium,"D.C. Frost, S. Hengrasmee,K.A.R. Mitchell,F.R. Shepherd and P.R. Watson,Surface Science,76(1978)1585-1589.